ALMA MATER STUDIORUM - UNIVERSITÀ DI BOLOGNA

DOTTORATO DI RICERCA IN:
Ingegneria Biomedica, Elettrica e dei Sistemi (IBES)
Curriculum in Bioingegneria

Ciclo XXXI

Settore Concorsuale: 09/G2
Settore Scientifico Disciplinare: ING-INF/06

ANALYSIS AND MEASUREMENT OF TUMOUR HETEROGENEITY THROUGH MULTI-MODALITY IMAGING

Presentata da: **Serena Baiocco**

Coordinatore Dottorato
Prof. Daniele Vigo

Supervisore
Prof. Alessandro Bevilacqua

Co-Supervisore
Prof. Giampaolo Gavelli

Esame finale anno 2019

To my parents

“A picture is worth a thousand words”

External reviewers

Prof. **Vicky Goh**, King's College London, United Kingdom,
email: vicky.goh@kcl.ac.uk

Prof. **Francesca Odone**, Università degli Studi di Genova, Italy,
email: francesca.odone@unige.it

Keywords

Image Processing

Texture Analysis

Heterogeneity

Tumour

Hybrid system

Multi-modality Imaging

Abstract (English version)

Cancer is among the leading causes of mortality worldwide. Despite cancer death rate has been decreasing thanks to the introduction of novel target therapies, improvements in tumour characterisation, staging, prognosis, as well as treatment monitoring and planning are required. The need for more effective functional biomarkers as well as the awareness of the complexity of the tumour biology, which reflects the widely studied tumour heterogeneity, have prompted the use of imaging modalities able to inquire into biological aspects of the intra-tumoural heterogeneity at different levels, structural, functional and molecular.

Dynamic Contrast Enhanced - Computed Tomography (DCE-CT), Magnetic Resonance Imaging (MRI) and Positron Emission Tomography (PET) have shown promising results, also leading to improvements in tumour diagnosis, staging and prognosis. However, there are still some open issues requiring proper reliability analyses, development of more quantitative approaches as well as more complex biomarkers involving the evaluation of the tumour heterogeneity.

Part I of the Thesis presents the topics and issues regarding the image-based biomarkers used till now, the obstacles preventing the use of DCE-CT in the clinical practice, as well as the methodological contributions introduced to face these issues; Part II of the Thesis is dedicated to the applications of the methodological approaches devised in Part I and in most cases already published. In particular, the reliability topic concerning the perfusion maps derived from DCE-CT image series has been faced. Downstream of this analysis, it has been investigated the ability of perfusion parameters, at diagnosis, to improve tumour characterisation of predominant lung cancer subtypes. Then, an automatic methodological approach has been developed to classify the spatio-temporal heterogeneity of lung tumour, as performed by expert radiologists through the visual interpretation of DCE-CT series. Afterwards, a novel local-based method has been developed to evaluate the intra-tumoural heterogeneity emerging from perfusion maps of lung

tumours. The ability of the features extracted to act as a prognostic image-based biomarker has been early assessed. To face the issue of the high variability present in PET data, a robust approach was introduced to represent a high uptake activity. To this purpose, a method to perform a 3D segmentation starting from PET images has been developed and applied to segment the whole kidneys in PET/CT series. Then, a multi-modal analysis of the intra-tumoural heterogeneity has been performed in the gastro-oesophageal junction (GOJ) cancer. In particular, the heterogeneity of GOJ tumours acquired with both FDG-PET/CT and FDG-PET/MRI has been analysed. The ability of the quantitative image-based biomarker extracted to predict distant metastasis has been early assessed. The results showed that more complex texture features have a better performance in prognosis compared to the PET- and MRI-derived parameters commonly used in clinical routine. Finally, an algorithm to detect sub-regions in tumour volumes has been developed to combine multi-modal information. To this purpose, a 3D registration algorithm was implemented in order to automatically transform and align the multi-modal dataset related to each patient into one x-y-z coordinate system.

Abstract (Italian version)

Il cancro è tra le principali cause di morte al mondo. Nonostante il tasso di mortalità si sia abbassato negli ultimi decenni grazie all'introduzione di nuove terapie *target*, miglioramenti nella caratterizzazione tumorale, stadiazione, prognosi, nonchè nel monitoraggio e nella pianificazione delle terapie sono comunque ancora necessari. Il bisogno di *biomarker* funzionali che siano maggiormente efficaci, così come la consapevolezza dell'estrema complessità biologica dei tumori, che si riflette in una eterogeneità del tessuto tumorale, hanno promosso l'utilizzo di tecniche di *imaging* in grado di rilevare gli aspetti biologici peculiari dell'eterogeneità a differenti livelli, strutturale, funzionale e molecolare.

La Tomografia Computerizzata perfusionale (TCp), la Risonanza Magnetica (RM) e la Tomografia ad Emissione di Positroni (PET) hanno mostrato risultati promettenti, che hanno anche condotto a miglioramenti nella diagnosi, nella stadiazione e nella prognosi. Tuttavia, questi successi sono ostacolati dalla quasi assenza di approcci orientati ad un'analisi quantitativa dei *biomarker*, di opportune analisi dell'affidabilità dei dati, così come dalla mancata valutazione dell'eterogeneità nella pratica clinica.

La prima parte della Tesi presenta gli argomenti e le problematiche relativi ai *biomarker* finora utilizzati, i limiti che ostacolano l'utilizzo della TCp nella routine clinica, e i contributi metodologici introdotti; la seconda parte della Tesi è dedicata alle applicazioni dei metodi sviluppati nella prima parte e nella maggior parte dei casi già pubblicati. In particolare, è stata effettuata un'analisi dell'affidabilità dei valori perfusionali. In seguito, è stata indagata l'abilità dei parametri perfusionali, alla diagnosi, di migliorare la caratterizzazione di due istotipi predominanti del carcinoma polmonare. Successivamente, è stato messo a punto un metodo automatico per classificare l'eterogeneità spazio-temporale, così come viene effettuato dai radiologi attraverso l'analisi visiva. È stato, inoltre, sviluppato un metodo basato sull'analisi locale per misurare l'eterogeneità

tumorale emergente dalle mappe perfusionali. Il valore prognostico delle *feature* estratte è stato preliminarmente valutato. Per fronteggiare il problema dell'elevata variabilità presente nei dati PET, è stato introdotto un metodo robusto in grado di dare una misura dell'elevata captazione di una struttura. Per questo scopo, è stato anche sviluppato un metodo per la segmentazione 3D a partire da immagini PET, che è stato poi applicato per segmentare reni da immagini PET/TC. In seguito, è stata eseguita un'analisi multi-modale dell'eterogeneità su tumori della giunzione gastro-esofagea. In particolare, l'eterogeneità di questi tumori è stata analizzata sulle immagini delle serie PET/TC e PET/RM, acquisite con un protocollo a singola iniezione. È stata quindi valutata l'abilità dei *biomarker* derivati dalle immagini multi-modali di predire la presenza di metastasi. I risultati hanno mostrato che le *texture feature* hanno una prestazione migliore nella valutazione della prognosi, confrontata con quella dei parametri derivati da PET ed RM, comunemente usati nella pratica clinica. Infine, è stato messo a punto un algoritmo per il rilevamento delle regioni interne ai volumi tumorali al fine di combinare le informazioni multi-modali. Per questo scopo, è stato implementato un algoritmo di registrazione 3D al fine di trasformare ed allineare i *dataset* multi-modali relativi ad ogni paziente in un unico sistema di coordinate x-y-z.

Contents

Abstract (English version) **11**

Abstract (Italian version) **13**

Contents **15**

Part I

1 Introduction **23**

2 Background **31**

2.1 Tumour 31

2.1.1 Heterogeneity 33

2.1.2 Angiogenesis 33

2.1.3 Cellular proliferation and metabolism 35

2.2 Imaging modalities 36

2.3 Image-based biomarkers 37

3 Imaging modalities used in oncology **41**

3.1 CT 42

3.1.1 DCE-CT 43

3.1.2 BF mathematical model 45

3.1.3 BF computation 46

3.1.4 Open issues in DCE-CT 49

3.2 MRI 50

3.2.1 T1- and T2-weighted MRI 52

3.2.2 DWI 54

3.2.3 Open issues in MRI 56

3.3 PET 58

3.3.1 Hybrid systems 60

3.3.2 Tracers 62
3.3.3 Open issues in PET 65

4 Texture Analysis 69
4.1 Background 69
4.2 Texture analysis methods 71
4.3 Statistical features 72
4.3.1 First-order features 73
4.3.2 Second-order features 74
4.3.3 Higher-order features 78

5 Novel features 83
5.1 Local features 83
5.2 Heterogeneity analysis on DCE-CT 87
5.2.1 Single-feature analysis 88
5.2.2 Multi-feature analysis 89
5.3 Reliability analysis on DCE-CT 89
5.3.1 Local coefficient of variation 92

6 Image processing and multi-modality approach 95
6.1 Segmentation 96
6.1.1 Segmentation of PET images 97
6.2 Registration 101
6.2.1 Similarity measures 104
6.2.2 Interpolation 106
6.2.3 Application on PET/CT and PET/MRI 108
6.2.4 Future works 120

Part II

7 Classification of lung tumour DCE-CT heterogeneity 125
7.1 Introduction 126
7.2 Materials and method 128
7.2.1 Heterogeneity taxonomy 129
7.2.2 Spatio-temporal indexes 130
7.3 Assessment of results 130
7.3.1 Generation of ground truth 130

7.3.2 Visual analysis 130
7.3.3 Quantitative results 131
7.4 Experimental results 132
7.4.1 Results 132
7.5 Discussion 135
7.6 Conclusion 136

8 Reliability analysis of BF maps from CTp of lung cancer 139
8.1 Introduction 140
8.2 Materials and methods 141
8.2.1 Perfusion CT protocol 142
8.2.2 Perfusion maps 142
8.2.3 Local coefficent of variation 142
8.2.4 Data Analysis 143
8.2.5 Statistical analysis 144
8.3 Results 144
8.4 Discussion 149
8.5 Conclusion 150

9 CTp analysis of two predominant lung cancer subtypes 151
9.1 Introduction 152
9.2 Materials and methods 154
9.2.1 Study population 154
9.2.2 Inclusion and exclusion criteria 154
9.2.3 CTp protocol 154
9.2.4 Perfusion maps 155
9.2.5 Data analysis 156
9.2.6 The “borderline” examinations 158
9.3 Assessment of results 158
9.3.1 Tumour location 159
9.4 Results 159
9.5 Discussion 165
9.6 Conclusion 166

10 Local analysis of lung tumours BF maps: correlation with OS 169
10.1 Introduction 170
10.2 Materials and methods 171

10.2.1 Study population 171
10.2.2 CTp protocol 172
10.2.3 Perfusion maps generation 172
10.2.4 Perfusion maps denoising 174
10.2.5 Computation of novel local-based features 176
10.2.6 Statistical Analysis 178
10.3 Results 179
10.4 Discussion 181
10.5 Conclusion 181

11 Kidneys ^{68}Ga-PSMA uptake reduction with mannitol infusion 183
11.1 Introduction 184
11.2 Materials and methods 185
11.2.1 Patient Enrolment 185
11.2.2 Image Acquisition 186
11.2.3 Image Analysis 186
11.2.4 Statistical Analysis 186
11.3 Results 187
11.4 Discussion 187
11.5 Conclusion 191

12 GOJ cancer: texture analysis of ^{18}F-FDG-PET/MRI 193
12.1 Introduction 194
12.2 Materials and methods 194
12.2.1 Patient Enrolment 194
12.2.2 Image Acquisition 195
12.2.3 Image Analysis 195
12.2.4 Statistical Analysis 196
12.3 Results 197
12.4 Discussion 199
12.5 Conclusion 200

13 Conclusions 203

List of figures 209

List of tables 215

List of equations **217**

Acronyms **225**

Bibliography **227**

Acknowledgements **267**

Part I

Chapter 1

Introduction

Cancer is the most common malignant disease and among the leading causes of death worldwide [1]. Despite the continuous decline in cancer death rate, globally decreased over the two last decades [2], a continuous research is required to improve tumour characterisation and prognosis, as well as treatment monitoring and planning.

Recently, cancers have been described as "aberrant" organs characterised by highly interactive cells [3], leading to a tissue biology even more complex than that of the normal healthy tissue [4]. The awareness of the complexity underlying the biological mechanisms has led to an increased interest for the analysis of the tumour micro-environment, since the study of the intra-tumoral heterogeneity could be the key to improve tumour characterisation and prognostication [5, 6, 7]. The last years have been characterised by the development of new target therapies, usually designed to inhibit cell growth, angiogenesis and proliferation, whose early effects do not reflect a reduction of the tumour volume.

The use of invasive biopsy may be inadequate in the presence of high intra-tumoral heterogeneity, due to the sampling errors caused by taking tissue specimens from small tumour portions [8]. Therefore, imaging technologies have gained more and more attention having the potentiality to capture the *in vivo* whole tumour heterogeneity in a minimally invasive way or, even, non-invasively [9, 10]. Moreover, imaging may provide novel quantitative approaches to assess the tumour response to the novel target therapy. Indeed, the traditional criteria, the mainstay for tumour evaluation, are based on the analysis of the morphological tumour changes through Computed Tomography (CT) and Magnetic Resonance Imaging (MRI), thus, resulting inadequate for an early evaluation of the efficacy of the target therapy [11].

The need for more effective functional biomarkers have prompted the use of Dynamic Contrast Enhanced (DCE) imaging, Diffusion Weighted Imaging (DWI), as well as Positron Emission Tomography (PET), particularly when combined with CT (PET/CT) and MRI (PET/MRI). For instance, the effects of anti-angiogenic therapies, can be earlier detected on the tissue vascular supply, but just later on morphology [8]. As a result, an increased interest for the development of biomarkers, useful to monitor status and changes of the tumour vascular network, has pushed for the use of the DCE-CT imaging technique [12]. Indeed, DCE-CT is probably one of the most promising methodologies for the early assessment of anti-angiogenic therapies efficacy, thanks to its wide availability, high spatio-temporal resolution and promising preliminary findings [11]. The perfusion parameters, which can be derived from DCE-CT sequences, have shown a high correlation with angiogenesis biomarkers, as the micro-vessel density (MVD) [13] and the vascular endothelial growth (VEGF) [14]. As regards PET imaging, this functional technique is mainly used to study tumour metabolism through ^{18}F-fluorodeoxyglucose (^{18}F-FDG), which permits a mapping of the tumour glucose avidity. Usually, higher FDG uptake correlates with poor prognosis and tumour aggressiveness [15, 16]. While, Apparent Diffusion Coefficient (ADC) parameters, which are MRI biomarkers used to evaluate changes in cellular proliferation, might be suggestive of tumour progression [17]. These imaging modalities have different strengths and weaknesses regarding derived parameters, availability, reproducibility and biological significance of the data (structural, functional, or molecular) [18].

Despite the high potentialities shown, which have already led to improvements in tumour diagnosis [19], staging [20] and prognosis [21], there are still some open issues requiring the development of more quantitative approaches and complex biomarkers involving the evaluation of the tumour heterogeneity. Indeed, visual analysis still represents the gold-standard approach in many procedures [22], and the biomarkers used till now are usually derived from global measurements, which, by the way, do not involve the evaluation of the intra-tumoral heterogeneity. As regards DCE-CT imaging, the lack of standardisation and reliability has even prevented the use of this technique in the routine clinical practice [23, 8].

In this Thesis, the reliability topic concerning the perfusion maps derived from DCE-CT image series has been faced. Downstream of this analysis, it has been investigated the ability of perfusion parameters, at diagnosis, to improve tumour characterisation of predominant lung cancer subtypes. Then, due to the need for visual analysis to gain objectivity, an automatic methodological approach has been developed to classify the spatio-temporal heterogeneity, present in lung lesions, as performed by expert radiologists through visual analysis. Afterwards, a novel method to evaluate the intra-tumoral heterogeneity emerging from perfusion maps of lung tumours has been also developed, and the ability of the features extracted to act as prognostic image-based biomarker has been early assessed. To face the issue of the high variability present in PET data, a more quantitative approach was introduced to represent the highest uptake activity through the use of a simple index, more robust than that routinely used in clinical practice. To this purpose, a method to perform a 3D segmentation starting from PET images has been developed and applied to segment the whole kidneys in ^{68}Gallium prostate-specific membrane antigen (^{68}Ga-PSMA) PET/CT series. Then, a multi-modal analysis of the intra-tumoural heterogeneity has been performed in the gastro-oesophageal junction (GOJ) cancer. The aim was to analyse the heterogeneity of GOJ tumours both acquired with a FDG-PET/CT and FDG-PET/MRI, with a single injection protocol. The ability of the quantitative image-based biomarker extracted to predict distant metastasis has been early assessed. The findings have shown that more complex features have a better performance in prognosis compared to the parameters PET- and MRI-derived commonly used in clinical routine. Moreover, an algorithm to detect sub-regions in tumour volume has been developed, having the potentiality to combine multi-modal information, enabling a comparison of the heterogeneity coming from the different modalities. To this purpose, a 3D registration algorithm was implemented to automatically transform the multi-modal dataset related to each patient into one x-y-z coordinate system.

The Thesis is divided into two parts:

- Part I, presenting the topics previously outlined as well as the methodological contributions introduced;
- Part II, reporting the applications of the methodological approaches previously introduced and, in most cases, already published.

As a result, besides the present introductory Chapter, the Thesis content is organised as follows:

- Chapter 2 contains the background concerning the biological aspects of the tumours. In particular, an introduction to the tumour heterogeneity and its specific functional aspects like the angiogenesis, the proliferation and the metabolism, essential factors for the tumour growth and spread, is reported. The imaging modalities able to detect these phenomena and, thus, improve the characterisation of the tumour micro-environment are also preliminary presented. Finally, an overview of the image-based biomarkers currently used and investigated is reported.

- Chapter 3 describes in a more detailed way the imaging modalities used in oncology, which have been considered during this Thesis work. In particular, CT and DCE-CT are introduced along with the benefits and most relevant open issues. A mathematical approach to derive tumour vascularity information is presented. Then, MRI principles of application along with the most widely used MRI image series are reported, followed by the most relevant open issues. Finally, PET principles and derived parameters are presented, followed by a short presentation of the two combined hybrid systems increasingly widespread in clinical practice, the PET/CT and the PET/MRI. A summary of the most common tracers and isotopes is also reported. Also in this case, the final section is dedicated to the open issues.
- Chapter 4 introduces the topic of the texture analysis, which could play an essential role in medical image application, having the great advantage of maximising the information, by exploiting available data without the need for additional acquisitions. The main texture analysis approaches currently used in literature are briefly discussed. Then, a deep analysis is reported about the statistical-based method, ranging from the first-order to the higher-order features, which have been considered and developed within this Thesis work.
- In Chapter 5, a novel approach based on the local analysis is introduced to overcome the limitations of the first-order statistical features, previously introduced. Two spatio-temporal indices conceived to exploit DCE-CT information and a third one summarising their joint behaviour are reported. These indices describe the evolution over time of the tumour spatial heterogeneity. As regards the reliability analysis of perfusion maps, an error index to establish which perfusion values are unreliable and a local-based index to evaluate the local spatial coherence of the perfusion maps are presented.
- In Chapter 6, the image segmentation is briefly described and formalised.

This is followed by an introduction to the registration methods currently used, along with the algorithmic choices required. Then, the method developed to perform a 3D PET segmentation of the kidneys on PET/CT images is reported. Then, the method used to perform the multi-modal 3D registration of GOJ tumours on FDG-PET/CT and FDG-PET/MRI series is presented. Afterwards, the algorithm developed to detect sub-regions in tumour volume having the potentiality to compare multi-modal information is shown.

- Chapter 7 reports the first application of one of the methodological approaches previously described, the spatio-temporal analysis of DCE-CT sequences. As previously mentioned, visual analysis represents the gold-standard for image interpretation. The need for more objective measures pushes towards an intensive use of software to automatically provide quantitative information useful in clinical routine. The ability of spatio-temporal features, devised in the Part I of the Thesis, to quantify and classify the lung tumour heterogeneities, as performed through visual analysis by experts, is discussed.

- Chapter 8 reports the use of the local-based index devised for the reliability estimation, which is able to discriminate between the tumour heterogeneity, featured by locally structured patterns, and the noise, characterised by sparse and unstructured values. As previously mentioned, currently, the assessment strategies rely on global measurements, which are inadequate to discriminate between noise and heterogeneity. This index enables a proper comparison between perfusion maps, thus improving the overall reliability of DCE-CT studies and favouring its translation into clinical routine.

- Chapter 9 reports the perfusion characterisation of two lung cancer subtypes, at diagnosis. This topic is widely debated in literature, which reports different and sometimes not statistically significant results. In this Thesis, the analysis of perfusion differences have been carried out after removing the unreliable perfusion values, through the methods presented in the Part I of the Thesis. Therefore, the significance of the results has been achieved by automatically detecting and excluding artefactual perfusion values as well as through a punctual analysis of the borderline cases, i.e. the most atypical lesions, whose perfusion values negatively affect the statistical significance of the study.

- Chapter 10 reports the approach to extract meaningful features from perfusion maps based on the local analysis presented in the Part I of the Thesis. The use of the local-based features, able to gather and exploit information owned by the hemodynamic heterogeneity patterns at local level, is reported. Features ability to act as a prognostic image-based biomarker for lung cancers has been assessed. In particular, the correlation between the feature-pair computed on perfusion maps and the survival of patients affected by lung tumours was explored and analysed in comparison with the staging, commonly used as prognostic indicator. The features devised proved a strong correlation with the survival, this suggesting a promising prognostic clinical application of the DCE-CT. Also in this case, a reliability analysis of the maps was performed to automatically detect and remove those pixels and regions undergoing high computing errors.

- Chapter 11 reports the approach used to analyse the potential of mannitol to reduce renal uptake of ^{68}Ga-PSMA, thus, the nephrotoxicity. To this purpose, a PET-derived index has been devised, able to represent a high uptake activity in a more robust manner than the clinical accepted PET parameters. Indeed, these parameters widely used in clinical practice are characterised by a large degree of variability due to physical and biological sources of errors. In order to identify a more representative parameter for the kidneys volume distribution of values, the segmentation method developed and presented in the Part I of the Thesis was used to segment the whole kidneys. The analysis of the index devised showed that the rapid administration of mannitol, carried out prior to the injection of the radiotracer, reduces the absorption of ^{68}Ga-PSMA by renal tubules, limiting the dose of the kidneys.

- Chapter 12 presents a multi-modal analysis of the tumour heterogeneity in patients affected by GOJ cancer. The features derived from FDG PET/MRI were analysed in order to establish if they could be able to predict for contemporaneous metastases. In particular, first- and second-order statistical features were computed on the available image series. The results showed that combined texture features can discriminate better than the parameters currently used in clinical routine. As a result, this analysis may complement current staging practice.

- In Chapter 13, the conclusions concerning the topics faced in this Thesis are drawn. A brief summary of the main methodological contributions achieved and the results obtained during this research work is also reported.

The work developed in this Thesis has been carried out in collaboration with:

- Computer Vision Group (CVG), Advanced Research Center on Electronic Systems (ARCES), University of Bologna, Italy. Head: Prof. Alessandro Bevilacqua
- Diagnostic Imaging Unit, Istituto Romagnolo per lo Studio e la cura dei Tumori (IRCCS-IRST), Meldola (Forlí-Cesena), Italy. Head: Dr. Domenico Barone
- Department of Cancer Imaging, School of Biomedical Engineering & Imaging Sciences, within the Faculty of Life Sciences & Medicine at King's College London, St Thomas Hospital, United Kingdom. Head: Prof. Dr. Vicky Goh.

The activities discussed in this Thesis pertain to the project PERFECT (Automatic analysis of hepatic and lung PERFusion through the usE of CT-4D image reconstruction), to the study aiming at investigating whether mannitol can reduce PSMA renal uptake, and to the prospective study regarding the multi-modality imaging characterisation of the gastro-oesophageal tumours heterogeneity.

The methods developed and the results achieved in this Thesis work have been partly published in four scientific papers on one national and three peer-reviewed international journals, one international conference paper, twenty-nine abstracts or extended posters, whose twenty-three on international and six on national conferences. In addition, they have been also presented in six oral communications. Finally, two papers have been submitted to international journals.

Chapter 2

Background

Contents

2.1 Tumour **31**
  2.1.1 Heterogeneity 33
  2.1.2 Angiogenesis 33
  2.1.3 Cellular proliferation and metabolism 35
2.2 Imaging modalities **36**
2.3 Image-based biomarkers **37**

This Chapter introduces the complexity of the tumours and, in particular, of the tumour heterogeneity which makes the clinical oncological practice very challenging. Indeed, the intra-tumoural heterogeneity involves specific functional aspects like angiogenesis, proliferation and metabolism, which are essential for the tumour growth and spread (Section 2.1). These processes require to be deeply analysed. The imaging modalities able to detect these phenomena and, thus, to improve the characterisation of the tumour micro-environment are also presented (Section 2.2). Finally, an overview of the image-based biomarkers proposed so far is reported (Section 2.3).

2.1 Tumour

Neoplasm is an abnormal new (*neo*) creation (*plasma*) of tissue. When the tissue growth forms a mass, it is commonly referred to as tumour. Basically, there are three types of tumours: benign, potentially malignant (pre-cancer), and malignant (cancer). Usually, benign tumours can be easily removed. They are localised and they can not metastasise, that is, spread around the body. Pre-cancer tumours are hardly distinguished from the other ones, since in their earlier phase they share common features with benign tumours, in the later with malignant ones. Given enough time, when not treated, they will transform into malignant tumours, cancers. During this process, as a result of genetic alterations, tumour acquires the so called "hallmarks of cancer" [24, 4]. Now, the concept of cancer as a closed, isolated and self-sufficient system of cells has been overcome. Recently, cancers have been recognised as aberrant "organs", being composed by highly organised and interactive cells with the well known ability to metastasise and destroy the surrounding tissue [3]. There are more than hundreds different tumours and several subtypes for specific body districts. However, even though the catalog of cancer cell genotypes is so really wide, in 2000, Hanahan and Weinberg suggested that it is the reflection of essentially six hallmarks: self-sufficiency in proliferative signalling, insensitivity to anti-growth safeguards, resistance to apoptosis, achievement of replicative immortality, induction of angiogenesis and activation of tissue invasion and metastasis, which depends on the acquisition of the other five capabilities [24]. In the last decade, as a result of extensive research in tumour biology, Hanahan and Weinberg added two emerging hallmarks involved in the pathogenesis of some or even all cancers. One is the capability to reprogram cellular metabolism in order to most effectively support neoplastic proliferation. The other concerns the capability to avoid immunological destruction [4]. In this perspective, tumour biology appears even more complex than that of the normal healthy tissue. Understanding the mechanism implies the study of the so called "tumour microenvironment". Indeed, even if at first the tumour should appear composed by reasonably homogeneous cell populations, in the course of its progression, hyperproliferation combined with increased genetic instability and reversible changes in cell properties bring to distinct clonal subpopulations. For this reason, many tumours are "heterogeneous". Being histopathologically different, they reflect regions with a different degree of proliferation, vascularity, inflammation and invasiveness. In addition, in recent years evidence has accumulated regarding the existence of a subclass of neoplastic cells within tumours, known as cancer stem cells (CSCs), which provide an explanation for the phenotypic and functional heterogeneity of cancer cells in some tumours [25].

2.1.1 Heterogeneity

Tumour heterogeneity is a phenomenon reflecting the highly complex tumour micro-environment. Tumour can be composed by cells showing different genetic, epigenetic and phenotypic profiles [26]. This phenomenon translates into variations of the tumour tissue in morphology, angiogenesis, metabolism, cellular proliferation and metastatic potential. Heterogeneity occurs both between tumours of the same organ, in this case it is referred as inter-tumour heterogeneity, and within the same tumour, namely intra-tumour heterogeneity. Inter-tumour heterogeneity leads to the definition of tumour subtypes, while intra-tumour heterogeneity means that tumour cells have different properties and can express different markers [27, 28, 29], as mentioned before. Therefore, the presence of tumour heterogeneity makes the clinical oncological practice very challenging, since introduces a great variability in tumours' response to available therapies as well as difficulty in the identification of patients who will benefit most from specific treatments [29]. Indeed, the phenotypic heterogeneity in tumour cell populations as well as the changes in cellular phenotypes resulting from adaptation to abnormal microenvironments need to be considered to improve the therapeutic outcome [30].

For this reason, in the last decade, an extensive research on tumour heterogeneity was conducted. As results, it has been found that its major clinical effects are the association with drug resistance and the difficulty in performing histological diagnoses. Indeed, in presence of tumour heterogeneity biopsy assay results to be limited if not even inappropriate [6]. In addition, the complexity of tumour pattern is increased by its degree of vascularization [31, 32]. Indeed, for tumours, inflammatory disease and also other chronic conditions, blood vessels proliferate in a really chaotic way through a process known as angiogenesis.

2.1.2 Angiogenesis

In 1969, a clinical cue studying a child retinoblastoma found evidence that tumour growth depends on angiogenesis. Some years later in 1971 Judah Folkman published this discovery, hypothesising that solid tumours are not able to grow more than 1-2 millimetres without recruiting new blood vessels [33]. As already mentioned, this process is known as angiogenesis and consists in the sprouting of blood vessels from pre-existing vessels [34, 35]. Also the physiologic growth of the body is based on angiogenesis. Indeed, with the enlarging of the vascularization, tissue is able to receive nutrients, also creating paths for cells to leave or enter the

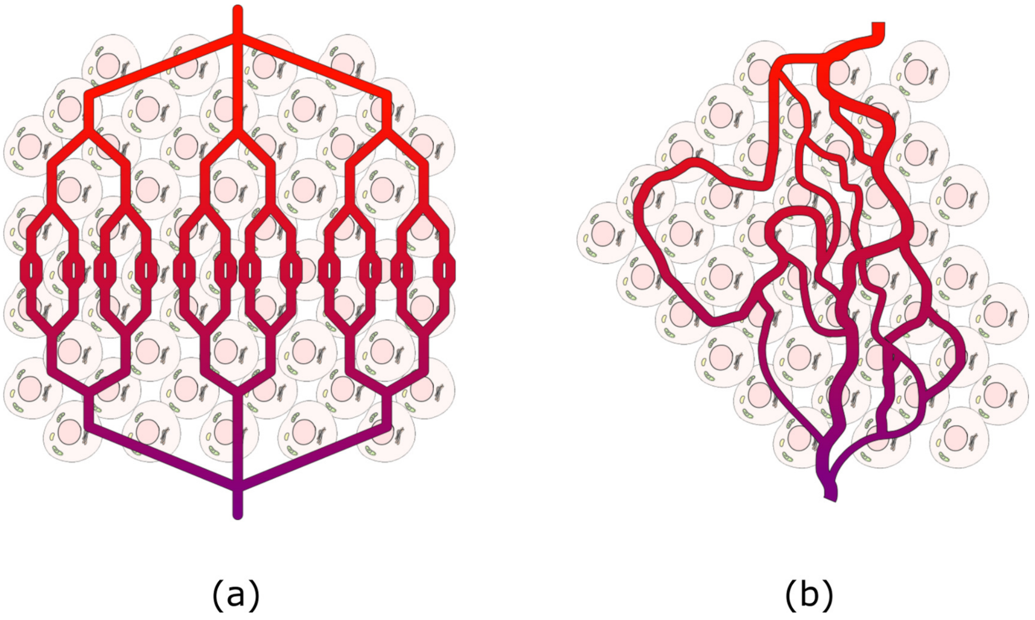

Figure 2.1: Normal (a) and tumoral (abnormal) micro-circulation (b).

blood circulation. Vascularization of normal tissue is organised in a hierarchical way consisting in arterioles, capillaries, venules, each having distinct functions. Normal blood vessels result lined by the endothelial cells, which create a thin monolayer constituting a barrier to control water, solutes and cells.

Tumour blood vessels have weird features: endothelial cells and vascular basement membrane are all abnormal and locally incomplete and "deteriorated" [36]. Besides the presence of interruptions, even extra layers of basement membrane are also reported [34]. In addition, tumour blood vessels present increased endothelial fenestrations, this leading to an increase of blood flow (BF), plasma leakage and permeability to large molecules present in the blood [37]. Endothelial cells proliferate in a disorganized way and, for survival, become dependent on vascular endothelial growth factor (VEGF) or other factors as well. Tumour enlargement results associated with an increased interstitial pressure, due to the structural vessels defects, leading to a locally decreased BF and, consequently, to an inadequate oxygen delivery for cells viability.

Numerous studies have been conducted to better understand the biology underlying the angiogenesis process and its role in metastases formation. In 2004, these studies led to the Food and Drug Administration (FDA) approval of the first antiangiogenic drug (bevacizumab, a humanised antibody targeting VEGF) as a first-line treatment for patients with metastatic colorectal cancer [38]. The approval of the first antiangiogenic agent gave rise to high expectations for the use of these treatments for malignant diseases, also raising several issues as the assessment of tumour response to antiangiogenic therapies [39]. Other studies encourage the idea of therapies targeting cells proliferation mechanism, even though these kinds of treatments should be considered carefully, since effects on tissue and tumour are at present difficult to predict [40].

2.1.3 Cellular proliferation and metabolism

Cellular proliferation is an essential biological activity for both physiological and pathological processes [41]. As already discussed, tumours are biologically heterogeneous. However, it is interesting to note that all tumours share the ability to proliferate in an aberrant way differently from normal tissue, where the growth is limited [40].

Normally, uncontrolled proliferation is prevented because cells absorb nutrients from surrounding environment only if stimulated by growth factors. Cancer cells acquiring genetic mutations overcome this growth factor dependence, altering the receptor-initiated signaling pathways, probably activating the metabolism of nutrients that both promote cell survival and fuel cell growth [42]. Therefore, proliferation and tumour growth result unavoidably linked and supported by the tumour metabolic reprogramming, considered as a hallmark of cancer.

The metabolic reprogramming consists in a tumour cells metabolic adaptation, based on oncogenic signalling pathways that increase acquisition of nutrients if they are abundant, also facilitating the assimilation of carbon into macromolecules such as proteins, lipids and nucleic acids [43]. Actually, recent works highlight also the capability of cancers with particular mutations, like the KRAS mutation in colon cancers, to be able to optimise metabolism when nutrients are scarce [44].

At present, it is well known that there are thousands of mutations, translocations, amplifications and deletions that may contribute to cancer progression. Likewise, there are several key oncogenic signalling pathways leading to tumour metabolism adaptation allowing cancer cells to survive and grow [45].

The relationship between tumour metabolism and tumour environment is not very clear, and it seems not following the cause - effect principle. Certainly, besides the genetic alterations, tumour cell micro-environment has an essential role in determining the tumour metabolic phenotype [46]. As already discussed, tumour vascularization is structurally and functionally abnormal, leading to a spatial heterogeneity [30], reflecting different oxygenation, pH, as well as glucose and other metabolites concentrations. Also this harsh environment induces several cellular stress responses that contribute to the alteration of the tumour metabolic phenotype [45].

The metabolic features of cancer cells can be exploited for cancer treatment. Indeed, being the majority of human cancer dependent on aberrant signaling pathway, these altered pathways represent attractive therapeutic targets [47]. However, even if finding a therapeutic window between proliferating cancer cells and normal cells remains challenging, the development of treatments targeting the tumour metabolic pathways has been receiving renewed attention [48].

2.2 Imaging modalities

All these tumour processes are of essential clinical interest and require to be analysed. At present, different imaging modalities are able to detect these phenomena, ranging from the heterogeneity reflecting the tumour micro-environment, to the specific functional aspects, like the angiogenesis, the proliferation and the metabolism necessary for the tumour growth and spread.

Tumour heterogeneity is probably one of the most complex process to be investigated and there is not one dedicated modality to detect this cancer feature. Consisting of subpopulations of cells with different genotypes and phenotypes [30], its spatial and temporal variability is increased by the presence of blood vessels, dead cells and different proliferative and metabolic activities. For this reason, the use of biopsy-based molecular assays could be inadequate because of the scarce representativeness of samples [6, 8].

The advantage of imaging techniques is their non-invasive or minimally invasive nature and the possibility to analyse *in vivo* the whole tumour heterogeneity [9]. Many techniques have been proposed for the quantification of tumour heterogeneity and the choice of a specific technique depends on which heterogeneity aspects we are interesting in. The imaging techniques mostly used for heterogeneity assessment include the MRI, CT, PET, single-photon emission computed tomography (SPECT), ultrasonography (US).

Angiogenesis can be detected through DCE-imaging techniques, like the DCE-CT and the DCE-MRI, through the analysis of the contrast agent passage after a bolus intravenous injection. DCE-based imaging permits to study *in vivo* the BF of tumour vascularization and the exchanges between the intra-vascular and the extra-vascular space [49].

Tumour perfusion and vascular volume can be also quantitatively measured by ^{15}O-labelled water ([^{15}O]H2O) PET, being this marker free to diffuse and pass into the intra-vascular and extra-vascular spaces. Even though this technique has shown its clinical feasibility, the need for an on-site cyclotron due to the short half-life of isotopes has thwarted its clinical application [17].

Tumour cells proliferation can be detected, for instance, through ADC parametric maps, clinically computed using MRI with DWI [50]. ADC maps reflect the degree of diffusion of water molecules through different tissues. Therefore, lower ADC values seem to reflect hyper-cellular areas where proliferation is higher [51]. Tumour proliferation, cell death and apoptosis can also be detected through the 3-deoxy-3-([^{18}F]Fluoro)-fluorothymidine, FLT-PET. Indeed, the accumulation of FLT in tissues has been shown to be associated with the cellular proliferation rate [52].

Tumour metabolism consisting in an enhanced glucose uptake inspired tumour imaging by FDG-PET, where FDG is an analogue of glucose, metabolised by tumour cells similarly to glucose. FDG-PET is widely used in clinical practice for tumours with high glucose metabolism, and has been shown to have a fundamental role in diagnosis and monitoring of treatment response [53].

2.3 Image-based biomarkers

During the last years there have been substantial improvements in cancer therapies with the advent of target therapies. However, survival remains poor for many common tumours.

Generally, new targeted treatment strategies have been designed to induce cytostasis, the inhibition of cell growth and proliferation, rather than the reduction of the tumour volume. Therefore, traditional response assessment criteria based on the measurement of tumour size through CT and MRI may be inadequate to assess tumour response to these specific therapies. For this reason, during the past decade the research has been focused on the possible use of specific imaging biomarkers, deriving tumour functional aspects. This led to an increase interest in the use of DCE-imaging, mostly DCE-CT and DCE-MRI, DWI, as well as PET, particularly when combined with CT (PET/CT) and MRI (PET/MRI).

The derived functional biomarkers have shown to be promising, but to date they have not been clinically validated, while the change in number of lesions and tumour size remains the gold standard for assessing tumour response to therapy [54]. More specifically, Response Evaluation Criteria in Solid Tumors (RECIST) are based on the measurement of the maximum tumour diameter (one-dimension measure) [55, 56, 57], while the World Health Organization (WHO) criteria are based on the two-dimensional long-axis measurements [58, 59]. Therefore, to evaluate the effects of molecularly targeted therapy, inducing cytostatic response, new and more effective biomarkers are needed [60, 8].

A very simple biomarker of tumour vascular supply is given by measuring the change in Hounsfield Unit (HU) of pre-contrast and post-contrast CT data. This gives a simple indication of the tumour ability to accumulate contrast medium. Much more refined biomarkers on tissue angiogenesis degree can be derived from DCE-CT and DCE-MRI, whose principal ones are similar to one another despite inherent differences in signal generation. Tracer kinetic modelling of dynamic imaging data allows deriving perfusion parameters like BF, blood volume (BV) and the capillary permeability. Several studies have shown that statistical parameters computed on these perfusion indices significantly change after treatment [61, 62]. In patients receiving anti-angiogenic therapies like bevacizumab, promising evidences have been reported of early effects in tumour perfusion (e.g., reduced BF and BV), occurring long before tumour reduction becomes visible [63, 64].

Probably the greatest use of PET is addressed to the study of tumour metabolism through ^{18}F-FDG, which permits a mapping of tumour glucose metabolism. Effects from vascular antiangiogenic therapy can be evaluated as FDG uptake reduction. While, higher FDG uptake proves the metabolic activity of tissues and correlate with poor prognosis and tumour aggressiveness [15, 16, 65]. PET measurements usually involve the use of the standardised uptake value (SUV). In particular, the maximum SUV ($\mathrm{SUV}_{\mathrm{max}}$) has become a clinical accepted parameter, representing the tracer uptake normalised to the injected dose and the patient body-weight. Authors in [66] found that a low ^{18}F-FDG $\mathrm{SUV}_{\mathrm{max}}$ is also associated with the presence of epidermal growth factor receptor (EGFR) mutations in patients with non-small cell lung cancer (NSCLC). This discovery highlights the increasing interest in finding indices able to differentiate tumour types, to be used as surrogate biomarker for tumour diagnosis.

[^{18}F]FLT SUV can estimate cell proliferation, as mentioned in the previous section. The authors in [67] found that [^{18}F]FLT SUV has a predictive value for patients with malignant recurrent glioma treated with bevacizumab and irinotecan. In particular, a reduction in SUV seems to be associated to an increased overall survival OS. Tumour cellular proliferation can be also estimated through the mean ADC value (ADC_{mean}), where a low value correlates with a high proliferation activity [51]. Indeed, this MRI biomarker is linked to changes in cellular packing and increased cell size or density might be suggestive of tumour progression [17].

Recently, with the emerging interest for the analysis of the intra-tumour heterogeneity, more complex biomarkers based on texture analysis methods were considered to represent it by quantitative information. Several evidences have been reported on the correlation of tumour heterogeneity measurements with tumour types, grading and response to therapy. For instance, authors in [5] have found that using CT texture analysis features, it was possible to differentiate high-risk thymic epithelial tumour from low-risk ones with a high diagnostic performance. While authors in [6], considering three independent data sets of lung and head-and-neck cancer patients, showed that combined CT texture features reflecting the intra-tumour heterogeneity had a strong prognostic value, also resulting associated with gene-expression profiles. In addition, in a recent retrospective study, including patients with esophageal cancer treated with chemoradiotherapy, the heterogeneity emerging from ^{18}F-FDG primary tumour, quantified through the use of statistical parameters, resulted predictive of tumour response [7].

Chapter 3

Imaging modalities used in oncology

Contents

3.1 CT **42**
3.1.1 DCE-CT 43
3.1.2 BF mathematical model 45
3.1.3 BF computation 46
3.1.4 Open issues in DCE-CT 49
3.2 MRI **50**
3.2.1 T1- and T2-weighted MRI 52
3.2.2 DWI 54
3.2.3 Open issues in MRI 56
3.3 PET **58**
3.3.1 Hybrid systems 60
3.3.2 Tracers 62
3.3.3 Open issues in PET 65

This Chapter describes imaging modalities widely used in oncology, which will be considered during this Thesis work. In particular, an introduction to the CT and the DCE-CT is presented in Section 3.1 along with a mathematical approach to derive tumour vascularity information. The benefits and the most relevant open issues are also reported. Section 3.2 introduces MRI principles of application along with the most widely used MRI image series, the T1- and T2-weighted as well as the DWI. At the end of the Section, the most relevant open problems are presented. Finally, Section 3.3 presents the PET principles and the derived parameters, followed by a short introduction to the two combined hybrid systems, the PET/CT and the PET/MRI. As for the other modalities, the final subsection describes the main open issues.

3.1 CT

Since its introduction in the early '70s, CT has revolutionised the world of the diagnostic imaging. CT is considered as the main diagnostic tool in tumour evaluation, including tumour staging and monitoring the response to therapies. Its increasing availability is due to the relatively low costs and the broad spectrum of pathologies that can be examined [68].

Schematically, the CT operation principle is based on an X-ray generator rotating around a patient and shooting narrow beams of X-rays through the body. As the X-rays leave the patient, they are picked up by the X-ray detectors, positioned at the opposite side of the ring with respect to the X-ray source.

After acquisition, the signals registered by the detectors undergo a pre-processing step and are transformed into X-ray attenuation values. An image reconstruction method derived from numerical analysis (inverse Radon transform) is used to calculate the local attenuation at each point within the CT section.

To reduce the dependence on the X-ray spectrum and to obtain numerical values of convenient size, the values are not displayed in the image as local attenuation coefficients but as CT numbers (CT_{N}). CT_{N} is determined by the X-ray attenuation μ occurring in the corresponding voxel. It is defined as follows:

$$CT_N = 1000\frac{\mu - \mu_{water}}{\mu_{water}} \tag{3.1}$$

where μ_{water} is the water attenuation coefficient.

The CT_{N} represents a quantitative measure of radiodensity and is expressed in HU from the name of its inventor, the English engineer G.N. Hounsfield. According to the Hounsfield scale, -1000 HU represents CT_{N} of air while 0 HU is the CT_{N} of water [69]. There is no an absolute upper limit for this scale, but the range of CT_{N} varies across scanners and according to available bits per pixel (e.g., with 12 bits the upper bound is 3071 HU).

If tissues with different attenuation properties lie in the same voxel, the resulting CT_{N} will represent with a good approximation the weighted sum of the different attenuation values [70]. This phenomenon due to the inability of the detector to differentiate different tissues is known as “partial volume effect”. It is defined as follows:

$$CT_N = v_1 CT_{N1} + v_2 CT_{N2} + .. \tag{3.2}$$

$$\sum_i v_i = 1 \tag{3.3}$$

where v_i are the partial volume elements. That means, for instance, that a big amount of cartilage and a thin layer of compact bone can cause the same attenuation in a voxel as hyperdense cartilage alone.

Over the years many changes and technological improvements have been made to increase CT performance. Probably, one of the most significant was the introduction of the multislice CT in 1998, where an increased scan speed was associated with a better z-axis spatial resolution [71]. Then, also the volume coverage was increased along with the temporal resolution. Even today the aim is to get thinner and thinner slices with smaller acquisition times.

The human eye can distinguish only a limited number of grey-levels (from about 40 to 100, depending on viewing conditions). Consequently, there is no point in assigning the complete diagnostic range of CT_{N} (some 4000 HU) to the available range of grey-levels (from white to black) because discrimination between structures with small differences in CT_{N} would no longer be possible. It is therefore better to display just a portion of the CT scale, as shown in 3.1. This so-called window is defined by its width, which affects image contrast, and by its level, which determines image brightness. Reducing the window width increases image contrast; decreasing the window level has the effect of brightening the image while, on the contrary, raising the window/level (W/L) will result in a darker image [72].

3.1.1 DCE-CT

In 1979, few years after G.N. Hounsfield introduced CT, Leon Axel first proposed a method for assessing tissue perfusion from DCE-CT data [73]. At first this procedure remains confined to research studies, being the CT scanners not able to satisfy the high resolution and short acquisition time requirements. After

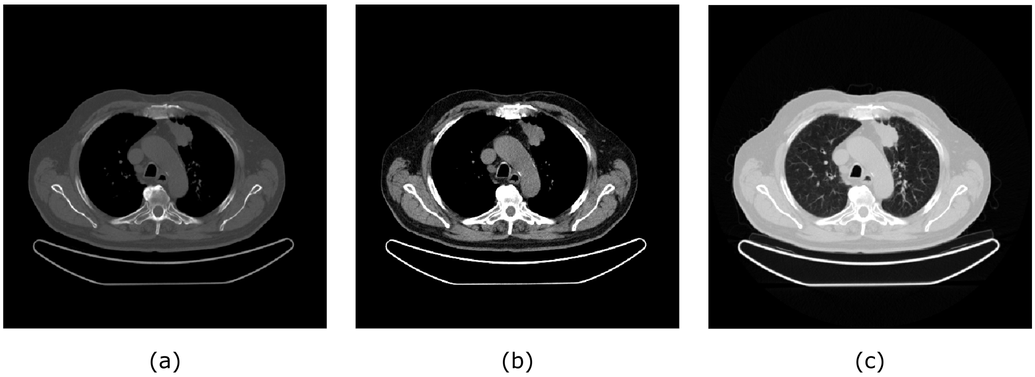

Figure 3.1: Images viewed at different window settings to enhance (a) bone (window 1500, level 300), (b) soft tissue (window 350, level 50) and (c) lung tissue (window 1500, level -400).

the introduction of the multislice systems, a renewed interest for DCE-CT, the functional imaging also known as CT perfusion (CTp), stimulated several clinical applications essentially targeting acute stroke and oncology.

Focusing on oncology applications, as mentioned before, the introduction of new therapies targeting tumour angiogenesis made CT and morphology-based criteria inadequate to evaluate tumour response. Immunohistochemical biomarkers of angiogenesis such as MVD, VEGF, and serum biomarkers such as circulating endothelial cells (CEC), have led to encouraging results, even if sometimes inhomogeneous [74]. However, none of these methods is considered a definitive indicator of the angiogenic activity for a functional tumour characterisation. Indeed, these potential biomarkers involve invasive, expensive and not widespread techniques, poorly suitable for a daily routine in the clinical practice [75, 76].

For this reason, even if CT remains the gold-standard for anatomical imaging in several tumours, there is a dire need to incorporate CTp into the existing CT protocols, being relatively inexpensive, almost non-invasive and already widely available. At present, CTp is widespread in both research and clinical trials, not yet in the routine clinical practice since protocols and software are far from being standardized. Its use permits the *in vivo* quantification of tissue perfusion through the temporal analysis of the Time Concentration Curves (TCCs), obtained by repeating scans over time after the administration of a contrast medium [77].

Multiple CTp parameters can be derived studying TCC signals, representing the temporal tissue density variations directly proportional to the quantity of contrast material trapped within the tissue. Several studies have shown correlations between CTp parameters and angiogenesis biomarkers (e.g., MVD and VEGF) in a wide spectrum of cancers, originated in different body districts including lung [13, 76], liver [14], prostate [78], stomach [79], kidney [80] and soft tissues [81].

The benefits of using DCE-CT to derive tumour vascularity information need to be balanced against the cancer risk associated to the radiation received during DCE-CT acquisition [12]. Among the most effective perfusion parameters permitting angiogenesis evaluation BF arises [82]. BF showed a high correlation with the tissue biomarker MVD [81] and can be measured by considering only the first passage of the contrast medium, this requiring a short-time examination and permitting to minimize the radiation dose administered to the patient, accordingly. Moreover, short-time acquisition also reduces the probability of patient movements, permitting to carry out perfusion studies with a single breath hold [83].

3.1.2 BF mathematical model

BF is one of the most significant perfusion parameters [82], which allows detecting the earliest functional changes on tumour vasculature even within the first week of anti-angiogenic therapy [84]. BF is defined as the transport of blood, consequently also of oxygen and nutrients, through a unit volume of tissue per unit of time (expressed in *ml/min/100g* or in *ml/min/100ml*). This is a phenomenon occurring at the capillary microvasculature level, not to be confused with the blood velocity, a concept usually applied for large vessels [68].

BF can be calculated for each voxel by considering a single-compartment model. This model represents both the intravascular and interstitial spaces with a temporal concentration of the tracer corresponding to the TCC of the tissue, $C_T(t)$. The system is characterized by a single inlet, the arterial input, with an arterial blood plasma concentration $C_A(t)$, and a single outlet, the venous outlet, with a venous blood plasma concentration $C_V(t)$, as shown in Figure 3.4. The relation between $C_A(t)$, $C_V(t)$ and $C_T(t)$ is given by the Fick's principle expressing the conservation of mass:

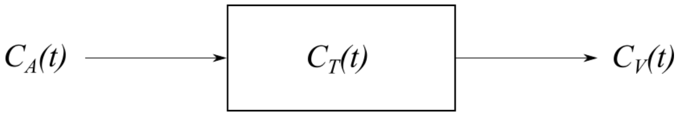

Figure 3.2: Single-compartment model outlining the perfusion tissue.

$$\frac{dC_T(t)}{dt} = \frac{BF}{V_T}[C_A(t) - C_V(t)] \tag{3.4}$$

One immediate simplification is to assume that during the measurement period there is no venous outflow, $C_V(t) \simeq 0$ (i.e., no contrast medium has reached the venous side of the circulation yet). This assumption is valid only for time periods less than the minimum transit time, when the injected contrast medium will all remain within the tissue. Under this assumption, Eq. (3.4) can be simplified as follows:

$$\frac{dC_T(t)}{dt} = \frac{BF}{V_T}[C_A(t) - C_V(t)] \simeq \frac{BF}{V_T}C_A(t) \tag{3.5}$$

This implies that the slope of the tissue curve, $dC_T(t)/dt$, reaches a maximum ("steepest slope") when the input function, $C_A(t)$, is at its maximum point [73]. Thus, the BF, expressed in mL/min/100 g, is given by

$$\frac{BF}{V_T} \simeq \frac{[\frac{dC_T(t)}{dt}]_{max}}{[C_A(t)]_{max}} \tag{3.6}$$

This is known as the Mullani-Gould formulation or single-compartment formulation. The approximation used in Eq. (3.5) results in an overestimation of the denominator of Eq. (3.6), and consequently in an underestimation of the BF if the bolus is large, or for organs with a rapid vascular transit. Accordingly, for organs such as spleen and kidney characterized by a complex microcirculation this assumption might not hold [85], but for most clinical applications the achievable accuracy and precision levels are appropriate [86] and the maximum slope method to calculate BF has been validated [87].

Figure 3.3 shows an ideal input function measured within a large tissue-feeding artery (red) and the concentration time curve measured in the tissue (blue). Usually, the proper input function is not detectable, this explaining why the steepest slope does not coincide with the maximum concentration time point [86].

3.1.3 BF computation

To obtain the samples needed to build $C_T(t)$ and $C_A(t)$, the target lesions and the arterial input (aorta) need to be segmented for each time instant, thus the-

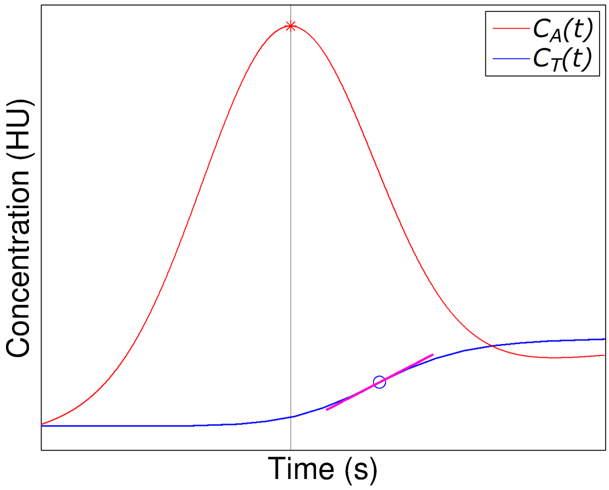

Figure 3.3: Representation of the aortic TCC signal, $C_A(t)$ (red), and the tissue TCC signal, $C_T(t)$ (blue). The red star points out the aortic peak, while the blue circle the steepest slope of the tissue curve. The grey vertical line indicates the time at which the aortic input is at its maximum, while the magenta line highlights tissue maximum slope.

oretically sampling the same body section. Generally, TCCs are built for the pixels belonging to the regions of interest (ROIs) by sampling the corresponding HU values. They appear as mainly composed of three phases: the baseline, the enhancement and the outflow. The first phase represents the time period before the arrival of the contrast medium in the tissue; the second phase is featured by an enhancement of the tissue corresponding to the arrival of the contrast medium; the last phase corresponds to the time period when the tracer leaves the tissue and starts the recirculation.

In order to obtain the TCC signal for each voxel of the tissue, several approaches are available in the literature, some of them being also quite recent [88]. In this Thesis, the sigmoid-shape model given by the *Hill Equation* has been adopted [89]. This model, described with the equation 3.7, is able to fit the main trend of the concentration samples in a robust manner [91].

$$y(t) = E_0 + (E_{max} - E_0)\frac{t^\alpha}{(EC_{50} + t)^\alpha} \tag{3.7}$$

where E_0 is the baseline concentration of the tissue, that is before the arrival of the tracer, E_{max} is the saturation value of the concentration reached after its arrival, EC_{50} is the time instant at the half-maximum value of the concentration,

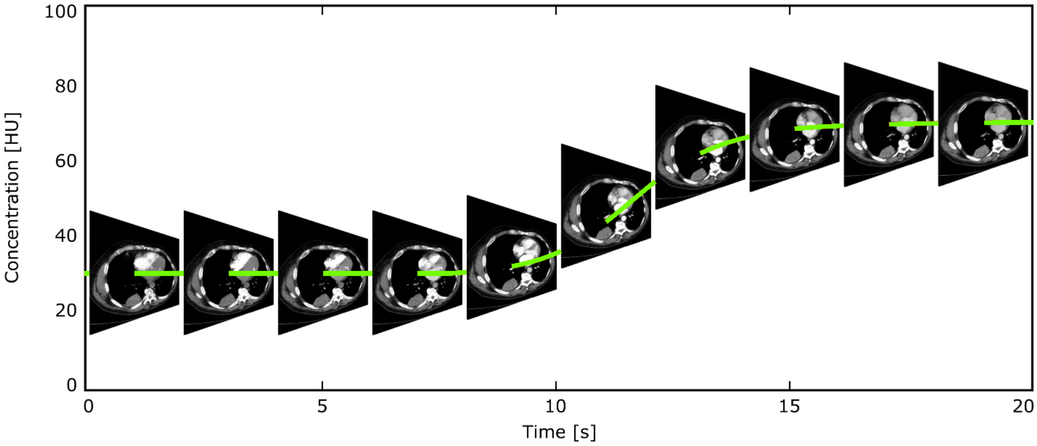

Figure 3.4: Representation of the sigmoidal model used for the fitting procedure, relative to the temporal sequence of a reference slice [90].

and α is the parameter which mainly affects the slope of the sigmoid curve.

The BF values of the reference slice are represented using functional colorimetric maps (Figure 3.5)). Blue regions point out low perfusion values, while regions characterised by hottest colours highlight the presence of highest perfusion areas. Pink colour points out the presence of unreliable pixels, that will be better described further on Section 5.3. These maps provide a useful view of the perfusion and the functional heterogeneity of the tumour, highlighting for instance

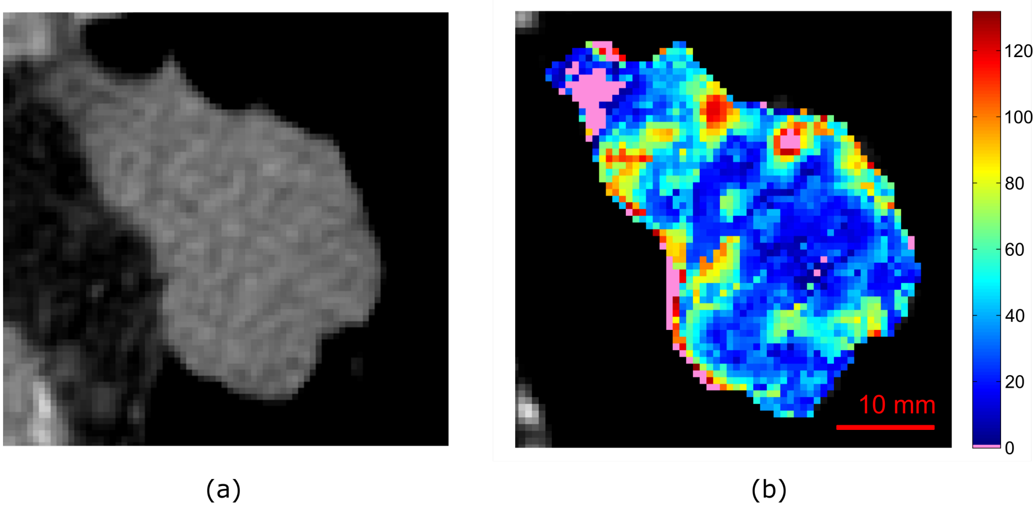

Figure 3.5: CT image (a) and corresponding BF map (b) of a lung tumour (squamous-cell carcinoma).

the presence of hypodense regions, hemorrhages, blood vessels and bronchi.

3.1.4 Open issues in DCE-CT

Despite CTp promising results in the oncological field, including early detection of the tumour, improvement of prognosis, earl assessment of effects following novel targeted therapies as well as diagnosis of tumour recurrence [92, 21, 11], CTp is not a clinical practice yet due to several challenges, mostly still open. These issues involve different aspects of DCE-CT utilisation. The lack of standardisation is one of the most serious [23], even if this problem has been partly faced by the Quantitative Imaging Biomarkers Alliance (QIBA), with the development of standardised protocols for DCE-CT and DCE-MRI [8]. Another relevant issue is the radiation dose, since the cancer risk associated to a CTp examination has to be justified by the benefits deriving from the knowledge of tumour perfusion [12]. In several studies, to decrease radiation dose tube voltage and/or mAs have been decreased [93]. This has been possible due to the new reconstruction techniques, which have improved the trade off between the noise introduced by the low-tube-voltage technique, which would lead to beam hardening artefacts, and the image quality. Repeatability and reproducibility are essential prerequisites to validate a new imaging technique. Indeed, especially when considering therapeutic monitoring, the assessment of measurement variability plays a primary role. Several efforts in this regard have been made in both human and animal models. Goh *et al.* analysed perfusion parameters (BF, BV, mean transit time or MTT, and permeability) derived from baseline and repeated CTp scans performed within 48 hours in 10 patients with histologically proven colorectal cancer. Results showed that perfusion parameters are reproducible with a within-subject coefficient of variation lower for tumour than for skeletal muscle [94]. Authors in [95] found a high correlation coefficient and a low variability of perfusion parameters between two successive CTp scans performed within 30 hours in 4 patients with advanced hepatocellular carcinoma (HCC). Another study [96] including 10 patients with histologically proven NSCLC reported both permeability and blood volume measurements were reproducible, with very low inter- and intra-observer variability. Also in another study [97] with 20 patients affected by NSCLC, examinations were repeated after 24 h. Low within-subject coefficient of variation for BF, BV, MTT and peak enhancement showed the repeatability of the first-pass CTp technique.

Despite the above promising results, there is still need for more reproducibility studies for CTp measurements since most of the previous works were performed on limited study populations coming from single centres. In addition, as shown in [98], absolute CTp values are jointly affected by motion correction and acquisition protocols, since longer acquisitions do not allow breath-hold condition, this leading to unavoidable movements and to increased variability [99]. Motion artefacts due to, for instance, respiratory and cardiac movements can jeopardise TCCs computation, leading to unreliable perfusion parameters, particularly in abdomen and thorax studies. Similarly, also the presence of physics-based artefacts, such as for instance cupping artefacts and streaks [70], as well as partial volume artefacts [84], may alter the calculation of perfusion parameters. Besides these factors, also tumour heterogeneity, reflecting the presence of chaotic and tortuous blood vessels, hypoxic regions, micro-calcification and blood loss [100, 101], is considered an intrinsic factor causing measurement variability [94]. Recently, very few studies have started focusing on the TCCs fitting error to identify which perfusion values are most likely unreliable at voxel level [102, 103], without considering the spatial coherence of the perfusion maps. Actually, the reliability analysis is mainly performed considering the inter- and intra-observer variability [98, 104, 96] through the use of statistical global measures of perfusion parameters, include variability caused by measure uncertainty and that intrinsic due to the intra-tumoral heterogeneity, this thwarting any assessment of perfusion reliability. This issue has been partly faced in 5.3.1, where a deep analysis has been carried out.

3.2 MRI

As discussed in DCE-CT, non-invasive staging of cancer often involves CT as a primary imaging investigation, because of its high accuracy reached through innovations in hardware and imaging tracers. CT plays an important role for the assessment of the extension of the primary tumour invading the nearby tissues, as well as for the detection of distant metastases [105]. It is well known that an accurate tumour staging is of relevant importance for determining prognosis, planning therapy and evaluating tumour response. Another aspect particularly crucial is the determination of the resectability based on accurate evaluation of tumour infiltration depth and invasion into surrounding structures [106]. Despite the medical imaging innovations, the assessment of local tumour extent and infiltration, for some organs, remains challenging. For instance, for cancers of the oesophagus or GOJ, the delineation of the tumour on CT images is hard, since tumour attenuation is similar to that of the oesophageal wall. In addition, it is also difficult to evaluate tumour infiltration through or beyond the oesophageal wall since the single layers composing the oesophageal wall cannot be resolved due to the lack of contrast characterising the soft tissue [107]. Currently, the endoscopic ultrasound (EUS) is the most accurate for the staging for oesophageal cancer [108]. However, there are lots of technical difficulties associated with the technique, due to the inability to pass the endoscope through stenotic tumours. Magnetic resonance imaging (MRI) has become a promising modality for the non-invasive staging of some cancers, as gastric, oesophageal and GOJ cancer.

The nuclear magnetic resonance (NMR) phenomenon in solids and liquids was first described in 1946 by Bloch and Purcell. In 1973 Paul Lauterbur proved that it was possible to use NMR to create an image. Similarly to the CT technique, MRI has rapidly evolved with the introduction of technological innovations as the superconducting magnets, leading to the first clinical applications in the early 1980s [109].

In order to produce detailed images, MRI exploits the body's natural magnetic properties. Indeed, in the body, mainly in water and fat, there is a great abundance of hydrogen nuclei which are single protons [110].

Hydrogen atoms possess a property known as spin, which under normal conditions, are randomly aligned. With the application of a strong static magnetic field (B_0) the protons axes aligned either in parallel (low-energy state) or antiparallel way (high-energy state) to the external field precessing (rotating) around the B_0 axis (3.6). Usually, in MRI B_0 strengths range between $0.5T$ and $3T$.

The frequency of the precession ω_0, known as resonance or Larmor frequency, is directly proportional to the magnetic field strength, B_0, and is defined as follow:

$$\omega_0 = \gamma B_0 \tag{3.8}$$

where γ is the gyromagnetic ratio and is constant for each atom.

By applying a second radiofrequency (RF) magnetic field B_1 perpendicular to B_0, usually consisting of short pulses lasting microseconds, nuclei with a spin can be excited [109]. The absorption of RF energy usually causes a transition of the nucleus from lower to higher energy levels, as well as a spontaneous in-phase spinning, that is simultaneous spinning. The energy absorbed and then emitted by the nuclei can be detected, amplified and displayed as "free-induction decay"

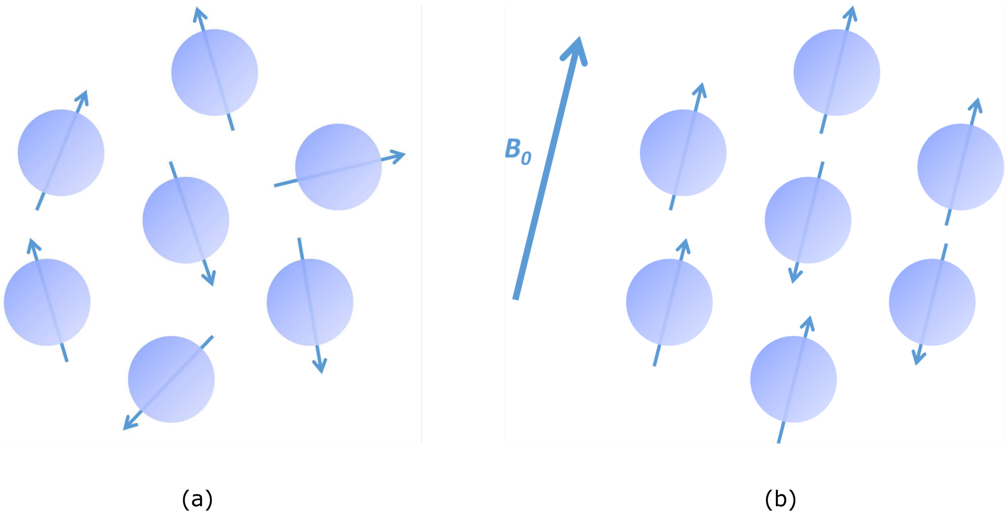

(a) (b)

Figure 3.6: Under normal conditions, hydrogen protons spin in the body are randomly arranged (a). In the presence of a strong magnetic field B_0, as occurs in an MRI scanner, protons align themselves parallel to the MRI magnetic field (b).

(FID).

In order to spatially localise the MR signal, magnetic gradients changing the Larmor frequencies of the spins are added to the static field strength in the three orthogonal directions [111]. Faster or slower frequency is detected as higher or lower MR signal respectively, this permitting to distinguish MR signals sources in the space and enabling image 3D reconstruction.

3.2.1 T1- and T2-weighted MRI

The application of multiple RF pulses in sequence allows to emphasise tissues and abnormalities [110]. When the RF pulse is switched off tissues protons relax (return to equilibrium) with different rates. The time taken for the protons to relax can be measured in two ways, by considering separately what occurs to the spins in the longitudinal and transverse plane.

The time taken for the protons to return to their original position, transferring the energy absorbed from the RF pulse to their surroundings, is known as T1 relaxation or "spin-lattice" relaxation [112]. It is defined as the time needed to achieve 63% of the original longitudinal magnetization. Simultaneously, the protons spinning in-phase in the transversal plane will no longer spin synchronously, losing transversal magnetization once the RF pulse is switched off. This phenomenon, known as dephasing, is due to the inhomogeneity of the MRI scanner magnetic field. T2 relaxation time, also known as "spin-spin" relaxation, is defined as the time needed to dephase up to 37% of the original transversal magnetization [109]. It is faster than T1 relaxation. It is possible to obtain images with a single tissue parameter, T1 or T2, which dominate the image contrast, creating the so-called T1-weighted or T2-weighted image, respectively.

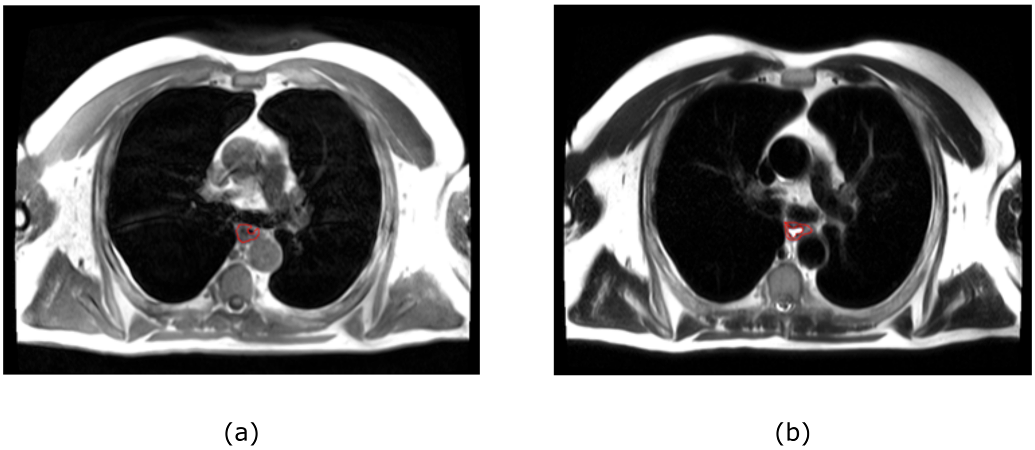
(a) (b)

Figure 3.7: Gastro-oesophageal junction cancer outlined in red in T1 (a) and T2 (b) images.

Different tissues have different T1 and T2 relaxation times, thus permitting their identification. Fat has a short T1 relaxation time as compared to water because it can more easily transfer its received energy to its surroundings and quicker dephase. T2 relaxation time for fat is less short than T1. Therefore, it appears bright on T1-weighted images and less bright in T2-weighted images. In practice, T1-weighted images are mainly used to analyse normal anatomy. Very few structures have a high signal intensity and appear bright on T1-weighted images (e.g., fat, blood, melanin, high-protein tissues). Also artefacts can appear as white structures. While, water and collagenous tissue have a lower signal intensity on T1-weighted images and appear darker. T2-weighted images are instead used to detect pathology, as shown in Figure 3.7, and fluids around the tumour [111]. Indeed, pathology is usually associated with edema/fluid, which makes T2 sequence very suitable, being characterised by a high signal intensity of water.

3.2.2 DWI

DWI is another MRI technique, sensitive to diffusion molecules. It relies on the detection of the random microscopic motion of free water molecules [113], known as Brownian movement, which is linked to the thermal kinetic energy [114]. This constant random motion, which characterised water molecules enclosed in a container, is known as free diffusion. In biologic tissue, the motion of water molecules is restricted because movement is limited by the presence of cell membranes, macromolecules and intra-cellular organelles [115].

DWI signal represents water molecules diffusion in the intra-vascular, intracellular and extra-cellular space [116]. It is not surprising that signal emerging from the intra-vascular space is higher since water molecules diffusion is less restricted and that for highly vascularized tissues DWI signal component coming from the intra-vascular space is significant [117]. In order to obtain DWI images, two additional symmetric gradient pulses are applied to the magnetic gradient pulses. The first is incorporated in order to dephase the nuclear spins, producing an effect similar to the T2 relaxation. After occurring the 180° echo pulse, the second magnetic pulse gradient is applied with the aim to rephase the nuclear spins. However, if the nuclei have moved, the rephasing process will be incomplete, resulting in signal loss. Differences in signal intensity due to incomplete spin rephasing are the basis of DWI signal. The degree of diffusion sensitization can be enhanced by increasing the amplitude, duration, and temporal spacing of the two added gradients. These gradient properties determine the so called b value, expressed in s/mm^2, an index of the degree of diffusion weighting.

In biological tissues DWI signal is inversely related to tissue cellularity as well as integrity of cell membranes [118], as shown in Figure 3.8. Therefore, it is possible to detect phenomena including water diffusion from the extra-cellular to intra-cellular spaces, restriction of cellular membrane permeability and depolarization disruption, and increased cellular density [117]. These features are commonly associated with malignancies and hypercellular metastases, being tumour tissue generally characterised by a high density of cells, most of all with intact cell membranes. In tissue micro-environment with less cells and defective cell membrane, as occurs in the necrotic core of a large mass, water molecules can move freely [119]. The ability of DWI to detect these characteristics along with the development of new technologies and stronger diffusion gradients explain the increased interest for DWI in the oncologic field. Oncologic applications include tumour

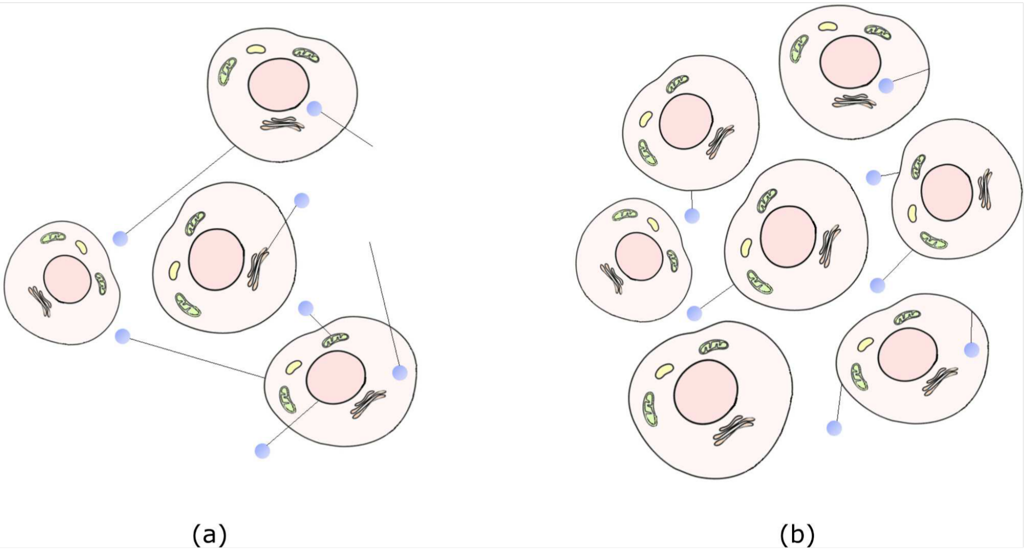

Figure 3.8: Diffusion of water molecules, represented by light blue circle moving along a direction, drawn as a black straight line. In the presence of low cellularity and disrupted cell membranes, water is freer to diffuse in the extra-cellular space, than in a more cellular environment. Disruptive cell membranes also permit the diffusion between the intra- and extra-cellular spaces (a). In the presence of a high cellularity and intact cell membranes water diffusion is restricted by the reduced extra-cellular space and by the membranes, which constitute a barrier for the diffusion (b).

diagnosis and characterisation as well as prediction and assessment of treatment response [120, 121]. DWI examinations usually last 1-5 minutes, thus permitting its inclusion into the MRI imaging protocol without significantly increasing the overall acquisition time. Another benefit of DWI is that no exogenous contrast material is required since image contrast is due to the inherent tissue contrast, determined by the random microscopic motion of water protons.

DWI images can be post-processed in order to obtain ADC maps [mm^2/s], providing functional tissue information [122]. Theoretically, it is possible to obtain maps of water diffusion by acquiring two images with different b values [123], according to the follow equation

$$ADC = \frac{\ln \frac{S_0}{S_1}}{b_1 - b_0} \tag{3.9}$$

where S_0 and S_1 are the signal intensity obtained with b_0 and b_1 values, respectively. This equation provides the real diffusion only if water can freely diffuse, condition that never occurs in biological tissues [124, 50]. The great power of ADC is its ability to represent, in some way at voxel level, the hidden physical processes occurring at much smaller scales, since water molecules can diffuse on distances of about few micrometres, interacting with other molecules and cellular organelles. The ADC can be computed for each voxel of the image and displayed as a parametric map, as shown in Figure 3.9.

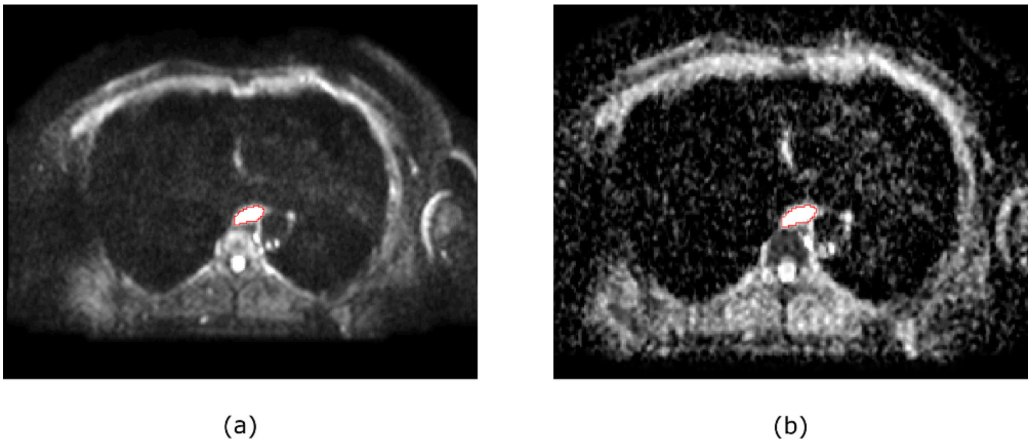
(a) (b)

Figure 3.9: Gastro-oesophageal junction cancer outlined in red in the DWI image and the corresponding ADC map.

Regions of restricted diffusion in highly cellular areas are represented by low ADC values, while less cellular areas are characterised by higher ADC values. It is worth noting that although areas of restricted diffusion appear to be higher in signal intensity on DWI images, these areas are contrarily characterised by a low-signal intensity areas on the ADC map [117].

Usually, ADC values are lower for malignant lesions than for benign lesions and healthy tissues [50]. As anticipated in Section 2.3, ADC values can be measured to evaluate changes in cellular packing, in order to monitor tumour response to therapy. Indeed, increased ADC values after chemotherapy has the potential to early suggest the inefficacy of chemotherapy [125], allowing the clinicians to switch to more efficient therapy.

3.2.3 Open issues in MRI

MRI is routinely used in clinical practice for the management of oncological patients, providing both structural and functional information, without involving the use of potentially harmful ionizing radiation [126]. MRI images are characterised by an excellent contrast between soft tissues [11], such as muscle, ligaments, articular cartilage and bone marrow. Although a lot of progress has been made in the cost and, consequently, in the availability of MRI, there is still need to further decrease the cost of MR scanners in order to improve the accessibility of this technique [109].

Despite the numerous clinical applications, MRI present several issues. MRI is particularly sensitive to physiological motions, such as the gastrointestinal peristalsis, respiratory and cardiac movements, which lead to artefacts [127]. Similarly, also vessels pulsations occurring in the presence of considerable BF, such as in aorta and pulmonary vessels, lead to the so-called flow artefacts. To reduce these artefacts, triggering and gating techniques should be applied. However, these techniques, being time-consuming, worsen the overall examination time, which still represents an issue [117]. Indeed, being the image acquisition time quite long, also patient movement must be considered. Moreover, MRI scanners may be uncomfortable for claustrophobic patients, and the image quality of the open scanners could be not adequate.

Other aspects that need to be considered are the geometric distortions, known as susceptibility artefacts, caused by the presence of metallic implants [128]. In these cases, CT may represent a more suitable choice. Probably, CT constitutes also a better alternative to investigate lung pathology. Indeed, besides being the thorax subject to respiratory motion artefacts, it is also affected by air susceptibility artefacts, directly related to a fast signal decay.

In central regions of the mediastinum the signal-to-noise ratio (SNR) may degrade. This issue can be faced by scanning at a higher magnetic field strength (i.e., 3T). However, scanning at higher field strength can lead to increased effect of magnetic susceptibility variations, which can affect the geometrical fidelity of MRI images [129].

In the last years, DWI has become more available in the clinical practice due to improvements of MR devices, proving to be a useful tool for diagnosis, tumour characterisation and monitoring tumour response to therapy, in a variety of organs such as oesophagus and stomach [130], liver [19], rectum [131], pancreas [132], and also in prostate [133]. One of the major issue, which limits the widespread adoption of DWI in the oncologic field, is the lack of standardization in the image acquisition, particularly with regard to the choice of b values, which has led to significant differences ADC estimates [134].

Another source of variability in ADC values regards the analysis of the results, which can lead to different clinical consideration. Indeed, as discussed in Section 2.1.1, tumour micro-environment is both spatially and temporally heterogeneous [117]. Analysing statistical indexes (e.g., mean or median value of ADC maps) has the great advantage of providing a single value to represent the whole tumour ROI or volume in a fast and intuitive way, generating parameters with a high inter-observer repeatability [135]. However, these statistical global values cannot reflect the underlying lesion heterogeneity. More sophisticated methods to describe data need to be introduced and further work is needed to better understand the pathologic variations associated with features observed in ADC maps.

3.3 PET

PET is a nuclear medicine imaging technique well established in the oncological field, able to image the metabolic and biological processes occurring in the body. It provides information regarding molecular processes taking place in healthy and pathological tissue, adding functional information with respect to the morphological characterisation, which can be derived using other imaging techniques as CT and MRI [136].

PET operation principle involves the use of radioactive agents, which are usually administered intravenously as radiopharmaceuticals. Radioactivity decay caused ionizing radiations within the body, which can be detected, measured, and imaged through the use of gamma cameras [137]. Indeed, the nuclear decay emits a positron, a $\beta+$ particle, that interacts with an electron, $\beta-$ particle. The annihilation event between the $\beta+$ and the electron produces two coincident γ rays (photons), as shown in Figure 3.10. If two detectors oriented at 180° detect the pairs of annihilation photons in coincidence, then the origin of the $\beta+$ emission can be identified along the line between the two detectors [138]. Thus, PET image intensity reflects the radiopharmaceutical activity concentration derived from the analysis of annihilation events.

The positron-emitting radionuclide is introduced into the body on a biologically active molecule. Indeed, PET tracers are characterised by two components:

- the so-called vector, vehicle or ligand which is the molecular structure, chemically and biologically interacting with target sites in the tissue;
- a positron emitting radionuclide, which will provide a detectable signal en-

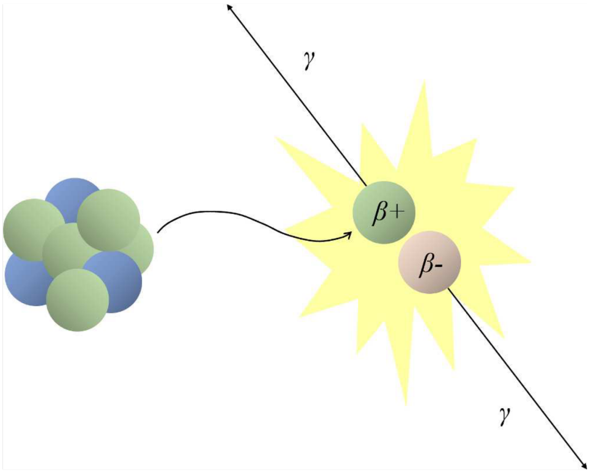

Figure 3.10: Positron and electron annihilation resulting in the emission of two anti-parallel γ rays.

abling the localization of the ligand.

Among the target sites usually considered there are specific receptor systems, antigens, enzymes, transporters, specific metabolic alterations [139].

The most widely used biologically active molecule in routine application in oncology, neurology and cardiology is the FDG, an analogue of glucose, first radiolabelled in 1978 [140]. In general, cancer cells, contrary to normal cells, metabolise glucose by aerobic glycolysis [42, 46, 45]. Otto Warburg noticed this general principle, known as the Warburg effect, characterised by increased glycolysis regardless of oxygen availability. Indeed, it is interesting to note that also malignant hypoxic cells, tend to use anaerobic metabolism, which requires even more glucose than the aerobic one [47]. Tumour glycolysis is usually associated with an increased glucose uptake, being many cancers characterised by a high metabolic rate. For this reason, enhanced glucose uptake derived from FDG-PET can be used as an early indicator of drug efficacy [53] and as a staging tool for several cancers, with the possibility to investigate the presence of cancer metastases.

FDG-PET images are traditionally visually interpreted through a qualitative analysis [141]. However, in the last years, some statistical parameters derived from standardized uptake value (SUV) maps have been established in the clinical practice. SUV reflects the decay-corrected uptake of the radiotracer within a region or volume of interest (ROI or VOI, respectively) normalised to the injected dose and the whole-body distribution, typically taking into account the patients body weight. SUV is an adimensional parameter usually normalised on body weight (BW) expressed in g and computed as follow:

$$SUV = \frac{activity \cdot BW}{dose \cdot decay} \tag{3.10}$$

where *activity* is the activity concentration in tissue (expressed in Bq/mL), *dose* is the total radiopharmaceutical dose administered to patient (Bq and *decay* is the decay factor used to correct the injected dose, computed as follows:

$$decay = 2^{\frac{t_i - t_a}{h}} \tag{3.11}$$

where t_i is the injection start time (s), t_a is the acquisition time (s), and h is the radionuclide half time (s).

Usually, SUV is reported as the mean (SUV_{mean}) or maximum (SUV_{max}) SUV of all voxels within a ROI or a VOI [142]. Among these, SUV_{max} is usually preferred to the mean value, which can vary with the region considered, due to the high heterogeneity of tumour FDG uptake. Therefore, contrarily to SUV_{max}, it is subject to both intra- and inter-observer variability [143]. The use of SUV_{max} has facilitated the comparison between patients, even if the practice of using SUV thresholds for diagnosis is still widely debated [144].

Routinely, PET is often performed in combination with CT through hybrid system known as PET/CT, even if recently a combination of PET and MRI has been proposed as a promising alternative [145].

3.3.1 Hybrid systems

Combined PET/CT has emerged as a powerful imaging modality for tumour diagnosis, staging and restaging, with dramatic improvements in the accuracy over the PET alone [20]. At present, FDG-PET/CT is used in most oncologic disease processes for several indications, including tumour response assessment, treatment planning and follow-up examinations for recurrence detection [146]. PET/CT scanners are characterised by two high-performance scanners, solving the problems of significant misalignments, met when fusing image-series coming from standalone systems [136].

CT acquisition of the whole body usually lasts less than 1 minute and is acquired before PET. As already mentioned, one of the greatest advantages of performing a whole-body CT is that functional images can be easily aligned with the underlying anatomy, emerging from CT images. Another essential advantage is that through CT attenuation maps is possible to directly correct PET images.

An example of PET/CT clinical use with a great impact in clinical practice is the evaluation of the nodal involvement. Indeed, if from one side CT enables a size evaluation of the lymph node, with PET is possible to derive its metabolic activity, detecting possible disease earlier than anatomic changes occur (e.g., size $> 10mm$) [136].

The devolpement of hybrid PET/MRI system is quite recent even if the idea to combine the PET and the MRI arose even before PET/CT introduction [147]. The reason of this delay and slow progress is that the integration of the PET with the MRI system is much more complex than that with the CT, due to the presence of magnetic fields. Anyway, although it was really challenging, many resources have been invested for the achievement of the multimodality PET/MRI, due to the great success of PET/CT systems [148].

As already mentioned, in PET/CT system CT images are not just used for anatomical details but also to easily perform coefficients attenuation correction. For a PET/MRI system the derivation of attenuation-correction maps from MRI images is much more complex [149] and although several methods have been developed, this problem has not been overcome yet. Moreover, the acquisition time for PET/MRI systems is longer than that of PET/CT ones.

Anyway, PET/MRI systems, despite their technical limitations, present valuable advantages, including the acquisitions being spatially and temporal simultaneous, with a great benefit for post-processing analysis, as the image registration. Moreover, the total dose administered to the patient can be reduced significantly as no dose is required by MRI scans.

As regards clinical applications, it is worth noting that MRI is the preferred imaging modality to examine diseases of the soft tissue, making PET/MRI systems very suitable for brain, breast and abdomen application. Indeed, because of its superior soft-tissue contrast MRI is able to provide a high spatial resolution of tumour as well as local disease extent, being also essential for characterisation of primary tumour in sites sub-optimally imaged with CT [150].

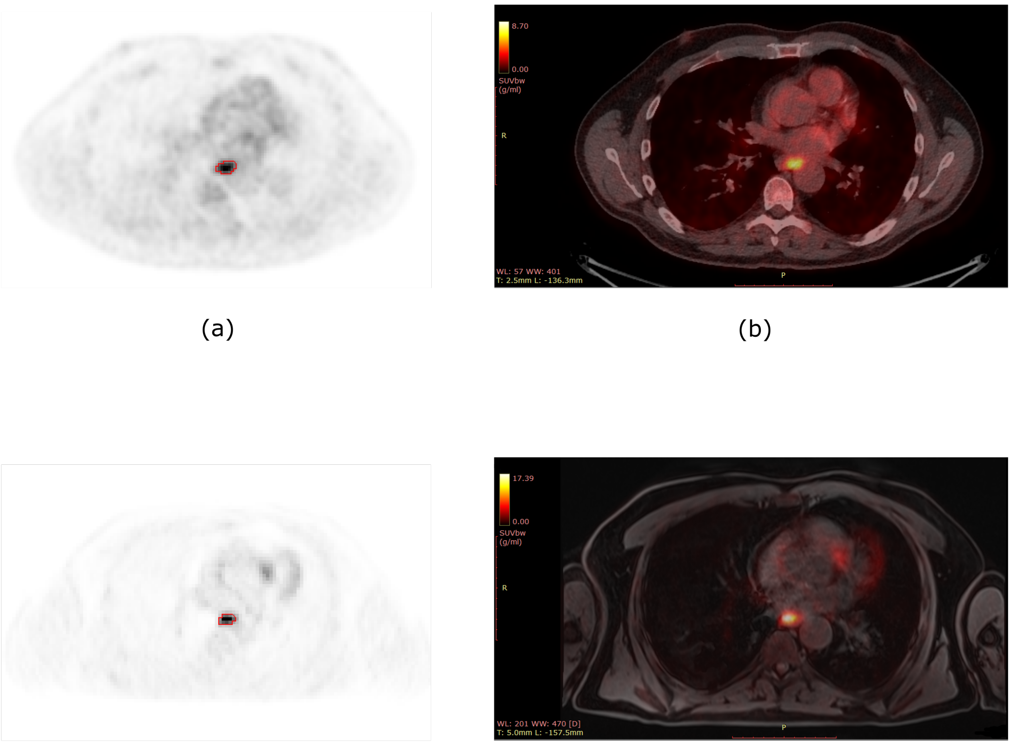
8.70
0.00
SUVbw
(g/ml)
R
WL: 57 WW: 401
T: 2.5mm L: -136.3mm
P
17.39
0.00
SUVbw
(g/ml)
R
WL: 201 WW: 470 [D]
T: 5.0mm L: -157.5mm
P

(a) (b)

(c) (d)

Figure 3.11: PET image acquired with PET/CT (a) and PET/MRI system (c) and corresponding SUV fusion with CT (b) and T1-weighted image (d). These images point out a gastro-oesophageal junction cancer, characterised by an increased abnormal FDG uptake outlined in red in (a) and (c).

3.3.2 Tracers

In the past decade, the number of beta-emitting compounds able to mark both metabolic pathways other than FDG and non-metabolic pathways has increased exponentially. These markers are mainly indicated for the assessment of clinical conditions that cannot be successfully imaged with the FDG radiopharmaceutical.

Table 3.1: A summary of the most common tracers and isotopes used to image specific molecular mechanism. Organs with the highest physiological uptake are also reported.

Molecular mechanism	**Tracer**	**Isotope**	**Organs with highest uptake**
Glucose metabolism	FDG	F-18	Brain, myocardium, breast, liver, spleen stomach, intestine, kidney, urinary bladder, skeletal muscle, lymphatic tissue, bone marrow, salivary glands, thymus, uterus, ovaries, testicle, brown fat
Proliferation	FLT	F-18	Bone marrow, intestine, kidneys, urinary bladder, liver
Bone metabolism	NaF	F-18	Bone
Phospholipid metabolism	Choline	C-11	Liver, pancreas, spleen, salivary glands, lachrymal glands, renal excretion, bone marrow, intestine
Somatostatin-receptor	DOTANOC	Ga-68	Pituitary gland, spleen, liver, adrenal glands, kidneys, urinary bladder
	DOTATOC	Ga-68	Pituitary gland, spleen, liver, adrenal glands, pancreas, urinary bladder, thyroid
	DOTATATE	Ga-68	Spleen, urinary bladder, liver
Prostate-specific antigen	PSMA	Ga-68	Lacrimal gland, parotid gland, submandibular gland, liver, spleen, small intestine, colon, kidney, urinary bladder, salivary glands

Among these, there are radiolabelled ones, including aminoacids, choline derivatives, nitroimidazole derivatives, and peptides targeting several different receptors. PET imaging enables the visualisation of molecular phenomena including metabolism and proliferation, as well as specific receptor and gene expression, as reported in Table 3.1, this explaining why it is considered as molecular imaging [151]. Even though FDG tracer remains the most widely used in the clinical practice, these new radiotracers pave the way for more personalised and specific imaging. For instance, Ga-68-labeled somatostatin-receptor analogs are widely spreading in clinical routine for diagnosis and treatment planning of neuroendocrine tumours (NET) [141]. It is worth noting that $SUV_{\max}$ derived from metabolic PET studies, such as ^{18}F-FDG-PET, reflects the rate of the tracer metabolism, thus the underlying metabolic activity of the tissue. In PET studies obtained with receptor-based radiotracers, such as ^{68}Ga-DOTA-peptides, the biologic meaning of $SUV_{\max}$ corresponds to the cells receptors availability. This information is particularly useful for NET lesions, since they overexpress somatostatin receptors, making the ^{68}Ga-DOTA-peptides particularly suitable for the assessment of these tumours, less glucose-avid than other tumours and, consequently, not easy to detect with ^{18}F-FDG PET scans. Moreover, ^{68}Ga-DOTANOC PET allowed the identification of patients who will benefit most from somatostatin analog therapy [152]. Some studies have also investigated the role of grading and staging of pancreatic NET, through the use of somatostatin receptor density as potential prognostic factors [153].

It is interesting to note that authors in [154] report that NET lesions are greatly heterogeneous. As mentioned before, these kinds of tumours are characterised by overexpression of somatostatin receptors on the cell membranes. The use of a dual-tracer approach with ^{18}F-FDG and ^{68}Ga-DOTA-TOC, has allowed assessing somatostatin receptors expression and glycolytic metabolism. This approach could improve the selection of the most suitable therapy in patients with NET. High $SUV_{\max}$ derived from ^{18}F-FDG images may suggest an aggressive tumour behaviour, providing a complementary information to the somatostatin receptor density, and representing a step towards a personalised medicine of NET patients.

As regards tracer able to highlight phospholipid metabolism, the most used is ^{11}C-Choline. This radiotracer was found being able to image several tumours, including prostate cancer. Indeed, several cancers have shown high levels of phosphorylcholine, much more significant than those found in normal tissue. However, what is responsible for tracer accumulation is currently not completely clear, even if experimental studies suggest that choline transport and not phosphorylation is the key step for choline uptake in malignant cells [151].

Actually, as regards prostate cancer, the most widely used radiotracer is ^{68}Ga-PSMA, able to image the expression of PSMA in cancer cells. ^{68}Ga-PSMA is a novel radiotracer that, analogously to the ^{68}Ga-DOTA-peptides for NET tumours, is able to detect prostate cancer and metastases by targeting tumour PSMA overexpression [155].

3.3.3 Open issues in PET

As reported in the previous Sections, PET imaging providing molecular and functional information of tumour biology has completely revolutionised the oncological clinical practice, leading to dramatic improvements in diagnosis, staging, restaging, preoperative assessment, therapy monitoring and selection [150]. One of the main disadvantages of PET scanners remains their high operating cost. Indeed, the technology is still expensive and, to exploit all PET potential, highly specialised radiochemistry expertise and a cyclotron unit are required, at least within a reasonable distance, due to the limited half-life, for instance, of ^{18}F isotope [141].

Standardisation of acquisition protocols, including patient preparation, is mandatory, since several biologic and technological factors can affect SUV computation [142]. Indeed, SUV can be affected by patient characteristics like body weight, biologic features as the blood glucose level, and also respiratory movements. As regard the technical aspects also the uptake time, the decay correction, the use of the time of flight, the scanner calibration, the methods for attenuation correction, the algorithms for the PET reconstruction and the use of contrast agent in hybrid system, cause variability in SUV measurements [156]. Some of these aspects concern in particular the PET/MRI, which despite being characterised by a better soft tissue contrast and less ionising radiation has some drawbacks including inferior PET data and higher susceptibility to artefacts due to respiratory and cardiac motion as well as air-tissue or air-bone interfaces.

Measurement variability prevents often both within-patient analysis, including comparison of values coming from follow-up examinations, and between-patient analysis, thus thwarting improvements in diagnosis and prognosis assessment. As regards tumour monitoring, a set of guidelines for the PET assessment of tumour response, similar to the RECIST, have been proposed in 2009 as PET Response Criteria in Solid Tumors [157].

The partial volume effect represents a phenomenon with dramatic impact on image quality. FDG accumulation in small tissue volumes appear larger in size and characterised by a weaker signal. Partial volume effect is partly due to the PET low spatial resolution, which introduces blurring effects, the lesion size, the surrounding background activity and the sampling errors due to the reconstruction algorithms [158]. Besides technical aspects, also respiratory and cardiac motion artefacts can amplify the partial volume effect. Therefore, SUV cannot be accurately measured in lesions with a diameter smaller than $2cm$, where the value will result probably underestimated [141].

There is currently no consensus regarding the definition of ROI used to measure tumour SUV. There are several different possibilities that include:

- free-hand segmentation of the tumour;
- fixed-size ROI positioned on the gravity centre of the tumour;
- isocontour defined as a percentage of tumour SUV_{max}.

As mentioned in Section 3.3, manually segmentation of the tumour ROI affects SUV_{mean} value, thus preventing its repeatability and reproducibility. In addition, this procedure may be subject to observer variability. To overcome the variability introduced by a subjective approach, the idea of a fixed-size ROI was proposed, automatically positioned based on geometrical lesion features. Despite this procedure has the advantage of removing observer variability, the fixed-size ROI introduces another type of variability, linked to the size of the lesions [159]. SUV_{mean} will erroneously include outer structures, which will lead to an under- or an over-estimation of the uptake. In this case, also SUV_{max} computation could be compromised. For this reason, the choice of isocontour has appeared as the most “reliable” and objective one, and 40% of SUV_{max} is usually considered as significant [160]. The drawback of this approach is that the percentage of SUV values considered for the SUV_{mean} measure, depending on the SUV_{max}, is strongly affected by the amount of noise of the images. Indeed, SUV_{max} represents just 1 pixel of the tumour, i.e. that having the maximum intensity value. Even though, in absence of noise this value represents the least affected by partial volume effect, unfortunately, in a real situation, SUV_{max} is strongly affected by noise. This issue will be deeply analysed in Chapter 11.

What probably has made SUV_{max} so popular, beyond its promising clinical results and despite its sensitivity to noise is that it is an observer-independent parameter more reproducible than SUV_{mean} [142, 161]. However, it worth noting that even in an ideal situation, lesions are heterogeneous, thus a single pixel cannot be considered as representative of the whole tumour uptake.

Chapter 4

Texture Analysis

Contents

4.1 Background **69**

4.2 Texture analysis methods **71**

4.3 Statistical features **72**

  4.3.1 First-order features 73

  4.3.2 Second-order features 74

  4.3.3 Higher-order features 78

This Chapter introduces the concept of “texture analysis”, a tool that has played an essential role in medical image application, having the great advantage of maximising the information, without the need for additional acquisitions (Section 4.1). The main texture analysis approaches currently used in literature are briefly discussed (Section 4.2). Then, the statistical-based methods, considered and developed within this Thesis work, have been reported ranging from the first-order to the higher-order features (Section 4.3).

4.1 Background

Image analysis is widely used in oncologic settings, playing an essential role in several medical applications, as diagnosis [19], staging [20], prognosis [21] and response evaluation to therapy [54]. As reported in Chapter 3, a variety of imaging modalities can be employed in the oncological clinical practice, including CT, MRI and PET. As shown, these modalities have peculiarities which make them suitable for different oncologic settings, being able to assess different biological mechanisms. Despite their particular use and technological features, they share the way images are clinically interpreted, that is mostly visually [162]. Generally, the aim of the clinician is to detect potential abnormalities, recognising patterns and linking the perceived patterns with possible diagnoses. Therefore, the success of a correct image interpretation strongly depends on the skills of the clinician [163].

As discussed in Section 2.3, when the analysis is carried out relying also on quantitative measurements, these are global statistical measures, most of times mean values computed, for instance, on HU or BF values derived from CT images, on ADC and SUV parameters from MRI and PET images, respectively. However, tumours are heterogeneous at different scale, from gene to tissue, as discussed in Section 2.1.1. Therefore, a global evaluation cannot be entirely representative, this preventing a proper tumour characterisation. A visual approach could allow a qualitative heterogeneity evaluation, that however will be prone to subjective variability. As a result, despite tissue heterogeneity has been proved to be strongly related to tumour aggressiveness [164], prognosis [165] and survival [166], its quantitative evaluation is still not included in the clinical practice.

On the other hand, by its very nature, quantitative evaluation through molecular characterisation, involving biopsies or invasive surgeries to get small tissue specimens, cannot adequately represent the features of the tumour as a whole [6]. On the contrary, imaging is able to provide voxel-based information for the whole tumour. It has the great potential to capture the *in vivo* intra-tumoral heterogeneity non-invasively [9], paving the way for a routine tumour monitoring and therapy response evaluation.

In the last decade, quantifying the salient features of the intra-tumoral heterogeneity has gained a great attention, also leading to a re-emerging of the texture analysis as an essential tool in the era of personalised medicine [162]. As stated in 1979 by Haralick, texture has not a satisfactory definition, assuming different meanings based on the context, being also perceived in a highly subjective way [167]. Anyway, we need a working definition of texture. Texture refers to the structures and the appearance of an object and its analysis involves several mathematical methods, which permit to derive features able to reflect the variation intensities and the underlying structure of the object.

Texture analysis includes several different techniques, which are not new in the medical field but date back to the early 70s, when texture measures were suggested for the detection of lung disease patterns [168]. The major advantage in clinical practice is that these mathematical approaches can offer information not visible by the human eye in an objective way, exploiting data routinely acquired [169].

Texture analysis for medical use represents an ongoing field of research, with applications ranging from automatic segmentation [170] and lesions detection [171], to differentiation between pathological and healthy tissues [172], or between benign and malignant tumours [173, 169].

4.2 Texture analysis methods

Texture analysis refers to a wide spectrum of mathematical methods, aiming at describing the spatial relationships between the intensity level within an image. As mentioned just before, the advantage of computing textural features in the medical field is that, being a post-processing technique, maximises the information that can be derived from standard images [164]. Different methods can be used to perform a texture analysis, including structural, model-based, transform-based and statistical methods [174].

The structural methods are based on the use of well-defined primitives known as texture elements, e.g. regularly spaced parallel lines and squares. The properties of the texture elements define the type of texture (structure) to be investigated. Various approaches have been proposed to detect set of textures, which appear as “distorted” versions of ideal textures. These require the use of different classes of transformations, which includes the projective transformations, the perceptual processes and those modelled for specific class of patterns [175]. Despite these efforts, these methods appear to be limited in medical application since they were conceived to work well when prior structures are known in advance [176], thus resulting not effective to describe the complex texture characterising tumour tissues [177].

The model-based methods use sophisticated mathematical models as the autoregressive (AR) models, the Markov random fields (MRF) and the fractal models, thus trying to interpret an image texture by using generative image model and stochastic model. Essentially, these techniques generate an empirical model of each pixel. The estimated parameters of the image models are used for image analysis as textural feature descriptors. The primary disadvantage of these approaches is the computational complexity involved in the estimation of these parameters, especially the stochastic ones. Even if the fractal model has been shown to be efficacy for some textures in medical image analysis, the main issue remains the inefficacy when describing local image structures [176]. Objects may exhibit a multifractal behaviour. Despite the multifractal analysis allows computing a spectrum or a set of fractal dimensions, numerical differences appear among the existing algorithms [163]. Moreover, the computation of the fractal dimension is complex for the textured images that, most of time, are not deterministic and have statistical variations [178].

Another approach consists in the analysis of the texture properties in different spaces, such as frequency and scale space. These methods are based, for instance, on the Fourier, Gabor or Wavelet transform [174]. The disadvantage of using the Fourier trasform is that the time-frequency resolution is limited. Gabor transform is essentially a windowed-Fourier transform, which allowed for a frequency and spatial localisation, remaining limited by its single filter resolution [179]. Wavelet transforms overcome this problem by using multiple channels for different frequencies, this requiring intensive computation. Gabor and Wavelet transforms due to their space-frequency decomposition abilities have been preferred for texture analysis, especially to treat images classification and segmentation problems. However, being texture analysis based on wavelet transform highly dependent on the "mother" wavelet chosen, it is difficult to find one setup for different kind of tissues and imaging modalities.

The last approach, deeply examined in the next section (Section 4.3), concerns the statistical methods, which have been reported to have higher discrimination ability on medical images than the structural and transform-based methods [174]. These methods are based on the representation of the image texture through the use of distribution properties and examining the relationships of the image intensity values. Statistical methods have been widely exploited in literature [180, 181], successfully used for discrimination and classification problems, also due to their simple computation and more intuitive interpretation [10].

4.3 Statistical features

Texture perception and more specifically texture discrimination were extensively studied by Julesz in the early 70s [182], [183]. Julesz's pioneering work focused on the possibility to discriminate two texture, despite being characterised by the same brightness, contrast, and colour [184]. His research is based on statistical methods including first- and second-order statistics.

First-order statistics are based on the histogram of pixels intensity values in the image. The features derived from values distribution depend only on single pixel values and not on the interaction or co-occurrence of neighbouring pixel values. The most common first-order statistic is the average intensity in an image. Second-order statistics are based on the likelihood of observing pixels pairs of specific intensity values. These features belong to the textural features, since they can represent the spatial distribution of image values.

Statistical methods have played an important role in several medical applications, helping in improving diagnosis, staging and early response assessment [185]. Indeed, the intensity variations of medical images, which characterise the texture, are supposed to reflect the underlying physical and biological variation.

Generally, features are automatically extracted from images and then used for classification tasks, as distinguishing benign from malignant nodules. Usually, feature calculation is performed after segmentation of ROIs or VOIs.

There are several ways to describe the perceived qualities of a texture, this explaining the wide number of methods and features used to describe it. Texture can be characterised by several features, such as uniformity, regularity, coarseness, roughness, density, linearity and directionality. In oncological application, the textural features that can be derived to describe these image characteristics provide a measure of the intra-tumoural heterogeneity.

4.3.1 First-order features

The statistical features are global features, which describe how intensity values within a ROI are distributed. Let $x = \{x_1, x_2, .., x_N\}$ be the set of L values of the N voxels in the image. Let $h = \{h_1, h_2, ..h_L\}$ be the histogram with count n_i of each intensity level i in x. The occurrence probability p_i for each intensity level is $p_i = \frac{h_i}{N}$. Accordingly, we can have the following definitions:

Mean μ

$$\mu = \frac{1}{N}\sum_{k=1}^{N} x_k \tag{4.1}$$

Standard deviation σ

$$\sigma = (\frac{1}{N}\sum_{k=1}^{N}(x_k - \mu)^2)^{\frac{1}{2}} \tag{4.2}$$

Skewness S

$$S = \frac{\frac{1}{N}\sum_{k=1}^{N}(x_k - \mu)^3}{[\frac{1}{N}\sum_{k=1}^{N}(x_k - \mu)]^{\frac{3}{2}}} \tag{4.3}$$

Kurtosis K

$$K = \frac{\frac{1}{N}\sum_{k=1}^{N}(x_k - \mu)^4}{[\frac{1}{N}\sum_{k=1}^{N}(x_k - \mu)^2]^2} - 3 \tag{4.4}$$

Coefficient of variation CV

$$CV = \frac{\sigma}{\mu} \tag{4.5}$$

Entropy E also known as Shannon entropy

$$E = -\sum_{i=1}^{L} p_i \;\log_2 p_i \tag{4.6}$$

Uniformity U

$$U = \sum_{i=1}^{L} p_i^2 \tag{4.7}$$

Other parameters derived from the histogram analysis also include: the *median*, the intensity level that divides a distribution in two halves, the *mode*, the value occurring frequently, the *minimum* and the *maximum*, that is the lowest and the highest pixel values, and the 10^{th} and 90^{th} *percentile*, more robust to outliers than *minimum* and *maximum*.

The main limit of these features, when used for heterogeneity evaluation, is that they perform global measures, not considering the local variations within the ROI. This issue will be addressed in Section 5.1.

4.3.2 Second-order features

Second-order statistics are based on the joint probabilities and provides co-occurrence measurements performed on matrices, known as grey level co-occurrence matrices (GLCMs), that reflect the spatial grey-level dependence. Actually, these matrices may contain any type of entity, besides grey levels. Each cell of these matrices represents how often a couple of pixel values (i, j) occurs, this being the basis for measuring the relationship between pixels. Therefore, these matrices provide valuable information about images since, as reported by *Haralick et al.*, tone and texture, which are always present in the images, bear an inextricable relationship [186].

The features that will be extracted from GLCM provide image statistical information regarding the distribution of pixels pairs along one of the image directions. GLCM provides a new image representation [167] and is an estimate of the second-order joint probability, p_{ij}, of the intensity values of two pixels i and j, separated by a distance δ ($\delta = 1$ for neighbouring pixels) along a given direction θ, (where usually θ can be horizontal, vertical, diagonal and anti-diagonal, i.e. $\theta = \{0°, 45°, 90°, \text{and } 135°\}$). This joint probability can be represented with a square matrix p_{ij}, with row and column dimensions equal to the number of discrete intensity levels L in the image. Each p_{ij} element contains the frequency of a combination of intensity levels pairs, i and j, at a certain distance δ, along a specific direction θ. The resulting GLCM is a symmetric matrix, as shown in Figure 4.1. For images tending to be flat, i.e. uniform with no texture, the resulting GLCM would be almost diagonal. Contrarily, for images with increased local intensity variations, i.e. with increased texture, the resulting GLCM will result characterise by more off-diagonal values, as shown in Figure 4.2.

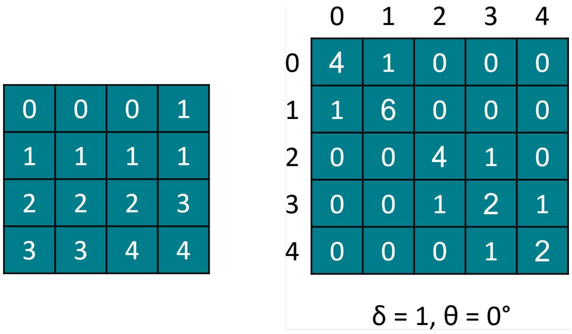

0	0	0	1
1	1	1	1
2	2	2	3
3	3	4	4

	0	1	2	3	4
0	4	1	0	0	0
1	1	6	0	0	0
2	0	0	4	1	0
3	0	0	1	2	1
4	0	0	0	1	2

δ = 1, θ = 0°

(a) (b)

Figure 4.1: Small image (a) and relative co-occurrence matrix (b) for $\delta = 1$ and $\theta = 0°$. The joint probability is obtained dividing the matrix in (b) for the total number of possible pixel pairs.

The choice of δ and θ in most cases is not obvious an must be made carefully to properly characterised and classified a texture. The features that will be derived from GLCM are local features that should encode in an efficient way, useful for classification tasks, the relevant information present in GLCM structures. Some of GLCM features reported below have a clear correspondence with human texture

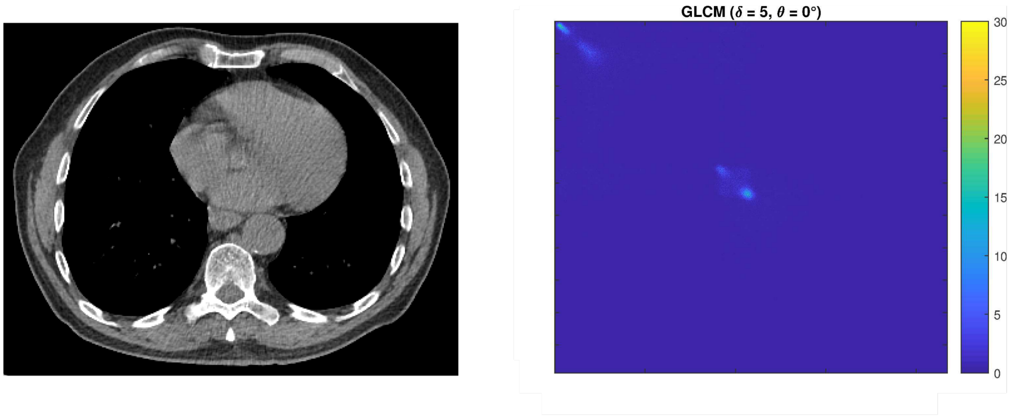

(a) (b)

Figure 4.2: CT image (a) and relative co-occurrence matrix (b) for $\delta = 5$ and $\theta = 0°$.

perception (e.g., coarseness, smoothness), while some others do not represent some specific visual properties, but they still encode texture information with high discriminatory power [187].

Joint maximum M_J is the probability corresponding to the most common GLCM co-occurrence and is defined as

$$M_J = max(p_{ij}) \tag{4.8}$$

Joint average μ_J is the weighted sum of the joint probabilities and is defined as

$$\mu_J = \sum_{i=1}^{L} \sum_{j=1}^{L} i \; p_{ij} \tag{4.9}$$

Joint variance σ_J^2 is a measure of the variability of the GLCM co-occurrences and is defined as

$$\sigma_J^2 = \sum_{i=1}^{L} \sum_{j=1}^{L} (i - \mu)^2 \; p_{ij} \tag{4.10}$$

where $\mu = joint\ average$.

Second order entropy E_J is defined as

$$E_J = -\sum_{i=1}^{L}\sum_{j=1}^{L} p_{ij} \ \log_2 p_{ij} \tag{4.11}$$

Angular second moment ASM [186] also called energy and uniformity is defined as

$$ASM = \sum_{i=1}^{L}\sum_{j=1}^{L} p_{ij}^2 \tag{4.12}$$

Contrast C a measure of the intensity levels variations is defined as

$$C = \sum_{i=1}^{L}\sum_{j=1}^{L} (i-j)^2 \ p_{ij} \tag{4.13}$$

Inverse difference IDF is defined as

$$IDF = \sum_{i=1}^{L}\sum_{j=1}^{L} \frac{p_{ij}}{1+|i-j|} \tag{4.14}$$

Inverse difference normalised $IDFN$ is defined as

$$IDFN = \sum_{i=1}^{L}\sum_{j=1}^{L} \frac{p_{ij}}{1+|i-j|/L} \tag{4.15}$$

Homogeneity H also known as inverse difference is defined as

$$H = \sum_{i=1}^{L}\sum_{j=1}^{L} \frac{p_{ij}}{1+(i-j)^2} \tag{4.16}$$

Homogeneity normalised HN is defined as

$$HN = \sum_{i=1}^{L}\sum_{j=1}^{L} \frac{p_{ij}}{1+(i-j)^2/L^2} \tag{4.17}$$

Correlation $CORR$ [186] is defined as

$$CORR = \frac{\sum_{i=1}^{L}\sum_{j=1}^{L} ij\ p_{ij} - \mu_x\mu_y}{\sigma_x\sigma_y} \tag{4.18}$$

where

$$\mu_x = \sum_{i=1}^{L} i \sum_{j=1}^{L} p_{ij} \tag{4.19}$$

$$\mu_y = \sum_{j=1}^{L} j \sum_{i=1}^{L} p_{ij} \tag{4.20}$$

$$\sigma_x = \sum_{i=1}^{L} (i-\mu_x)^2 \sum_{j=1}^{L} p_{ij} \tag{4.21}$$

$$\sigma_y = \sum_{j=1}^{L} (j-\mu_y)^2 \sum_{i=1}^{L} p_{ij} \tag{4.22}$$

Autocorrelation A is defined as

$$A = \sum_{i=1}^{L}\sum_{j=1}^{L} i\ j\ p_{ij} \tag{4.23}$$

4.3.3 Higher-order features

Higher-order features include parameters describing regions or zones, thus reflecting the relationship of each voxel with the neighbouring voxels [188]. Higher-order approach includes the grey level run length matrix (GLRLM), introduced by Galloway in the 70s [189], who defined a wide variety of visual texture features, based on the distribution of pixels with the same intensity value along a given direction. Like the GLCM, GLRLM assesses the distribution of the intensity values in an image or in a stack of images. However, whereas GLCM assesses co-occurrence of grey levels couple within a given distance and orientation, GLRLM measures the so-called run lengths. A run length is defined as the length of a consecutive sequence of pixels with the same grey-level intensity in a pre-set direction. Thus, the GLRLM represents the occurrences of runs with length j for a discretised grey level i. The run-length matrix has a great potentiality since it is able to reflect the granularity of a texture: fine texture is expectedly characterised by short run-lengths with similar grey-level intensities, whereas coarse texture by longer runs with different grey-level intensities [179].

It is worth noting that for small images most of the elements of the GLRLM could be zero-valued, since there is not much space for runs. Moreover, if the range of grey-level intensities is wide, many runs would contain only one pixel. Therefore, before calculation of texture features, it is necessary to discretise the tonal range of the image by grouping the grey-levels into bins. The number of calculations needed to build the GLRLM is directly proportional to the pixels number in the image [189].

Once the run-length matrices are calculated along each direction, analogously to the Haralick features extracted from GLCM, it is possible to extract several descriptors from GLRLM. These descriptors are able to capture the texture properties and discriminate among different textures. They can be used either with respect to each direction or by merging them to have a global view of the texture information.

Let r_{ij} be the $(i,j)^{th}$ entry in the given GLRLM, L be the number of grey levels in the image, representing the channel depth of the DICOM image, R be the number of different run lengths, Nr be the total number of runs (the normalising factor) and N be the number of pixels or voxels in the image. The texture descriptors that can be derived from a given GLRLM are described below.

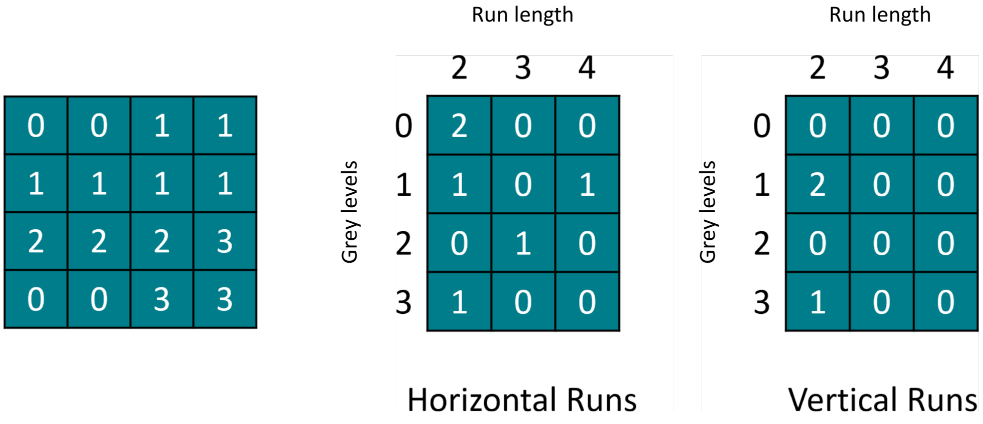

0	0	1	1
1	1	1	1
2	2	2	3
0	0	3	3

	2	3	4
0	2	0	0
1	1	0	1
2	0	1	0
3	1	0	0

	2	3	4
0	0	0	0
1	2	0	0
2	0	0	0
3	1	0	0

(a) (b) (c)

Figure 4.3: Small image (a) and relative GLRLM matrix for the horizontal (b) and the vertical direction (c).

The short runs emphasis *SRE* emphasises the short runs. Being highly dependent on the occurrence of short runs, it is expected high for fine textures. *SRE* is defined as

$$SRE = \frac{1}{N_r} \sum_{i=1}^{L} \sum_{j=1}^{R} \frac{r_{ij}}{j^2} \tag{4.24}$$

The long runs emphasis *LRE* emphasises the long runs. Contrarily to *SRE*, being highly dependent on the occurrence of long runs, it is expected high for coarse textures. *LRE* is defined as

$$LRE = \frac{1}{N_r} \sum_{i=1}^{L} \sum_{j=1}^{R} r_{ij}\ j^2 \tag{4.25}$$

The low grey level run emphasis *LGRE* is analogue to *SRE*, but instead of short runs, it emphasises the low grey-level values. It is defined as

$$LGRE = \frac{1}{N_r} \sum_{i=1}^{L} \sum_{j=1}^{R} \frac{r_{ij}}{i^2} \tag{4.26}$$

The high grey level run emphasis *HGRE* feature is analogue to *LRE*. This feature emphasises high grey levels and is defined as:

$$HGRE = \frac{1}{N_r} \sum_{i=1}^{L} \sum_{j=1}^{R} r_{ij}\ i^2 \tag{4.27}$$

The short run low grey level emphasis *SRLGE* emphasises short runs and low grey-level values and is defined as

$$SRLGE = \frac{1}{N_r} \sum_{i=1}^{L} \sum_{j=1}^{R} \frac{r_{ij}}{i^2 j^2} \tag{4.28}$$

The short run high grey level emphasis *SRHGE* emphasises short runs and high grey-level values and is defined as

$$SRHGE = \frac{1}{N_r} \sum_{i=1}^{L} \sum_{j=1}^{R} \frac{r_{ij} i^2}{j^2} \tag{4.29}$$

The long run low grey level emphasis *LRLGE* emphasises long runs and low grey-level values and is defined as

$$LRLGE = \frac{1}{N_r} \sum_{i=1}^{L} \sum_{j=1}^{R} \frac{r_{ij} j^2}{i^2} \tag{4.30}$$

The long run high grey level emphasis *LRHGE* emphasises long runs and high grey-level values and is defined as

$$LRHGE = \frac{1}{N_r} \sum_{i=1}^{L} \sum_{j=1}^{R} r_{ij} j^2 i^2 \tag{4.31}$$

The grey level non-uniformity *GLNU* measures the similarity of grey-level intensity values in the image. A low *GLNU* value correlates with runs equally distributed along grey levels. It is defined as

$$GLNU = \frac{1}{N_r} \sum_{i=1}^{L} (\sum_{j=1}^{R} r_{ij})^2 \tag{4.32}$$

The normalised version of the *GLNU* feature, *GLNUN*, is defined as

$$GLNUN = \frac{1}{N_r^2} \sum_{i=1}^{L} (\sum_{j=1}^{R} r_{ij})^2 \tag{4.33}$$

The run length non-uniformity *RLNU* measures the similarity of runs. A low *RLNU* value correlates with runs equally distributed along run lengths. It is defined as

$$RLNU = \frac{1}{N_r} \sum_{j=1}^{R} (\sum_{i=1}^{L} r_{ij})^2 \tag{4.34}$$

The normalised version of the *RLNU* feature, *RLNUN*, is defined as

$$RLNUN = \frac{1}{N_r^2} \sum_{j=1}^{R} (\sum_{i=1}^{L} r_{ij})^2 \tag{4.35}$$

The run percentage *RPC* assesses the fraction of the number of realised runs and the maximum number of potential runs, the number of voxels in the ROI. It is a measure of the coarseness of a texture. A low RPC value is associated to highly uniform images and pictures with linear structures [189]. This feature is defined as

$$RPC = \frac{N_r}{N} \tag{4.36}$$

Chapter 5

Novel features

Contents

5.1 Local features **83**

5.2 Heterogeneity analysis on DCE-CT **87**

  5.2.1 Single-feature analysis 88

  5.2.2 Multi-feature analysis 89

5.3 Reliability analysis on DCE-CT **89**

  5.3.1 Local coefficient of variation 92

In this Chapter, a novel approach based on the local analysis (Section 5.1) is introduced to overcome the limitations of the global features described in Section 4.3. Two spatio-temporal indices conceived to exploit DCE-CT information and a third one summarising their joint behaviour are reported in Section 5.2. These features describe the evolution over time of the tumour spatial heterogeneity. In Section 5.3, an error index to establish which perfusion values are unreliable and a local-based index to evaluate the local spatial coherence of the perfusion maps are introduced.

5.1 Local features

Images are inherently corrupted by noise, which usually emerges as random variations in intensity values and structured artefacts [190]. The presence of noise can affect image measurements, especially local measures, leading to unreliable results. Global measures can mitigate the effects of noise.

Several techniques exist to manipulate images and are used not only to reduce image noise but also, for instance, to enhance details and sharpen edges, i.e. boundaries of structures within the image [191]. Traditionally, the concept of filtering has its roots in the frequency domain, especially in the use of the Fourier transform. Filtering operations performed on the pixels of an image are usually known as "spatial" filtering. Substantially, the spatial filtering is performed through a convolution of the image with a sub-image known as mask, kernel or window. Basically, through an iterative procedure, the filter mask is moved from point to point in an image and the response of the filter for each point (pixel) is calculated by performing a predefined neighbourhood operation [192].

The simplest filter is the linear one, where the response is given by the product of the mask coefficients and the corresponding pixel values. Considering the 3×3 mask of Figure 5.1, the response R to the linear filtering at a point (x, y) in the image is computed as follows:

$$R = \sum_{i=-1}^{1} \sum_{j=-1}^{1} w(i,j) f(x+i, y+j) \tag{5.1}$$

where $w(i, j)$ is the $(i, j)^{th}$ weight coefficient and $f(x+i, y+j)$ is the corresponding image value. In particular, the coefficient $w(0, 0)$ coincides with $f(x, y)$, indicating that the mask is centred at (x, y) when the response is determined. Averaging filters or mean filters are generally used for denoising and can be seen as low-pass filters. These filters result ineffective when removing impulsive noise [193]. In this case, non-linear filters as the median filter are preferred, being able to remove noise while maintaining edges [194].

In this Thesis, a similar methodological approach has been used to overcome the limitations introduced by the first-order features presented in Section 4.3.1. Indeed, when computing first-order features tissue heterogeneity information within an image is almost disregarded. For this reason, the global features previously presented have been also implemented as local features, by considering the spatial relations among neighbour pixels. This could allow to somehow preserve the tissue heterogeneity information within the considered ROI.

To perform a local analysis a procedure similar to the image filtering has been performed. More specifically, the first-order features are computed locally within the ROI, considering a square patch W centred on a pixel at which, in the feature map, the resulting value is stored. This procedure is repeated for each pixel within the ROI, by using a sliding window, as shown in Figure 5.2.

The choice of W is not trivial and must be made carefully, also taking into

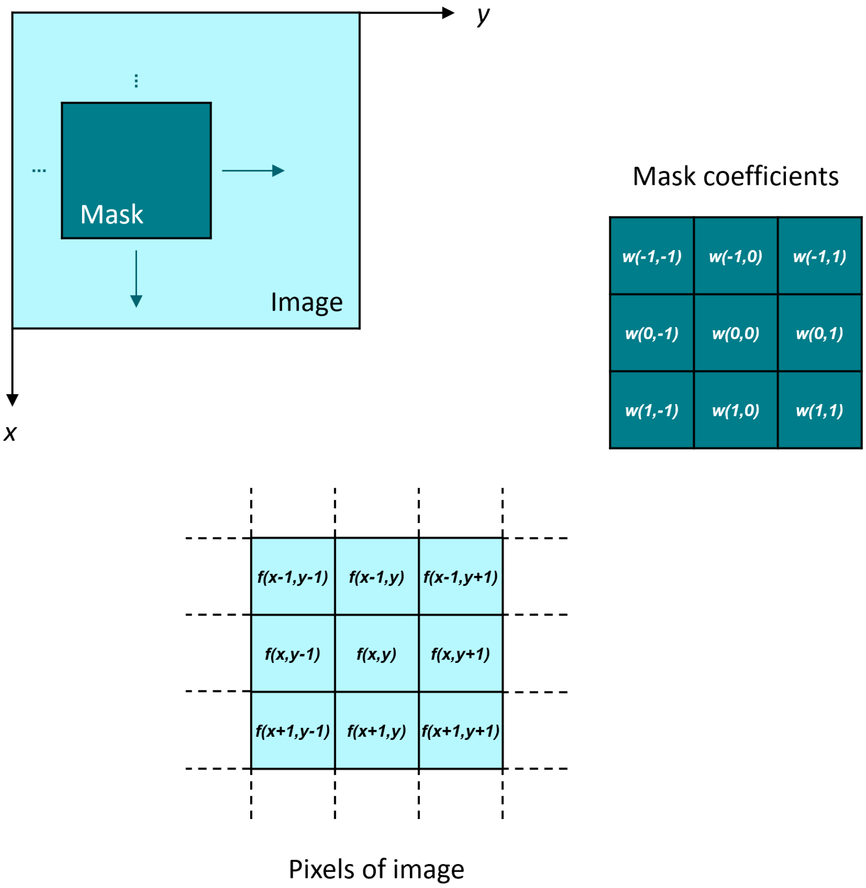

Mask coefficients

w(-1,-1)	w(-1,0)	w(-1,1)
w(0,-1)	w(0,0)	w(0,1)
w(1,-1)	w(1,0)	w(1,1)

Pixels of image

f(x-1,y-1)	f(x-1,y)	f(x-1,y+1)
f(x,y-1)	f(x,y)	f(x,y+1)
f(x+1,y-1)	f(x+1,y)	f(x+1,y+1)

Figure 5.1: Representation of the spatial filtering showing a 3×3 mask and the region of the image considered for the filtering.

account the resolution of the modality being considered, to properly detect the smallest coherence heterogeneity pattern. Indeed, the tumour tissue is characterised by gradual transitions that occur with a spatial coherence. At the end of this procedure, global statistical indices as the mean value of the local features can be calculated on the local-feature maps. This methodological approach takes benefits from the local analyses, able to preserve the heterogeneity information, and the use of a global feature to summarise the outcome, which reduces the noise effects.

While local features as the local average and the local median coincide with the filters mentioned above, local features as the local entropy, uniformity, standard deviation, kurtosis, skewness and CV (see Eq. 4.6, Eq. 4.7, Eq. 4.2, Eq. 4.4,

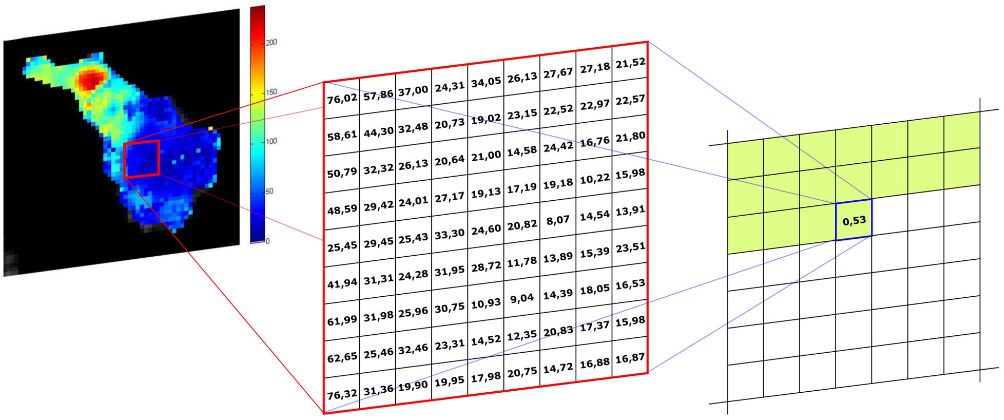

76,02	57,86	37,00	24,31	34,05	26,13	27,67	27,18	21,52
58,61	44,30	32,48	20,73	19,02	23,15	22,52	22,97	22,57
50,79	32,32	26,13	20,64	21,00	14,58	24,42	16,76	21,80
48,59	29,42	24,01	27,17	19,13	17,19	19,18	10,22	15,98
25,45	29,45	25,43	33,30	24,60	20,82	8,07	14,54	13,91
41,94	31,31	24,28	31,95	28,72	11,78	13,89	15,39	23,51
61,99	31,98	25,96	30,75	10,93	9,04	14,39	18,05	16,53
62,65	25,46	32,46	23,31	14,52	12,35	20,83	17,37	15,98
76,32	31,36	19,90	19,95	17,98	20,75	14,72	16,88	16,87

(a) (b) (c)

Figure 5.2: From left to right, BF map (a) and sliding window of 9 × 9 pixel (b) showing the perfusion values considered for the computation of the local coefficient of variation (lCV), stored in the corresponding pixel of the lCV map (c).

Eq. 4.3, Eq. 4.5, respectively) constitute novel simple features that can provide a new representation of the image. The importance of performing a local CV (lCV) and its possible application will be discussed in Section 5.3.1 and Chapter 8, respectively. Beyond providing more representative feature values, this procedure also allows the visualization of features colorimetric maps. For instance, the local entropy and local uniformity maps are of particular interest. As an example, Figure 5.3 reports the CT slice of a lung tumour (adenocarcinoma) outlined in red and the corresponding local entropy and local uniformity maps. The local entropy provides a representation of the local irregularity present within a ROI, while the local uniformity refers to local homogeneities.

Perfectly flat images will be characterised by an entropy equal to zero, while images with long runs of pixels, i.e. pixels with same values, will have a low entropy, contrarily to images characterised by short runs and high contrast, which will be characterised by a high entropy. Similar but opposite considerations can be made when referring to the local uniformity. It is worth noting that entropy and uniformity are indirectly related but not linearly dependent. An application of these local features on BF maps is reported in Chapter 10.

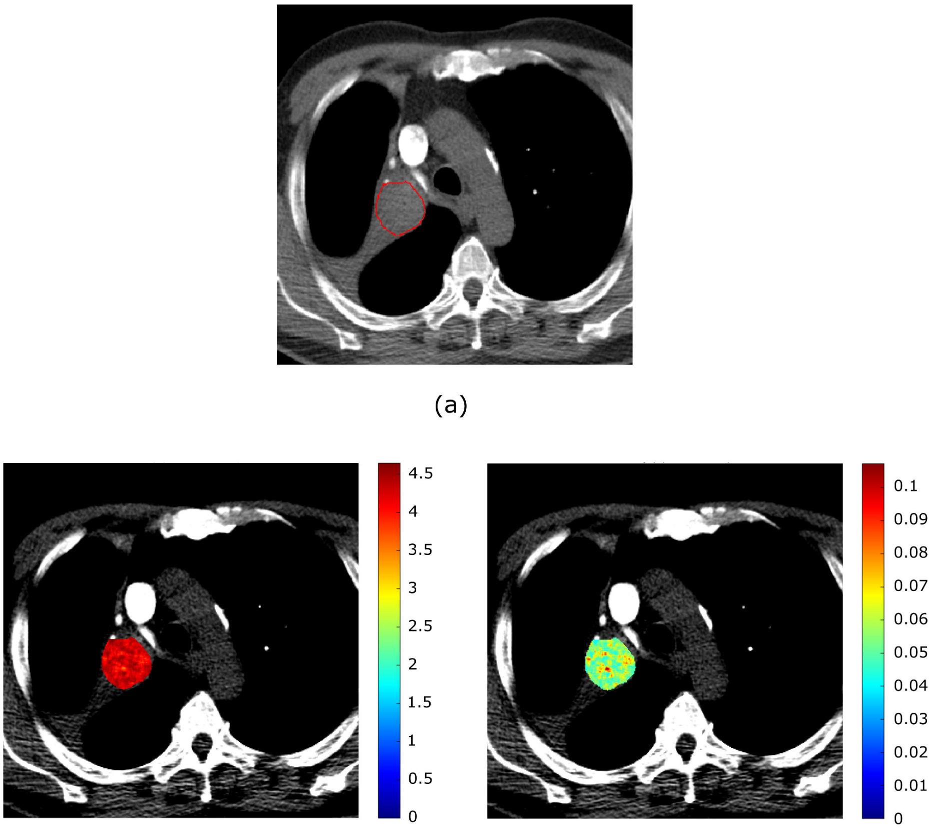

(a)

(b) (c)

Figure 5.3: CT image of a lung adenocarcinoma outlined in red (a), and relative local entropy (b) and local uniformity maps (c).

5.2 Heterogeneity analysis on DCE-CT

In order to exploit both spatial and temporal DCE-CT information, two novel indexes have been conceived to perform a spatio-temporal analysis. These indexes are computed on the DCE-CT sequences of a slice, by studying the TCCs group properties inside a ROI for local windows $W(x, y)$ of size $w \times w$ and centred on the slice coordinate (x, y), whose values in the image domain are denoted by Ω_W. Let $\sigma(\Omega_W(m))$ be the *spatial* standard deviation of the TCC values assumed in $W(x, y)$, at the generic time sample t_m. The following indexes have been analysed:

- MS (temporal Mean value of local Standard deviation), the *temporal* mean value of the $\sigma(\Omega_W(m))$ values on the whole sequence of the reference slice is computed, thus yielding $E(\Omega_W)$ (where $E(\cdot)$ stands for expectation). MS was conceived to provide an estimate of temporal persistence of local spatial homogeneity within the ROI;

- SS (temporal Standard deviation of local Standard deviation), the *temporal* standard deviation of the $\sigma(\Omega_W(m))$ values on the whole sequence of the reference slice is computed, thus yielding $\Sigma(\Omega_W)$. SS quantifies the temporal stability of the local texture.

5.2.1 Single-feature analysis

The two indexes MS and SS represent the first two features considered for DCE-CT heterogeneity analysis. In practice, a low MS value points out regions that keep locally homogeneous (i.e., with a low contrast) over time, while high values highlight voxels belonging to a heterogeneous tissue, which could be characterised by a constant or a variable enhancement.

As regards SS, it shows a low value when the local spatial distribution of the contrast agent has a time steady dispersion, that is, the TCCs' family is characterised by a temporal coherence of spatial properties of tissue, whether it is a homogeneous or heterogeneous tissue. For instance, this occurs in case of variance-preserving transformations, like spatially uniform enhancement. On the other hand, high SS values may occur when voxels belonging to different structures fall into the same window W, for instance, in case of a not negligible motion of the patient, when the drawn ROI does not perfectly fit the lesion, or when the local enhancement changes dynamically, for instance in the presence of blood vessels.

The outcome of each index was also represented by means of colorimetric maps (referring to HU values), so as to enable a visual comparison with the ground truth established by radiologists. As an example, Fig. 5.4 shows the colorimetric maps of SS (middle) and MS (right) referred to a ground truth examination, manually

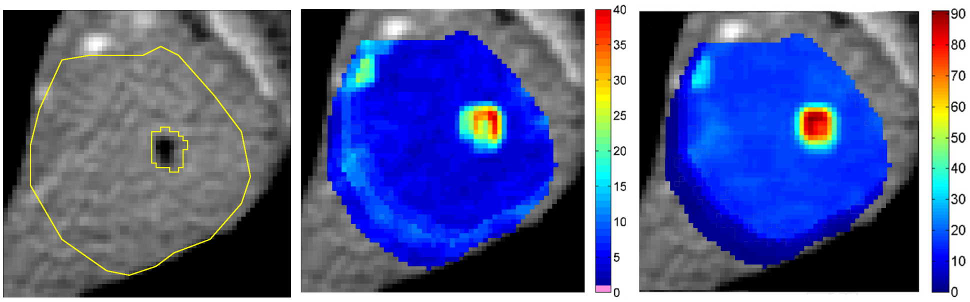

Figure 5.4: Ground truth (left), colorimetric maps of SS (middle) and MS (right).

outlined by radiologists, whose heterogeneity is of Type 3 (left).

5.2.2 Multi-feature analysis

In order to explore the joint behaviour of the single indexes, a 2D feature analysis was also performed by implementing an unsupervised classification. In practice, a k-means clustering algorithm was used to find out groups of lesion voxels characterised by the same SS and MS behaviour, with k=4 number of different classes (or clusters). The Squared Euclidean distance is the distance measure used to quantify the similarity of patterns. Results are also given using a colorimetric Cluster Mask, CM, that represents the third feature. The scatter plot of Fig. 5.5 (left) shows an example of voxels clustered into four classes, visualised in red, blue, green and cyan, respectively, encompassing similar MS and SS values, then mapped within the lesion ROI by forming a colorimetric mask (right), keeping the same cluster colours as in the scatter plot, so as to enable a visual comparison with the ground truth established by radiologists. This also provides a spatial visualisation of the clusters, thus improving interpretation of results.

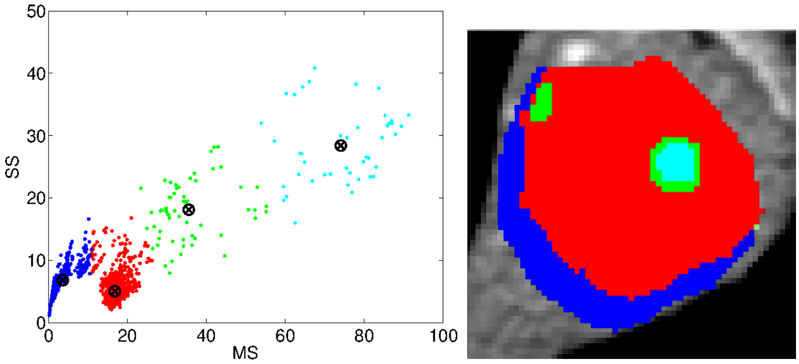

Figure 5.5: MS-SS scatter plot (left) and its respective clusters mask (right). Data have been partitioned into four clusters, mapped by the red, blue, green and cyan colours, respectively.

5.3 Reliability analysis on DCE-CT

As discussed in Section 3.1.4, the reliability of DCE-CT sequences still represents an open issue. Among the factors playing a major role in affecting DCE-CT examinations there are the acquisition artefacts, the motion artefacts, especially in thorax and abdomen studies, and the presence of anatomical structures close to the tumour, for instance heart and aorta, as well as structures directly present within the mass, such as bronchi, haemorrhages and small blood vessels. The structures directly involved in the lesion are usually manually excluded from the perfusion analysis [195], since they can jeopardise the computation of global or local perfusion-based parameters, also affecting the visual analysis of the perfusion colorimetric maps.

In lung cancer studies, respiratory movements can induce the lesion motion, causing mis-registrations [196] in both transverse (x-y plane) and craniocaudal (z axis) directions and leading to inconsistent TCC fitting and, consequently, unreliable perfusion parameters. The effects of motion artefacts and data acquisition time on the absolute values and reproducibility of perfusion parameters where no motion compensation procedures have been adopted are reported for both lung and liver tumours [197, 198].

In this Thesis, this issue has been overcome by performing a manual and rigid translation of the ROIs in both transverse and craniocaudal plane, by exploring the adjacent slices in order to obtain through a 3D manual alignment the "best" sequence for the considered slice, known as reference slice [199, 90, 200]. An example of choice among adjacent slices is reported in Figure 5.6 where Z^* is the reference slice. Once the best sequence has been selected, the TCC signal for each pixel inside the ROI is computed as reported in Section 3.1.3. The quality of the fitting has been assessed by considering the residuals of each TCC signal, computed as the differences among the observed HU samples Y_{TCC} and the relative values computed through the fitting $\overline{Y}_{TCC}$ for each time instant t:

$$\epsilon(t) = \left|Y_{TCC}(t) - \overline{Y}_{TCC}(t)\right| \tag{5.2}$$

Being ϵ directly proportional to the distance between the detected and the computed HU sample, it will highlight the differences among these samples. The reliability of the single TCC has been assessed by computing the temporal mean value μ_ϵ of the residual ϵ relative to the considered pixel. The distribution of this error has been used to detect those values undergoing high fitting errors in order to exclude them from the analysis. There are several advantages for the computation of μ_ϵ. This errors distribution can be visualised as a colorimetric map, allowing clinicians to make fairer consideration, being aware of regions and BF values with highest computing errors. BF values characterised by high μ_ϵ

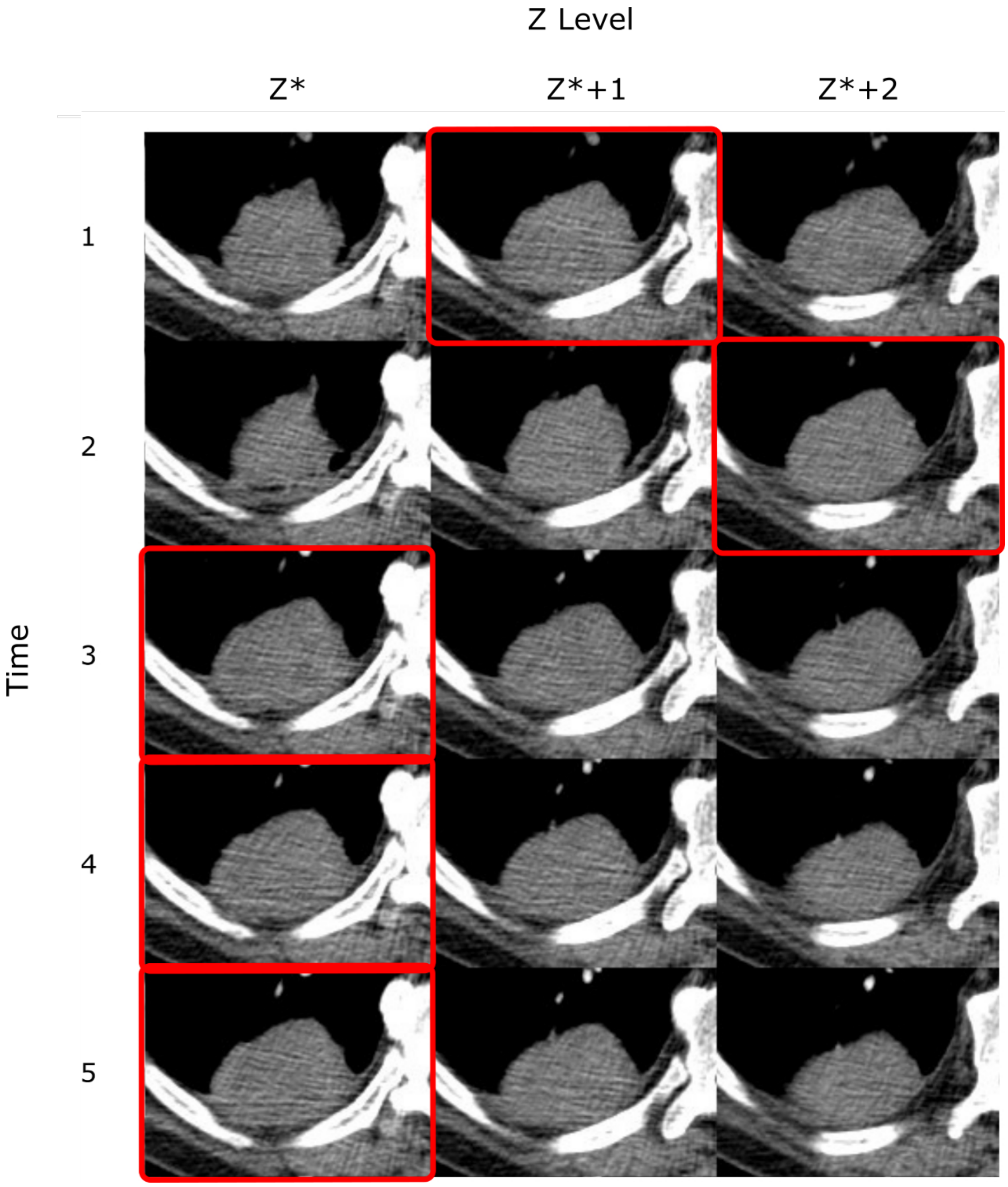

Figure 5.6: Example of selection of the best sequence for a lung tumour perfusion study, performed to achieve the best matching with the Z levels contiguous with the reference slice level, represented by Z^*.

errors should not be included in the analysis, since BF values derive from TCCs not correctly fitted. High errors usually occur in the presence of noise, artefacts (both physics and due to motion) and anatomical structures, such as bronchi and blood vessels, which responding differently from the tissue to the passage of the contrast medium are not adequately modelled through a sigmoid. Through the use of this index, these structures usually manually removed, can be excluded from the analysis by adopting a cut-off value. Several kinds of thresholding can be adopted to automatically exclude unreliable values from the perfusion maps. In this Thesis, the “triangle” method reported in [201] has been adopted. At the end of the analysis, unreliable BF values can be easily visualised in the colourmap, since they are pointed out with the pink colour.

5.3.1 Local coefficient of variation

As reported in Section 4.3.1, the CV is a statistical parameter defined as the ratio between the standard deviation σ and the arithmetic mean μ of the considered distribution (see Equation 4.5). It represents a relative dispersion index and measures the variability within a range of values in relation to their mean. This makes the CV a very attractive tool because it permits the comparison of distributions free from scale effects.

Considering a mean value > 1, always verified in perfusion studies, if the range of values is narrow, the resulting CV will be low, indicating a greater homogeneity of values. For instance, for a mostly uniform image CV is very low, being all values almost equal to each other. Conversely, a wider range of values reveals a greater heterogeneity, thus resulting in a higher value of CV.

Any index aiming at assessing the reliability of the estimated perfusion maps must necessarily taking into account the relations among neighbour voxels. Indeed, the TCC signals belonging to a small tissue area should be usually characterised by gradual and coherent transitions. For this reason, the index conceived arises from local measures, based on the lCV. Using a window size comparable to the grain of the tumour lesions heterogeneity reduces the effects of the same on statistical measures, thus, it actually allows considering the local variability, the spatial inconsistency due to other causes. In addition, lCV colorimetric maps provide radiologists with a panoramic view of the reliability in BF maps, where regions characterised by lower lCV values suggest a greater local spatial coherence of the BF maps,while the higher values point out an inconsistent variability, which could mislead clinical consideration.

Eventually, a single and easily extractable index was calculated from the lCV values. This statistical index is the mean of lCV values, μ_{lCV}, which is able to take into account the local heterogeneity of the perfusion map. The benefits of using the μ_{lCV} have been deepened in Chapter 8, where this index has been early validated in 16 patients with primary lung cancer [200]. In this study, μ_{lCV} proved its capability to discriminate between the inherent tumour heterogeneity and the noise affecting images.

Chapter 6

Image processing and multi-modality approach

Contents

6.1 Segmentation **96**
  6.1.1 Segmentation of PET images 97
6.2 Registration **101**
  6.2.1 Similarity measures 104
  6.2.2 Interpolation 106
  6.2.3 Application on PET/CT and PET/MRI 108
  6.2.4 Future works 120

In this Chapter, the methods developed to perform a 3D segmentation on PET images and a multi-modal registration are presented. In particular, in the first part of this Chapter, the segmentation procedure is briefly described and formalised in Section 6.1. Then, the method developed to perform a 3D PET segmentation of the kidneys in ^{68}Ga-PSMA PET/CT images is reported. While kindeys appear well defined and simply detectable, the gold standard for tumour segmentation remains the manual delineation performed by experts. In the second part of the Chapter, the image registration methods currently used and the algorithmic choices required are described in Section 6.2. Then, an application regarding the multi-modal 3D registration of GOJ tumours manually outlined on FDG-PET/CT and FDG-PET/MRI series, acquired during the period abroad at the King's College London, is presented.

6.1 Segmentation

The extraction of quantitative tumour image-based parameters as well as the analysis of tumour heterogeneity relies on the definition of ROIs. These ROIs represent anatomical structures, such as tumours or organs under examination, and are used to define areas from which image features are calculated. ROIs can be defined both manually by experts, semi-automatically and automatically. This process, known as segmentation, consists in the classification of the voxels of an image into a set of distinct classes. In the medical field, segmentation has been identified as a key problem remaining one of the most studied and challenging of the image processing [202]. It plays a fundamental role in diagnosis [203], staging [204], treatment and radiation therapy planning [205] as well as disease monitoring [206].

Image segmentation can be formulated as follows [207]. Let Ω be the 2D image domain and P_i the n partitions (image observation) of Ω:

$$\begin{cases} P_i \subset \Omega \\ \bigcup_{i=1}^{n} P_i = \Omega \\ P_i \cap P_j = \emptyset \quad i \neq j \end{cases} \tag{6.1}$$

Ideally, the segmentation procedure should identify objects that correspond to distinct anatomical structures or semantically coherent aggregates (i.e. humans) in the image [208].

In the clinical practice, the gold standard remains the manual delineation performed by expert radiologists and nuclear medicine physicians [202], who can visually interpret images, define the boundaries of the structure of interest detecting and excluding areas which could mislead subsequent analyses as, for instance, inflammation regions in proximity of the tumours, as shown in figure 6.1.

There are several approaches to automatically segment an image, as the thresholding methods [209], the region growing [210], the classifiers and clustering approaches [211] and the artificial neural networks [212]. Independent on the approach utilised, the segmentation procedure leads to the creation of a ROI mask R, where each pixel i is defined as:

$$\begin{cases} R(i) = 1 & \text{if } i \in \text{ROI} \\ R(i) = 0 & otherwise \end{cases} \tag{6.2}$$

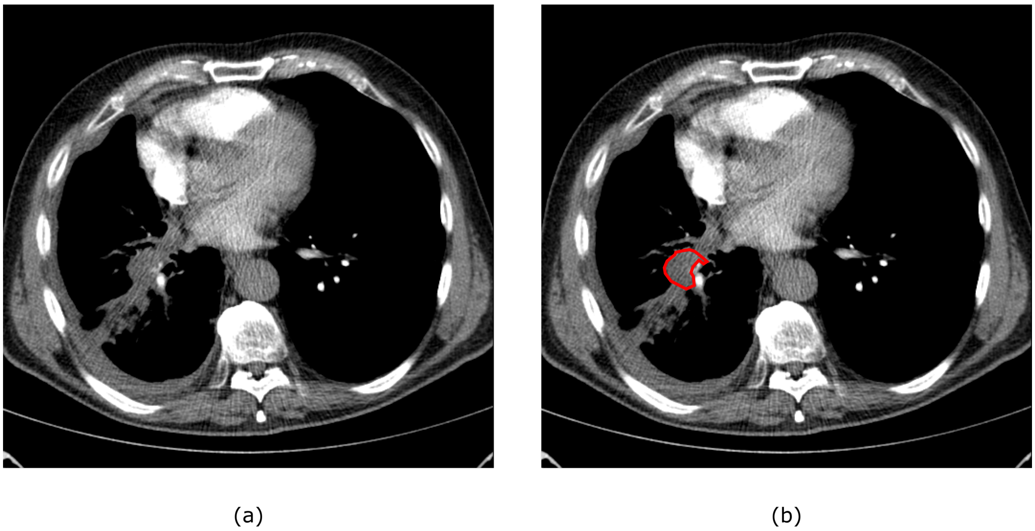

Figure 6.1: CT image of a lung tumour (a) and its manual segmentation performed by a radiologist with more than 25 years experience (b).

6.1.1 Segmentation of PET images

As discussed in Section 3.3.3, at present there is no consensus in the nuclear medicine field regarding the definition of the ROI used to derive SUV values. The difficulty in PET image segmentation is mainly due to the low spatial resolution and the presence of noise. However, the identification of dark objects on a light background (or the opposite) in PET images is relatively simple. For this reason, thresholding methods could be the most suitable choice. The basic result is that the initial grey level image is converted into a binary image based on a threshold value T:

$$\begin{cases} R[I(x)] = 1 & \text{if } I(x) \geq T \\ R[I(x)] = 0 & \text{if } I(x) < T \end{cases} \tag{6.3}$$

where I is the intensity and x is the spatial coordinate of the image [202].

In this Thesis, an assisted method to perform a 3D segmentation starting from PET images has been developed and applied to perform a 3D segmentation of the kidneys in ^{68}Ga-PSMA PET/CT series. This clinical application will be deeply described, further on, in Chapter 11. The segmentation was performed using ImageJ software (v1.47 or later) [213], Java3D plugin collection and Java 1.6 or later. As shown in Figure 6.2, the procedure can be divided into three phases:

pre-processing, processing and post-processing phase.

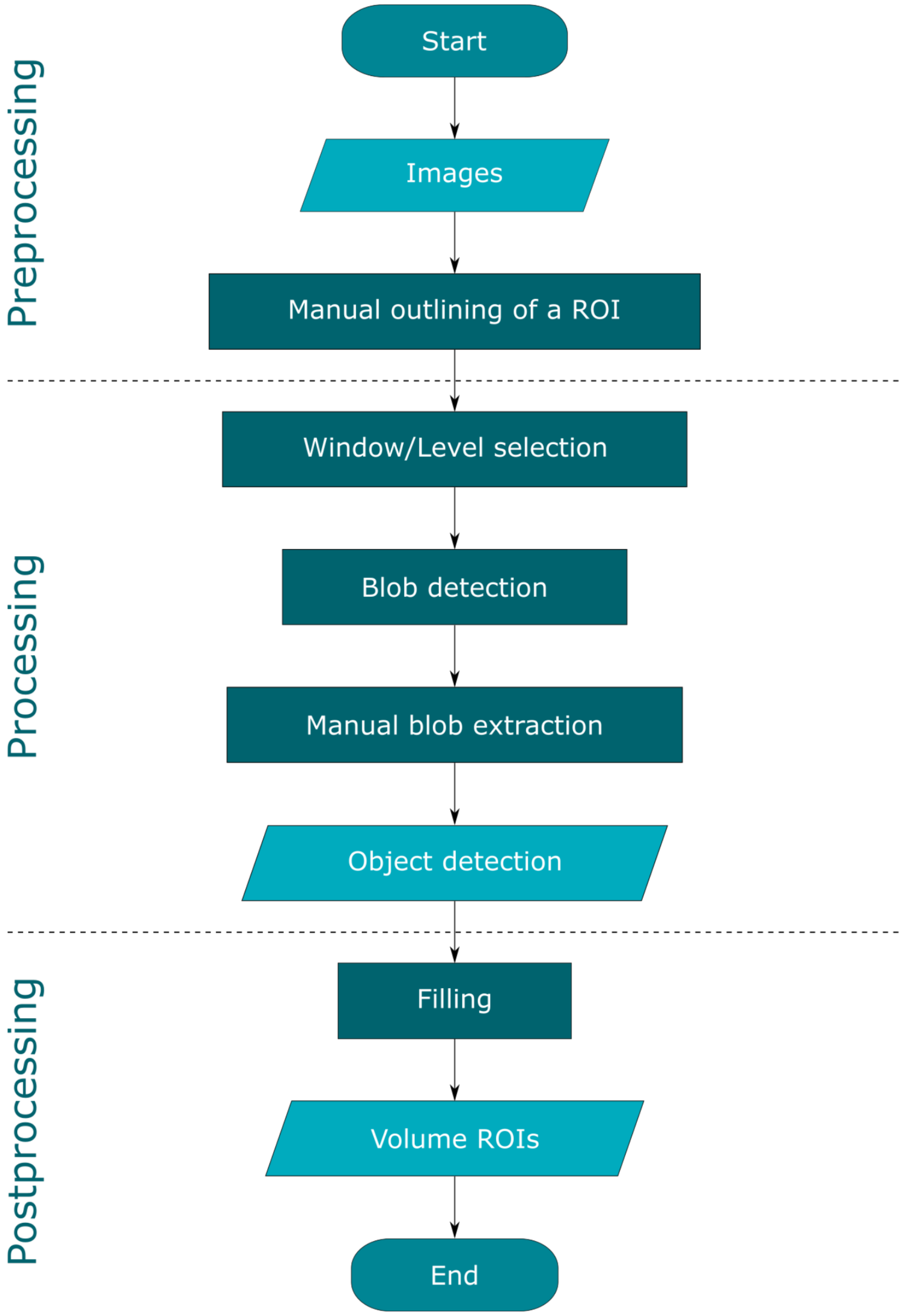
Preprocessing
Start
Images
Manual outlining of a ROI
Processing
Window/Level selection
Blob detection
Manual blob extraction
Object detection
Postprocessing
Filling
Volume ROIs
End

Figure 6.2: Flowchart of the assisted 3D kidneys segmentation.

The pre-processing phase involves the manual delimitation of the structure to be segmented only in one of the slices that compose it, for instance, with a circle, as shown in Figure 6.3 (a) and (b). This procedure is normally not mandatory but in the most complex cases it improves the overall result of the segmentation. The reason is that it permits to consider the local histogram of the structure considered, facilitating the subsequent processing steps. The processing phase starts with the selection of an appropriate W/L. The W/L can be automatically set clicking on the Imagej tool icon and selecting the option *Auto* from the popup menu. For instance, in the use case reported in Chapter 11, after circumscribing one of the kidneys, the W/L were automatically selected in order to enhance the kidneys, as one can see in Figure 6.3 (c). Then, a connexity analysis for the blobs detection was performed through the use of the 3D Object Counter plugin, which embeds a threshold-based segmentation method [214]. This plugin automatically identifies a threshold value, which can be adjusted by the user using a slider and looking at the preview. Segmentation results were visualised through the 3D Roi Manager plugin [215], which permits to identify the structures (or blobs) of interest and to manually export them. In the use case described in Chapter 11, this plugin led to the extraction of the kidneys. As one can see, both in the section reported in Figure 6.3 (d) and in the whole volume reported in Figure 6.4, at this point of the procedure the kidneys, which are the objects detected, result to be as hollow organs.

The post-processing phase involves the filling of the objects detected, as shown in Figure 6.3 (e). For this purpose, an ImageJ macro was developed able to fill and integrate the ROIs of the structure of interest. In this way, it was possible to obtain the full kidneys volume, thus also including the regions characterised by a lower captation like the renal pelvis, which is discarded during the previous steps. The output of the macro is the whole set of ROIs of the structure of interest, which will be used for subsequent analyses and 3D measurements.

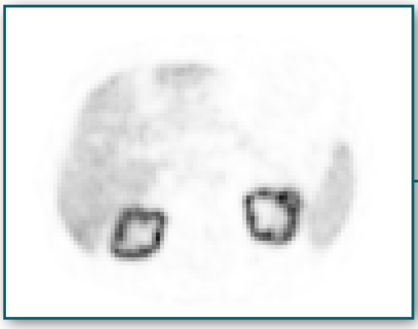

(a) Original Image

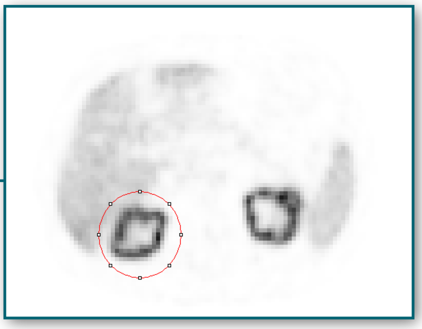

(b) ROI manually outlined

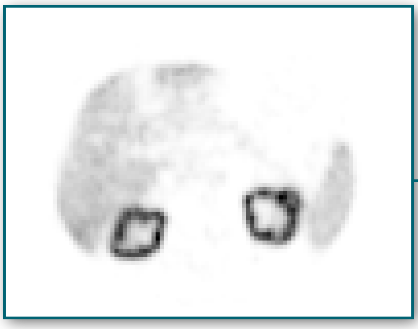

(c) Image after W/L selection

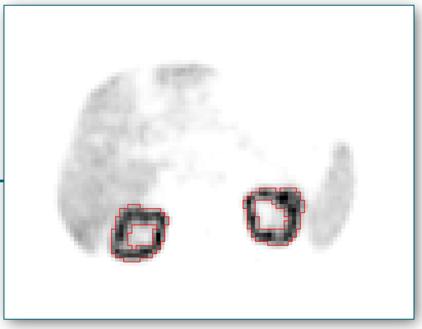

(d) Object detected

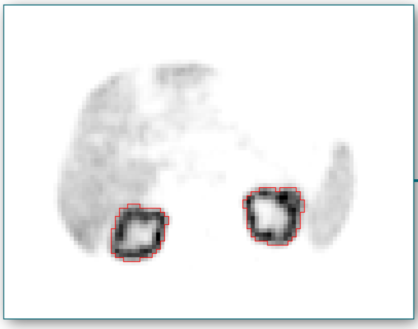

(e) ROI after filling

Figure 6.3: Example of segmentation of the right kidney in (a). The procedure starts with the manually outlining of the kidney and the selection of the W/L (b). The resulting image (c) is used for the object detection.

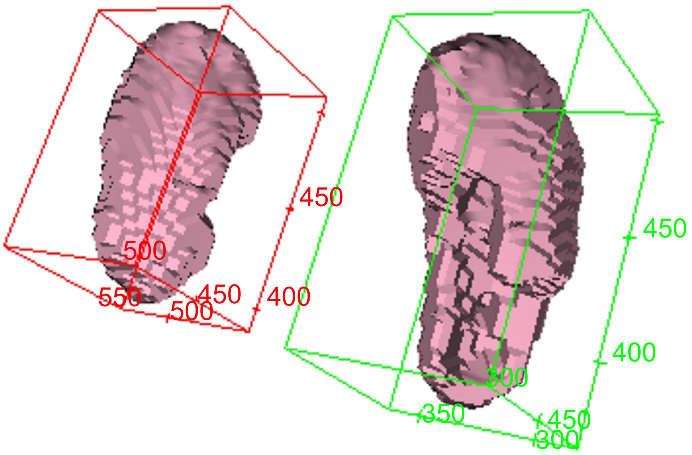

Figure 6.4: 3D visualization of the kidneys, the "objects" detected during the processing phase. As one can see, the less captating regions like the renal pelvis is almost discarded during the processing phase. In order to allow subsequent analysis and 3D measurements, results of the object detection were post-processed through an in-house developed ImageJ macro.

6.2 Registration

Medical images acquired with different modalities can provide complementary information about the anatomy and the physiology [216]. For this reason, huge efforts have been made to develop methods for the multi-modality registration. Geometric registration is the process of overlaying two or more images representing the same scene acquired at different times, from different viewpoints, and/or with different detectors, that is by different modalities [217]. In other words, the aim of the registration algorithms is to determine the spatial transformation, which maps the points of a second image to be registered to the corresponding points of the first image. Because of the aspects mentioned above as time, location and sensor type, which make the images inherently different, there is no one method to perform image registration. Therefore, due to the diversity of images, different methods have emerged to be specifically efficient. Essentially, these methods differ for the architectural and algorithmic choices. Among these, one of the most distinctive elements concerns the type of geometric deformation between the images, which will be estimated. Other essential elements are the similarity (or distance) measure and the interpolation technique, which one should adopt.

Therefore, the co-registration algorithms can be distinguished from each other for the particular solutions used to solve the previous sub-problems, i.e. the transform model estimation (e.g., rigid or non-rigid) as well as the similarity measure and the interpolation method to be applied. Nevertheless, the algorithmic flow-chart of a co-registration method can be generically schematised as reported in Figure 6.5.

As one can see, the registration process involves an optimisation problem: the transformation to align the two input images, the reference (fixed image) and the template one (moving image), is iteratively estimated in order to maximise their similarity.

One of the most used criteria for classifying co-registration methods refers to the way the two input images, the reference and the template, are compared. It is possible to identify four categories of co-registration:

- manual or assisted;

- landmark-based;

- surface-based;

- intensity-based.

In the manual co-registration the user, generally a radiologist or a physician, is asked to visually align the images through the use of assisted image processing tools, provided with sophisticated graphical interfaces, which make manipulation of graphical data easier. Beyond being hugely time-consuming, among the major limitations there is the accuracy level, which depends on the user's judgement and experience and consequently it can be affected by both inter- and intra-observer variability.

The landmark-based co-registration consists in identifying the positions of the corresponding markers in the two images and in the subsequent determination of the transformation, which aligns the pairs of these points [218, 219].

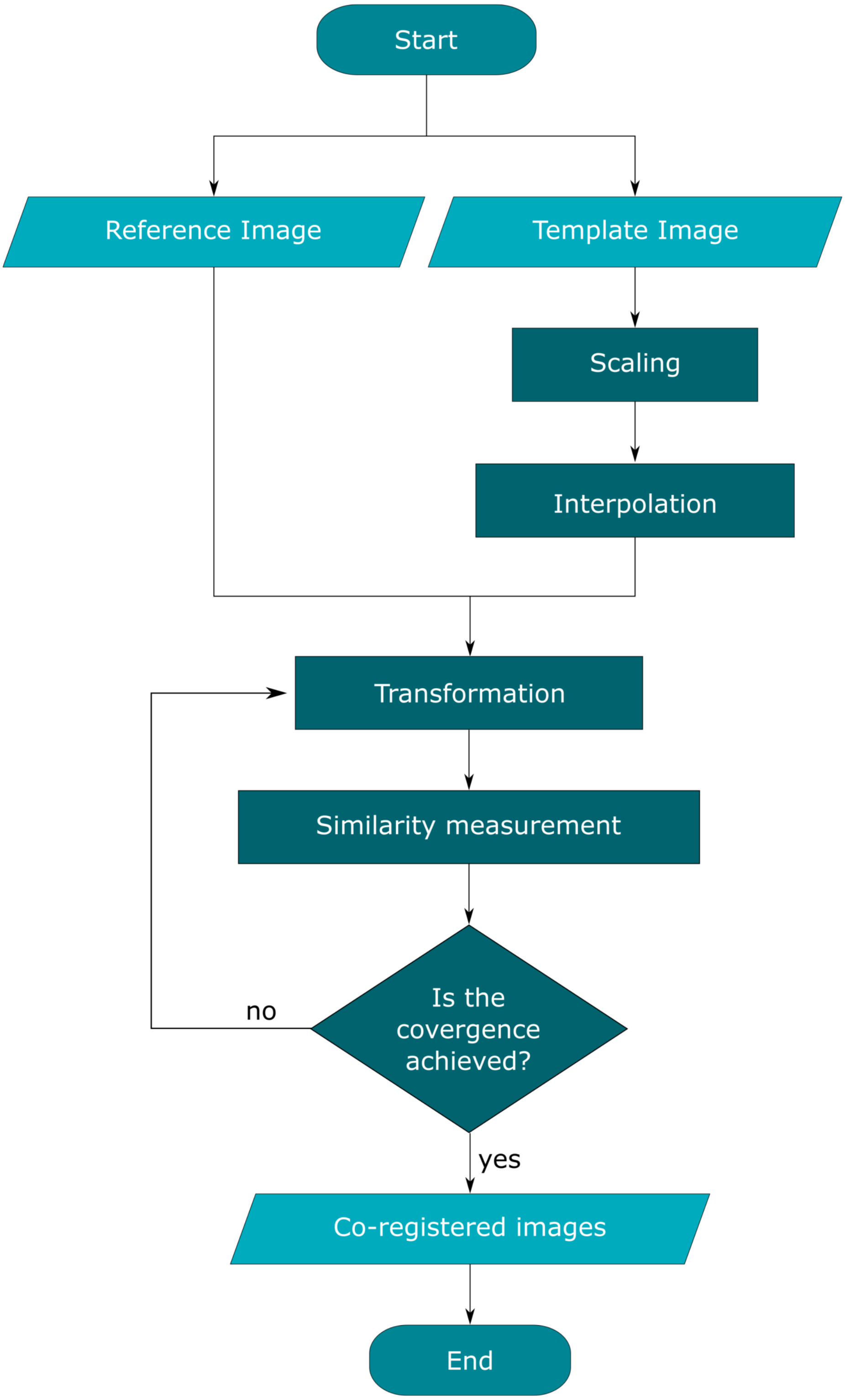
Start
Reference Image
Template Image
Scaling
Interpolation
Transformation
Similarity measurement
Is the covergence achieved?
no
yes
Co-registered images
End

Figure 6.5: General framework for the co-registration of two images, the reference and the template ones.

There are two types of markers: internal and external. Internal markers, commonly known as anatomical markers, are anatomical features, easy to find and identify in the images. The identification of the anatomical structures is usually performed by experts through software tools. Instead, the external markers are visible and easily identifiable objects attached to the patient during image acquisition. The landmark-based co-registration essentially consists of two steps:

- detection of the landmarks (anatomical or external) in the reference and template images;
- calculation of the geometric transformation that minimises a cost function based on the landmark offsets.

The surface-based co-registration involves the extraction of the object surfaces present in the images and the determination of the transformations [220], which minimise the distance between the corresponding surfaces. The success of this method essentially depends on the segmentation phase of the set of surfaces to be considered.

The intensity-based co-registration is probably the most widely used in literature [221]. Statistically, an image can be seen as a distribution of a random variable, which is the intensity level of the images. The co-registration method based on the intensity levels of the images involves the use of similarity measures, computed on the images to be aligned, and their optimisation, obtained by changing the transformation parameters.

6.2.1 Similarity measures

The most widely used similarity measures are based on:

- intensity differences;
- intensity cross-correlation;
- information theory.

The similarity measures based on the intensity difference are usually performed on the sum of squared differences (SSD), which is defined as follows:

$$SSD = \frac{1}{N}\sum_{i=1}^{N}[A(i) - B_T(i)]^2 \tag{6.4}$$

where A and B_T are the reference and the transformed template images, respectively; $A(i)$ and $B_T(i)$ are their i^{th} pixel values and N is the total number of pixels of A. The assumption behind the SSD, computed voxel by voxel, is that the structures in the reference and template images have same intensity values. Therefore, this measure is suitable for mono-modality image registration and the lower the SSD, the better the images registration.

The similarity measures based on the cross-correlation are performed as the correlation coefficient or normalised correlation coefficient (NCC), which is defined as:

$$NCC = \frac{\sum_{i=1}^{N}[A(i) - \overline{A}(i)] \cdot [B_T(i) - \overline{B_T}(i)]}{\sqrt{\sum_{i=1}^{N}[A(i) - \overline{A}(i)]^2} \cdot \sqrt{\sum_{i=1}^{N}[B_T(i) - \overline{B_T}(i)]^2}} \tag{6.5}$$

where A, B_T, $A(i)$, $B_T(i)$ and N are defined as reported above for the Equation 6.4. The cross-correlation overcomes the limitation introduced by the SSD, whose assumption is having similar intensity values of the images. Indeed, NCC measures the similarity between images, which may be acquired with different conditions. NCC is based on the assumption that there is a linear relation between the intensity values of the two images. Thus, the greater the cross-correlation, the better the images registration. However, this condition is not always true for multi-modal images and may lead to misregistration.

The information theory measures are mostly based on the mutual information (MI), which measures the statistical dependence between two random variables or the amount of information that one variable contains (or explains) about the other [222]. Usually, MI is based on the Shannon entropy, which is defined by the Eq. 4.6. As reported in Chapter 4.3.1, for an image X the entropy $E(X)$ is computed on the occurrence probabilities p_i related to image intensity histogram. Entropy will reach a maximum value if all the intensity levels have equal probability of occurring, minimum value of zero if the occurring probability of one of the intensity levels is equal to 1, i.e. uniform image. As regards the image registration procedure, the joint entropy $E(X, Y)$ between two images X and Y is also considered. $E(X,Y)$ measures the amount of information present in the combined images and it is calculated using the joint histogram of two images. Every value of the joint histogram corresponds to the occurrence of the intensity levels in the two images (X and Y) at the same positions. If the images are totally unrelated, then the joint entropy will be the sum of the entropies of the individual images. The more similar the images are, the lower the joint entropy is. Therefore, the relation between joint and individual entropies can be formalised as follow:

$$E(A, B_T) \geq E(A) + E(B_T) \tag{6.6}$$

MI is defined as follows:

$$MI(A, B_T) = E(A) + E(B_T) - E(A, B_T) \tag{6.7}$$

MI is widely used for multi-modality image registration since it does not assume any relationship between the intensity values of the two images [223]. Therefore, *MI* method has an inherent degree of robustness and the optimal transformation is reached by maximising *MI*.

Beyond the similarity measures used and the registration approaches adopted to register images, as one can see in Figure 6.5, at the heart of these registration methods lies the image scaling and interpolation. Indeed, images coming from different modalities may have different size and resolution. Therefore, images resizing is a necessary step to perform image registration. This process leads to images with the same number of pixels and the same pixel spacing.

6.2.2 Interpolation

Once the template image is scaled, interpolation algorithms provide an estimate of the voxel intensities at non-grid positions, starting from the grey level values of the original grid. There are no clear indications whether upsampling or downsampling schemes are preferable. Indeed, whilst up-sampling requires inference and introduces artificial information, down-sampling to the smallest dimension leads to loss of information.

Algorithms usually considered for image interpolation are:

- Nearest-neighbour; the output pixel is assigned the value of the pixel at the closest grid position, since a weight of one is assigned that pixel, while the other pixels receive zero weights and, thus, are not considered;

- Bilinear; the output pixel value is assigned a weighted average computed on the grey-level values of the pixels in the nearest 2-by-2 neighbourhood;
- Bicubic; the output pixel value is assigned a weighted average computed on the grey-level values of the pixels in the nearest 4-by-4 neighbourhood.

Therefore, the voxel intensity at a non-grid position is interpolated as a weighted sum of the voxel intensities at neighbouring grid positions. The weighting procedure is determined by the interpolation kernel adopted, shown for one dimension in Figure 6.6.

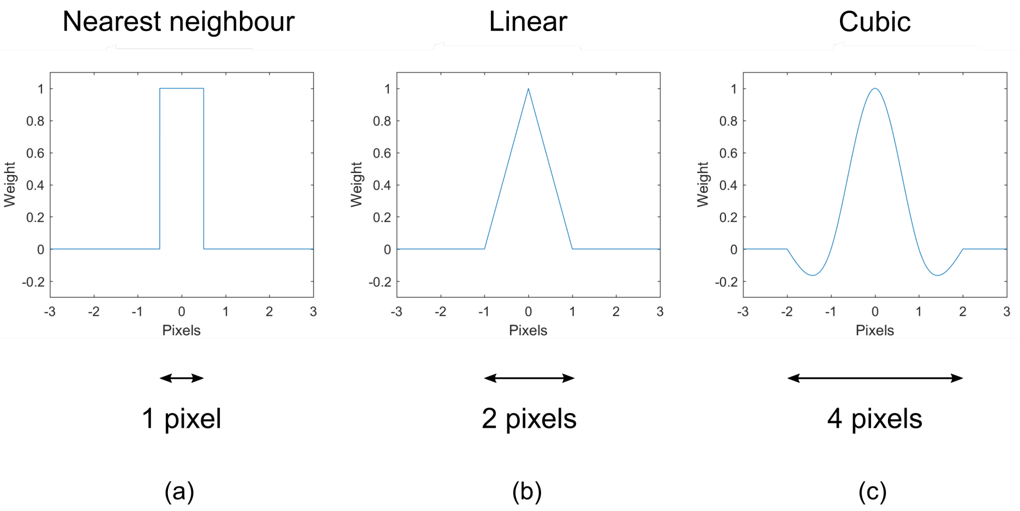

Figure 6.6: One dimension kernel for the nearest neighbour (a), linear (b) and cubic (c) interpolation. The bandwidth (number of pixels) considered for each method is also reported.

As one can see, the nearest-neighbour interpolation is performed through a uniform kernel, the linear interpolation through a triangle kernel and the cubic interpolation through a cubic spline. The width of the interpolation kernel determines the number of neighbour pixel values involved in the weighting procedure.

The same approaches can be adopted to interpolate 3D stacks of images. In 3D, the interpolation algorithms referred to as trilinear and tricubic interpolation. Regardless of the application, which may involve a 2D (slice) or a 3D (image stack) interpolation, the choice of the optimal interpolation algorithm is often context-driven. The nearest-neighbour and the linear interpolation are adequate in most cases [217]. Cubic and higher order interpolations can produce out-of-range grey values. This does not occur, for instance, with the linear interpolation, which is probably considered the most conservative choice, suitable in many cases.

In order to allow subsequent analysis, voxel interpolation also requires rescaling the ROI mask R to the same dimensions of the interpolated image.

6.2.3 Application on PET/CT and PET/MRI

During my period at the King's College London, while collaborating with the St Thomas Hospital, I extended the research work to the multi-modal analysis of the intra-tumoural heterogeneity in GOJ cancer. This cancer is associated with poor prognosis and survival [224], especially for advanced stages. Although tumour infiltration and nodal involvement are essential prognostic indicators [225], novel means are needed to better stratify GOJ patients.

The main aim of this project was to extract quantitative image-based biomarkers for predicting distant metastases in GOJ patients, which will be deeply addressed in Chapter 10. The secondary purpose was detecting sub-regions in tumour volumes, with the potentiality to combine the information coming from the different modalities. The latter has required a within-patient multi-modal registration of GOJ tumours. For this project, 20 patients prospectively recruited underwent both FDG-PET/CT and FDG-PET/MRI with a single injection protocol. Information regarding patients enrolment and image acquisition are reported in Section 12.2. As shown in Figure 6.7, the available image series were the two PET series coming from the PET/CT and the PET/MRI, and the CT, T1, T2, DWI and, consequently, the ADC series.

For each sequence investigated, segmentation of the whole tumour volume was manually performed by a dual trained nuclear medicine physician/radiologist (with more than 5 years experience) using ImageJ [213]. A 3D registration algorithm was implemented on MATLAB (MathWorks, Natick, MA, USA) to automatically transform the dataset related to each patient into one x-y-z coordinate system.

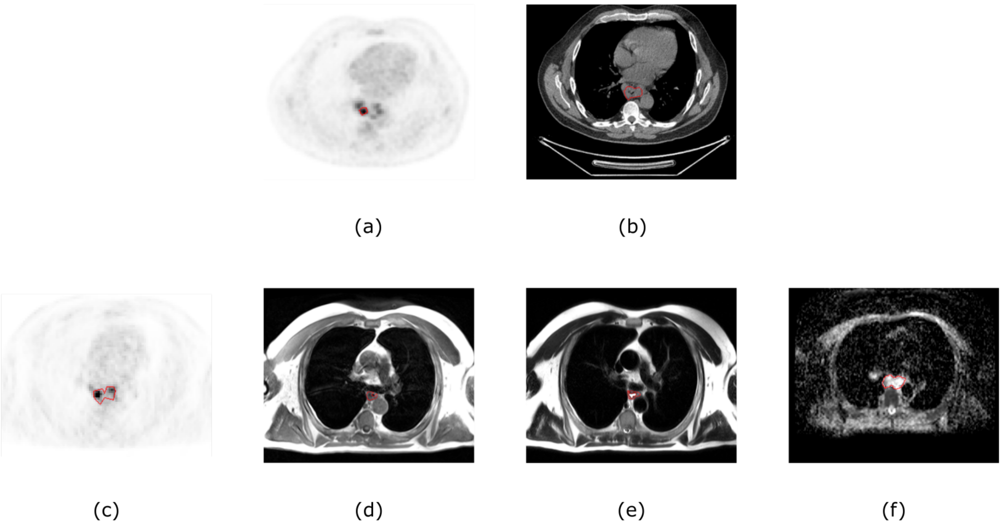
(a) (b)

(c) (d) (e) (f)

Figure 6.7: Patient ID1. Example of the available image series: from the PET/CT, PET (a) and CT (b); from the PET/MRI, PET (c), T1 (d), T2 (e) and DWI (f). In red, the ROI attained by GOJ segmentation, manually performed by a dual trained nuclear medicine physician/radiologist, is also reported.

As described in Section 6.2, image registration methods require many choices as the image interpolation to apply on the moving image, the coordinate transformation model and the definition of a cost function. Since the acquisition of PET/CT and PET/MRI were performed for each patient within the one hour, the hypothesis was that these tumours, being linked to the junction that separates the esophagus from the stomach, would not change in size neither transform but, at worst, they would move due to the unavoidable peristaltic movements. For this reason, only rigid transformation, in particular global translations, were considered. As the reference image, CT images were considered for their high anatomical details. Actually, also MRI series show high anatomical details of soft tissues. However, being the CT series faster than the MRI ones, they are likely less prone to motion artefacts and tumour displacements.

To avoid information loss, image up-sampling was performed by considering MRI resolution as a reference. The linear interpolation was applied to the moving images, in order to avoid the out-of-range values, which may result using cubic interpolation, and the effect of noise, which may be enhanced using the nearest neighbour. Then, the registration was performed for the entire volume estimating, slice by slice in an iterative fashion, the rigid image transformation that maximises *MI* (Figure 6.8).

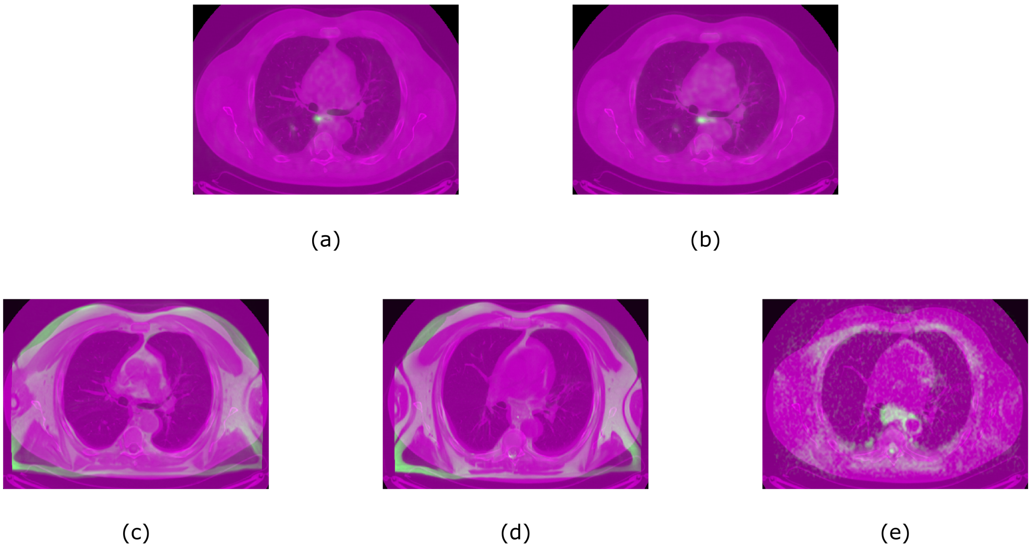

(a) (b)

(c) (d) (e)

Figure 6.8: Patient ID1. Example of slice overlapping after registration on CT, showing the PET from PET/CT (a), the PET from PET/MRI (b), the T1 (c), the T2 (d) and the DWI (e).

Therefore, it is not a rigid registration of the tumour volumes, but being computed slice by slice, it may reduce the effects of motion artefacts due to unavoidable peristaltic movements. The optimal estimated transformation was also used to transform the ROI mask previously scaled accordingly.

In Figure 6.9, as an example, the volumes overlapping of the PET, coming from the PET/CT (in red) and the PET/MRI (in green), with the CT (in blue) is reported. The quality of the registration was considered very good by the expert who performed the manual segmentation. As one can see in Figure 6.9, the PET volumes from the PET/MRI appear bigger than those from PET/CT, probably for technical reasons. These are partly discussed in Section 3.3.1, where the main differences between the PET/CT and the PET/MRI hybrid systems are reported.

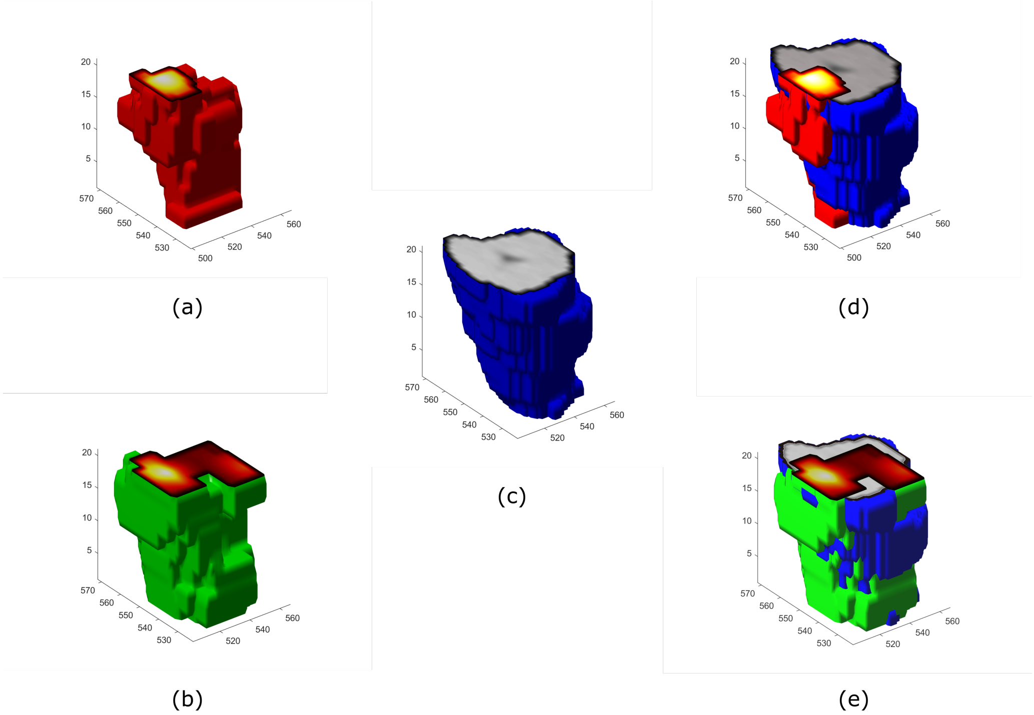

Figure 6.9: Tumour volumes of patient ID1. PET volumes from PET/CT (a) and PET/MRI (b); CT volume and overlapping with the PET volumes (d, e) after 3D registration.

Since the use of FDG-PET has gained acceptance in radiation oncology, a comparison between the pairs of PET volumes coming from the two different modalities was of particular interest. Indeed, different metabolic volumes could have strong implication in the radiotherapy planning. To this purpose, the registration between PET volumes from PET/CT and PET/MRI performed minimising the *SSD*, one of the most robust similarity measures for mono-modality studies, was preliminary analysed.

The similarity of these PET volumes pairs coming from the PET/CT and PET/MRI was measured by taking into account the Sørensen-Dice index (SDI). This index is a similarity coefficient, often used to evaluate the performance of a segmentation method compared to another considered as a gold standard [226]. *SDI* is usually measured on a reference mask X and a candidate mask Y and defined as follows:

$$SDI = \frac{2|X \cap Y|}{|X| + |Y|} \tag{6.8}$$

where $|X|$ and $|Y|$ are the cardinalities of X and Y.

In this case, the goal was not to compare two segmentation methods but to measure the similarity of the segmented PET volumes coming from the two different PET series. Indeed, *SDI* is able to quantify how similar two binary objects are. Therefore, it is also a measure of how two volumes overlap. The similarity coefficient ranges from 0 to 1, where 1 points out a perfect match between volumes, and 0 means that those volumes do not overlap at all.

Similarity results for each patient are summarised and reported in arbitrary units (a.u.) in Table 6.1. Results reflect differences in shape, size and/or 3D registration efficacy of PET volumes. Below, I briefly examined the three best results (ID2, ID12, ID16), the three worst (ID6, ID14, ID18) and, for completeness, the case reported in Figure 6.9 (ID1). As one can see, in the first three cases (Fig. 6.10, Fig. 6.11 and Fig. 6.12) volumes registration and overlapping are almost perfect. Indeed, it is impossible to reach similarity values equal to 1, since the two PET volumes are never identical.

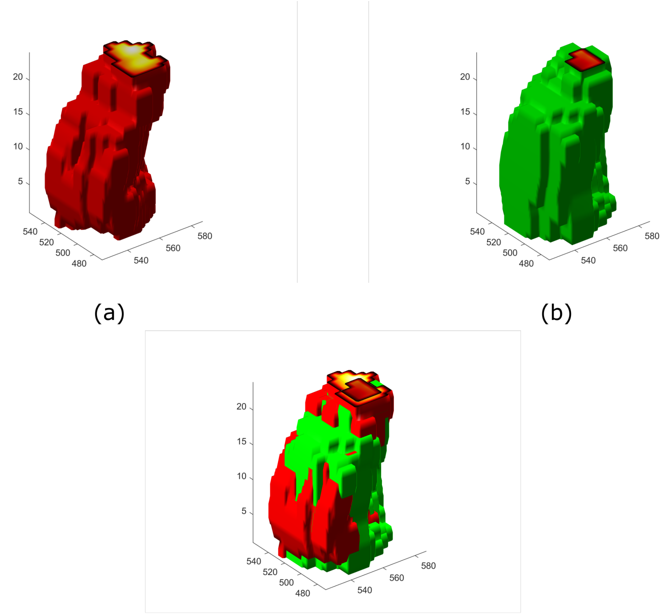

(a) (b)

(c)

Figure 6.10: Tumour volumes of patient ID2 from PET/CT (a), PET/MRI (b) and their overlapping after 3D registration (c)

Table 6.1: Summary of Sørensen-Dice similarity coefficient (SDI) relative to each patient (ID), reported in arbitrary units [a.u.].

Patient	SDI [a.u.]
ID1	0.62
ID2	0.79
ID3	0.63
ID4	0.60
ID5	0.51
ID6	0.46
ID7	0.53
ID8	0.58
ID9	0.59
ID10	0.73
ID11	0.67
ID12	0.81
ID13	0.51
ID14	0.12
ID15	0.63
ID16	0.78
ID17	0.72
ID18	0.40
ID19	0.65
ID20	0.71

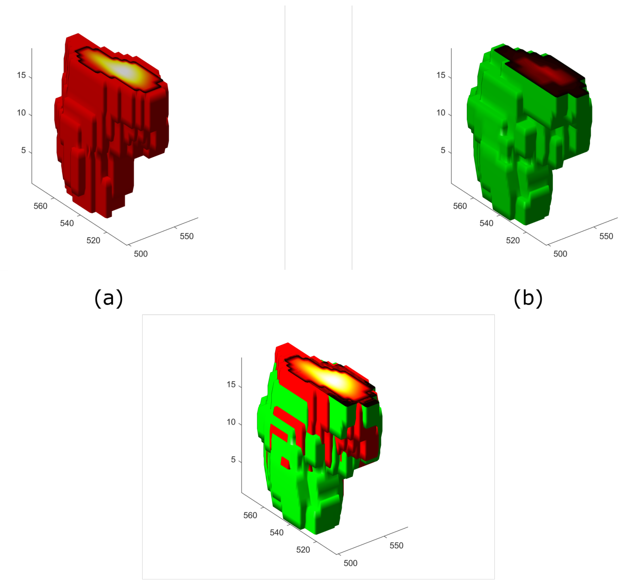
15
10
5
560
540
520
500
550

(a) (b)

(c)

Figure 6.11: Tumour volumes of patient ID12 from PET/CT (a), PET/MRI (b) and their overlapping after 3D registration (c)

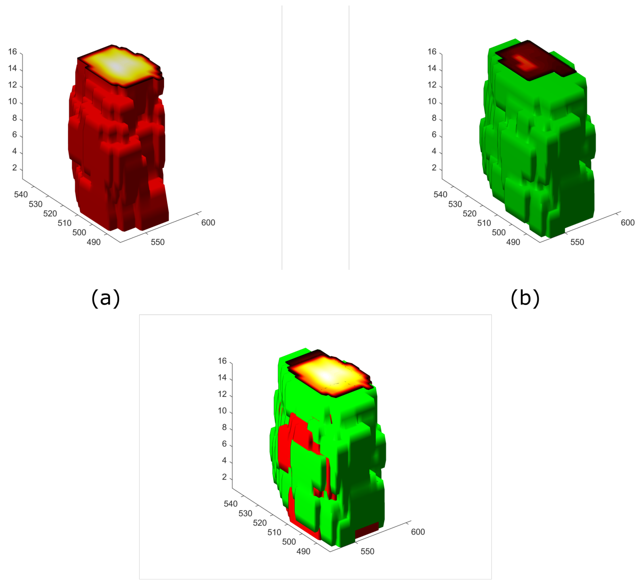
16
14
12
10
8
6
4
2
540
530
520
510
500
490
550
600

(a) (b)

(c)

Figure 6.12: Tumour volumes of patient ID16 from PET/CT (a), PET/MRI (b) and their overlapping after 3D registration (c)

The worst cases need to be analysed separately. Probably, the low similarity value of the first one (Fig. 6.13) is not due to a failure of the 3D registration procedure. The tumour appears unconnected and the dual trained nuclear medicine physician/radiologist met with difficulties in outlining the thinnest part, suggesting removing that from the analysis.

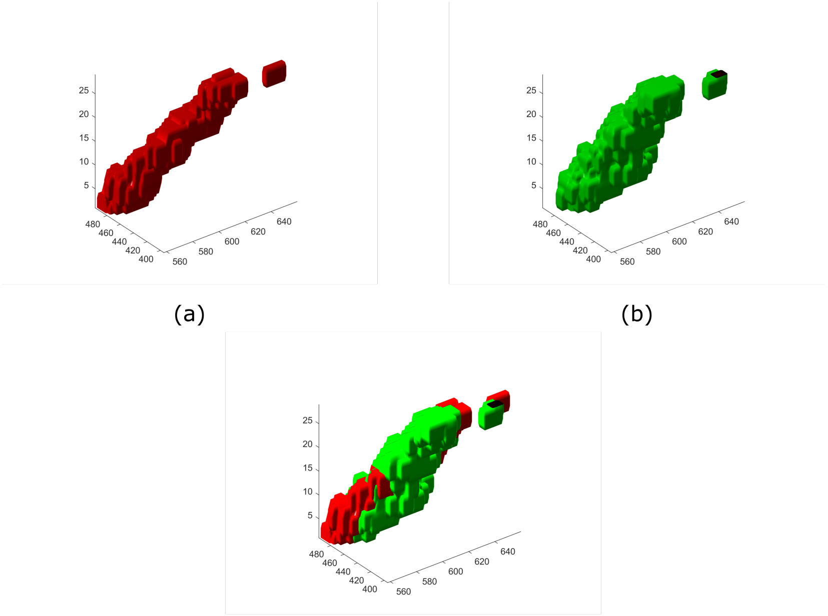

(a) (b)

(c)

Figure 6.13: Tumour volumes of patient ID6 from PET/CT (a), PET/MRI (b) and their overlapping after 3D registration (c)

As regards the second one (Fig. 6.14), volumes overlapping appears very bad, this reflecting on the similarity value which not surprisingly is the smallest one. At first, this mismatching was attributed to a failure of the registration procedure. However, the expert confirmed that the two PET series appeared very different and that the tumour was well detectable on the PET series coming from the PET/MRI sequence and not from the PET/CT one. Examining the slices of the PET/CT series (Fig. 6.15) and the related ones of the PET/MRI (Fig. 6.16) this result is not surprising. The ROIs appear very different and apparently located in different parts, as one can see in Fig. 6.15 and Fig. 6.16.

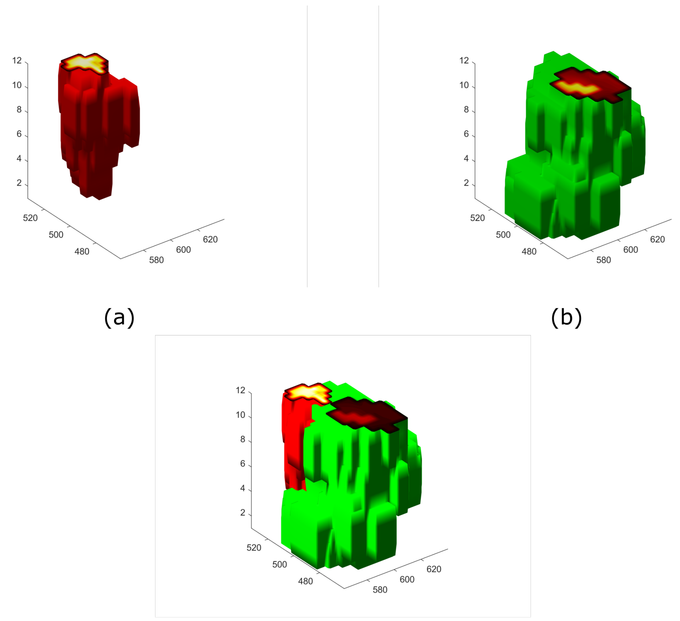

(a)

(b)

(c)

Figure 6.14: Tumour volumes of patient ID14 from PET/CT (a), PET/MRI (b) and their overlapping after 3D registration (c)

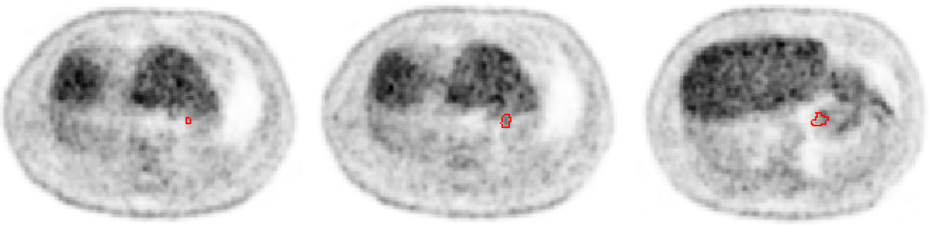

Figure 6.15: Three slices from PET-CT series showing in red the tumour outlining (patient ID14)

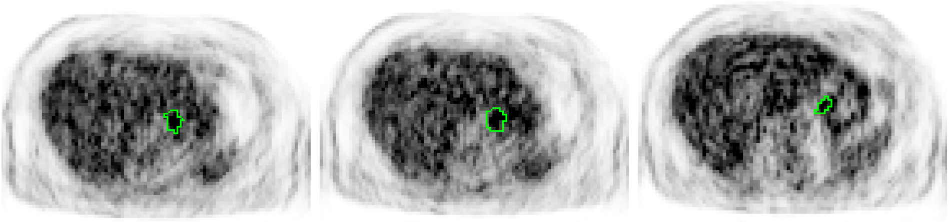

Figure 6.16: Three slices from PET-MRI series showing in green the tumour outlining (patient ID14)

As regards the third case (Fig. 6.17), the low similarity value is due to the large difference in size of the two volumes, which however appear well registered.

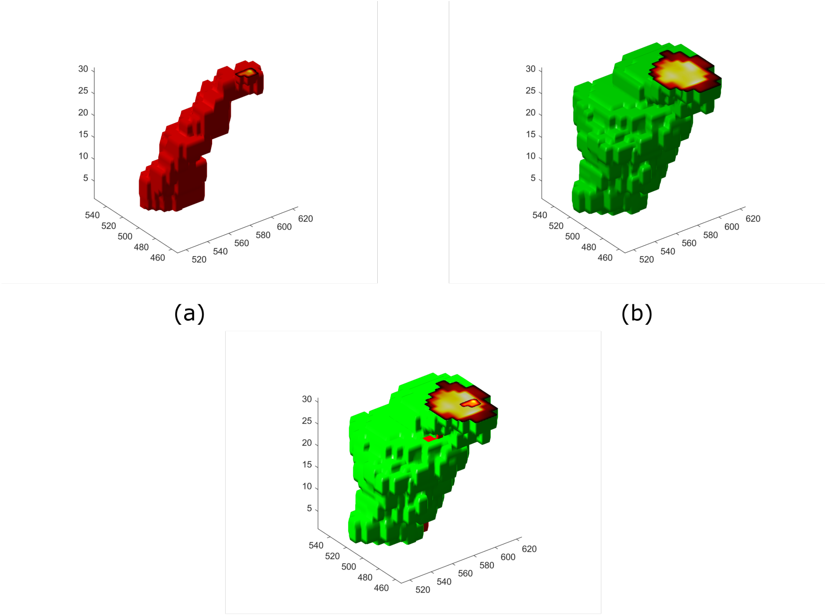
30
25
20
15
10
5
540
520
500
480
460
520
540
560
580
600
620
30
25
20
15
10
5
540
520
500
480
460
520
540
560
580
600
620
30
25
20
15
10
5
540
520
500
480
460
520
540
560
580
600
620

(a)

(b)

(c)

Figure 6.17: Tumour volumes of patient ID18 from PET/CT (a), PET/MRI (b) and their overlapping after 3D registration (c)

As regards ID1, the case first considered (Fig. 6.9), the similarity was of 0.62, pointing out that PET volumes are quite similar. This not particularly high value is due to the difference in size of the volumes (Fig. 6.18), as discussed before for the previous case.

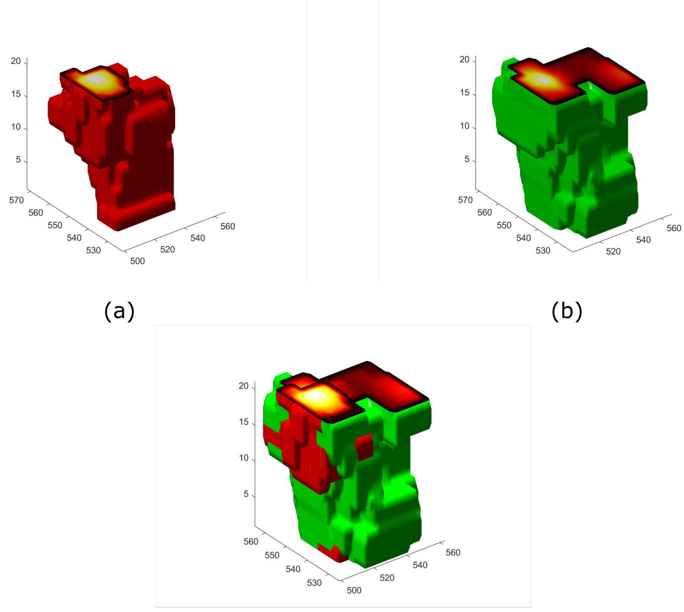

(a) (b)

(c)

Figure 6.18: Tumour volumes of patient ID1. PET volumes from PET/CT (a) and PET/MRI (b) and their overlapping after 3D registration (c).

The algorithm to perform the clustering and 3D mapping of similar values inside the volumes was set up and early used for the pairs of PET volumes. It is based on the use of the k-means clustering algorithm, which permits the grouping of the voxels inside the volume having similar values. This simple algorithm takes as input the number of clusters k and the set of observation vectors to be clustered. After the clustering procedure, each voxel is mapped within the ROI of each slice, providing a visualization of the clusters in the ROI, as shown in Figure 6.19 ($k = 4$). It is worth noting that the clusters reflect the spatial coherence of the regions, which can be visually identified in the original image.

This algorithm has been conceived for the heterogeneity analysis, since it has the potentiality to allow a comparison of tumour regions coming from different registered modalities. Indeed, it permits to compare the clusters obtained with the original image stack data, as well as the clusters originated by the voxel-wise features, as the local features described in Section 5.1, performed slice by slice.

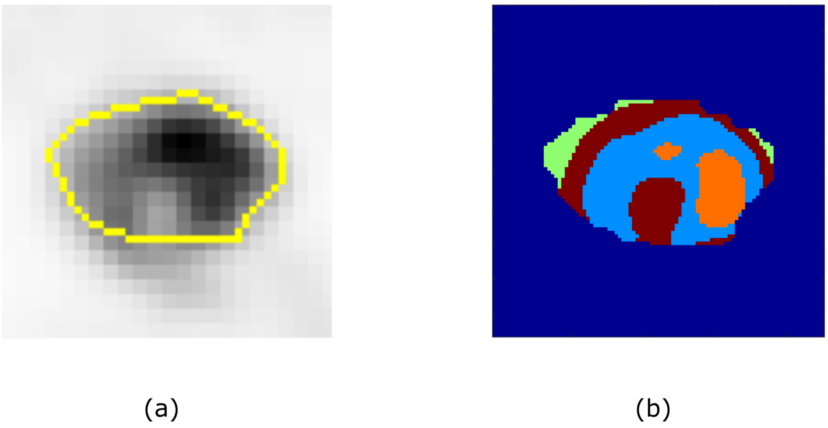

Figure 6.19: Close-up view of a GOJ tumour in a single PET slice (a) and corresponding clustering and mapping results ($k = 4$) (b).

When computed on the original data, it could be very useful to automatically exclude air and fluids as well as to perform an automatic segmentation. For instance, Figure 6.20 reports clustering ($k = 4$) and mapping of the two PET volumes of ID1, showing the same tumour acquired with the two hybrid systems. These volumes, being manually outlined, appear quite different in shape. Actually, the inner clusters, characterised by a higher uptake, almost coincide. Thus, the difference between the two volumes is due to the green parts, which correspond to the cluster with the lowest uptake values and that may not even be a tumour part. The high-uptake regions are visible in transparency and highlighted in ascending order with purple, red and cyan colours. These findings justifies further studies regarding the impact of using different modalities for the radiotherapy planning and the different perception of the same structure from the PET/CT and the PET/MRI system, which has the great advantage of involving less dose to the patient.

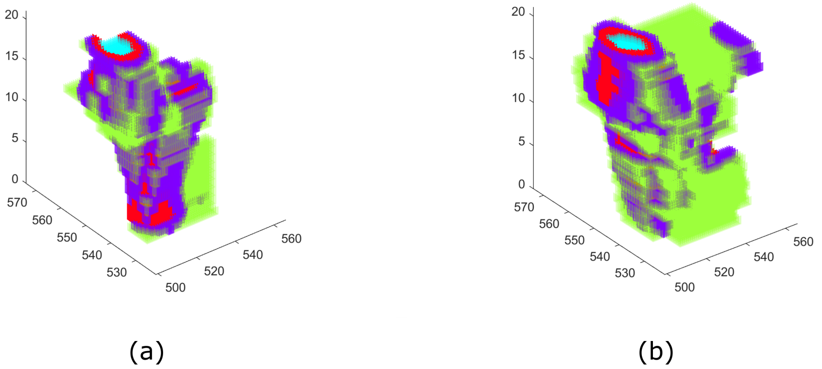

Figure 6.20: Patient ID1. Clustering and mapping results obtained with the raw PET values of PET/CT (a) and PET/MRI (b) volumes.

6.2.4 Future works

The results obtained in the previous Section 6.2.3 can be considered as a promising start for a more complex registration procedure. Using all the voxels values from the fixed image is the most straightforward strategy even if it is time-consuming for large images. Authors in [227] suggest other approaches including, for instance, the use of a voxels subset selected on a uniform grid or also random sampled. Another strategy includes the use of a mask in order to force the sampler to pick voxels in a small neighbourhood and not from the entire image domain. This last approach could improve the registration of the structure of interest, especially in the presence of artefacts far from the structure, which can be easily removed from the analysis.

As regards the 3D clustering and mapping, a deep analysis of the regions, which can be detected using the available image series, could be very useful to better understand the biological mechanisms underlying the tumour biology. Further on, the analysis of the impact on the radiotherapy planning of using the PET/CT and the PET/MRI systems should be investigated. Indeed, authors in [228] found that the use of different imaging modalities produced significantly different gross tumour volumes for oropharyngeal squamous cell carcinoma and that the delineation based on the multi-modality imaging has the potential to improve the accuracy of the volume definition. Moreover, the use of FDG-PET in radiotherapy planning has gained acceptance in the oncological clinical practice [229]. Therefore, a comparison between the combined volumes coming from the

PET/CT series (PET and CT) and from the PET/MRI ones (T1, T2 and DWI) should be performed to determine the differences in the dose coverage, focusing in particular on the variations between the metabolic volumes.

Part II

Chapter 7

Classification of lung tumour DCE-CT heterogeneity

Contents

7.1 Introduction **126**

7.2 Materials and method **128**

  7.2.1 Heterogeneity taxonomy 129

  7.2.2 Spatio-temporal indexes 130

7.3 Assessment of results **130**

  7.3.1 Generation of ground truth 130

  7.3.2 Visual analysis 130

    Manual annotation 130

    Visual matching 131

  7.3.3 Quantitative results 131

7.4 Experimental results **132**

  7.4.1 Results 132

7.5 Discussion **135**

7.6 Conclusion **136**

As described in Section 3.1, DCE-CT has emerged as a promising technique to perform functional hemodynamic studies, with wide applications in the oncologic field. It pushes towards an intensive use of software to automatically provide quantitative information useful in the clinical routine. This requires that visual analysis, representing the gold-standard for CT image interpretation, gains objectivity. This Chapter reports the application of the spatio-temporal features presented in the Section 5.2 to quantify and classify the lung tumour heterogeneities from DCE-CT sequences, as performed by experts through visual analysis. To this purpose, a proper heterogeneity taxonomy was conceived together with two experienced radiologists and described in Section 7.2. The qualitative and quantitative approaches used to generate the results is further detailed and discussed in Section 7.3. The acquisition protocol used to perform the perfusion examinations and the results achieved with the features devised, which were assessed using multiple binary classification tests according to the "one vs. all" strategy, are reported in Section 7.4. Finally, Section 7.6 outlines conclusion and highlights perspectives for future works. [1]

7.1 Introduction

CT has always been considered the reference technology for morphological analysis of organs and tissues, because of its high spatial resolution and its well-established spread over the area. It is widely known that visual assessment represents the reference approach for tissue morphological studies [162]. In general, visual analysis is widely exploited in medicine and represents the gold-standard approach in many disciplines, to diagnose pathologies according to the symptoms expressed by patients or during screening studies, by visual interpreting medical images and, often, to directly determine through visual assessment the best possible therapeutic procedures [22]. Visual evaluation is the key step in several decision making processes, ranging from histopathology, where the visual score is still the gold standard in morphometric [230] and immunohistochemistry staining evaluation [231], to the nuclear medicine, where in PET assessing whether an abnormal uptake is greater than the normal activity, also providing information regarding its origin (primary tumour or distant metastases), is performed visually [232]. For this reason, in several medical fields visual evaluation has been regulated so as to provide it with more objectivity. The most relevant example can be found in digital mammography, where systems for the visual description and analysis of the density patterns are well-defined and categorised. These systems allow distinguishing between benign findings (e.g., characterised by round opacities with microcalcifications or fatty densities) or likely malignancies (e.g., amorphous microcalcifications or hyperdensities with convex contours) [233]. At present, visual features in mammograms represent the most important features employed to train computer aided diagnosis systems [234].

---

[1] This article was republished with permission of World Scientific Publishing Company, from Automatic classification of lung tumour heterogeneity according to a visual-based score system in dynamic contrast enhanced CT sequences, Alessandro Bevilacqua, Serena Baiocco, International Journal of Modern Physics C, Vol. 27, No. 10 (2016) 1650106.

In the oncologic field, visual assessment with CT modalities represents the basis for the analysis of tumour heterogeneity, which is an important prognostic factor, as high intra-tumour heterogeneity showed to be associated with higher tumour grades [235]. As previously discussed in Section 2.1.1, it is also worth noting that the very small bioptic samples are not often adequate to catch the whole tumour heterogeneity properties, since they cannot represent the full extent of phenotypic or genetic variations of tumour. Indeed, it is known that tumour tissues have extraordinarily interconnected heterogeneities both at genetic and histopathological levels, ranging from genes, proteins, cells, microenvironment and tissues [236], and reflecting areas of high cell density, angiogenesis, necrosis, haemorrhage and myxoid change [179]. What CT, or Contrast Enhanced-CT (CE-CT), can do is addressing the macroscopic heterogeneity level referring to the tissue morphology. For instance, texture analysis is employed on CT images to detect changes in tumour heterogeneity after treatment [237], or to find possible correlations between CE-CT fine-texture features and poorer 5-year overall survival rate in patients with primary colorectal cancer [181]. As discussed in Section 3.1.1, the upgrade of CT technology, both in terms of number of detectors and gantry rotation speed, made these devices also suitable for dynamic analyses and the study of heterogeneity has been shifting towards heterogeneity functional parameters. DCE-CT has emerged as a promising technique to perform functional hemodynamic studies [238] and perfusion analyses [199, 103], with a wide application in the oncological field, providing information in diagnosis, tumour staging and prognosis [18]. Recently, it has been used to try assessing heterogeneity of different perfusion values. In [239], fractal analysis is used with the aim of evaluating the spatial heterogeneity of the tumour vasculature in DCE-CT perfusion sequence. The outcome of the method consisted in global parameters used to see whether these values could be correlated to the presence of tumours. In [240], concentric regions of perfusion maps referring to healthy and tumour tissue are considered and visually compared to find out possible correlations. Thus, in the age of personalised medicine, a non-invasive and automatic method to assess tumour heterogeneity might be of clinical benefit, whereas the evaluation is still accomplished through visual procedure.

In this Chapter is reported an automatic methodological approach to classify the intra-tumour spatial (morphological) heterogeneity present in NSCLC lesions as performed by expert radiologists through visual analysis. To this purpose, a taxonomy of possible heterogeneity degrees is defined by expert readers, who assigned a score each, on a 3-point basis. This information was also employed to build the ground-truth stemming from a set of DCE-CT examinations. The two voxel-wise spatio-temporal indexes presented in Section 5.2 were adopted. These indexes, based on the time distribution of statistical parameters computed on regional textures, were used both separately and jointly for one- and two-dimension feature analyses to build colorimetric maps. The heterogeneity was assessed on these maps and visually compared with the ground truth, where the visual matching procedure was explicitly ruled. Matching results were quantitative analysed for each type of heterogeneity and for each feature, using confusion matrices and provided in terms of sensitivity (SE) and specificity (SP). Experimental results confirm that each heterogeneity type is recognised with a high specificity by at least one of our indexes, that however show a slightly worse sensitivity. Finally, it is worth noting that temporal data also enriches the radiologists' knowledge regarding lesion heterogeneity, by providing supplementary information concerning physiological status of tumour.

7.2 Materials and method

The common CE-CT offers *static* information regarding the heterogeneity of tissue morphology, that however can be enriched through *dynamic* examinations, also yielding information regarding the lesion status. For instance, what statically could appear as a low density region, could be interpreted as a homogeneous necrotic region, or even a vessel can be better detected and identified through contrast enhancement. For this reason, the approach proposed relies on the estimation of tissue contrast agent delivery in DCE-CT sequences, acquired through axial scanning. The kinetics of a contrast agent in tissue directly depends on the tissue properties themselves, so it can be used to estimate them. Usually, in oncology an initial low-dose, unenhanced full-body CT scan is performed on a patient to identify the target lesions at baseline conditions. Then, soon after administering a contrast agent, the same volume section is repeatedly scanned over time and the voxel-based tissue TCCs signals (in HU) of the reference slices are generated by the contrast agent before, during, and after reaching the tumour lesion. As discussed in Section 3.1.1, the TCC of each voxel is represented by the collection of the attenuation values of the discrete temporal signal representing the dynamic evolution of the tracer in that voxel. ROIs are created by the radiologists by manually outlining each lesion in those slices where the clinical features of the lesions are considered as being the most representative ones (the so-called “reference” slices).

7.2.1 Heterogeneity taxonomy

At present, there is not any ground truth reported in the literature as a visual reference for the morphological heterogeneity degrees of primary lung tumour tissues and the evaluation of the heterogeneity is still left to the subjectivity of radiologists assessment. In order to automatically exploit the heterogeneity information in a computer vision system, the heterogeneity has to be assessed in an objective manner. Therefore, the first step we carried out was to identify the possible different heterogeneity degrees shown by a lung tumour tissue, so as to cover as many clinical scenarios as possible. Subsequently, a proper taxonomy was defined in agreement by two 25-year experienced readers, based on a 3-point scale:

- homogeneous pattern (Type 1), where the lesion tissue does not present heterogeneous regions;
- micro-inhomogeneous pattern (Type 2), where regions with different point densities are homogeneously present and distributed over the entire lesion;
- macro-inhomogeneous pattern (Type 3), characterised by the presence of one or more homogeneous regions, whose tissue density is markedly different from the background (generally represented by low density necrotic regions).

Changes in tissue density within the tumour may be ascribed to different causes, such as the presence of bronchi or a disorganised vascular structure, which after the passage of the contrast medium appears as dark or bright objects, respectively. In addition, a rapid tumour growth outstripping the vascular supply leads to hypoxia [30] and, subsequently, results in the presence of necrotic regions which even after the injection of contrast medium show a reduced enhancement.

7.2.2 Spatio-temporal indexes

In order to exploit both spatial and temporal information, a spatio-temporal analysis was performed by using the two indexes MS and SS conceived and presented in Section 5.2.1. Also the joint behaviour of these indexes, represented by CM the index presented in Section 5.2.2, was considered for a multi-feature analysis. This index permits the generation of a mask, which provides a spatial visualization of the clusters characterised by similar MS and SS pixel values.

7.3 Assessment of results

7.3.1 Generation of ground truth

For each examination, two experienced radiologists looked through the entire scan sequence so as to form in their mind the morphological structure of lesion, also exploiting dynamic information. Then, they visually scored the degree of lesion heterogeneity in the reference slices using the 3-point scale defined in Sect. 7.2.1. After that, for each lesion they detected and manually outlined in those slices the heterogeneity regions represented by anatomical structures such as vessels, bronchi, micro-calcifications, high-density areas and necrosis, and the presence of physics-based artefacts too. The two radiologists started by performing this analysis in double blind, and then they reviewed together all the selected cases so as to reach an agreement. Usually, whole vessels and bronchi are well identifiable, while detecting artefacts and necrotic regions is much harder and, even when succeeding, both boundaries and extent are detected with a poor accuracy.

7.3.2 Visual analysis

Manual annotation

An analysis similar to that used to generate the ground truth was performed for the colour maps of the spatio-temporal indexes conceived. In this case, the regions on the maps which appear spatially semantically coherent were manually bounded and outlined. Instead, for the colour masks, resulting from the clustering of the spatio-temporal indexes, the regions with uniform colours were directly considered [201]. Then, each map and each mask well assigned a visual score with the same 3-point scale used in Sect. 7.3.1, by considering them as belonging to Type 3 (macro-inhomogeneous, with well-defined regions semantically consistent), Type

2 (micro-inhomogeneous, with micro-areas differing from the background, without a defined anatomical meaning), or Type 1 (homogeneous, fully consistent from a semantic point of view).

Visual matching

At the beginning, the segmentation of the spatio-temporal indexes maps into connected ROIs as well as the use of cluster mask as-is, were considered to perform an automatic matching between manual and computed ROIs. However, the way the anatomical structures and artefacts were detected and outlined, mainly the uncertainty in delineating necrotic regions and artefacts, drove the choice of the approach to compare the regions manually outlined by radiologists (i.e., the ground truth) with the regions identified in the cluster masks and in the spatio-temporal indexes maps. For this reason, the comparison was performed through a visual matching of these regions by considering a successful match in case of (at least, a partial) overlap between the ROIs of ground truth and those of the features we devised. Nevertheless, in few cases at the end of the visual matching procedure some maps and masks, previously resulted in uncertain classification, lead the Readers to reconsider the corresponding ground truth and re-assigning it to a different type, by including the supplementary knowledge introduced by the temporal evolution of the cancer tissue texture.

7.3.3 Quantitative results

In order to assess the performance of the spatio-temporal indexes and of the cluster mask, a multiple binary classification test according to the "*one-vs.-all*" strategy was carried out. As it commonly occurs, the capability of a single feature to discriminate one class from the remaining ones is assessed through using the well-known 2×2 contingency table. Accordingly, there are four different outcomes from the matching procedure: "hit" or true positive (TP), false positive (FP), true negative (TN), "miss" or false negative (FN), all arranged into nine contingency tables, one for each class and for each feature [241].

A simple example using one feature (e.g., SS) and three classes is useful to clarify how this approach works. Hypothesising that radiologists assigned a lesion "Type 1" as a true condition and the SS colorimetric map suggests "Type 2". Then, this mismatch is classified as a FN, a FP, and a TN in the "Type 1", "Type 2", and "Type 3" contingency tables, respectively. Nonetheless, in case that SS correctly suggested “Type 1”, this match would have been annotated as a TP in the “Type 1” contingency table and as a TN in “Type 2” and “Type 3” ones. The same principle can be extended to all features.

7.4 Experimental results

37 datasets, corresponding to 22 DCE-CT examinations (including follow-ups) were considered in this study, referring to 13 patients (age range 36-81 years), each with one NSCLC lesion, who underwent axial DCE-CT perfusion, performed on a 256-slice CT system (Brilliance iCT, Philips Medical System, Best, The Netherlands). A 50-mL intravenous bolus of contrast agent (Iomeron, Bracco, Milan, Italy) was injected in each patient at 5 mL/s. A single acquisition of duration 25 s, with patient instructed for breath-hold, giving 20 temporal scans of the same volume section (11 slices with 5-mm slice thickness, yielding 55 mm of z-coverage, 0.4-sec rotation time, at 80 kV, 250 mA, 100mAs). Image data are reconstructed to 220 cine images (512×512 pixel, 350-mm×350-mm, 5-mm slice spacing, 16-bit grey-level depth, 1.25-s sampling period).

All images were analysed on a computer monitor and the heterogeneity regions were outlined using a graphic device (Intuos®Pro, Wacom, Krefeld, Germany). The environmental lighting level of the reading room was kept as low as possible, since it is known that the amount of surrounding light influences diagnostic performance.

The algorithm was implemented in Matlab© (MathWorks, Natick, MA, USA). The elapsed time required to process DCE-CT images and generate and displayed one spatio-temporal map is less than 4 s on an Intel i5 CPU M480, 2.67 GHz, thus being negligible as far as our needs are concerned.

7.4.1 Results

The 37 slices chosen by radiologists where manually annotated and classified to build the ground truth, according to what reported in Table 7.1, that also includes results of the visual matching between the ground-truth annotations and the features considered (SS, MS, CM), collected in contingency tables and analysed in terms of SE and SP. In the remaining parts of this Section, some meaningful examples referring to four different patients (ID1, ID2, ID3, ID4) are showed and discussed.

Table 7.1: A summary of the contingency tables for the three types of heterogeneities

Ground truth	(#)	Feature	TP	TN	FP	FN	SE	SP
Type 1	(22)	SS	17	14	1	5	77	93
		MS	18	13	2	4	82	87
		CM	18	13	2	4	82	87
Type 2	(7)	SS	6	26	4	1	86	87
		MS	4	27	3	3	57	90
		CM	4	29	1	3	57	97
Type 3	(8)	SS	6	26	3	2	75	90
		MS	5	24	5	3	63	83
		CM	6	23	6	2	75	79

The first feature considered, SS, results extremely specific for the three types of heterogeneity, producing the best results for Type 1 (SP=93%) and Type 3 (SP=90%), and also resulting highly sensitive. In particular, in terms of sensitivity it produces the best results for Type 2 (SE=86%). Figure 7.1 shows the colorimetric map of SS (right) for patient ID1, referring to a lesion whose ground truth (left) is classified as belonging to Type 2. As one can see, the colorimetric map correctly matches and the texture appears micro-inhomogeneous, with small regions characterised by different densities, having different dynamic behaviours, homogeneously distributed over the entire lesion.

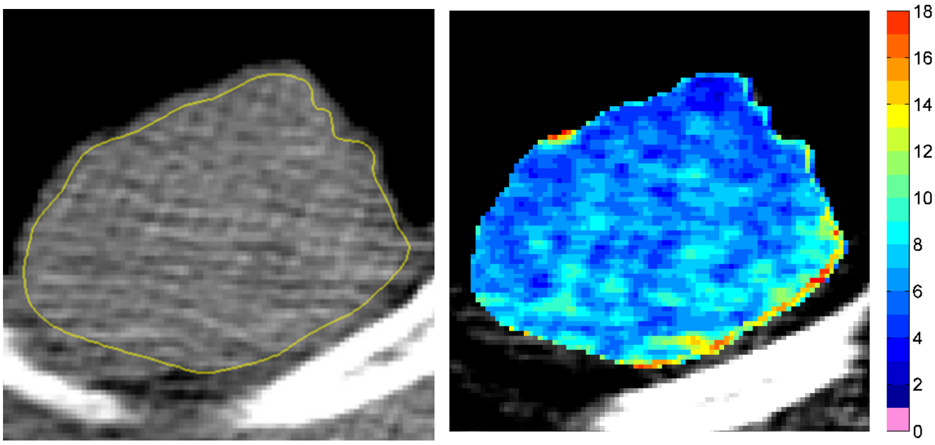

Figure 7.1: Patient ID1: ground truth (left), colorimetric map of SS (right).

The second feature considered, MS, is highly specific for Type 2 but, differently from SS, it is not sensitive enough. On the contrary, it produces good results both in terms of sensitivity and specificity for Type 1, while it results quite specific but not sensitive enough for Type 3. Figure 7.2 shows an example of a MS colorimetric map (right) for patient ID2, referring to a lesion whose ground truth (left) is classified as belonging to Type 1, which correctly matches and reproduces a homogeneous texture.

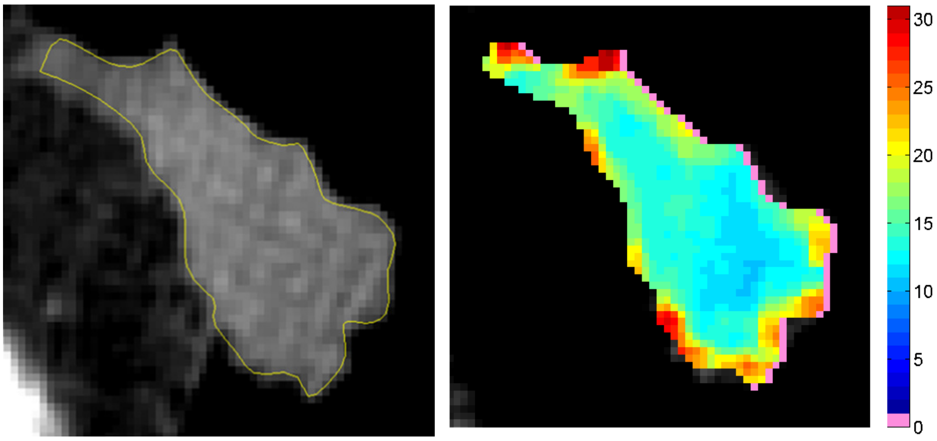

Figure 7.2: Patient ID2: ground truth (left), colorimetric map of MS (right).

The third feature, CM, returns the same good results as MS for Type 1. For Type 3 it results less specific than the other features and more sensitive than MS, showing in this case the same result as SS. For Type 2, it is extremely specific, having the highest values among these features (SP=97%), but it results to be poorly sensitive, similarly to MS and differently from SS. Figure 7.3 reports results related to CM mask (middle) which perfectly matches and reproduces the original ground truth manually outlined by radiologists (left) and classified as belonging

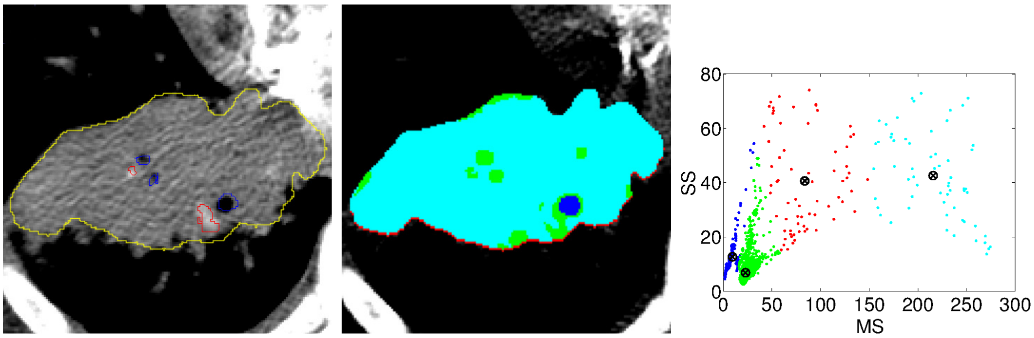

Figure 7.3: Patient ID3: ground truth (left), colour mask of CM (middle), MS–SS scatter plot (right).

to Type 3. This lesion, undergoing a light motion during examination (referred to the thin outer red region), appears as being homogeneous (wide cyan), with inner bronchi and blood vessels (in green and blue). All these tissue structures are characterised by the same behaviour in terms of MS and SS, as one can see in the scatter plot of Figure 7.3 (right), showing four clusters highlighted by as many colours, with their centroids. The homogeneity of the lesion (cyan) is characterised by low MS and SS values, while the big bronchus (blue) is characterised by the widest SS and MS, because during the lesion motion incorporates both air and tissue and, also moving along z-axis, its shape changes over time. Small bronchi and blood vessels belong to the same cluster (green) characterised by high MS and SS values. The bronchi present high values, though preserving the same shape over time, because of the lesion movement, while the high values of blood vessels are due to the increasing enhancement caused by the tracer passage.

The results discussed so far show that MS is a useful index, if it is used as a support to reinforce the results of SS through the construction of CM. On the contrary, SS alone appears to be effective in recognising these three types of heterogeneities, even the most indefinite micro-inhomogeneous tissue.

7.5 Discussion

As expected Type 1, because of its intrinsic homogeneity, is more simple to be identified by all the features, without any difference between MS and CM. Type 2 is better identified by SS, which results more sensitive to highlight different structural inhomogeneities, showing high values when the local range of HU values is not preserved over time. On the other side, MS and CM fail to detect the lesion heterogeneity belonging to this type which is, however, the type the radiologists themselves identify with the greatest uncertainty. As far as Type 3 is concerned, it is better identified by SS and CM. The difficulty in detecting this type of heterogeneity arises from the contemporary presence of characteristics of the other two types, homogeneity and micro inhomogeneity, in the same lesion. The predominance of one of these features could affect the recognition of Type 3. Nevertheless, whenever Type 3 is detected all the features enrich the knowledge of the clinicians by showing regions of clinical interest often not visually identified even at the ground truth definition stage. Generally speaking, bronchi, blood vessels and haemorrhages are perfectly reproduced by the colorimetric maps referring to all the features, while hypodense necrotic regions outlined by radiologists have a weak correspondence with the colour regions of our features. Nevertheless, it is worth noting that the extent of these regions, usually large and homogeneous inside, cannot be clearly outlined even by radiologists. This is highlighted in the ground truth image of Figure 7.4 (top left) where the hypodense region is only partially indicated by these features. In this case, all our three features show only a part of the macro region contours identified by radiologists. However, it is interesting to note how SS colorimetric map (top right) and, yet more, MS colorimetric map (bottom left) and CM colour mask (bottom right) point out one more hypodense area in the peripheral top region. Although this was not initially identified by radiologists, its presence was confirmed further on, when our features were then submitted to their attention in the matching stage. The same occurred with the blood vessels identified by these features, which could not be detected at the ground-truth generation stage, but were subsequently identified by radiologists in other time instants.

7.6 Conclusion

This work led to a publication [101], the first work using sequences of DCE-CT to assess the morphological heterogeneity levels of lung tumours, even through a semi-automated approach. As shown, in this work a well-defined procedure to generate the ground truth images and proper numerical features were devised to perform the visual matching and to assess the results. The indices computed on the TCC signals proved to be effective to describe, and measure, the heterogeneity features visually detected by radiologists on single reference slices. In fact, the approach developed permits an automatic classification of heterogeneities, with a high certainty degree (minimum specificity$\geq$0.90) for all types, with a good sensibility (minimum value $\geq$0.75). Yet more these features, the first ones based on spatio-temporal measures, enrich the radiologist's knowledge regarding the morphological heterogeneity of cancer tissue by providing supplementary information regarding tracer dynamics, hence physiological status. The main advantages of our approach include the introduction of objectivity in a crucial visual assessment task and the possibility to exploit heterogeneity information within an automatic software pipeline. For this reason, the methodology developed could be employed in decision making process relying on the quantification, or the detection, of the different types of heterogeneities, thus constituting a valid tool to assist radiologists in clinical activities. As regards future works, these findings could also

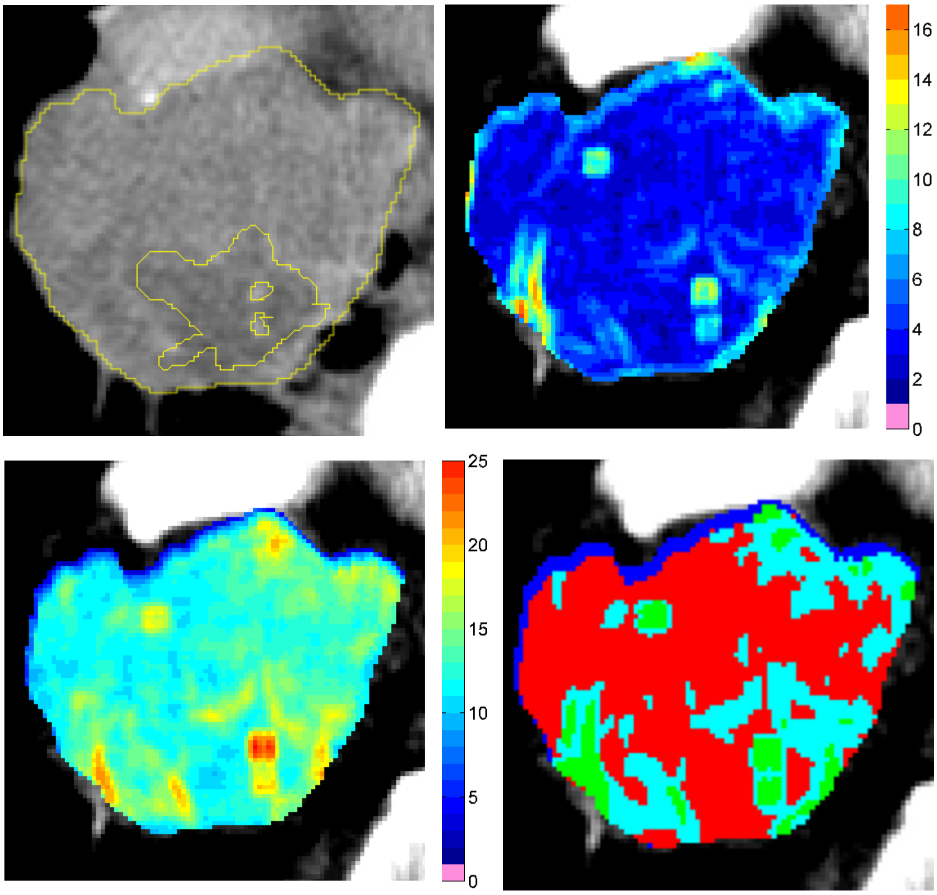

Figure 7.4: Patient ID4: ground truth (top left), colorimetric map of SS (top right), colorimetric map of MS (bottom left), colour mask of CM (bottom right).

enable a comparison between the morphological heterogeneities assessed on HU images and the functional heterogeneities derived by the typical colorimetric perfusion maps. Potentially, these indices could even be used for semi-quantitative comparative analyses between patients, or within patient during follow-ups to automatically monitor the evolution of a given heterogeneity types or even to detect a change in heterogeneity. The correlation analysis could bring new information regarding the overall tumour heterogeneity that, not to forget, involves all levels and all scales.

Chapter 8

Reliability analysis of BF maps from CTp of lung cancer

Contents

8.1 Introduction **140**

8.2 Materials and methods **141**

  8.2.1 Perfusion CT protocol 142

  8.2.2 Perfusion maps 142

  8.2.3 Local coefficent of variation 142

  8.2.4 Data Analysis 143

  8.2.5 Statistical analysis 144

8.3 Results **144**

8.4 Discussion **149**

8.5 Conclusion **150**

As discussed in Section 2.1, in the last few years, cancer treatments have improved significantly with the introduction of new therapies aiming at reducing tumour angiogenesis. CTp is being emerged as a promising functional technique for assessing tumour response to these new treatments, which yield a reduction of perfusion heterogeneity, occurring long before morphological reduction. However, several factors, such as noise induced by respiratory and physiological involuntary motion, prevent a reliable quantitative assessment, hence the clinical use of CTp. Currently, the assessment strategies rely on global measurements that fail in discriminating between noise and heterogeneity of tumour perfusion, both characterised by a wide value dispersion. This Chapter reports the use of the local-based index presented in Section 5.3 for the reliability estimation, which is able to discriminate between the tumour heterogeneity, featured by locally structured patterns, and the noise, characterised by sparse and unstructured values. This index enables a proper comparison between perfusion maps and can replace the parameters based on the global mean, thus improving the overall reliability of CTp studies and favouring the translation into clinical routine. [1]

8.1 Introduction

As discussed in Section 3.1, CTp represents a promising imaging technique in the oncological field, expectedly providing information in diagnosis, to discriminate benign from malignant lesions [242], tumour staging [75] and prognosis [21]. Recently, CTp has shown the potentiality of monitoring tumour response [243], demonstrating the ability to identify reduced perfusion even after a single administration of anti-angiogenic agent. However, this technique is delaying its entrance in the clinical routine because of the strong difficulties met to obtain reliable and reproducible results, and even to assess the reliability itself [244].

One of the main obstacles preventing the use of CTp in the clinical routine arises from the unreliability of CTp measurements, introduced by the examination protocol, the presence of physics-based artefacts, the partial volume artefacts and the methods of data processing and analysis [245]. Besides these factors, also tumour heterogeneity is considered an intrinsic factor causing measurement variability [94]. Finally, the motion artefacts are considered among the most common causes hampering the CTp technique in clinical practice [199], particularly problematic in abdomen application where movements, mostly due to breathing, are almost inevitable.

All these factors lead to random and systematic errors, which may reflect both in the construction of the TCCs and in the estimation of the perfusion parameters, thus jeopardising the final quality of the perfusion maps. Just recently, very few studies have started focusing on the TCCs fitting error to identify which perfusion values are unreliable at voxel level [102, 103], but neglecting the spatial coherence of the perfusion maps. In general, the reliability analysis is primarily performed in terms of inter- and intra-observer variability [104, 96, 98] where, to assess the variability of measures, the CV is often used. This index is calculated on global parameters, that is mean and standard deviation of perfusion parameter values computed on the whole maps [94]. In addition, CV has also been directly used as a global-based index to assess the quality [246] of the perfusion maps, despite the limit of using global measurements have repeatedly been highlighted [102]. In fact, global measures of perfusion parameters include variability due to both measurements uncertainty and physiological tumour heterogeneity, this preventing any assessment of reliability of perfusion maps.

---

[1] This article was published in Biomedical Signal Processing and Control, 31, A. Bevilacqua, D. Barone, S. Baiocco, G. Gavelli, A novel approach for semi-quantitative assessment of reliability of blood flow values in DCE-CT perfusion, 257–264, Copyright Elsevier (2017).

This Chapter reports the application of the novel approach for the reliability estimation presented in Section 5.3, which aims at partially overcoming the low specificity of global measures [200]. A spatial analysis of the perfusion maps was performed by introducing the lCV index, the structure-based coefficient, able to gather and exploit information regarding tumour heterogeneity at local level, thus expectedly isolating the effects of variability based on noise only. The results of the local-based reliability analysis can be shown through colorimetric index maps, where high lCV values suggest, for those voxels, unreliable BF values.

The effectiveness of this approach was assessed by using pairs of BF perfusion maps of primary lung cancer, computed according to the maximum slope method, before and after 3D motion registration, assuming that the motion corrected maps are always improved [199]. Three different motion degrees (MD) are considered. Both the “global” CV (gCV, the common CV computed on the whole map) and our index based on lCV values have been computed for each pair of perfusion maps and the significance of the outcome have been statistically computed. Results prove that only CV index always succeeds in selecting the CTp maps with the best quality, independent of the examinations MD.

8.2 Materials and methods

The dataset for this study was selected from a retrospective CTp study, approved by the institutional review board (IRB), consisting of examinations regarding 16 patients (range 36 - 81 years) with primary lung tumours. All patients had been instructed for breath-hold, but some of them were able to hold their breath just partly, thus, introducing motion artefacts in the exam. By taking into account follow-up studies, 21 cases in total have been analysed, each consisting of two data-sets obtained before and after motion compensation. For each examination, the MD was ranked by radiologists according to a 3-point scale, representing heavy

(2),moderate (1), and lack of motion (0). This information was reported in Table 8.1.

8.2.1 Perfusion CT protocol

The patients underwent cine CTp, performed on a 256-slice CT system (Brilliance iCT, Philips Medical System, Best, The Netherlands), feet first in the supine position. An initial low dose unenhanced full-body CT scan was performed to identify the target lesions at baseline conditions. A 50-mL intravenous bolus of contrast agent (Iomeron, Bracco, Milan, Italy) was then injected at 5 mL/s for axial cine contrast enhanced CT. A single acquisition of duration 25 s, with patient instructed for breath-hold, giving 20 scans with 55 mm of z-coverage (11 slices × 5 mm slice thickness, 0.4 s rotation time, at 80 kV, 250 mA). Image data are reconstructed to 220 cine images (512 × 512 pixel, 11 slices, 350 mm × 350 mm, 5 mm slice spacing, 1.25-s temporal resolution).

Accordingly, the generic protocol provides for M scans, each corresponding to different sampling instants, of K levels each (e.g., $M = 20$, $K = 11$).

8.2.2 Perfusion maps

For each voxel a single-compartmental model was considered for the calculation of the BF, among the most significant perfusion parameters [82], since permits the early detection of the functional changes in tumour vascular supply, within the first week from the administration of the anti-angiogenic therapy [84]. As reported in Section 3.1, to generate the TCC signal the sigmoid-shape model was adopted to robustly describe the main trend of the M concentration sample.

The target lesions and the arterial input (aorta) were selected in agreement by two radiologists on a *reference slice*. For each lesion the radiologists manually drawn the ROI on the *reference slice*. BF functional maps of the *reference slice* were obtained using an in-house algorithm developed in Matlab© (MathWorks, Natick, MA, USA).

8.2.3 Local coefficent of variation

The lCV index was computed on all the available maps. As described in Section 5.3, the computation of the lCV value is performed iteratively by assigning the proper value to the pixel displaced at the same position of the BF map. This procedure repeated for each pixel within the ROI is performed by using a sliding window of 9 × 9 pixels, corresponding to 6.15 × 6.15 mm, inside the ROI. The tumour tissue is characterised by gradual transitions occurring with a spatial coherence, and this window size is suitable to detect the smallest coherent functional heterogeneity pattern, this heavily reducing the effects of noise on statistical measurements. In particular, the choice of the window size was first driven by the radiologists of our team, stating that in the clinical practice regions smaller than 5 mm-side are rarely considered. On the other hand, it is well established that CT texture features finer than 4 mm would represent noise and should not be considered [247]. The choice of 6 mm was made so as to improve the significance of the patch. For these reasons, most of the remaining spatial inconsistency of BF values can be ascribed to causes other than physiological ones.

lCV can be visualized through colorimetric maps, which provide radiologists with a global view of the reliability in BF maps, highlighting the regions characterised by a greater spatial coherence and those by an inconsistent variability. The lCV maps can be represented through pseudo-colours using a hotcold colour map. The brown colour points out the pixels where the lCV values are not computed because the minimum number of adjacent values is not available.

Finally, the single statistical index μ_{lCV} introduced in Section 5.3.1 was calculated from the lCV values of each BF map.

8.2.4 Data Analysis

Usually, it is taken for granted that the CV parameter (here, gCV), computed on global perfusion values (e.g., the mean of perfusion parameters) or even on the whole map, is implicitly related to the quality of perfusion maps [246] and therefore can distinguish between variability due to physiological factor or noise sources. Actually, to verify this capability, maps of known quality should be available. Of course, an absolute quantitative quality index does not exist. Therefore, to properly analyse the capability of gCV, and μ_{lCV}, in discriminating maps with a different quality, it is necessary to consider maps characterised by a known quality rank. To this purpose, we consider perfusion maps obtained using motion corrected and unregistered CTp sequences, assuming that motion compensation always leads in some way to improve the perfusion maps, as reported in [199]. Indeed, the uncorrected maps result more greatly affected by motion artefacts, compared to the registered ones.

The motion correction was performed as reported in Section 5.3, involving manually x-y-z translation, performed by radiologists on the *reference sequence*, so that the borders of the lesion visually match. According to this procedure, a 3D rigid alignment is achieved. Instead, the unregistered approach consists in keeping the *reference ROI* fixed along the *reference sequence*.

The effectiveness of the proposed approach was assessed in three steps. First, we validated the novel index, μ_{lCV}, by measuring its capability to discriminate between pairs of maps of different known quality, aware that lower μ_{lCV} values hint at a greater regional coherence of the whole BF map, which is neglected by gCV. Then, the ability of gCV to accomplish the same task was considered. Finally, the outcome achieved with μ_{lCV} and gCV were compared to draw further considerations.

8.2.5 Statistical analysis

In order to assess the statistical significance of the differences in μ_{lCV} between the motion corrected maps and the uncorrected ones the Welch two-sample t-test was used, according to [248]. [249] suggests the same statistical test to assess the differences in gCV values. P values $\leq .01$ were considered statistically significant. All statistical analysis was performed using R software (version 3.0.1, The R Foundation for Statistical Computing).

8.3 Results

Figure 8.1 shows the couples of μ_{lCV} (top) and gCV (bottom) values, computed on the whole datasets of perfusion maps and referred to the registered (in the blue colour) and unregistered (in red) sequences. For reader's convenience, the samples have been joined and displayed with dashed blue and solid red lines, respectively. Numerical values are reported in Table 8.1.

Figure 8.1 (top) clearly shows that the μ_{lCV} values of the unregistered maps always result greater than those of the corrected ones, and these differences have statistical significance except for ID16, where μ_{lCV} values are statistically equivalent. In particular, in the thirteen examinations characterised by large movements of lesions (ID1-ID8, ID11, ID17, ID19-ID21), both in the craniocaudal and in the transaxial directions (for instance, caused by breath-hold being kept only partially), the differences between the values of μ_{lCV} for corrected and uncorrected maps are greater (see IDs with MD=2 in Table 8.1). In fact, in such cases the

Table 8.1: Numerical values for μ_{lCV} and gCV achieved on motion corrected and unregistered perfusion maps, with p-values, endowing each examination ID with its own motion degree (MD).

		Perfusion Maps Variability					
		μ_{lCV}			gCV		
IDs	MD	Corrected(%)	Uncorrected(%)	p-value	Corrected(%)	Uncorrected(%)	p-value
ID1	2	32.81	38.44	$\sim 10^{-11}$	41.88	68.42	$\sim 10^{-5}$
ID2	2	48.61	52.60	$\sim 10^{-43}$	63.36	70.07	$\sim 10^{-4}$
ID3	2	42.12	47.91	$\sim 10^{-18}$	75.33	68.06	$\sim 10^{-58}$
ID4	2	46.13	52.92	$\sim 10^{-65}$	60.70	83.32	**0.940**
ID5	2	60.75	68.21	$\sim 10^{-5}$	90.63	89.52	**0.918**
ID6	2	53.64	62.80	$\sim 10^{-68}$	60.40	90.53	$\sim 10^{-45}$
ID7	2	53.19	56.88	$\sim 10^{-12}$	59.86	65.81	$\sim 10^{-45}$
ID8	2	67.23	72.96	$\sim 10^{-39}$	79.12	84.40	**0.092**
ID9	1	44.63	46.23	0.007	60.75	61.24	$\sim 10^{-4}$
ID10	1	51.10	52.54	0.006	76.53	78.93	**0.441**
ID11	2	50.63	61.07	$\sim 10^{-26}$	59.78	76.61	**0.177**
ID12	1	60.38	61.78	$\sim 10^{-6}$	84.43	84.52	**0.495**
ID13	1	49.51	52.74	$\sim 10^{-7}$	59.93	65.18	$\sim 10^{-7}$
ID14	1	47.71	49.36	$\sim 10^{-6}$	59.65	61.00	**0.825**
ID15	1	49.25	52.98	$\sim 10^{-7}$	77.25	78.54	**0.086**
ID16	0	62.26	62.86	**0.158**	83.29	84.66	**0.889**
ID17	2	46.76	53.78	$\sim 10^{-29}$	83.83	84.71	0.001
ID18	1	50.09	52.23	$\sim 10^{-8}$	63.18	67.65	**0.021**
ID19	2	51.33	69.15	$\sim 10^{-40}$	60.64	92.31	**0.050**
ID20	2	48.40	65.20	$\sim 10^{-53}$	79.34	89.77	0.005
ID21	2	76.53	81.12	$\sim 10^{-26}$	90.66	97.08	0.004

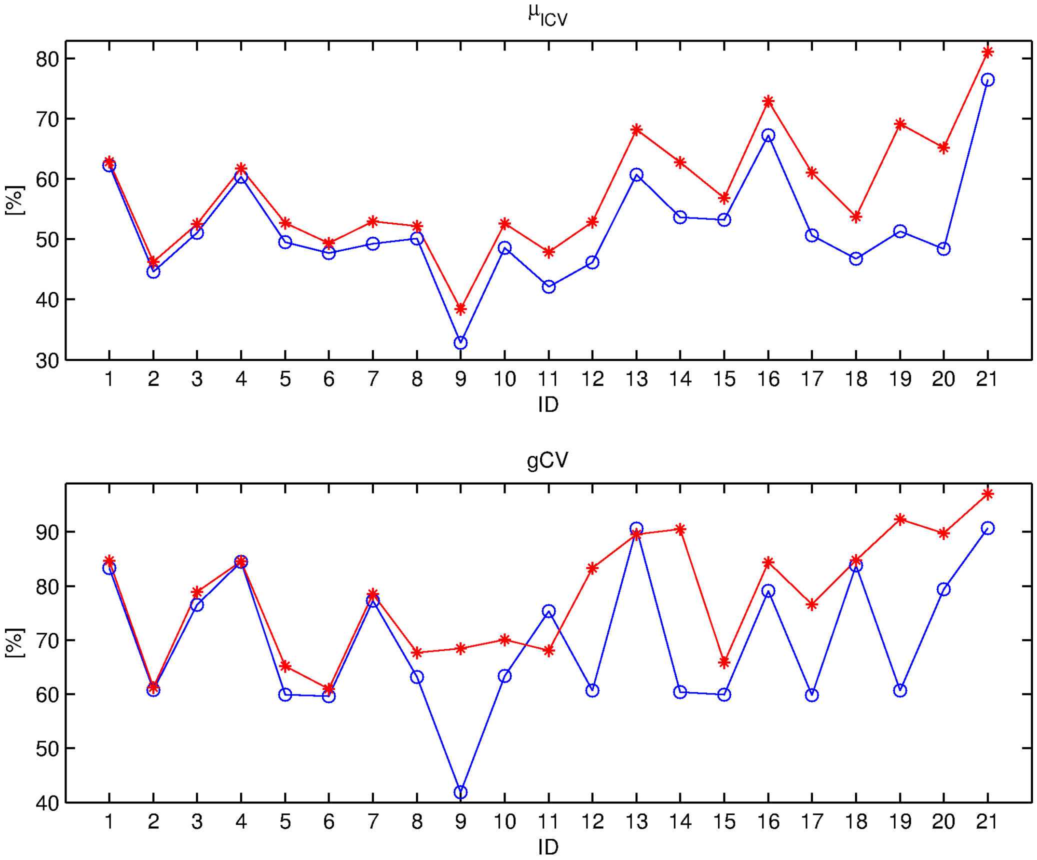

Figure 8.1: μ_{lCV} (top) and gCV (bottom) values referring to the unregistered maps (highlighted in red colour) and to the corresponding registered ones (pointed with blue colour).

uncorrected perfusion maps are characterised by a higher variability and the motion correction plays a more decisive role. On the contrary, for the seven lesions (ID9, ID10, ID12-ID15, ID18) relatively stable (IDs with MD=1 in Table 8.1) during the CTp acquisition, the effects of motion correction are appreciable with difficulties, this leading to more comparable μ_{lCV} values, although keeping statistically different. However, the p-values are several orders of magnitude lower than those referring to examinations undergoing heavy motion. Finally, for motionless examinations (ID16) μ_{lCV} values are statistically coincident (P= .16), coherently with our expectations, this really representing a pair of perfusion maps with a comparable reliability degree, as one can see in Figure 8.2.

In order to test the same ability by gCV, we computed its values for the same perfusion maps and the results, graphed in Figure 8.1 (bottom) and reported numerically in Table 8.1, are consistent with those reported in other studies [98].

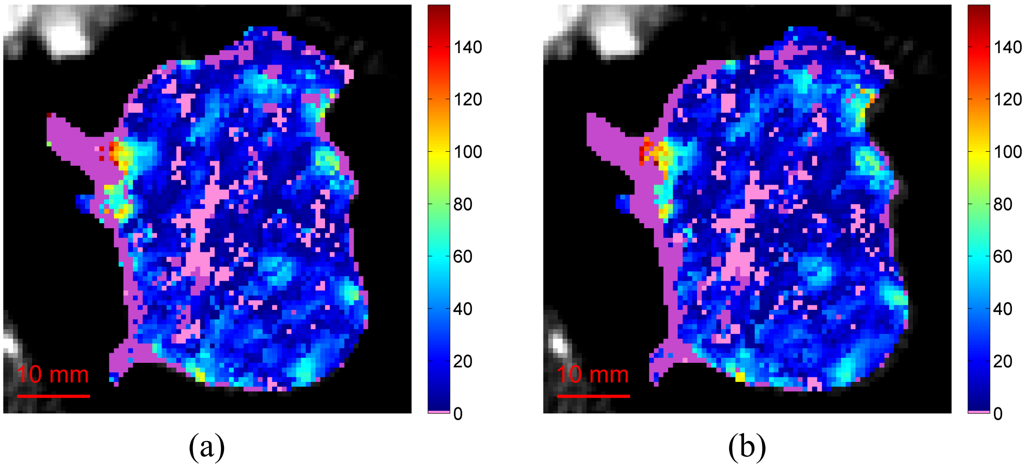

(a) (b)

Figure 8.2: Perfusion maps related to ID16, with (a) and without (b) motion compensation.

The values of gCV for the uncorrected maps again result to be generally higher than those computed on the registered ones, as expected. In particular, the gCV succeeds in discriminating between 7 out of 13 couples of perfusion maps referring to examinations with heavy motion (ID1, ID2, ID6, ID7, ID17, ID20, ID21), where the presence of noise in perfusion maps is greater. Nevertheless, gCV fails with the examination ID3, returning a lower and significant value for the uncorrected map. Things worsen when dealing with examinations undergoing a moderate motion and it just succeeds for ID9 and ID13 (2 out of 7). In addition, gCV cannot detect significant differences between the couple of maps of the examination ID16, in line with what has already been stated regarding the stability of the lesion.

On the whole, two main outcomes arise from these results. The first is that μ_{lCV} never fails in detecting the best quality, and ones only the difference is not statistically significant, when it should not, that is in the absence of motion. Second, gCV may assign a better quality to a noisier perfusion map.

To understand the main reasons standing behind this behaviour, the concept of intra-tumour heterogeneity must be considered. In fact, in the presence of heterogeneity (nevertheless, a low degree is almost always present), a perfusion map can be seen as a set of local homogeneities which can be captured by the local analysis underlying the lCV computation, thus yielding quite low μ_{lCV} values. On the contrary, gCV is based on a global average and it cannot distinguish whether high perfusion values are sparsely arranged or come from local homogeneities (e.g., local perfusion peaks). In fact, noise introduced by motion "breaks" these homogeneities, always leading μ_{lCV} to increase. Nevertheless, the changes of μ and σ (Eq. 4.5) of perfusion values are not due to noise only, but also to the spreading of the homogeneity, and gCV cannot distinguish between these different causes. For instance, Figure 8.3 shows the perfusion maps of the lesion ID3, with (a) and without (b) motion compensation, along with the related lCV maps (c) and (d). Lesion ID3 moves and incorporates air samples within the fixed ROI, yielding noisy TCCs (reflecting in the increasing perfusion values in the low-left side of the lesion, Figure 8.3 (b)). After motion correction (Figure 8.3 (a)) μ reduces from 108.71 to 54.34, while σ from 73.98 to 40.93, thus leading to an increasing

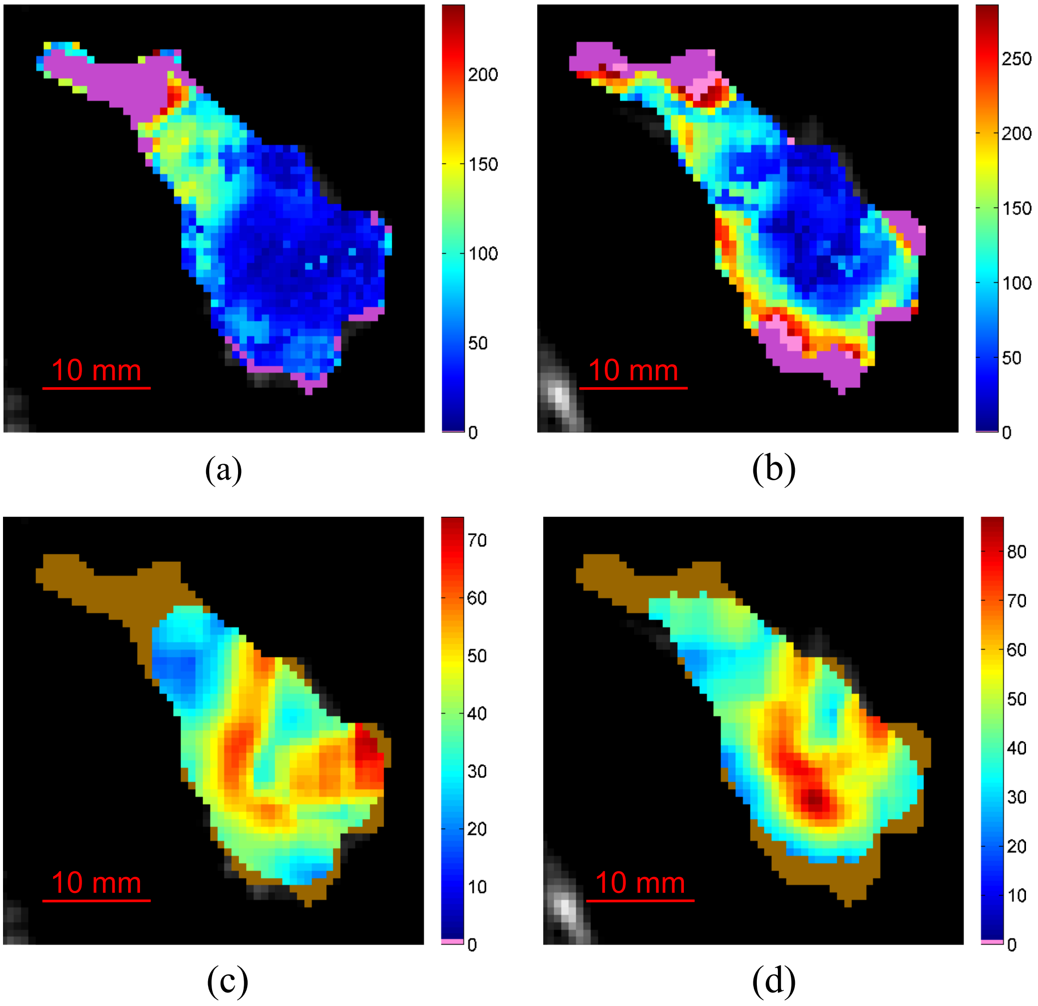

Figure 8.3: Perfusion maps referring to ID3, with (a) and without (b) motion compensation, with related lCV maps (c) and (d).

of the gCV. Meanwhile, the lCV recognises the improvements in terms of local homogeneities (Figure 8.3 (c) and (d)), and the overall μ_{lCV} decreases.

8.4 Discussion

Assessing the reliability of a CTp map still is an open problem and represents one of the main obstacle to the clinical utilisation of CTp methodology. Quantitative imaging has just recently emerged as a need also in dynamic studies involving CT. So far, limited published data exist concerning the variability of CTp measurement and almost always with reference to the cranial circulation where, moreover, the near absence of movement reduces the measurement error. Till now, the well-known CV (what in this study was named gCV) has been employed beyond its capabilities, as a global index to assess the overall quality of perfusion maps, subsequently used to draw clinical considerations. The approach presented in this Chapter, highlighted two different types of errors when using gCV for such purposes. First, it often fails to detect the most reliable perfusion maps, here represented by those improved through motion compensation. Second, and this is yet a more serious issue, gCV may erroneously confer a higher quality to worse maps. Both these errors produce serious drawbacks.

In the first case, the scientific outcome of perfusion studies, where the choice of a contrast agent [246] or of the TCC sampling frequency [250], or the reproducibility of CTp parameters [96] have been computed on the basis of gCV assessments, could be misleading and definitely compromised. In the second case, the consequences are yet more severe and could even yield a misdiagnosis. For instance, the two perfusion maps referring to ID3 and reported in Figure 8.3 (a) and (b) may induce completely different clinical considerations and induce opposite therapeutic decision. In fact, the incorrect map suffering from motion artefacts and chosen by gCV as being the best one (Figure 8.3 (b)) shows the lesion as being characterised by only one small necrotic core and a significant peripheral perfused area, this may erroneously suggest a change of therapy. Nonetheless, in reality it is almost completely necrotic (Figure 8.3 (a)), this correctly hinting at a therapy working successfully.

8.5 Conclusion

The experimental results suggest that gCV is not suitable to assess the quality of perfusion maps, because it is not able to detect the presence of heterogeneities, neither to neglect their influence. To date, an index to really assess the measurement variability had not been presented yet.

The novel index discussed in this work, the μ_{lCV}, is the first index in CT perfusion studies able to take the intra-tumour heterogeneity into account, by ensuring that its effect slightly interfere with the measurement of variability due to noise. It never fails in ranking the quality of the pairs of maps, while it assigns same value to different maps achieved with almost negligible motion correction. It is worth remarking that the differences between the μ_{lCV} values of the pairs of maps are correlated to the motion degree of the examinations, and to the amount of improvements introduced by the CTp alignment, accordingly, this proving the high discriminatory power of μ_{lCV}.

As a secondary, yet important, advantage of using this approach is that lCV colorimetric maps provide radiologists with an overall view of the reliability in BF maps, where regions characterised by lower lCV values suggest a greater local spatial coherence of the BF maps, also in the presence of apparent variability, while higher values point out an inconsistent variability, which could mislead clinical considerations.

On the whole, this approach constitutes an improvement of the daily activities of the experts in interpreting the CTp studies and their reliability, this representing an important advance towards a reliable measurement of the effectiveness of anti-angiogenic therapies and, ultimately, for the translation of the CTp technique in the clinical standard practice.

Chapter 9

CTp analysis of two predominant lung cancer subtypes

Contents

9.1 Introduction **152**

9.2 Materials and methods **154**

  9.2.1 Study population 154

  9.2.2 Inclusion and exclusion criteria 154

  9.2.3 CTp protocol 154

  9.2.4 Perfusion maps 155

  9.2.5 Data analysis 156

  9.2.6 The “borderline” examinations 158

9.3 Assessment of results **158**

  9.3.1 Tumour location 159

9.4 Results **159**

9.5 Discussion **165**

9.6 Conclusion **166**

This Chapter reports the perfusion characterisation of two lung cancer subtypes at diagnosis. As discussed in Section 9.1, this topic is widely debated in literature, which reports different and sometimes not statistically significant results. The quantitative approach used to newly investigate the perfusion of this two histotypes and to generate the results is further detailed and discussed in Section 9.2. The qualitative and quantitative approaches used to assess the results are reported in Section 9.3. The significance of the results discussed in Section 9.4 has been achieved by automatically detecting and excluding artefactual perfusion values as well as through a punctual analysis of the "borderline" cases. These are the less representative lesions, where the two histotypes have similar perfusion values, which negatively affect the statistical significance of the study. Finally, Sections 9.5 discusses the results, while Sections 9.6 outlines the conclusion, highlighting perspectives for future works. [1]

9.1 Introduction

As discussed in Section 2.1, tumorigenesis involves angiogenesis, a complex mechanism consisting in the generation of a vascular network nourishing the tumour that is highly disorganised [251]. Studying abnormal vascular patterns, and their temporal changes, may be essential for tissue characterisation [101]. To this purpose, the interest in CTp methodologies has been recently confirmed [252], since CTp supplies both high spatial and temporal resolution and allows computing perfusion parameters from the analysis of the TCCs [253], generated by the contrast agent reaching the tumour. Among the most effective perfusion parameters allowing angiogenesis evaluation [254], BF arises [82] mainly because of its high correlation with the tissue biomarker MVD [81]. BF can be measured by considering the first passage of the contrast medium, thus minimising the dose administered to the patient [255]. Clinical applications of BF information computed at diagnosis include the lesion characterisation [256], especially relevant for inoperable patients, who need to schedule non-surgical treatments [257]. Or else, higher baseline BF values in patients with advanced lung carcinoma could suggest a better response to therapy [258].

The differences in BF values between responders and non-responders have prompted a tumour hemodynamic characterisation, which also embodies cancer histological subtypes. Characterising the perfusion of NSCLC has shown to provide useful information concerning their status, in particular as regards their hypoxia degree, deeply affecting tumour response to treatment [259]. In particular, it was shown that the adenocarcinoma (AC) subtype has a significantly lower hypoxia degree than the squamous cell carcinoma (SCC) one [260]. The authors in [261] found that various perfusion parameters differ between lung cancer subtypes. In particular, the authors in [262] indicate that AC is characterised by a more abundant blood supply than SCC, as the higher peak of their TCCs suggested. Moreover, also BV and flow-extraction product resulted to be significantly higher in AC than in SCC [260]. Nevertheless, the literature shows discordant results. For instance, the authors in [13] found that AC has apparently a higher perfusion than SCC, but these results were not statistically significant, in spite of MVD resulted significantly more intense in AC than in SCC. Other studies [263, 264, 265] highlighted no differences in perfusion parameters among these two histological subtypes, also finding that they are characterised by a similar MVD [266].

---

[1] This article was published in BioMed Research International, A. Bevilacqua, G. Gavelli, S. Baiocco, D. Barone, CT Perfusion in Patients with Lung Cancer: Squamous Cell Carcinoma and Adenocarcinoma Show a Different Blood Flow, Volume 2018, Article ID 6942131, 10 pages (2018).

When considering these discordant results, we must bear in mind that BF computation of lung tumours is exposed to several sources of error [200], arising from respiratory motion [196], CTp artefacts [70] and, not to forget, tumour location [267], which can affect the reliability of BF values [268], thus dimming the real nature of tumours. As regards tumour location, its influence on BF values is rarely considered in CTp studies. Nonetheless, it has been shown that perfusion in central carcinomas is significantly lower than in peripheral ones, due to the different recruitment of vessels [269]. It is worth noting that also anatomical structures inside lesion, such as vessels and bronchi, can be responsible for jeopardising perfusion analyses [268].

The aim of this study was to evaluate the characteristics of lung tumour at diagnosis (i.e., at baseline condition), newly investigating possible significant differences in perfusion between AC and SCC, the two predominant NSCLC phenotypes. Nevertheless, as previously shown, the literature presents discordant results in AC and SCC perfusion characterisation, caused by too a high measurement variability, stemming from clinical and physiological factors as well as external causes (e.g., patient movements and artefacts). To reduce such a variability, unreliable perfusion values were automatically detected and removed. In addition, lesions' position, central or peripheral, and their proximity to large vessels, were examined to analyse how these factors could affect lesions' perfusion. Finally, for each histotype we analyse the less representative lesions, whose perfusion values are shifted to the group mean value characterising the other histotype.

9.2 Materials and methods

9.2.1 Study population

This study was approved by the IRB that waived informed consent for the retrospective data analysis of the patients. In addition, a written consensus was obtained by all patients before each study. Between September 2010 and April 2013, a total of 32 consecutive patients (22 men, 10 women; age range 36-81 years) with primary NSCLC, subdivided in 24 AC and 8 SCC, were identified and enrolled for data analysis. Tumour stage was determined in all patients according to the TNM classification of malignant tumours (seventh edition): 1 patient was diagnosed stage IB, 3 patients were diagnosed IIIA, 5 patients IIIB and 23 patients IV tumour stage.

9.2.2 Inclusion and exclusion criteria

The patients included in this study were selected according to the following criteria: over eighteen years old, with histologically verified NSCLC, and no prior history of chemotherapy, surgery or thoracic radiation therapy. Patients were excluded if the longest axial lesion diameter was less than 10 mm in at least one slice, if the examination was severely affected by physics-based artefacts, in case of a clinically significant cardiovascular disease and a known history of deep vein thrombus or pulmonary embolus. The final population included 26 patients, 19 AC and 7 SCC. Besides subtypes and staging, Table 9.1 includes lesion's location and position as the cancer features. For the sake of completeness, also the widest axial tumour section is reported.

9.2.3 CTp protocol

At diagnosis, the patients underwent axial CTp performed on a 256-slice CT system (Brilliance iCT, Philips Medical System, Best, The Netherlands), feet first in the supine position. Initially, an unenhanced low-dose full-body CT scan was performed to identify the target lesion at baseline conditions. Then, a 50 mL intravenous bolus of contrast agent (Iomeron, Bracco, Milan, Italy) was injected at 5 mL/s for axial cine contrast enhanced CT, followed by a flush with physiological saline solution (30 mL, 5 mL/s). Five seconds later, each patient underwent a single acquisition of 25-s duration, under breath-hold condition. This protocol yields 20 scans, each corresponding to different sampling instants, with 55 mm of

Table 9.1: Summary of the histological diagnosis, tumour stage, position and location (for details see Section 9.3.1), and area of the widest tumour slice relative to each lesion.

Patient ID	Diagnosis	Stage	Position	Location	Size $[cm^2]$
ID1	AC	IV	Left	Peripheral	2.4
ID2	AC	IV	Left	Extended	15.9
ID3	AC	IV	Left	Peripheral	4.6
ID4	AC	IV	Right	Extended	7.0
ID5	AC	IV	Right	Extended	16.1
ID6	AC	IV	Right	Peripheral	15.0
ID7	AC	IIIA	Right	Extended	5.9
ID8	AC	IV	Left	Peripheral	1.5
ID9	AC	IV	Right	Extended	29.0
ID10	AC	IIIA	Right	Peripheral	2.5
ID11	AC	IV	Right	Extended	20.3
ID12	AC	IV	Right	Extended	3.9
ID13	AC	IV	Right	Peripheral	0.6
ID14	AC	IV	Left	Extended	2.5
ID15	AC	IV	Left	Extended	10.8
ID16	AC	IV	Right	Extended	1.9
ID17	AC	IV	Left	Peripheral	1.5
ID18	AC	IV	Left	Central	3.8
ID19	AC	IIIB	Right	Central	10.7
ID20	SCC	IB	Left	Peripheral	2.1
ID21	SCC	IV	Left	Central	7.2
ID22	SCC	IV	Right	Peripheral	5.2
ID23	SCC	IIIB	Right	Central	10.3
ID24	SCC	IIIB	Right	Extended	22.8
ID25	SCC	IV	Right	Central	8.2
ID26	SCC	IIIB	Right	Central	16.1

z-coverage (11 slices × 5-mm slice thickness, 0.4-s rotation time, at 80 kV, 250 mA, 100 mAs). Image data are reconstructed to 220 cine images (512×512 pixel, 11 slices, 350 mm × 350 mm, 5-mm slice spacing, 1.25-s temporal resolution).

9.2.4 Perfusion maps

A ROI in the descending aorta was selected as the input function. A second ROI was manually drawn in consensus by two expert radiologists (25-year experience each) on a reference slice, where the tumour showed the widest area, similarly to what done in [265, 269]. Then, for each lesion, the radiologists performed a 3D alignment according to the procedure described in Section 5.3. In order to obtain the TCCs relative to each voxel, the values of the temporal sequence were fitted using the sigmoid-shape model, arising from the Hill Equation [91], as deeply described in Section 3.1.1. The curve fitting is achieved employing an in-house fitting algorithm based on the nonlinear, least squares, Levenberg-Marquardt minimization algorithm (lsqcurvefit, Matlab©; MathWorks, Natick, MA, USA). After TCCs computation, BF values, expressed in mL/min/100 g, were computed for AC and SCC subtypes using the Maximum-Slope method [73, 270] by considering the first-pass phase only [62] and representing each voxel with a one-compartment model, including both the intravascular and the extravascular spaces [271]. This allowed performing short-time examinations with a great benefit for patients, in terms of absorbed radiation dose and examination quality, since motion artefacts were reduced by the possibility for patients to hold their breath.

9.2.5 Data analysis

As explained in Section 5.3 unreliable BF values were excluded from the analysis and highlighted in the colour map with the pink colour. In particular, BF values strictly lower than 1 mL/min/100 g were automatically removed, being considered unlikely compliant with physiological values and rather ascribable to numerical errors. Similarly, BF values undergoing high TCC fitting errors due to the presence of structures, such as blood vessels and bronchi, or dynamic artefacts, were automatically detected as unreliable through the method presented in [268]. Finally, mean BF values were computed for each examination and considered to identify hemodynamic differences between the two histological NSCLC subtypes, AC and SCC.

To better understand the implications of the denoising methods used, in Figure 9.1 we report two BF maps related to ID15, obtained by using the denoising method [268] (a) and by manually removing (i.e., clipping) the highest BF values (b), supposedly out of the physiological range, as it is normally done. The removed values are shown in the pink colour in both maps. As one can see, the denoising method removes unreliable regions, including the outer ones, that is, those suffering from partial volume effect, which pure clipping normally keeps. Nevertheless, this method preserves a range of BF values wider than clipping does. This behaviour is underlined by the BF histogram of Figure 9.2 (b), showing that, by clipping, the highest BF values (in red) are removed independently

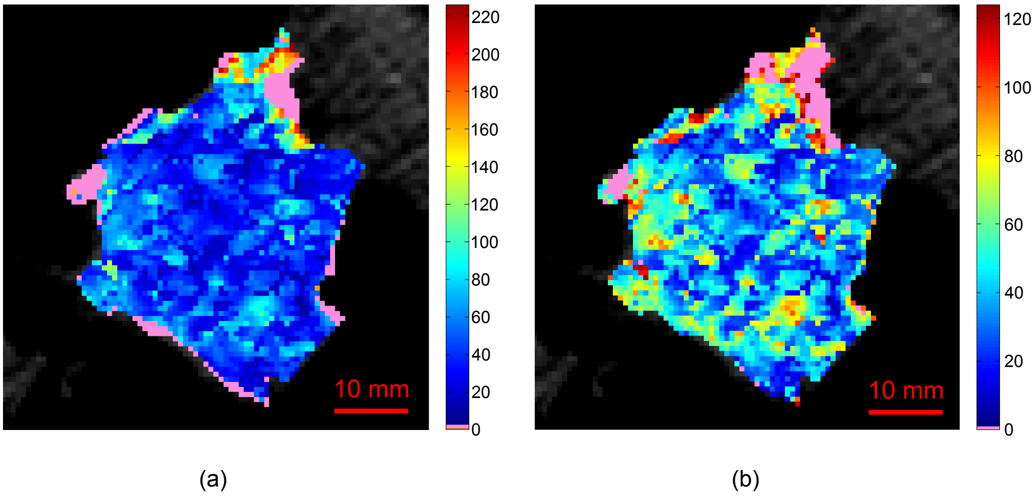

Figure 9.1: Perfusion maps of ID15 achieved through the use of the automatic denoising method (a) and by hand clipping the highest BF values (b). In pink, the unreliable values.

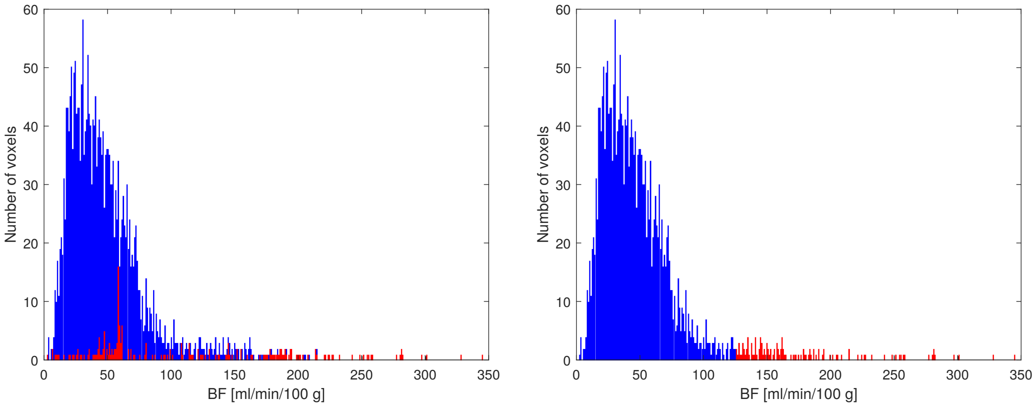

Figure 9.2: In blue, the histograms related to the original ID15 BF map and, in red, the BF values that were removed through the use of the automatic denoising method (a) and by hand clipping the highest BF values (b).

from their reliability, and the range of values narrowed. On the other side, the BF histogram of Figure 9.2 (a) highlights the clear advantage of the denoising method, which "saves" those high values which are generated with no appreciable errors. Furthermore, one can see how this method is able to even automatically remove unreliable low values falling within the physiological BF range. This explains why the range of BF values is wider, though the regions removed have a wider extent. Although these two maps are apparently very similar, the real benefit of the denoising method definitely arises in the subsequent analysis. For instance, as regards the perfusion analysis, the mean BF value of the clipped map (mean BF = 44.1 mL/min/100 g) is smaller than that of the corresponding denoised map (mean BF = 47.7 mL/min/100 g) by almost 10%. This underestimation of the mean BF value, due to the inclusion of unreliable BF values and exclusion of high BF values regardless of their reliability, could severely affect the statistical analysis of all perfusion studies. Of course, in the presence of bronchi, vessels and, above all, artefacts this difference can be even larger.

9.2.6 The "borderline" examinations

After performing the automatic error analysis to detect and exclude unreliable values, we looked for the other causes that could affect the perfusion of the "borderline" cases. Indeed, these are the less representative lesions of the two classes, whose parameter values are nearest to each other, which negatively affect the statistical significance of the study. If from one side they could simply originate from artefacts, from the other side, more interestingly, they can reflect the inherent variability of data and the intrinsic tumour properties.

9.3 Assessment of results

The main purpose of this research is to determine whether AC and SCC are characterised by a different baseline perfusion. In order to assess the statistical significance of the differences in BF between AC and SCC subtypes, the one-tail Welch's t-test was used for mean, while the one-tail Wilcoxon Rank Sum test (also known as Mann-Whitney U-test) was used for median. For both, the statistical significance is achieved with p-value < 0.05. The statistical analysis was performed using R software (version 3.0.1, The R Foundation for Statistical Computing).

As regards the analysis of the borderline cases, several factors that may cause perfusion variability were examined. The site where tumours arose, right or left lung, was considered since it is proved that they drain to different lymph node groups according to their position [272]. In this context, also the tumour location, central or peripheral, was considered since central tumours can be almost completely fed by the bronchial circulation, while the peripheral tumours, mainly at their early growth stage, can have a significant pulmonary contribution [265]. Finally, a study of the extrinsic effects on perfusion computation was performed, focusing on the beam hardening artefacts, which for instance occur in tumour localised near bony regions of the chest and, also, where the contrast medium is highly concentrated [70].

9.3.1 Tumour location

For each examination, two radiologists examined the entire scan sequences. They divided tumours into three groups according to their locations, also reporting if they are in the left or right lung. A tumour was considered peripherally located if it is 20 mm of the costal pleura, within the pulmonary parenchyma without direct connection to mediastinal structures. A tumour is centrally located if it is 20 mm of the mediastinal structures, in a close relationship with the central airways. Otherwise, it is considered as an extended tumour (that could be either large or small). The two radiologists started by performing this analysis in double blind and, then, they reviewed together all cases to reach an agreement. This information is reported in Table 9.1.

9.4 Results

Table 9.2 resumes the main BF parameter values for AC and SCC subtypes, while

Table 9.2: BF stratified by NSCLC Subtypes.

NSCLC Subtypes	BF [mL/min/100 g]				
	Mean	Median	Minimum	Maximum	SD
AC	83.5	79.2	33.0	141.3	29.4
SCC	57.0	44.3	28.0	98.4	27.2

Note: SD = standard deviation.

Figure 9.3 graphically shows the distribution of BF values for the two subtypes. The outcome highlights that the baseline BF mean value of AC examinations is definitely greater than that of SCC ones (p-value = 0.02), as well as the BF median value (p-value = 0.03). Figure 9.4 shows the averaged BF values of each AC (top) and SCC (bottom) examination. For reader's convenience, the samples were joined and displayed with solid blue lines, whereas the group mean and standard deviation (SD) values were shown with solid red and green lines, respectively. As one can see, as it often happens each subtype may have some

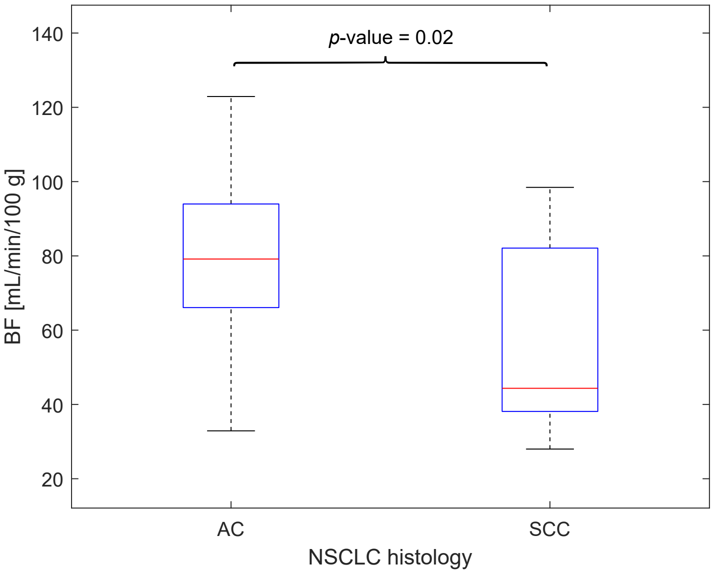

Figure 9.3: Box plots showing the BF values of AC (left) and SCC (right) lesions. The median is indicated as a red line in the boxes, whereas the vertical size gives the interquartile range.

borderline examinations nearer to the group mean value of the other subtype (the green disks in Figure 9.4), which are responsible for reducing the statistical significance of the between-group mean difference. Accordingly, the focus was on the three AC examinations (ID5, ID10, ID15) whose BF values are closer to the SCC group mean value and two SCC's (ID23, ID26) with mean values closer to AC group mean, to assess whether their mean value really reflects phenotypical features.

The first consideration concerns ID10 (mean BF = 32.9 mL/min/100 g), the AC lesion characterised by the lowest perfusion and shown in Figure 9.5. This lesion is a very small peripheral carcinoma, one of the smallest examined, located in the subpleural parenchyma, probably characterised by a predominant pulmonary circulation, which could not have activated the angiogenesis process yet [273]. As regards the other two AC lesions with a low perfusion, ID5 (mean BF = 50.5 mL/min/100 g) in Figure 9.6 (a) and ID15 (mean BF = 47.7 mL/min/100 g) in Figure 9.6 (b), these share similar properties that could explain their low perfusion. In fact, both of them are large and extended lesions, presenting wide hypoxic regions that lower the mean BF values. Altogether, these three cases seem not showing any external characteristic artificially altering their BF. For instance,

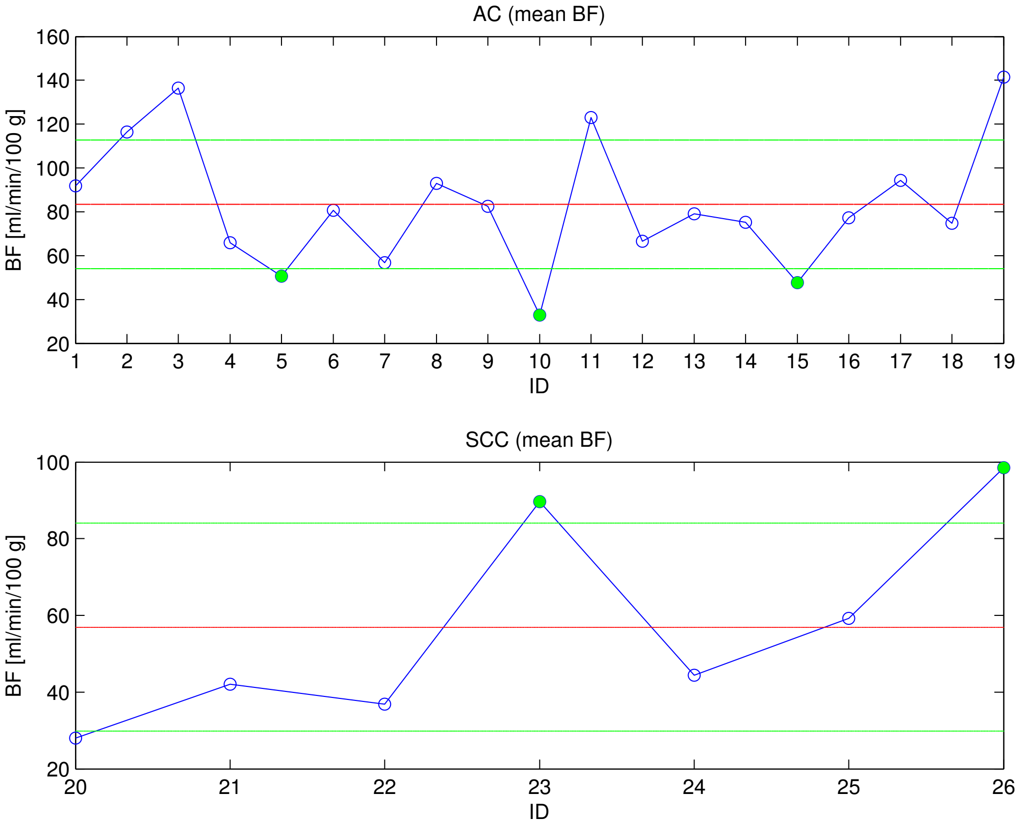

Figure 9.4: Mean BF values of AC (top) and SCC (bottom) examinations (blue circles), along with the corresponding group mean (solid red line) and SD (solid green line) values. The green circles highlight the examinations for each subtype that are closer to the mean value of the other subtype.

ID19 (mean BF = 141.4 mL/min/100 g) is a central carcinoma, as large as ID15, with a high perfusion value (the highest one). As a matter of fact, lesions of such a dimension are often characterised by a hypoxic core, due to the presence of weak and disorganised capillaries characterising tumour angiogenesis. These vessels, being more permeable than normal, increase the liquid of the extravascular space, causing the adjacent cells moving away from the vessels and, consequently, the low oxygenation of the surrounding tissue. However, the presence of segmental vessels inside ID19 still nourished the core of the lesion.

As far as SCC are concerned, the two examinations ID23 (mean BF = 89.7 mL/min/100 g) and ID26 (mean BF = 98.5 mL/min/100 g) (Figure 9.7), showing a higher perfusion compared to the others SCC, share a common feature. Indeed, they are both central SCC lesions positioned at the right lung, directly connected

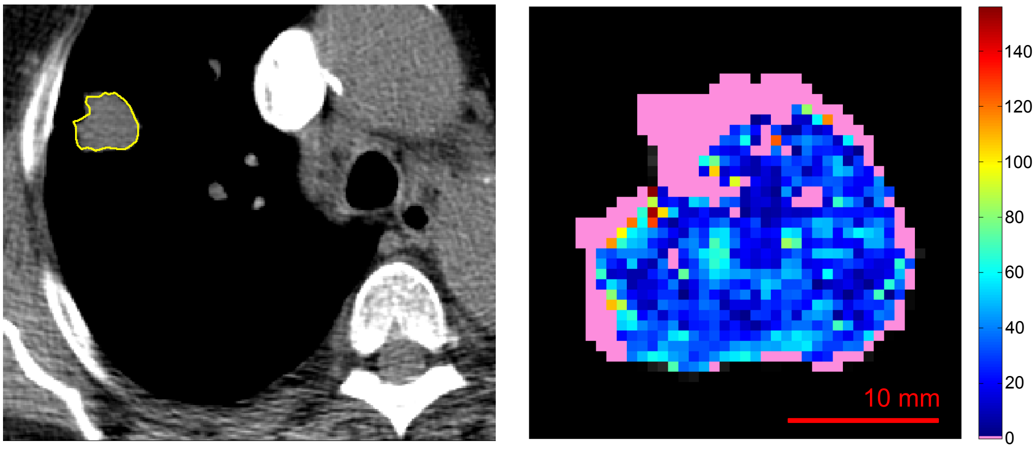
10 mm
140
120
100
80
60
40
20
0

(a) (b)

Figure 9.5: Reference slice (a) and perfusion map (b) related to ID10. In pink, the unreliable values.

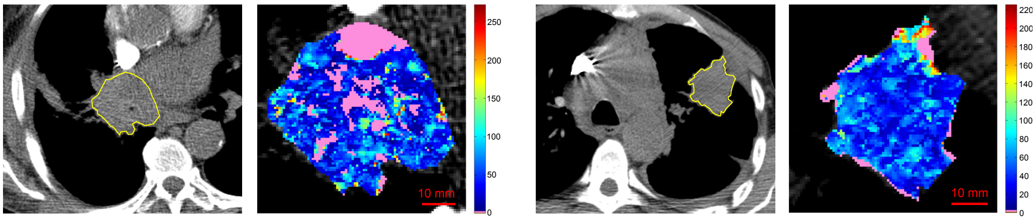
10 mm
250
200
150
100
50
0
10 mm
220
200
180
160
140
120
100
80
60
40
20
0

(a) (b) (c) (d)

Figure 9.6: Reference slice and perfusion map related to ID5 (a, b) and ID15 (c, d). In pink, the unreliable values.

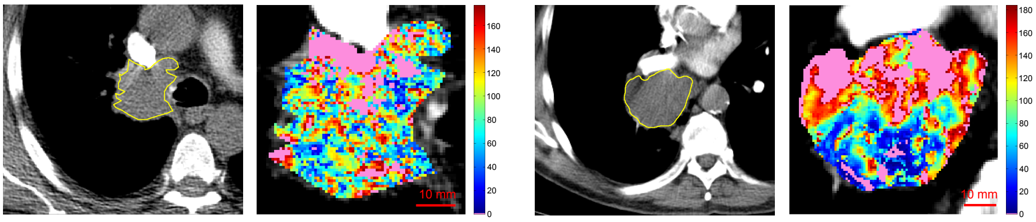
10 mm
160
140
120
100
80
60
40
20
0
10 mm
180
160
140
120
100
80
60
40
20
0

(a) (b) (c) (d)

Figure 9.7: Reference slice and perfusion map related to ID23 (a, b) and ID26 (c, d). In pink, the unreliable values.

to the vena cava and the pulmonary artery, respectively. This particular location, in proximity of these large blood vessels, may yield several artefacts during image acquisition, as shown in the original slices of Figure 9.7, which are responsible for an artificial increasing of BF values. A detail of six artefacted slices of ID23, referred to the same couch position, is shown in Figure 9.8. Nonetheless, one other central lesion, ID25 (mean BF = 59.3 mL/min/100 g) in Figure 9.9 (a), suffers for moderate artefacts, while the last one, ID21 (mean BF = 42.0 mL/min/100 g) in Figure 9.9 (b), is not artefacted. It is worth mentioning that if the artefacts in ID23, ID25, ID26 were removed manually, BF values for SCCs would rise to mean BF = 63.5 mL/min/100 g and SD BF = 36.9 mL/min/100 g, this yielding the difference between the overall means of the histotypes not to be statistically significant (p-value = 0.08). As a marginal note, it is interesting to see how the SCC lesion characterised by the lowest mean BF value in our court, ID20 (mean BF = 28.0 mL/min/100 g), shown in Figure 9.10, is staged IB.

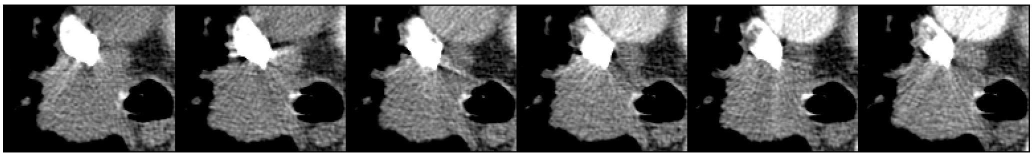

Figure 9.8: A sequence of six slices of ID23, referring to same couch position, shows the effect of beam hardening artefacts on lesions.

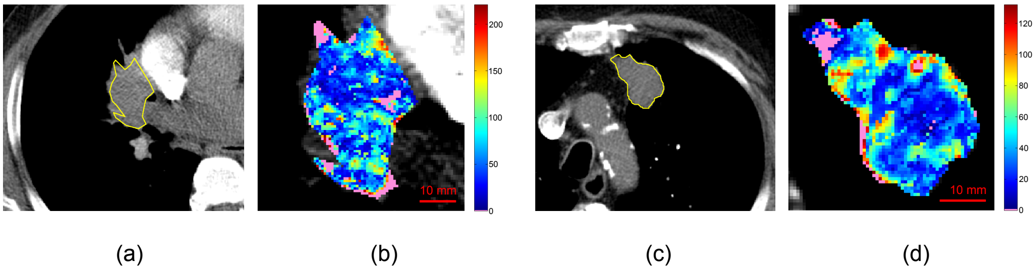

(a) (b) (c) (d)

Figure 9.9: Reference slice and perfusion map related to ID25 (a) and ID21 (b). In pink, the unreliable values.

At the end, the mean BF values of each lesion in relation to position and location were analysed. Each of the four peripheral ACs in the left lung has a mean value greater than the group mean they belong to, as well as the three right peripheral lesions have a lower mean BF, probably because of two bronchial arteries

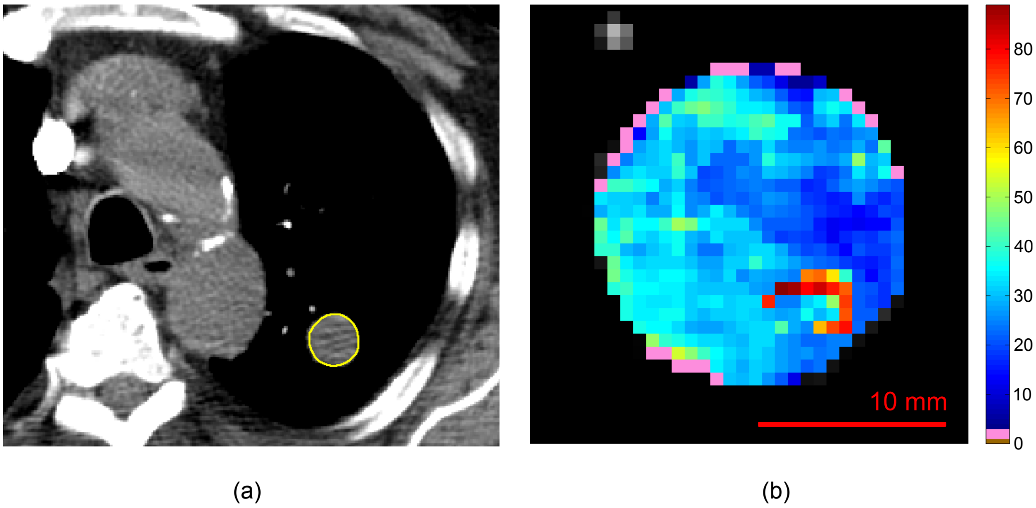

Figure 9.10: Reference slice (a) and perfusion map (b) related to ID20. In pink, the unreliable values.

usually running to the left lung, while one only to the right lung. Similarly, all the extended AC lesions, neglecting their position, have a mean value lower than the group mean, except for ID2 and ID11 (Figure 9.11, (a) and (b), respectively),

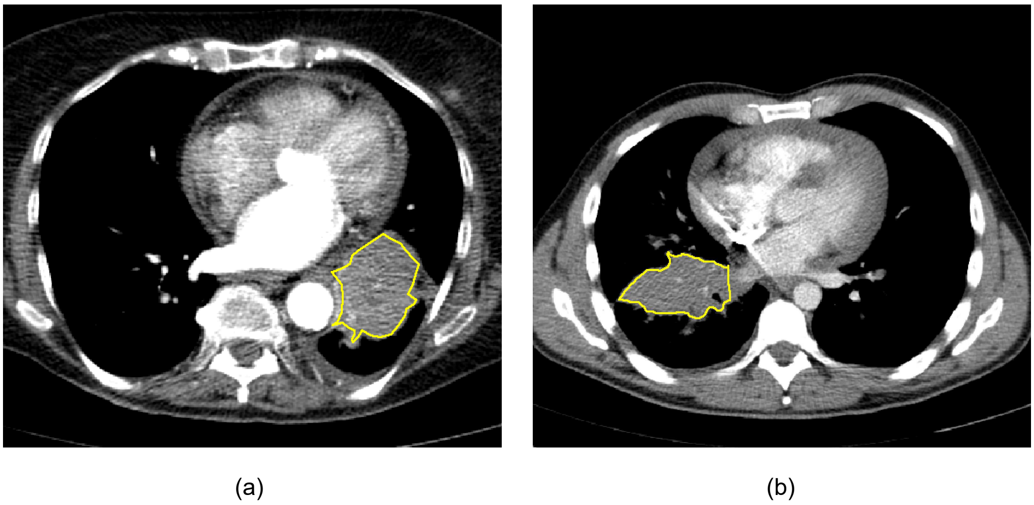

Figure 9.11: AC examinations ID2 (a) and ID11 (b) undergoing beam hardening artefacts.

that represent large lesions undergoing light beam hardening artefacts, from left and right atrium, respectively.

9.5 Discussion

The work reported in this Chapter investigated the perfusion baseline characteristics of AC and SCC, the two major NSCLC subtypes, after that the literature has reported discordant outcomes [274]. This analysis was performed through the use of the BF mean value, commonly used as significant statistical parameter in several studies [81, 275]. The results show that, before treatments, the AC histological type has a BF mean value significantly greater than SCC subtype, which generally shows a lower perfusion associated with an increased presence of necrotic areas. These results arise from the reliability analysis of the BF maps, and are enforced by the analysis of borderline cases.

The reliability assessment, carried out through an automatic and objective error detection method [268], allowed removing the anatomical structures (mainly, blood vessels and bronchi) and regions undergoing artefacts that could compromise the correct interpretation of perfusion maps, thus considerably improving their reliability. In particular, automatically removing and excluding all the artefacted regions from the subsequent analysis is probably the main reason why this study found a clear statistical significance of the different BF properties of AC and SCC histotypes.

Besides improving perfusion reliability, the borderline cases were analytically examined. These are the less specific examinations of the two histotypes, whose perfusion values are so near to the mean value of the other histotype as to partly lose their representativeness. In particular, the possible presence of some external causes, besides phenotypical properties, was investigated to motivate the mean BF value of each borderline cases. As far as the three ACs are concerned, it was not possible to find any external cause that could explain their lower BF values. Rather, the wide range covered by the AC histotype could be suggestive of the existence of sub-populations with different perfusion behaviours. Although there is not any statistical evidence regarding probable effects of tumour's position and location on the BF mean values, interesting tendencies were found regarding subgroups of the AC histotypes, that could support this hypothesis and are worth to be investigated separately in a dedicated study. On the contrary, the predominantly central position of SCCs makes them prone to beam hardening artefacts, due to the high concentration of the contrast medium in large neighbouring vessels, such as vena cava and the pulmonary artery. Indeed, it is known that artefacts may yield false results in tumours localised near to large central vessels [269]. In particular, the results proved that without automatically removing those artefacted regions from perfusion computation in two borderline SCCs, their BF mean values would expectedly be higher so as that the difference between AC and SCC means would not be significant any more. This could explain the discordant results emerging in the literature regarding the perfusion characterisation of these lung cancer subtypes, since the "noise" emerging from the colour maps was almost disregarded. As an example, the study carried out in [261] reports group mean and SD BF values for AC (74.7 ± 28.2 mL/min/100 g) and SCC (68.7 ± 32.1 mL/min/100 g) that are so near to each other as to conclude that their difference is not statistically significant. However, a deep analysis of SCCs could highlight that they underwent artefacts and using our same method to remove them could have led to the opposite conclusion.

As an added value of this research, it is worth noting that these results have been achieved using a short-time, dose-saving, protocol, that could foster other studies aiming at investigating the peculiarities of AC subgroups, as far as BF is concerned. Nonetheless, increasing the examination time would jeopardise the possibility for patients to hold their breath, and motion artefacts introduced after a 25-s period would worsen the quality of the image sequence [269].

This study has also some limitations. The first is the relatively small cohort of patients. However, other works in the literature reported a similar number of examinations, such as that in [275] (22 AC, 8 SCC), or smaller, like in [263] (14 AC, 9 SCC), [265] (18 AC, 5 SCC) and [260] (6 AC, 8 SCC). Nonetheless, removing the unreliable perfusion values improved the statistical significance of the examinations at our disposal. The second limitation stems from the first one, as the number of examinations prevented us to explore BF properties of possible AC subgroups. Finally, we have studied the BF only. However, considering other parameters was beyond the purpose of this research.

9.6 Conclusion

The main purpose of this work was to investigate the BF properties of AC and SCC at diagnosis, before treatment, and clear perfusion differences emerged from these NSCLC cancer subtypes that should be considered during their treatment planning. Nonetheless, the two methodological contributions introduced allowed this study, with a non-large size cohort and a short-time protocol, to achieve a clear outcome. These contributions, which could benefit other cancer perfusion studies, consist in the use of a method to improve the reliability of single examinations and the accurate analysis of those borderline lesions less characterising for the histotype they belong to. In particular, it is important to explicitly investigate the causes that may be responsible for those values because, besides permitting to detect values that are artificially high (or low), the borderline lesions could contain even more valuable information than the other ones.

Among the practical advantages, the capability of achieving more accurate results could prevent the need of using a higher tube voltage, for instance, when investigating central carcinomas, which reduces the sensitivity to the contrast medium and increases the exposure of the patient [269].

We encourage the authors of all the previous studies on AC and SCC to review their analysis in the light of the methodological approaches presented in this research. In this age of personalised medicine, a non-invasive profiling of the tumour in terms of perfusion characteristics, apparently an independent surrogate biomarker, could have important implications in treatment strategy, particularly in the identification of the patients, mainly with AC, that will most benefit from antiangiogenic therapies.

Chapter 10

Local analysis of lung tumours BF maps: correlation with OS

Contents

10.1 Introduction **170**

10.2 Materials and methods **171**

  10.2.1 Study population 171

  10.2.2 CTp protocol 172

  10.2.3 Perfusion maps generation 172

  10.2.4 Perfusion maps denoising 174

  10.2.5 Computation of novel local-based features 176

  10.2.6 Statistical Analysis 178

10.3 Results **179**

10.4 Discussion **181**

10.5 Conclusion **181**

This Chapter reports the use of the local-based features presented in Section 5.1 derived from perfusion maps. The ability of the local-based features, able to gather and exploit information owned by the hemodynamic heterogeneity patterns at local level, to act as a prognostic image-based biomarker for lung cancers has been assessed. In particular, the correlation between the feature-pair computed on CT perfusion maps and the survival of patients affected by lung tumours was explored and analysed in comparison with the staging, commonly used as prognostic indicator (Section 10.3). The features devised proved a strong correlation with survival, this suggesting a promising prognostic clinical application of the

DCE-CT. Also in this case, the reliability analysis presented in Section 5.3 was performed on the BF maps to automatically detect and remove those pixels and regions undergoing high computing errors. [1]

10.1 Introduction

Lung cancer is the most common malignant disease and the leading cause of cancer death worldwide [276, 277]. 85% of lung cancers are NSCLCs [278]. Despite the introduction of more advanced therapeutic strategies, including antiangiogenic treatments, NSCLC remains associated with poor prognosis and OS [279]. Tumour staging is recognised as the most important prognostic factor of survival. However, heterogeneity within the same stage grouping suggests individual factors influence survival outcomes [280]. In this era of personalised therapy, one of the challenges remains the identification of more effective markers of prognosis for a better stratification of NSCLC patients [247], with strong implications in treatment choices and consideration of alternative therapies [281].

As discussed in Section 2.1, several studies have focused on the analysis of the intra-tumoral heterogeneity and the underlying biological mechanisms in order to identify more accurate prognostic biomarkers [236, 282, 181]. Indeed, NSCLC tissues are extremely heterogeneous both at genetic and histopathological level, reflecting the presence of angiogenesis, hypoxia, high cell density, necrosis and haemorrhage [179, 101]. Angiogenesis involving the chaotic proliferation of new blood vessels from pre-existing ones [283] may cause local reductions in BF thus leading to hypoxia [30]. This is a universal cancer hallmark determining tumour response to treatment in NSCLC, reducing radiosensitivity as well as sensitivity to some chemotherapeutic agents [284].

As discussed in Section 3.1, CTp has been accepted as a clinical technique in the oncologic field, primarily for the early evaluation of tumour response to anti-angiogenic therapies [285]. Indeed, CTp allows capturing tumours vascular patterns through the analysis of the TCCs, representing the tissue density temporal variations [68], directly proportional to the quantity of contrast medium within the tissue. The BF parameter proved to detect the earliest functional changes on tumour vasculature even within the first week of anti-angiogenic therapy [84].

---

[1] © 2018 IEEE. Reprinted with permission from Serena Baiocco, Domenico Barone, Giampaolo Gavelli, Alessandro Bevilacqua, Analysis of CT Perfusion Blood Flow Maps in Patients with Lung Cancer: Correlation with the Overall Survival, 2018 23rd Conference of Open Innovations Association (FRUCT), Nov. 2018.

Moreover, BF shows a high correlation with MVD tissue biomarker , permitting the detection of abnormal vascular patterns within tumour tissue [82, 81]. However, several factors may affect the reliability of BF maps. Among these, respiratory and cardiac motion artefacts, especially in abdomen and thorax studies, partial volume artefacts as well as physics-based artefacts, for instance, occurring in tumour located near structures with a high concentration of contrast agent (e.g., heart and great blood vessels) and bony regions of chest [70]. Therefore, a reliability analysis is needed to properly characterise the tissue heterogeneity and, finally, to derive quantitative features [200].

In this Chapter, the method to evaluate the intra-tumoral heterogeneity emerging from BF maps, presented in Section 5.1, is applied. To this purpose, BF maps were computed according to the Maximum-Slope method. The reliability analysis of the BF maps, reported in Section 5.3, was performed to automatically detect and remove those pixels and regions undergoing high computing errors due to artefacts or wrong fitting, which could hamper the evaluation of the tissue microcirculation. The two local-based statistical indexes introduced in Section 5.1 were derived from the BF maps. These indexes are able to gather and exploit information owned by the hemodynamic heterogeneity patterns at local level and, expectedly, to isolate the effects of variability due to image artefacts and tumour size. At diagnosis, the correlation between the feature-pair computed on BF maps and the OS of patients affected by NSCLC was explored to assess whether these features could work as a prognostic image-based biomarker for NSCLC. The discrimination ability of the feature-pair was analysed in comparison with staging, a disease variable commonly associated with OS. The new developed features proved a strong correlation with OS [286].

10.2 Materials and methods

10.2.1 Study population

This study was approved by the IRB that waived informed consent for the retrospective data analysis of patients. Between September 2010 and December 2012, a total of 36 consecutive patients (25 men, 11 women; age range 36-81 years) with primary NSCLC, subdivided in 28 AC, 6 SCC and 2 Large-cell carcinoma (LCC),were enrolled for data analysis. Tumour stage was determined in all patients according to the TNM classification (seventh edition) of malignant tumours:

2 patients were diagnosed stage IB, 3 stage IIIA, 4 stage IIIB and 27 stage IV. Patients inclusion criteria were: (a) over eighteen years old, (b) with histologically verified NSCLC, and (c) no prior history of chemotherapy, surgery or thoracic radiation therapy.

Exclusion criteria were: (a) clinically significant cardiovascular disease, (b) pregnancy or lactation, (c) a known history of deep vein thrombus or pulmonary embolus, (d) patients lost to follow-up for unknown reasons ($n = 8$), (e) patients alive at the time of the study ($n = 4$), (f) patients whose lesion has the longest axial diameter of the lesion shorter than 10 mm in at least one slice ($n = 3$), and (g) examination severely affected by physics-based artefact ($n = 2$).

The final population included 19 patients. The variable considered as a reference for the survival prediction was the staging. This variable was dichotomised so as to divide in early stage patients likely receiving curative surgery or curative chemoradiotherapy (stage I - IIIA) and advanced stage patients (stage IIIB - IV) likely receiving palliative chemotherapy, radiotherapy, or molecular therapies.

Table 10.1 includes the previous information along with the histological subtype (AC, SCC, LCC), and patients OS data, defined as the time interval in months between the date of baseline CT examination and the date of death.

10.2.2 CTp protocol

At the diagnosis stage, the patients underwent axial CTp performed on a 256-slice CT system (Brilliance iCT, Philips Medical System, Best, The Netherlands), feet first in the supine position. Initially, an unenhanced low-dose full-body CT scan was performed to identify the target lesions at baseline conditions. Then, a 50 mL intravenous bolus of contrast agent (Iomeron, Bracco, Milan, Italy) was injected at 5 mL/s for axial cine contrast enhanced CT. Each patient performed a single acquisition lasting 25 s under breath-hold condition. This protocol yields 20 scans, each corresponding to different sampling instants, with 55 mm of z-coverage (11 slices × 5-mm slice thickness, 0.4-s rotation time, at 80 kV, 250 mA). Image data are reconstructed to 220 cine images (512 × 512 pixel, 11 slices, 350 mm × 350-mm, 5-mm slice spacing, 1.25-s temporal resolution).

10.2.3 Perfusion maps generation

The target lesions and the arterial input (aorta) were selected in agreement by two radiologists on a reference slice. For each lesion on the reference slice, the

Table 10.1: Summary of the histological diagnosis, tumour stage and OS data (months) relative to each patient.

Patient ID	Diagnosis	Stage	OS
ID1	LCC	IIIB	6
ID2	AC	IV	4
ID3	SCC	IB	14
ID4	AC	IV	13
ID5	AC	IV	5
ID6	AC	IB	5
ID7	AC	IV	6
ID8	AC	IV	10
ID9	SCC	IV	17
ID10	SCC	IV	52
ID11	AC	IV	6
ID12	AC	IV	6
ID13	AC	IV	4
ID14	AC	IV	8
ID15	AC	IV	12
ID16	SCC	IIIB	11
ID17	AC	IV	12
ID18	AC	IV	0
ID19	AC	IV	7

radiologists manually drawn the ROI and translated it on the remaining slices of the reference sequence, so that the borders of the lesion visually match. Moreover, when appropriate, adjacent slice levels were visually explored by the radiologists who chose, for each scan, the levels which visually offer the best match with the reference slice, as described in Section 5.3 and shown in Fig. 10.1. According to this procedure, a 3D rigid alignment of the lesion in the reference slice is achieved.

BF values were computed by considering the first-pass phase only [62] and representing each voxel with a single-compartment model. This allowed performing short-time examinations with the effect of reducing motion artefacts, since patients had the possibility to remain in apnoea. As reported in Section 3.1.1, the model adopted is characterised by a single inlet, the arterial input, with an arterial blood plasma temporal concentration $C_A(t)$, and a single outlet, the venous outlet, with a venous blood plasma temporal concentration $C_V(t)$. $C_T(t)$ represents the TCC of the tissue. The relation between $C_A(t)$, $C_V(t)$ and $C_T(t)$ can be expressed through the Fick's principle 3.4. No venous outflow was assumed to occur during the measurement period ($C_V(t) \simeq 0$).

In order to obtain the TCC signal for each voxel, the sigmoid-shape model given by the *Hill Equation* in Eq. (3.7) [91], was adopted. The curve fitting is achieved using an in-house fitting algorithm based on the nonlinear, least squares, Levenberg-Marquardt minimization algorithm (lsqcurvefit, Matlab©; MathWorks, Natick, MA, USA).

10.2.4 Perfusion maps denoising

The analysis of tumours BF maps includes the denoising process presented in Section 5.3, which consists in detecting and excluding unreliable BF values, a necessary step to be performed before the local analysis and features extraction. Basically, BF values strictly lower than 1 mL/min/100 g were automatically removed, being considered unlikely as physiological values and rather attributable to numerical errors, as the algorithm of perfusion computation forces the values to be positive. The quality of the fitting has been assessed by considering the residuals (ϵ) of each TCC signal, measured as reported in Eq.5.2 The reliability of the single TCC has been assessed by computing the temporal mean value μ_ϵ of the residual ϵ relative to the considered pixel. The distribution of this error has been used to detect those BF values undergoing high fitting errors in order to exclude them from the analysis.

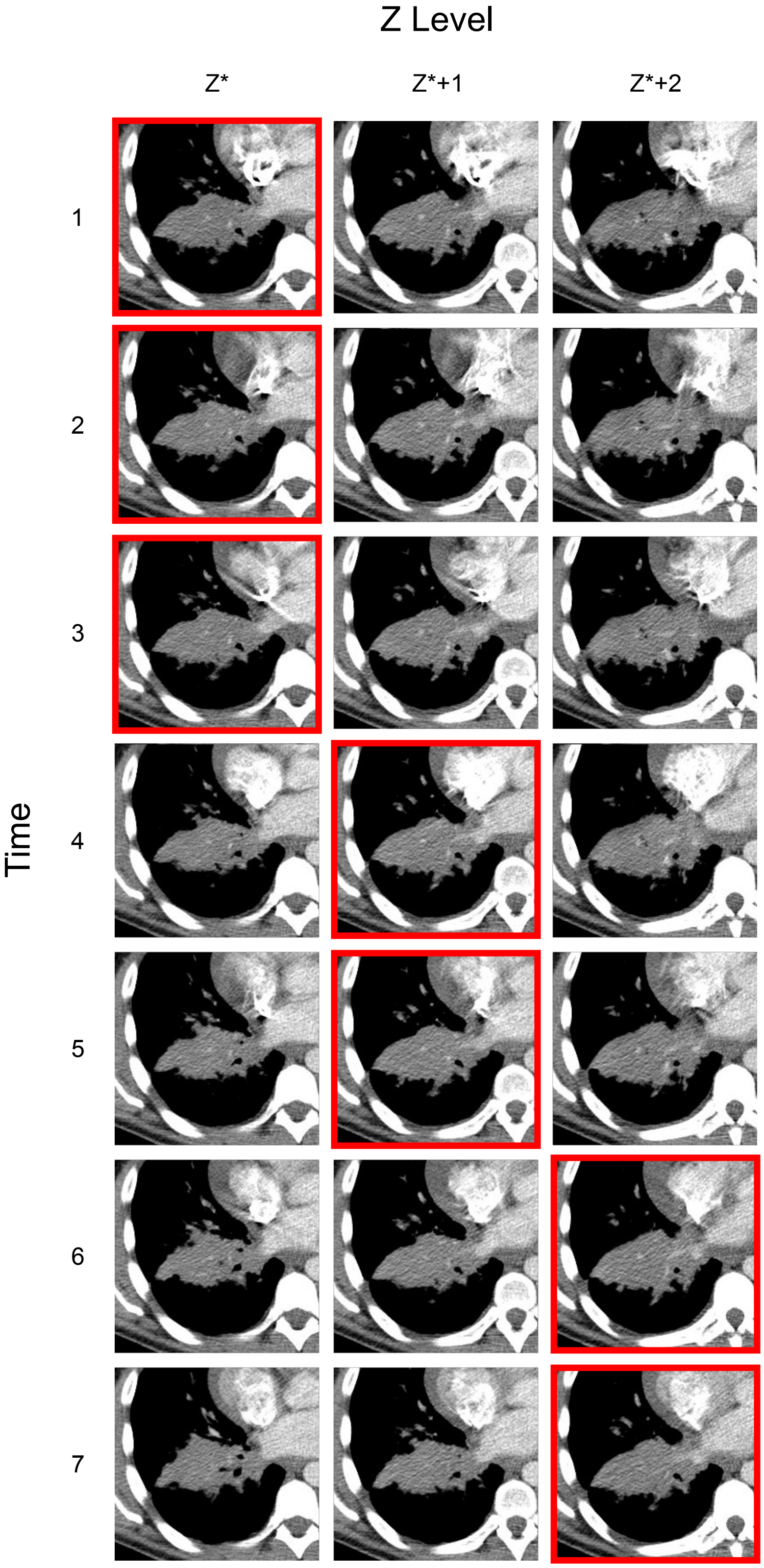
Z Level
Z*
Z*+1
Z*+2
Time
1
2
3
4
5
6
7

Figure 10.1: Example of selection of the best sequence for a lung tumour perfusion study, performed to achieve the best matching with the Z levels contiguous to the reference slice level, represented by Z^*.

High errors usually occur in the presence of noise, artefacts (both physics and due to motion) and anatomical structures, such as bronchi and blood vessels. Through the use of this index, these structures usually manually removed have been automatically excluded from the analysis by adopting an automatic cut-off value. To this purpose, the "triangle" method reported in [201] has been used. At the end of these automatic procedures, the removed BF values appear highlighted in the colour maps with the pink colour, as shown in Fig. 10.2, reporting reference slice Fig. 10.2 (a) and related BF map Fig. 10.2 (b). As one can see, the denoising method removes unreliable regions also including the edge ones, which are affected by partial volume effect, still preserving a wide range of BF values [274].

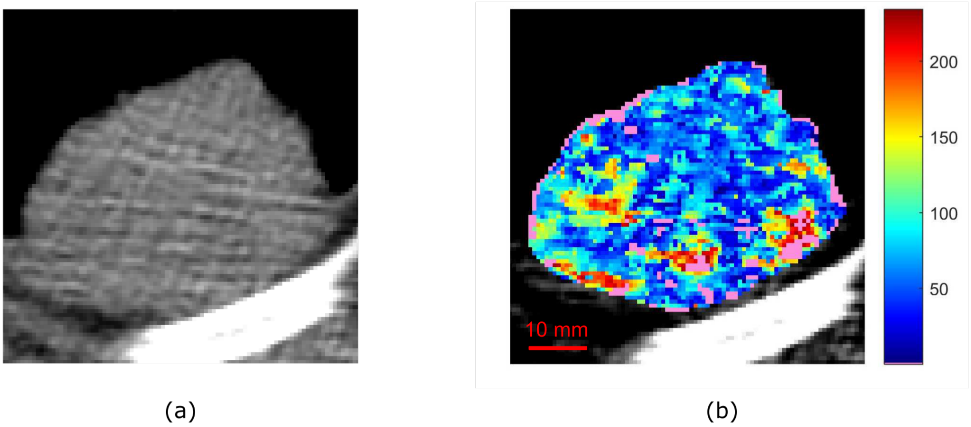

(a) (b)

Figure 10.2: Reference slice (a) and BF colorimetric map (b) of an adenocarcinoma examination (patient ID8). The pink colour points out unreliable BF values.

10.2.5 Computation of novel local-based features

After denoising, the functional heterogeneity arising from lesions' BF maps was assessed using an in-house software developed in Matlab© (MathWorks, Natick, MA, USA).

Entropy (E) (Eq. 4.6) was chosen to analyse the functional heterogeneity. This first-order statistics feature, commonly used to measure image irregularity or randomness [287], has recently shown a huge prognostic potential in patients with colorectal cancer [288], gliomas [289] and breast cancer [290].

The analysis was computed locally on denoised BF maps, within the same

ROI drawn for the perfusion map computation, by using a window W centred on the pixel that will be replaced with the resulting value. The choice of W, representing the anatomical scale considered to perform the local analysis, was first driven by the radiologists of our team, stating that in the clinical practice patches smaller than 5×5 mm are rarely considered and patches of about 1×1 cm are more representative for NSCLC functional heterogeneity. On the other hand, it is well known that CT texture features finer than 4 mm would represent mostly noise and should not be considered [247]. For this reason, entropy was computed locally for each pixel of the BF map, considering a square region with side of 15 pixels, corresponding to 10.3 mm, centred on the pixel itself. This procedure was iteratively repeated for each pixel within the ROI by using the sliding window W. At the end, a local entropy ($locE$) map was achieved and the mean value of $locE$ maps, μE, was considered as a feature of the functional heterogeneity.

As an example, Fig. 10.3 (a) shows the $locE$ map relative to the BF map in Fig. 10.2. As one can see, the $locE$ map highlights the presence of a greater heterogeneity in the lower region of the tumour, caused by the presence of the small areas with different tissue density characterising the BF map. The great advantage of performing a local analysis and, then, considering the mean values of the local feature values, is that it heavily reduces the effects of tumour size on statistical measurements. The clinical potentiality of the other first-order statistics

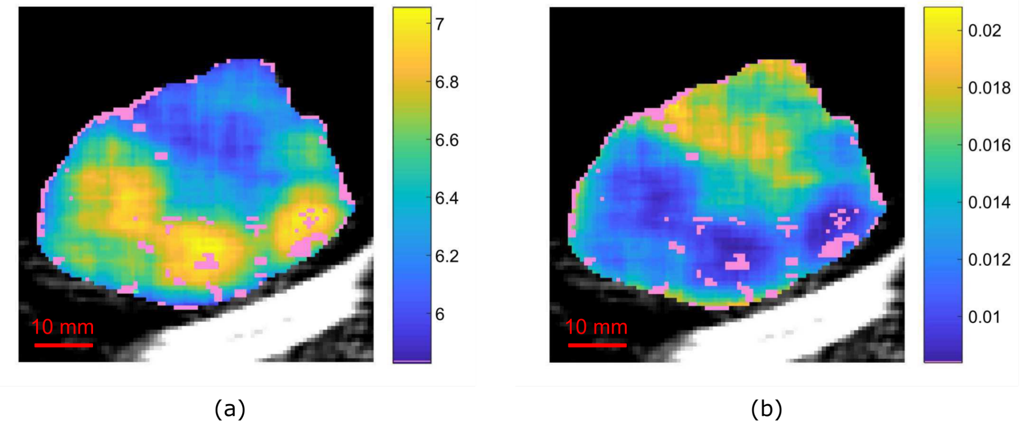

Figure 10.3: Patient ID8.$locE$ (a) highlights a high heterogeneity of the BF values in the lower region of the tumour; $locU$ map (b) highlights an increased uniformity of BF values in the upper region of the tumour.

features (mean, standard deviation, median, skewness, kurtosis, and uniformity) were also explored focusing on uniformity (U), the feature related to the image homogeneity, showing high values in the presence of small BF transitions in the map. U is defined as in Eq. (4.7). Also in this case, the mean value of the local uniformity ($locU$) maps, μU, was considered as a feature of the tumour functional heterogeneity. As an example, Fig. 10.3 (b) shows the $locU$ map relative to the BF map reported in Fig. 10.2. The high values of the $locU$ map in the upper region of the tumour point out the presence of a homogeneous hypodense area. It is worth noting that $locE$ and $locU$ values are inversely related but not linearly dependent.

10.2.6 Statistical Analysis

The principal purpose of this work was to determine whether local features directly extracted from denoised BF maps could work as a surrogate prognostic biomarker. To avoid overfitting, the features selected were analysed both separately as well as jointly in pairs. In order to assess their prognostic potential, the correlation between the feature-pair and the OS was investigated by using the k-means clustering algorithm. Mean survival for the entire cohort of patients ($\mu_{OS} = 10.5$) was used as threshold to separate patients with highest ($OS \geq \mu_{OS}$) and lowest ($OS < \mu_{OS}$) survival expectation. k-means ($k = 2$) was set up so as to automatically group patients in two different classes (or clusters), characterised by similar features behaviour. As similarity measure to resolve the membership of the feature-pairs, the Squared Euclidean distance was considered. In order to determine to what extent the feature means differ between clusters identified by the algorithm, a multivariate analysis of variance (MANOVA) was performed (p-value < 0.001). SE, SP, positive predictive value (PPV), negative predictive value (NPV) and accuracy (ACC) were calculated to quantify the discrimination ability of both features selected and staging, which is the variable used as reference for survival prediction. In particular, we defined as condition true a low survival expectation and as condition false a high survival expectation. The positive prediction is represented by the advanced stage condition while the negative prediction by the early stage one. Therefore, patients with advanced stage and low survival expectation belong to the TP, patients with early stage characterised by a high survival expectation are the TN, while the patients with advanced stage and a high survival expectation are the FP, and patients with early stage and low survival expectation are the FN.

Statistical analysis was performed using Matlab© (MathWorks, Natick, MA, USA).

10.3 Results

μE and μU are the features characterised by the highest discriminatory power in distinguishing patients with different survival expectations (SE=100%, SP=71%, PPV=86%, NPV=100%, ACC=90%). Results in terms of μE and μU for each patient are summarised and reported in arbitrary units (a.u.) in Table 10.2.

μE and μU are able to group patients with the lowest ($OS < \mu_{OS}$) and highest ($OS \geq \mu_{OS}$) survival expectation. Cluster 1 (highlighted in red in Fig. 10.4), characterised by higher μE and lower μU values, encloses all the patients with the worst prognosis ($OS < \mu_{OS}$), with the exception of ID4 and ID15 pointed out in Fig. 10.4.

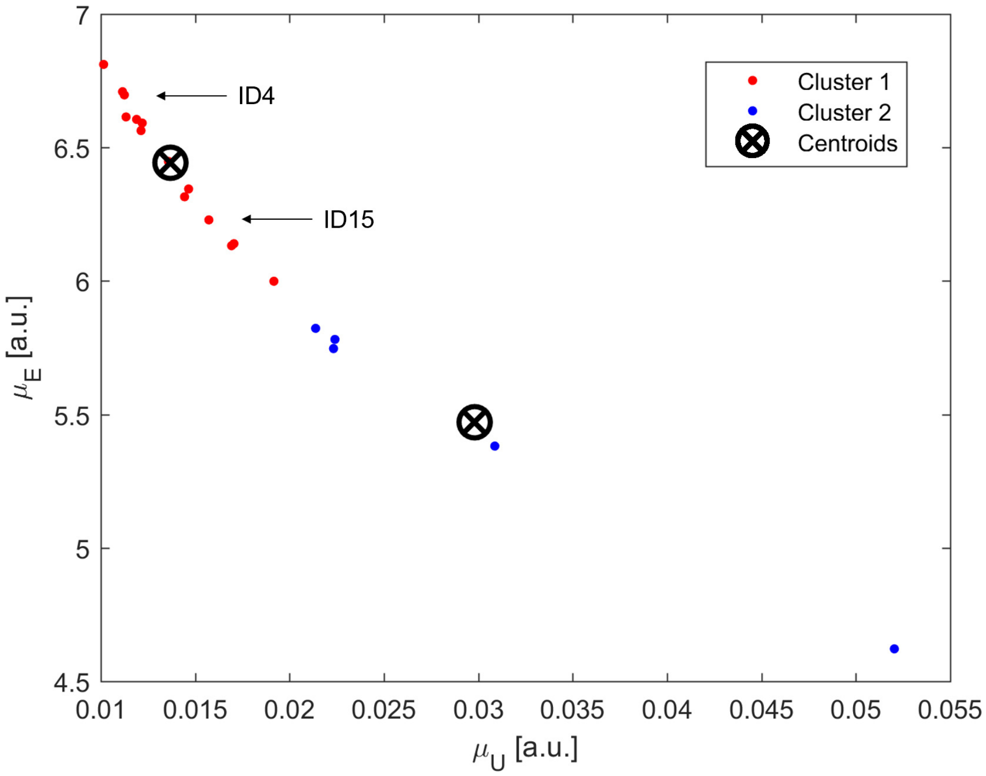

Figure 10.4: Scatter plot of μE and μU values related to all the examinations are reported in arbitrary units (a.u.). 14 examinations belong to Cluster 1 (in red), 5 to Cluster 2 (in blue).

Table 10.2: Summary of μE and μU relative to each examination (ID), reported in arbitrary units (a.u.).

Patient ID	μE **[a.u.]**	μU $(\cdot 10^{-2})$ **[a.u.]**
ID1	6.00	1.92
ID2	6.59	1.22
ID3	4.62	5.20
ID4	6.70	1.12
ID5	6.81	1.01
ID6	6.56	1.21
ID7	6.13	1.69
ID8	6.45	1.36
ID9	5.78	2.24
ID10	5.38	3.09
ID11	6.32	1.44
ID12	6.61	1.19
ID13	6.14	1.70
ID14	6.71	1.11
ID15	6.23	1.57
ID16	5.75	2.23
ID17	5.82	2.14
ID18	6.34	1.46
ID19	6.61	1.13

On the contrary, the samples belonging to Cluster 2 (highlighted in blue in Fig. 10.4) referred to all patients characterised by the best prognosis in this study ($OS \geq \mu_{OS}$). The outcome of MANOVA proves that μE and μU of the two clusters differ significantly, with a p-value $\sim 10^{-4}$.

Staging (SE=92%, SP=14%, PPV=65%, NPV=50%, ACC=63%) performed worse as survival predictor.

10.4 Discussion

As discussed in Chapter 4, in the last decade, quantifying the perceived features of the intra-tumoral heterogeneity has gained a great attention, leading to a renewed interest for statistical features and texture analysis as essential tools in the era of personalised medicine. First-order statistics features widely used in literature [291, 292] do not take into account the spatial information of the images but just the distribution of values. Therefore, when computing first-order features tissue heterogeneity information within an image is almost disregarded. The local features devised preserve the tissue heterogeneity information within the considered ROI. Results showed that these features have a valuable prognostic potential, proving a high correlation with OS when computed on BF maps, where unreliable BF values were previously automatically removed. In particular, a greater heterogeneity of BF values seems to be associated with a higher tumour aggressiveness, which heavily affects the OS parameter. Moreover, the results showed that these features, used in combination, had a better performance than the staging parameter, commonly used in clinical routine for prognosis. It is worth noting that this approach can be easily performed on CTp data, without the need for additional examinations and maximising the information that can be derived from these functional studies.

10.5 Conclusion

Although only essential parameters are routinely quantified in the clinical practice, this study shows that the two local-based statistical indexes considered to capture the hemodynamic heterogeneity could work as a prognostic image-based biomarker for NSCLC. This finding represents a promising approach for the clinical utilization of CTp.

Chapter 11

Kidneys ^{68}Ga-PSMA uptake reduction with mannitol infusion

Contents

11.1 Introduction **184**
11.2 Materials and methods **185**
    11.2.1 Patient Enrolment 185
    11.2.2 Image Acquisition 186
    11.2.3 Image Analysis 186
    11.2.4 Statistical Analysis 186
11.3 Results **187**
11.4 Discussion **187**
11.5 Conclusion **191**

This Chapter 11 reports the approach used to analyse the potential of mannitol to reduce the renal uptake of PSMA, first proposed in [155] and presented in Section 11.1. To this purpose, a SUV-based index has been devised, able to represent a high uptake activity in a more robust manner than the clinical accepted SUV parameters (Section 11.2). Indeed, these parameters widely used in clinical practice are characterised by a large degree of variability due to different sources of errors. In order to identify a more representative parameter for the entire kidneys volume distribution of values, the segmentation method developed and presented in the Section 6.1 was used to perform a 3D segmentation of the kidneys. The analysis of the index devised improved and enforced the results previously obtained through the use of $SUV_{\max}$ (Section 11.3), showing that the rapid administration of mannitol reduces the absorption of the renal tubules, thus limiting the dose of the kidneys (Section 11.4).

11.1 Introduction

Prostate cancer (PC) is the leading cancer in men and the third cause of cancer death worldwide [293]. The diagnostic capability of the conventional imaging modalities, as CT, MRI and bone scintigraphy (BS) for metastasis screening, has resulted limited in the detection of loco-regional and distant metastatic lesions in PC patients [294].

Recently, ^{68}Ga-PSMA-PET has emerged as a promising diagnostic tool for PC patients [295]. Indeed, the new radiotracer ^{68}Ga-PSMA has shown a great potential for theranostic approaches [296], with excellent diagnostic performance for primary and secondary staging thanks to the ability to detect the expression of PSMA, even at low level of serum prostate-specific antigen (PSA) [294].

Despite the benefits of using ^{68}Ga-PSMA-PET, several studies have shown that PSMA is physiologically expressed by the lacrimal and salivary glands, liver, spleen, intestine and, especially, by the kidneys, which receive the highest dose rate [293]. In the kidneys, PSMA is expressed in the apical epithelium of the proximal tubules [297]. Osmotic diuretics, such as mannitol, can facilitate water excretion, while inhibiting the reabsorption of sodium, chloride, and other solutes.

Clinicians of our team investigated the potential of mannitol to reduce kidneys uptake of ^{68}Ga-PSMA and, therefore, the kidneys' toxicity in [155]. By analysing the $SUV_{\max}$ of baseline and follow-up ^{68}Ga-PSMA-PET examinations, obtained with concomitant intravenous infusion of 10% mannitol, they were able to identify the best infusion protocol for mannitol to reduce PSMA kidneys' uptake.

However, as discussed in Section 3.3.3, $SUV_{\max}$ represents the activity of few or even just 1 pixel (i.e. that having the maximum intensity value). Therefore, it cannot be representative of the high activity concentration of the structure considered. As discussed in [158], $SUV_{\max}$ is strongly affected by noise and can behave in an unpredictable manner. For the same reason, also the use of other SUV parameters derived from isocontour based on $SUV_{\max}$, a choice appearing as the most "reliable" and objective one (40% of $SUV_{\max}$ is usually considered as significant [160]), could lead to an under- or an over-estimation of the SUV parameter (e.g., SUV_{mean}). Indeed, the drawback of this approach is that the percentage of SUV values considered for the SUV_{mean} measure, depending on the SUV_{max} is affected by the amount of noise of the images. Moreover, the SUV_{mean} parameter, being dependent on the ROIs definition, is less reproducible than the SUV_{max}, which is an observer-independent parameter [142, 161].

Anyway, despite the apparent benefits of using the SUV_{max}, which led to its popularity, as already mentioned the use of this parameter for comparing baseline and follow-up examinations is problematic, since changes in SUV_{max} may be often statistical fluctuations rather than real changes in radiotracer uptake. For this reason, baseline and follow-up examinations from ^{68}Ga-PSMA-PET/CT have been reanalysed considering the distribution of SUV values and seeking a more robust statistical index to better represent the tracer accumulation. To this purpose, the method developed in Section 6.1.1 has been applied to perform the 3D kidneys' segmentation and derive the distribution of SUV values.

11.2 Materials and methods

11.2.1 Patient Enrolment

9 patients affected by PC were considered for this study (age 71 ± 5 [64-78] years). These patients were treated with radical prostatectomy for PC of intermediate/high risk (pathological Gleason score 7-9) and referred for ^{68}Ga-PSMA-PET/CT imaging following biochemical recurrence. The mean PSA level at the time of the image acquisition was 2.25 ± 0.96 [0.89-3.21] ng/ml. The patients underwent baseline ^{68}Ga-PSMA-PET/CT (b-PET/CT) to localise the site of relapse. The patients with a negative b-PET/CT scan and PSA progression during follow-up examination underwent a second ^{68}Ga-PSMA-PET/CT scan with concomitant intravenous infusion of 10% mannitol (m-PET/CT). Two different protocols were used for the mannitol infusion:

- 500 ml of mannitol infused over 40 minutes, immediately after the injection of ^{68}Ga-PSMA (A-infusion).
- 250 ml mannitol infused over 15 minutes immediately before and again after ^{68}Ga-PSMA injection (B-infusion).

A-infusion was adopted for the first three patients, B-infusion for the following six patients. The mean injected activity of ^{68}Ga-PSMA was (173 ± 19) [52-198] MBq.

11.2.2 Image Acquisition

^{68}Ga-PSMA-PET/CT images were acquired with Biograph mCT Flow PET/CT system (Siemens Healthineers, Erlangen, Germany) 60 minutes after intravenous injection of ^{68}Ga-PSMA. All patients were asked to void before the scan was initiated. An unenhanced CT scan (120 kV, 80 mA/s) was acquired before the PET series. PET data were corrected for decay, random and scatter events. The attenuation correction was performed using the low-dose CT, component of the study [155].

11.2.3 Image Analysis

In the first study [155], ^{68}Ga-PSMA-PET/CT images were examined by two nuclear medicine specialists who independently calculated the $SUV_{\max}$. As previously discussed, $SUV_{\max}$ is characterised by a large degree of variability due to physical and biological sources of error. In order to find out a more robust SUV-based parameter to represent a high uptake, the entire distributions of kidneys SUV values have been derived. To this purpose, the 3D segmentation method devised and reported in Section 6.1.1 has been adopted.

Once derived the kidneys' SUV distributions related to each examination, the Tukey method [298] was used to identify possible outliers in SUV distributions. As expected, these distributions often present outliers and almost always these are the highest SUV values. This implies that in many cases $SUV_{\max}$ represents a distribution outlier. For this reason, to feature a high uptake level, a more robust statistical parameter than $SUV_{\max}$ has been introduced. This parameter, less affected by the presence of distribution outliers, is the median computed on the upper 10% of the SUV distribution ($SUV_{10\%}$), the last distribution decile representing a high activity.

11.2.4 Statistical Analysis

The differences in $SUV_{10\%}$ between b-PET/CT and m-PET/CT examinations were assessed for the statistical significance, independently of the type infusion, due to the reduced number of cases. To this purpose, the Kruskal-Wallis test, used to compare groups medians, was performed on the upper 10% of the SUV distributions for each kidney. The statistical significance is achieved with p-value < 0.001.

Statistical analysis was performed on Matlab© (MathWorks, Natick, MA, USA).

11.3 Results

Table 11.1 resumes SUV_{max} and $SUV_{10\%}$ values (presented as mean ± standard deviation) obtained with the two mannitol infusion protocols, derived from both kidneys and referred to b-PET/CT and m-PET/CT examinations. Figure 11.1 and Figure 11.2 show for right and left kidneys, respectively, the couples of SUV_{max} (top) and $SUV_{10\%}$ (bottom) values, computed on the whole dataset and referred to the baseline (b-PET/CT, in the blue colour) and the follow-up (m-PET/CT, in red) examinations. For reader's convenience, the A-patients samples were joined with a solid line, while B-patients samples with a dashed one.

As one can see, in the three A-infusion patients (ID7, ID8 and ID9), SUV_{max} (top) globally increased during the m-PET/CT examinations for both right and left kidneys. Actually, ID7 showed just a slightly increased SUV_{max} value for the right kidney, remaining unchanged for the left one. As regards the six B-infusion patients (from ID1 to ID6), the SUV_{max} follow-up values were lower than the baseline ones in both kidneys, with the exception of ID5 for both right and left kidneys. These results were only partly confirmed by $SUV_{10\%}$. Indeed, $SUV_{10\%}$ showed that ID7, the A-infusion patient having similar values of SUV_{max}, was characterised by a lower uptake of the follow-up examination. Instead, as regards the B-infusion patients, follow-up $SUV_{10\%}$ values were always lower than the corresponding baseline ones. This occurred also for ID5, which instead showed similar values of SUV_{max} for both kidneys. The outcomes of the Kruskal-Wallis test computed for each kidney prove that differences between baseline and follow-up $SUV_{10\%}$ values were significant (p-value < 0.001).

11.4 Discussion

Dosimetry studies have shown that organs as kidneys, lacrimal and salivary glands exhibit tracer accumulation, which may limit the use of radiolabelled PSMA ligands [299]. The study reported in [155] is the first to investigate the potential protective effect of mannitol to reduce the renal uptake of PSMA and, therefore, the dose administered to the kidneys. The results of this study have shown that PSMA kidneys' uptake can be safely reduced with concomitant mannitol infusion

Table 11.1: Summary of SUV_{max} and $SUV_{10\%}$ values from b-PET/CT and m-PET/CT in both kidneys (right and left) of patients undergoing different administration schemes (A-infusion and B-infusion).

		Right kidney		**Left kidney**	
SUV index [a.u.]	**Administration protocol**	**b-PET/CT**	**m-PET/CT**	**b-PET/CT**	**m-PET/CT**
SUV_{max}	A-infusion	42.9 ± 4.6	48.7 ± 8.3	44.6 ± 7.8	48.1 ± 10.3
	B-infusion	61.0 ± 10.8	46.2 ± 10.5	59.0 ± 15.8	45.8 ± 12.0
$SUV_{10\%}$	A-infusion	31.9 ± 1.7	36.1 ± 11.1	31.8 ± 3.0	36.3 ± 12.2
	B-infusion	41.2 ± 8.1	30.9 ± 9.7	40.3 ± 6.1	29.2 ± 9.4

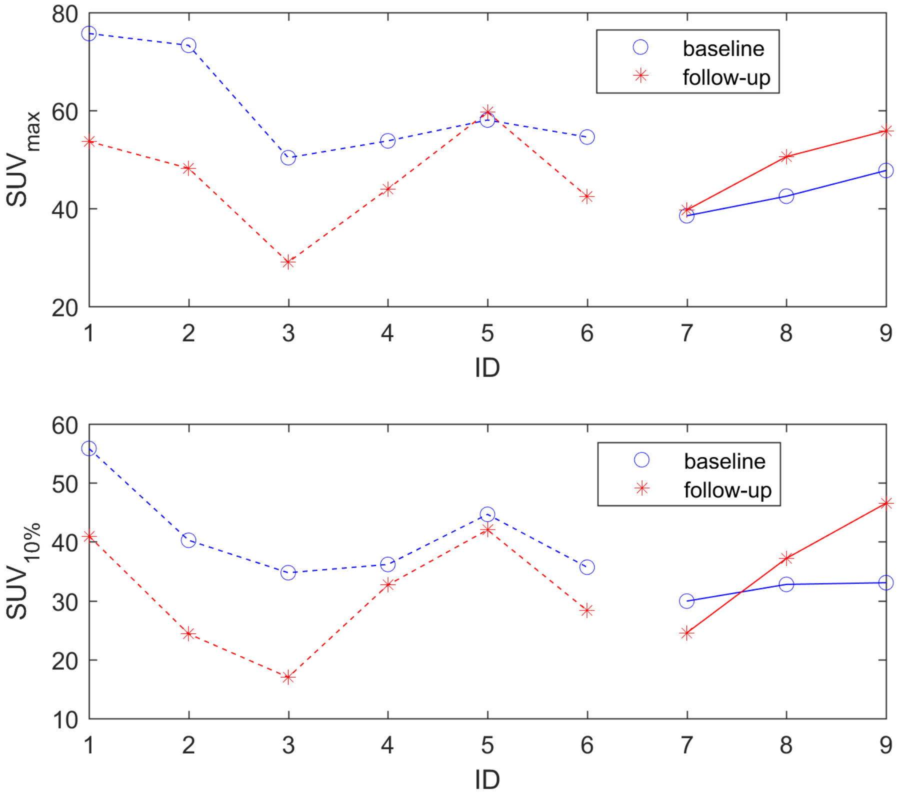

Figure 11.1: Right kidneys. SUV_{max} (top) and $SUV_{10\%}$ (bottom) values referring to the baseline (blue) and to the corresponding follow-up examination (red). A-patients samples are joined with a solid line (ID7-ID9), while B-patients samples with a dashed one (ID1-ID6).

and that the B-infusion scheme is the most effective one. These outcomes were obtained through the use of the SUV_{max} parameter.

As previously discussed, SUV_{max} is a parameter commonly used in clinical practice having several attractive features. It can simply reflect the most metabolically active part or the part with the highest expression, which may be the most significant clinical one [300]. SUV_{max} can be easily measured and is slightly affected by partial-volume effects. However, it is dramatically susceptible for unpredictable variations due to noise, reflecting the activity of only one pixel in a potentially heterogeneous mass.

$SUV_{10\%}$ introduced in this work overcomes the vulnerability of $SUV_{\max}$, which represents a single-pixel measurement, and results much less affected by noise, since it considers a statistically significant part of the values distribution by tak-

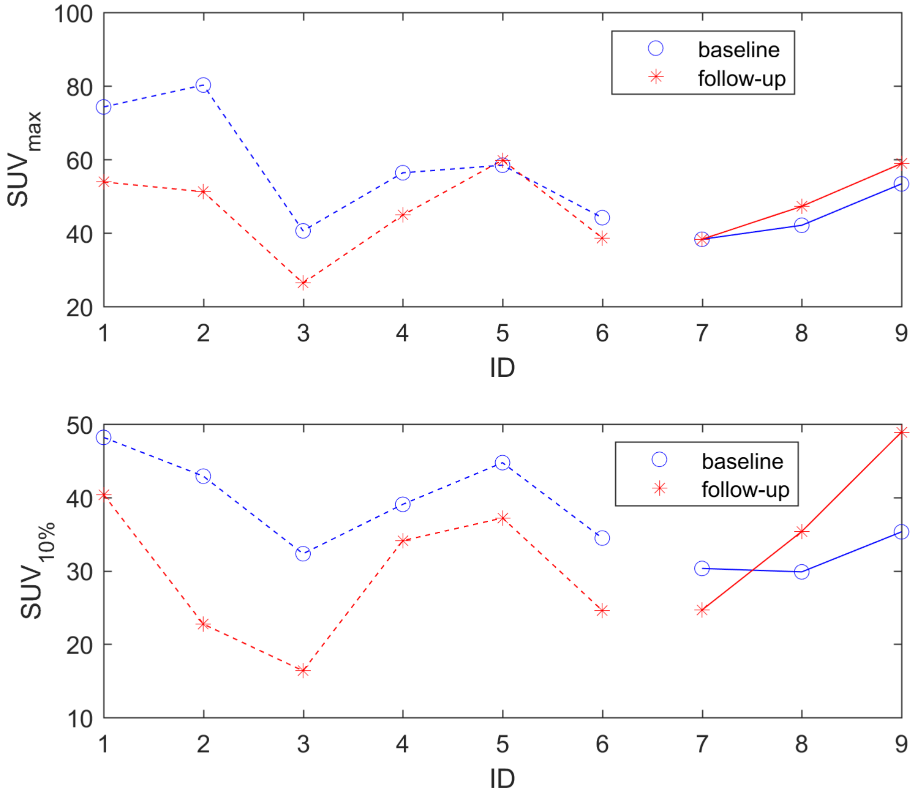

Figure 11.2: Left kidneys. SUV_{max} (top) and $SUV_{10\%}$ (bottom) values referring to the baseline (blue) and to the corresponding follow-up examination (red). A-patients samples are joined with a solid line (ID7-ID9), while B-patients samples with a dashed one (ID1-ID6).

ing the median value. It also overcomes the limits of SUV_{mean}, usually conditioned by partial volume effect and segmentation, commonly performed through isocontour based on the $SUV_{\max}$. Even more important, $SUV_{10\%}$ preserves a clinical meaningful value by representing the highest PET activity, in a more robust way. Results obtained with $SUV_{10\%}$ improve and statistically enforce those obtained through $SUV_{\max}$. $SUV_{10\%}$ findings confirm the B-infusion protocol as the best one to safely reduce PSMA renal uptake. For all the patients included in this study, $SUV_{10\%}$ values referred to baseline and follow-up examinations resulted significantly different, even for ID5 and ID7, the cases showing similar baseline and follow-up $SUV_{\max}$ values. In this context, it is worth noting that $SUV_{10\%}$ values obtained for ID5, one of the six B-infusion patients, strengthen the effectiveness of the B-infusion protocol as the best administration scheme to reduce renal uptake. Indeed, the values obtained through $SUV_{10\%}$ coherently showed that the short mannitol infusion performed through the B-infusion scheme (ID1 - ID6) leads to a reduction of kidneys uptake in the follow-up examinations.

This study highlights the advantages of using $SUV_{10\%}$ compared with $SUV_{\max}$. $SUV_{10\%}$ proved a greater ability in values separability and, being derived as the median value of a distribution, it resulted less affected by the presence of outliers. Otherwise, almost always $SUV_{\max}$ represents a distribution outlier and, for this reason, it cannot be statistically representative for the mass considered.

Nevertheless, optimal cut-off values based on $SUV_{\max}$ are often proposed in literature as surrogate predictive biomarkers [301, 302, 303], due to the failure of standardised criteria for the evaluation of tumour response to therapy. We believe that previous studies could benefit from the methodological approach presented in this research, which paves the way for more reliable evaluation of clinical outcome and response assessment, playing a decisive role in therapeutic decision-making.

11.5 Conclusion

In this Chapter, a simple SUV-based statistical index has been proposed to feature a high uptake activity in a more robust manner than $SUV_{\max}$, widely adopted in clinical practice. In the case study considered, $SUV_{10\%}$ was able to enforce the preliminary results obtained with $SUV_{\max}$, confirming that mannitol, an inexpensive and well-tolerated mean, could play an important role in reducing the dose received by kidneys during a PSMA-PET/CT.

Chapter 12

GOJ cancer: texture analysis of ^{18}F-FDG-PET/MRI

Contents

12.1 Introduction **194**

12.2 Materials and methods **194**

  12.2.1 Patient Enrolment 194

  12.2.2 Image Acquisition 195

  12.2.3 Image Analysis 195

  12.2.4 Statistical Analysis 196

12.3 Results **197**

12.4 Discussion **199**

12.5 Conclusion **200**

This Chapter presents a multi-modal analysis of the tumour heterogeneity in patients affected by GOJ cancer. Despite improvements in OS, a better patient stratification remains a key issue for a better management of GOJ patients (Section 12.1). The statistical features reported in Section 4.3 were derived from the FDG-PET/MRI image series Section 12.2. Then, an analysis was performed in order to establish their ability to predict for contemporaneous metastases. Section 12.3 reports the results of the best pair of second-order statistical features computed on SUV and ADC maps. These combined texture features proved a better discrimination ability compared to the parameters currently used in clinical routine (Section 12.4). As a result, this analysis may complement current staging practice for GOJ cancer (Section 12.5).

12.1 Introduction

GOJ cancers are leading causes of cancer deaths worldwide [304]. Surgery combined with neoadjuvant chemotherapy or chemoradiotherapy offers the best chance of cure [305, 306, 307]. Despite improvements in survival expectation, OS remains poor and a better patient stratification remains a key challenge for GOJ patients, since most of the times the quality of life remains poor after surgery, taking up to 3 years to return to pre-therapy levels [308].

^{18}F-FDG PET/MRI has shown promising results, providing a slightly superior TNM staging for GOJ cancer [309]. ^{18}F-FDG-PET/MRI also gives a chance to improve GOJ phenotyping by combining molecular, functional and anatomical characteristics, directly providing radiomic approaches [310].

As discussed in Section 2.1, an extensive research on tumour heterogeneity have been performed in the last decade, since its presence hints at tumour cells having different properties and likely expressing different markers. Recent studies reported that the presence of tumour heterogeneity introduces a great variability in therapy response [29, 311].

In this Chapter, the statistical texture analysis method developed and reported in Section 4.3 were applied to evaluate the intra-tumoural heterogeneity emerging from the PET, T1, T2, DWI series as well as SUV and ADC maps. The working hypothesis was that tumours with metastatic potential would be associated with greater heterogeneity. Thus, the aim of this study was to identify whether texture features derived from ^{18}F-FDG-PET/MRI are associated with distant metastases at staging in patients with GOJ cancer. The discrimination ability of the features was analysed in comparison with parameters commonly used in clinical practice as the $\mathrm{SUV}_{\mathrm{max}}$, $\mathrm{ADC}_{\mathrm{mean}}$ and the tumour diameter (defined as the maximum axis length of the tumour volume).

12.2 Materials and methods

12.2.1 Patient Enrolment

Following IRB approval and informed consent, 24 prospective patients with histologically proven GOJ cancer were recruited from 2015 to 2018. None of the patients had a history of previous malignancy. All patients had undergone standard staging investigations, which included EUS, CE-CT of the thorax and abdomen and ^{18}F-FDG-PET/CT. Final staging was documented in a multidisciplinary team (tumour review board) meeting.

12.2.2 Image Acquisition

Patients were injected with 326 ± 28 MBq of ^{18}F-FDG. PET/MRI examinations were performed on an integrated PET/MRI system (Siemens Biograph mMR, Erlangen, Germany) immediately following a clinical PET/CT acquisition. The time between injection of ^{18}F-FDG and PET/MRI examination was 156 ± 23 minutes. PET/MRI was acquired from the skull base to mid-thigh. The sequences acquired included: T1-weighted Dixon VIBE (in-phase, out of phase, fat, water images), T2-weighted Half-Fourier-Acquired Single-shot Turbo spin Echo (HASTE) and free breathing diffusion-weighted sequences (DWI, b values of 50 and $900 s/mm^2$).

Tumour stage was determined in all patients according to the TNM classification of malignant tumours (seventh edition) to determine metastatic versus non-metastatic disease. TNM stage was defined by all standard staging investigations (not including PET/MRI) and documented in a multidisciplinary team meeting.

Four patients were excluded for technical reasons (incomplete scan, bulk motion, DIXON fat water swap, poor quality diffusion imaging) precluding texture analysis, leaving 20 patients (18 male, 2 female, median age 67 years, range: 52-86 years). Their tumour characteristics are summarised in Table 12.1. 10 patients had evidence of metastases including liver (3), lung (2), bone (1), and distant lymph nodes, e.g. retroperitoneal (7).

12.2.3 Image Analysis

For each sequence investigated, segmentation of the whole tumor volume was performed manually by a dual trained nuclear medicine physician/radiologist (with > 5 years experience) using ImageJ [213]. Feature generation and selection were performed using an in-house software based on Matlab© (MathWorks, Natick, MA, USA). The first-order and second-order statistical features, reported in Section 4.3, were computed for PET and SUV maps as well as MRI series as T1, T2, DWI and ADC maps from the whole tumour volume (Figure 12.1). The maximum tumour diameter was also measured. Given the sample size, no more than two features were analysed jointly so as to minimise overfitting and avoid spurious results. Feature selection started performing a k-means ($k = 2$) clustering algorithm. Squared Euclidean distance was considered as similarity measure

Table 12.1: Summary of tumour characteristics for the 20 patients, including tumour type and TNM staging.

Tumour Characteristics		**Number of patients**
Tumour Type	Adenocarcinoma	17
	Squamous carcinoma	3
T Stage	T1/2	0
	T3/4	20
N Stage	Node negative	2
	Node positive	18
M Stage	Non metastatic	10
	Metastatic	10

to determine the membership of the feature-pairs. Then, as a second step, the correlation of feature-pairs with the presence of metastases was automatically analysed. Linear discriminant analysis (LDA) was used to determine the linear discrimination boundary.

12.2.4 Statistical Analysis

MANOVA was performed to assess the statistical separability of the groups identified by feature-pairs (p-value < 0.001). SE, SP, PPV, NPV and ACC were calculated to quantify the discrimination ability of features in comparison with SUV_{max}, ADC_{mean} and tumour size. In order to assess the impact that inter-observer variability might have on the feature reproducibility, the segmentation of tumour volumes was perturbed by performing automatic dilation and erosion altering the lesion boundary by one pixel. Intraclass correlation coefficient (ICC) was computed by considering the feature values derived from dilated and eroded volumes.

Statistical analysis was performed on Matlab© (MathWorks, Natick, MA, USA).

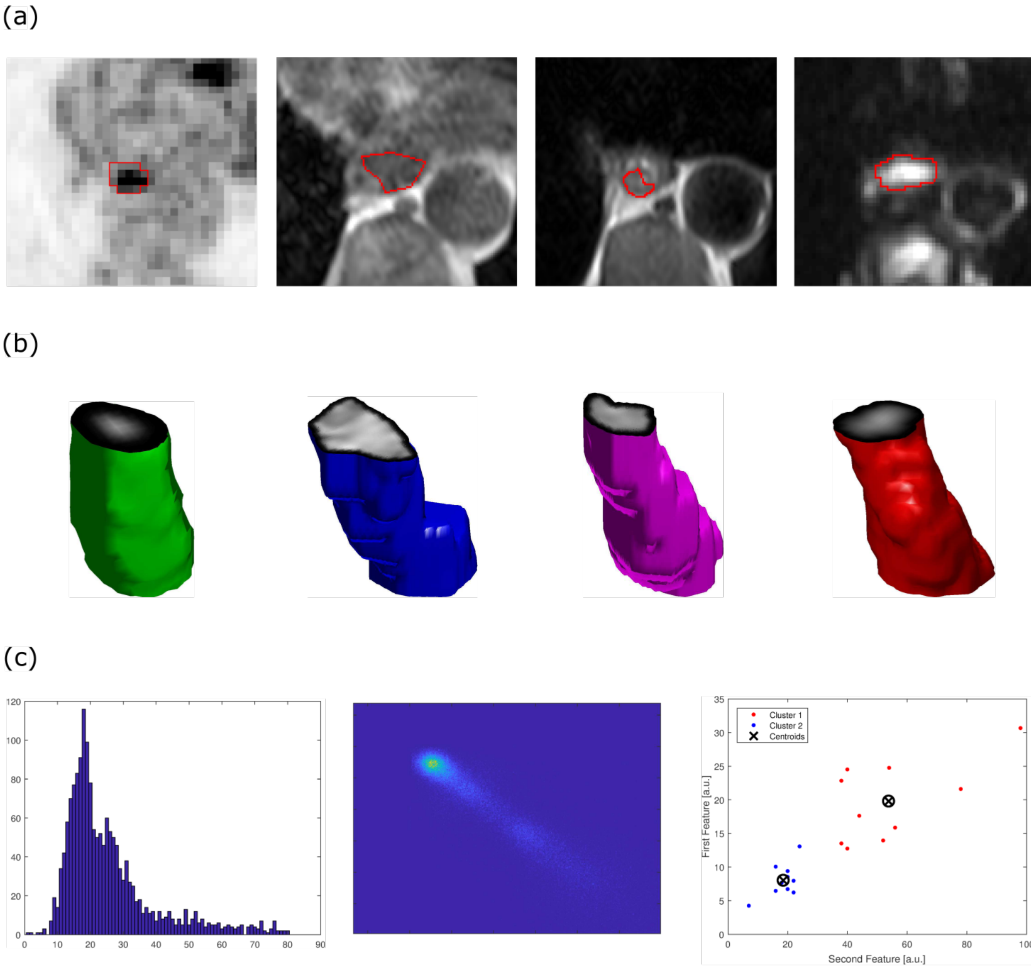
(a)
(b)
(c)
0
20
40
60
80
100
120
0
10
20
30
40
50
60
70
80
90
Cluster 1
Cluster 2
Centroids
First Feature [a.u.]
Second Feature [a.u.]
0
5
10
15
20
25
30
35
0
20
40
60
80
100

Figure 12.1: Schema showing tumour segmentation on ^{18}F-FDG PET, T1-weighted, T2-weighted and diffusion weighted axial image of a GOJ cancer (a), respective tumour volumes (b) and subsequent feature generation, extraction and selection (c).

12.3 Results

GLCM joint entropy derived from both SUV and ADC maps were the best feature-pair for discriminating patients with and without metastases (SE = 80%, SP = 80%, PPV = 80%, NPV = 80%, ACC = 80%). In particular, Cluster 1 (Fig. 12.2, highlighted in red), which combined lower GLCM entropy derived from SUV and higher GLCM entropy from ADC, reflecting higher parameter

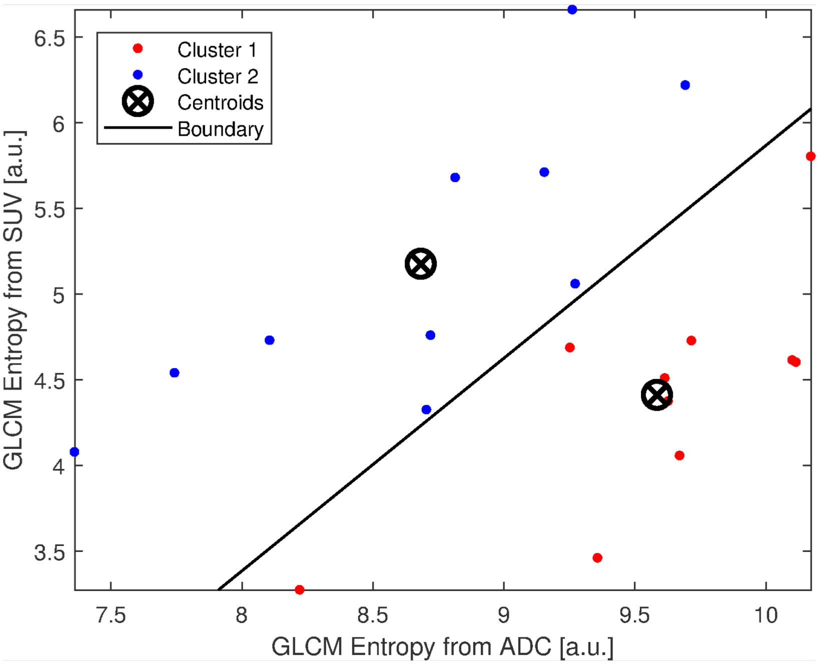

Figure 12.2: Distribution of GLCM entropy from ADC and SUV. Cluster 1 (highlighted in red) represents patients with metastatic disease, while Cluster 2 (highlighted in blue) those without metastatic disease.

spatial homogeneity and heterogeneity, respectively, is associated with metastatic disease. Instead, Cluster 2 (highlighted in blue in Fig. 12.2), which is in some way characterised by the combined presence of homogeneity (or heterogeneity) of ADC and SUV maps, is associated with no metastatic disease.

LDA proved the two groups identified by the clustering were linearly separated. The equation for the optimal separation of patients with and without metastatic disease is

$$K + L_1 e_{ADC} + L_2 e_{SUV} = 0 \tag{12.1}$$

where $K = 40.90$, $L1 = -7.75$, $L2 = 6.25$, e_{ADC} and e_{SUV} are the second-order entropy from ADC and SUV, respectively.
Patients with metastatic disease belonged to the half-plane given by the following inequality:

$$K + L_1 e_{ADC} + L_2 e_{SUV} < 0 \tag{12.2}$$

Instead, patients without metastatic disease belonged to the half-plane formally expressed by the following inequality:

$$K + L_1 e_{ADC} + L_2 e_{SUV} > 0 \tag{12.3}$$

MANOVA confirmed that the means of these features for the two groups of patients differed significantly, with a p-value < 0.001. In comparison, $\mathrm{SUV}_{\mathrm{max}}$ (SE = 30%, SP = 80%, PPV = 60%, NPV = 53%, ACC = 55%), $\mathrm{ADC}_{\mathrm{mean}}$ (SE = 20%, SP = 70%, PPV = 40%, NPV = 47%, ACC = 45%) and maximum tumour diameter alone (SE = 10%, SP = 90%, PPV = 50%, NPV = 50%, ACC = 50%) had poorer sensitivity and accuracy.

As far as the variability analysis is concerned, computing automatic dilation and erosion altered the PET volumes by $34.8 \pm 8.1\%$ and $30.6 \pm 6.2\%$, respectively. Feature reproducibility errors for dilation and erosion were only $3.4 \pm 3.0\%$ and $3.1 \pm 2.3\%$, respectively. Analogously, while ADC volume variations for dilation and erosion were $14.6 \pm 2.8\%$ and $13.9 \pm 2.5\%$, feature reproducibility errors were $2.5 \pm 1.1\%$ and $3.1 \pm 1.8\%$, respectively. ICC for ADC and SUV GLCM entropy derived from dilated volumes were 0.96 and 0.98, respectively, while derived from eroded volumes were 0.94 and 0.98, this proving the features selected to be highly reproducible.

12.4 Discussion

Better patient stratification remains a key challenge for the optimal management of GOJ patients. The preliminary results of this study show that combined ^{18}F-FDG PET and MRI texture features are associated with contemporaneous metastatic disease in GOJ cancer. In particular, the combination of lower joint entropy derived from SUV maps and higher joint entropy from ADC, which represents lower and higher local texture heterogeneity, respectively had SE and SP of 80% for the presence of metastatic disease. Sensitivity was higher than $\mathrm{SUV}_{\mathrm{max}}$, $\mathrm{ADC}_{\mathrm{mean}}$ or maximum tumour diameter alone where SE was 30%, 20% and 10%, respectively. Usually most cancers, including GOJ cancers, show an increased accumulation of ^{18}F-FDG [15, 16, 312], this permitting cancer detection. As discussed in Chapter 11, $\mathrm{SUV}_{\mathrm{max}}$ represents the highest value of the normalised radioactivity concentration through the measurement of a single voxel. To date ^{18}F-FDG PET/CT prognostic studies using SUV_{max} alone have reported mixed findings [313, 314, 315, 316]. However, the meta-analysis reported in [317] has not attributed a prognostic value to the SUV_{max}. These mixed results have pushed for radiomic studies with ^{18}F-FDG PET/CT [318, 180, 7]. Recent studies reported an improvement to the prediction of response through the use of second-order and higher-order statistical features derived from PET images [319, 320]. As discussed in Section 3.2, contrarily to higher FDG uptake, diffusion of water molecules is typically reduced in most cancers, again permitting cancers detection and therapy response monitoring [124, 50]. ADC represents the apparent diffusion of water molecules and ADC_{mean}, having a good repeatability, is the most commonly used parameter [321]. This parameter is influenced by several factors, including microscopic perfusion, bulk motion, acquisition sequence parameters and tissue orientation [50]. Currently, few diffusion MRI studies have been performed for GOJ cancer with variable outcomes [322, 323]. Some studies have evaluated the prognostic potential of tumour size, for instance, suggesting that it should be considered as prognostic factor in oesophageal squamous cell cancer [324]. In this study, maximum tumour size had a low sensitivity for metastatic disease.

This is the first study to assess the prognostic value of the combination of SUV and ADC information. SUV and ADC may highlight different aspects of the tumour phenotype. The majority (85%) of the tumours were adenocarcinomas, which demonstrate a tubular, tubulopapillary or papillary growth pattern. The metastatic signature found in this study and involving a greater local homogeneity of SUV combined with a higher ADC heterogeneity may be promising. The greater homogeneity of SUV uptake on a local level may relate to higher cellular versus stromal volume, i.e. more tightly packed predominantly FDG-avid tumour cells produce a more homogeneous tracer distribution. Greater local ADC heterogeneity likely reflects the varying glandular content, i.e. greater heterogeneity represents a more aggressive histotype.

12.5 Conclusion

In summary, a combined radiomic approach has the potential to improve risk stratification of GOJ patients, with strong implications for long-term outcome. Quantitative combined ^{18}F-FDG PET and MRI texture features of the primary tumour from simultaneous PET/MRI scans are associated with a metastatic phenotype and may, in the future, help identifying patients who will benefit from alternative therapeutic strategies or closer surveillance.

Chapter 13

Conclusions

Cancer is among the most common cause of mortality worldwide. Despite progress has been made in cancer care through the introduction of the target therapies, there are several obstacles preventing moving forward. Among the main issues:

- the exiguity of techniques to properly characterise the tumour tissue and early assess novel target therapy efficacy;
- the lack of methods involving the evaluation of the intra-tumoural heterogeneity, which reflects the presence of different cells population and may introduce a significant variability in tumours' response to the available therapies.

This Thesis aims at facing these issues and filling in some gaps, so as to lead to improvements in tumour diagnosis and prognosis, by introducing more quantitative approaches. The most relevant achievements can be summarised as follows:

- methods and indexes devised to detect unreliable perfusion values from DCE-CT examinations;
- local-based features able to gather and exploit the information owned by the heterogeneity patterns;
- methods and indexes able to exploit the evolution over time of the tumour spatial heterogeneity emerging from DCE-CT studies;
- SUV-based index to represent a high uptake activity;
- method to perform a 3D segmentation of the structures in PET images;

- method to perform a multi-modal 3D registration;
- algorithm to detect sub-regions in tumour volume and compare the multi-modal information.

The method conceived and realised to assess the reliability of the perfusion values provides the reader with an overview of the perfusion maps reliability. Regions characterised by lower lCV values suggest a greater local spatial coherence of the maps, while the higher values highlight an inconsistent variability, which could mislead clinical consideration.

Reliability analysis of the perfusion values led to significant improvement on the accuracy of results and, consequently, of the clinical findings, accordingly. The local-based approach has allowed to overcome the limitations of the first-order features, which almost disregard the tissue heterogeneity information. This approach proved to be able to preserve the intra-tumoural heterogeneity. Moreover, the features derived from the local maps take benefit from both the local analyses "saving" the heterogeneity information, and the global ones that summarise the outcome reducing the noise effects. Moreover, the spatio-temporal indexes developed proved to effectively describe and quantify the heterogeneity features visually detected by radiologists on single DCE-CT reference slices.

To face the issue of variability present in PET data, a simple statistical index was introduced to better represent a high uptake activity. $SUV_{10\%}$ has proved a greater robustness compared to the $\mathrm{SUV}_{\max}$ commonly used. Indeed, $\mathrm{SUV}_{\max}$ representing just one pixel of the tumour is strongly affected by noise. The index devised is derived from the SUV values distribution of the volume of interest, segmented through the method set up starting from PET/CT series.

During the PhD period abroad at the King's College London, I have also had the opportunity to work at a rare dataset of patients affected by GOJ cancer, underwent both FDG-PET/CT and FDG-PET/MRI with a single injection protocol. The registration method developed has pointed out differences in tumour volumes, allowing a direct comparison of the PET volumes derived from the PET/CT and PET/MRI series. The algorithm developed to detect sub-regions in tumour volumes may bring several advantages. Among these, a direct comparison of tumour regions coming from different registered modalities, as well as the automatically exclusion of air and fluids. Moreover, it has also shown its utility in automatic segmentation procedures.

It is worth noting that these methodological approaches also yield to preliminary clinical achievements. The most relevant ones can be summed up as follows:

- the lCV-based index has proved to be able to detect the most reliable perfusion maps, while the index commonly used often fails and, even worst, sometimes erroneously confers a higher quality to worse maps. This could lead to unfair comparisons of within-patient perfusion maps (e.g., follow-up examinations) or to misleading clinical considerations from low quality perfusion maps;

- the features devised to exploit the information owned by the hemodynamic heterogeneity patterns at local level showed a prognostic potential as surrogate biomarker for lung cancers. These features proved a strong correlation with OS, while tumour staging performed worse as survival predictor;

- the spatio-temporal indexes devised perfectly identified and reproduced bronchi, blood vessels and haemorrhages manually outlined by radiologists. Only hypodense regions have a weak correspondence and, sometimes, the features detected more of them. Radiologists, who initially did not identify these regions confirmed their presence further on, when the features were submitted to their attention in the matching stage. Therefore, the methodology developed may be employed in decision making processes relying on the quantification, or the detection, of different types of heterogeneities. These analyses may be useful to objectively examine changes of heterogeneity levels as response to therapies;

- the $SUV_{10\%}$ parameter devised was able to improve the results obtained with $SUV_{\max}$, identifying the best infusion protocol of mannitol to reduce PSMA renal uptake and, consequently, the dose administered to the kidneys. The results obtained with this approach were statistically more significant than those obtained through the use of $SUV_{\max}$;

- the multi-modal registration of the tumour volumes has preliminary highlighted that the choice of the modality used could impact on the dose coverage in the radiotherapy planning;

- the multi-modal analysis of the tumour heterogeneity in GOJ cancer has shown that the second-order texture features derived from FDG-PET/MRI can discriminate better than the parameters currently used in the clinical routine for predicting contemporaneous metastases.

For the sake of completeness, it is worth remarking that all the methods and the algorithms, devised and developed for the heterogeneity assessment, can be applied independently from the imaging modality used for the image acquisition (except for the spatio-temporal indexes, which can be applied on DCE-images only).

The encouraging outcomes achieved in this Thesis should push for further studies, involving larger patients' cohorts as well as repeatability and reproducibility analyses. Indeed, a large amount of high-quality data is a mandatory prerequisite to realize powerful predictive classifiers [325]. This requirement could lead to many obstacles, due to the need of sharing data from different institutions, which leads to technical and legal issues. It is worth noting that the need for a reliable quantitative imaging has been also recently recognized by the National Cancer Institute [326]. This has led to the formation of the Quantitative Imaging Network that promotes biomedical research, development, standardization and clinical validation of quantitative imaging methods with the aim to improve the clinical decision making, through the collaboration of oncologists, radiologists, medical physicists, and computer scientists [327].

The potential of the promising features devised in this Thesis, able to detect valuable *in vivo* characteristics, should be prospectively evaluated. The results obtained also encourage the deepening of the unknown relationship between imaging findings and biologic features. One of the major challenge in this field remains the combination of the features selected with other patients' characteristics.This would permit to comprehensively understand the specific cancer biology of individual patient and infer phenotypic signatures containing predictive or prognostic values. For instance, the detection of low-perfused regions associated with a high cell density could reveal the presence of an aggressive cell population likely resistant to treatments.

Unlike biopsies, quantitative imaging could permit a longitudinal monitoring of the intra-tumour heterogeneity and, consequently, of the "specific" habitats and their changing over time, since clinical examinations can be easily repeated during the therapy [325]. In this perspective, another area of the quantitative imaging has been widely explored. This research area regards the texture analysis of apparently metastasis-free areas of the liver with surprising results in the indirect detection of a metastatic status, even without morphological changes [328].

In conclusion, the analysis of the tumour heterogeneity should be further explored to achieve a personalization of medicine. Indeed, having the potential to identify the patients who would benefit most from consideration of alternative therapies and treatment intensification, it could lead to a customization of the therapy.

List of figures

2.1 Normal (a) and tumoral (abnormal) micro-circulation (b). 34

3.1 Images viewed at different window settings to enhance (a) bone (window 1500, level 300), (b) soft tissue (window 350, level 50) and (c) lung tissue (window 1500, level -400). 44

3.2 Single-compartment model outlining the perfusion tissue. 45

3.3 Representation of the aortic TCC signal, $C_A(t)$ (red), and the tissue TCC signal, $C_T(t)$ (blue). The red star points out the aortic peak, while the blue circle the steepest slope of the tissue curve. The grey vertical line indicates the time at which the aortic input is at its maximum, while the magenta line highlights tissue maximum slope. 47

3.4 Representation of the sigmoidal model used for the fitting procedure, relative to the temporal sequence of a reference slice [90]. . . 48

3.5 CT image (a) and corresponding BF map (b) of a lung tumour (squamous-cell carcinoma). 48

3.6 Under normal conditions, hydrogen protons spin in the body are randomly arranged (a). In the presence of a strong magnetic field B_0, as occurs in an MRI scanner, protons align themselves parallel to the MRI magnetic field (b). 52

3.7 Gastro-oesophageal junction cancer outlined in red in T1 (a) and T2 (b) images. 53

3.8 Diffusion of water molecules, represented by light blue circle moving along a direction, drawn as a black straight line. In the presence of low cellularity and disrupted cell membranes, water is freer to diffuse in the extra-cellular space, than in a more cellular environment. Disruptive cell membranes also permit the diffusion between the intra- and extra-cellular spaces (a). In the presence of a high cellularity and intact cell membranes water diffusion is restricted by the reduced extra-cellular space and by the membranes, which constitute a barrier for the diffusion (b). 55

3.9 Gastro-oesophageal junction cancer outlined in red in the DWI image and the corresponding ADC map. 56

3.10 Positron and electron annihilation resulting in the emission of two anti-parallel γ rays. 59

3.11 PET image acquired with PET/CT (a) and PET/MRI system (c) and corresponding SUV fusion with CT (b) and T1-weighted image (d). These images point out a gastro-oesophageal junction cancer, characterised by an increased abnormal FDG uptake outlined in red in (a) and (c). 62

4.1 Small image (a) and relative co-occurrence matrix (b) for $\delta = 1$ and $\theta = 0°$. The joint probability is obtained dividing the matrix in (b) for the total number of possible pixel pairs. 75

4.2 CT image (a) and relative co-occurrence matrix (b) for $\delta = 5$ and $\theta = 0°$. 76

4.3 Small image (a) and relative GLRLM matrix for the horizontal (b) and the vertical direction (c). 79

5.1 Representation of the spatial filtering showing a 3×3 mask and the region of the image considered for the filtering. 85

5.2 From left to right, BF map (a) and sliding window of 9×9 pixel (b) showing the perfusion values considered for the computation of the local coefficient of variation (lCV), stored in the corresponding pixel of the lCV map (c). 86

5.3 CT image of a lung adenocarcinoma outlined in red (a), and relative local entropy (b) and local uniformity maps (c). 87

5.4 Ground truth (left), colorimetric maps of SS (middle) and MS (right). 88

5.5 MS-SS scatter plot (left) and its respective clusters mask (right). Data have been partitioned into four clusters, mapped by the red, blue, green and cyan colours, respectively. 89

5.6 Example of selection of the best sequence for a lung tumour perfusion study, performed to achieve the best matching with the Z levels contiguous with the reference slice level, represented by Z^*. . 91

6.1 CT image of a lung tumour (a) and its manual segmentation performed by a radiologist with more than 25 years experience (b). . . 97

6.2 Flowchart of the assisted 3D kidneys segmentation. 98

6.3 Example of segmentation of the right kidney in (a). The procedure starts with the manually outlining of the kidney and the selection of the W/L (b). The resulting image (c) is used for the object detection. 100

6.4 3D visualization of the kidneys, the "objects" detected during the processing phase. As one can see, the less captating regions like the renal pelvis is almost discarded during the processing phase. In order to allow subsequent analysis and 3D measurements, results of the object detection were post-processed through an in-house developed ImageJ macro. 101

6.5 General framework for the co-registration of two images, the reference and the template ones. 103

6.6 One dimension kernel for the nearest neighbour (a), linear (b) and cubic (c) interpolation. The bandwidth (number of pixels) considered for each method is also reported. 107

6.7 Patient ID1. Example of the available image series: from the PET/CT, PET (a) and CT (b); from the PET/MRI, PET (c), T1 (d), T2 (e) and DWI (f). In red, the ROI attained by GOJ segmentation, manually performed by a dual trained nuclear medicine physician/radiologist, is also reported. 109

6.8 Patient ID1. Example of slice overlapping after registration on CT, showing the PET from PET/CT (a), the PET from PET/MRI (b), the T1 (c), the T2 (d) and the DWI (e). 110

6.9 Tumour volumes of patient ID1. PET volumes from PET/CT (a) and PET/MRI (b); CT volume and overlapping with the PET volumes (d, e) after 3D registration. 111

6.10 Tumour volumes of patient ID2 from PET/CT (a), PET/MRI (b) and their overlapping after 3D registration (c) 112
6.11 Tumour volumes of patient ID12 from PET/CT (a), PET/MRI (b) and their overlapping after 3D registration (c) 114
6.12 Tumour volumes of patient ID16 from PET/CT (a), PET/MRI (b) and their overlapping after 3D registration (c) 114
6.13 Tumour volumes of patient ID6 from PET/CT (a), PET/MRI (b) and their overlapping after 3D registration (c) 115
6.14 Tumour volumes of patient ID14 from PET/CT (a), PET/MRI (b) and their overlapping after 3D registration (c) 116
6.15 Three slices from PET-CT series showing in red the tumour outlining (patient ID14) 116
6.16 Three slices from PET-MRI series showing in green the tumour outlining (patient ID14) 116
6.17 Tumour volumes of patient ID18 from PET/CT (a), PET/MRI (b) and their overlapping after 3D registration (c) 117
6.18 Tumour volumes of patient ID1. PET volumes from PET/CT (a) and PET/MRI (b) and their overlapping after 3D registration (c). 118
6.19 Close-up view of a GOJ tumour in a single PET slice (a) and corresponding clustering and mapping results ($k = 4$) (b). 119
6.20 Patient ID1. Clustering and mapping results obtained with the raw PET values of PET/CT (a) and PET/MRI (b) volumes. 120

7.1 Patient ID1: ground truth (left), colorimetric map of SS (right). . 133
7.2 Patient ID2: ground truth (left), colorimetric map of MS (right). . 134
7.3 Patient ID3: ground truth (left), colour mask of CM (middle), MS–SS scatter plot (right). 134
7.4 Patient ID4: ground truth (top left), colorimetric map of SS (top right), colorimetric map of MS (bottom left), colour mask of CM (bottom right). 137

8.1 μ_{lCV} (top) and gCV (bottom) values referring to the unregistered maps (highlighted in red colour) and to the corresponding registered ones (pointed with blue colour). 146
8.2 Perfusion maps related to ID16, with (a) and without (b) motion compensation. 147

8.3 Perfusion maps referring to ID3, with (a) and without (b) motion compensation, with related lCV maps (c) and (d). 148

9.1 Perfusion maps of ID15 achieved through the use of the automatic denoising method (a) and by hand clipping the highest BF values (b). In pink, the unreliable values. 157
9.2 In blue, the histograms related to the original ID15 BF map and, in red, the BF values that were removed through the use of the automatic denoising method (a) and by hand clipping the highest BF values (b). 157
9.3 Box plots showing the BF values of AC (left) and SCC (right) lesions. The median is indicated as a red line in the boxes, whereas the vertical size gives the interquartile range. 160
9.4 Mean BF values of AC (top) and SCC (bottom) examinations (blue circles), along with the corresponding group mean (solid red line) and SD (solid green line) values. The green circles highlight the examinations for each subtype that are closer to the mean value of the other subtype. 161
9.5 Reference slice (a) and perfusion map (b) related to ID10. In pink, the unreliable values. 162
9.6 Reference slice and perfusion map related to ID5 (a, b) and ID15 (c, d). In pink, the unreliable values. 162
9.7 Reference slice and perfusion map related to ID23 (a, b) and ID26 (c, d). In pink, the unreliable values. 162
9.8 A sequence of six slices of ID23, referring to same couch position, shows the effect of beam hardening artefacts on lesions. 163
9.9 Reference slice and perfusion map related to ID25 (a) and ID21 (b). In pink, the unreliable values. 163
9.10 Reference slice (a) and perfusion map (b) related to ID20. In pink, the unreliable values. 164
9.11 AC examinations ID2 (a) and ID11 (b) undergoing beam hardening artefacts. 164

10.1 Example of selection of the best sequence for a lung tumour perfusion study, performed to achieve the best matching with the Z levels contiguous to the reference slice level, represented by Z^*. . . 175

10.2 Reference slice (a) and BF colorimetric map (b) of an adenocarcinoma examination (patient ID8). The pink colour points out unreliable BF values. 176
10.3 Patient ID8.$locE$ (a) highlights a high heterogeneity of the BF values in the lower region of the tumour; $locU$ map (b) highlights an increased uniformity of BF values in the upper region of the tumour. 177
10.4 Scatter plot of μE and μU values related to all the examinations are reported in arbitrary units (a.u.). 14 examinations belong to Cluster 1 (in red), 5 to Cluster 2 (in blue). 179

11.1 Right kidneys. SUV_{max} (top) and $SUV_{10\%}$ (bottom) values referring to the baseline (blue) and to the corresponding follow-up examination (red). A-patients samples are joined with a solid line (ID7-ID9), while B-patients samples with a dashed one (ID1-ID6). 189
11.2 Left kidneys. SUV_{max} (top) and $SUV_{10\%}$ (bottom) values referring to the baseline (blue) and to the corresponding follow-up examination (red). A-patients samples are joined with a solid line (ID7-ID9), while B-patients samples with a dashed one (ID1-ID6). 190

12.1 Schema showing tumour segmentation on ^{18}F-FDG PET, T1-weighted, T2-weighted and diffusion weighted axial image of a GOJ cancer (a), respective tumour volumes (b) and subsequent feature generation, extraction and selection (c). 197
12.2 Distribution of GLCM entropy from ADC and SUV. Cluster 1 (highlighted in red) represents patients with metastatic disease, while Cluster 2 (highlighted in blue) those without metastatic disease. 198

List of tables

3.1 A summary of the most common tracers and isotopes used to image specific molecular mechanism. Organs with the highest physiological uptake are also reported. 63

6.1 Summary of Sørensen-Dice similarity coefficient (SDI) relative to each patient (ID), reported in arbitrary units [a.u.]. 113

7.1 A summary of the contingency tables for the three types of heterogeneities 133

8.1 Numerical values for μ_{ICV} and gCV achieved on motion corrected and unregistered perfusion maps, with p-values, endowing each examination ID with its own motion degree (MD). 145

9.1 Summary of the histological diagnosis, tumour stage, position and location (for details see Section 9.3.1), and area of the widest tumour slice relative to each lesion. 155

9.2 BF stratified by NSCLC Subtypes. 159

10.1 Summary of the histological diagnosis, tumour stage and OS data (months) relative to each patient. 173

10.2 Summary of μE and μU relative to each examination (ID), reported in arbitrary units (a.u.). 180

11.1 Summary of SUV_{max} and $SUV_{10\%}$ values from b-PET/CT and m-PET/CT in both kidneys (right and left) of patients undergoing different administration schemes (A-infusion and B-infusion). . . . 188

12.1 Summary of tumour characteristics for the 20 patients, including tumour type and TNM staging. 196

List of equations

Eq. (3.1), CT number 42

Eq. (3.2), Partial volume effect 43

Eq. (3.4), Fick's principle 46

Eq. (3.5), Fick's principle (no venous outflow) 46

Eq. (3.6), Blood Flow 46

Eq. (3.7), Hill equation 47

Eq. (3.8), Larmor frequency 51

Eq. (3.9), ADC 55

Eq. (3.10), SUV 60

Eq. (3.11), Decay factor 60

Eq. (4.1), Mean 73

Eq. (4.2), Standard deviation 73

Eq. (4.3), Skewness 74

Eq. (4.4), Kurtosis 74

Eq. (4.5), Coefficient of variation 74

Eq. (4.6), Entropy 74

Eq. (4.7), Uniformity 74

Eq. (4.8), Joint maximum 76

Eq. (4.9), Joint average 76

Eq. (4.10), Joint variance 76

Eq. (4.11), Joint entropy 77

Eq. (4.12), Angular second moment 77

Eq. (4.13), Contrast 77

Eq. (4.14), Inverse difference 77

Eq. (4.15), Inverse difference normalised 77

Eq. (4.16), Homogeneity 77

Eq. (4.17), Homogeneity normalised 77

Eq. (4.18), Correlation 78

Eq. (4.23), Autocorrelation 78

Eq. (4.24), Short runs emphasis 80

Eq. (4.25), Long runs emphasis 80

Eq. (4.26), Low grey level run emphasis 80

Eq. (4.27), High grey level run emphasis 80

Eq. (4.28), Short run low grey level emphasis 80

Eq. (4.29), Short run high grey level emphasis 80

Eq. (4.30), Long run low grey level emphasis 81

Eq. (4.31), Long run high grey level emphasis 81

Eq. (4.32), Grey level non-uniformity 81

Eq. (4.33), Normalised grey level non-uniformity 81

Eq. (4.34), Run length non-uniformity 81

Eq. (4.35), Normalised run length non-uniformity 81

Eq. (4.36), Run percentage 82

Eq. (5.1), Linear filtering response with a 3 × 3 kernel 84

Eq. (5.2), Fitting residuals 90

Eq. (6.1), Segmentation formalization 96

Eq. (6.2), ROI mask formalization 97

Eq. (6.3), Threshold-based segmentation 97

Eq. (6.4), Sum of squared differences 105

Eq. (6.5), Normalized correlation coefficient 105

Eq. (6.6), Relation between joint and individual entropies 106

Eq. (6.7), Mutual Information 106

Eq. (6.8), Sørensen-Dice index 111

Acronyms

AC Adenocarcinoma. 152, 153, 154, 155, 156, 158, 159, 160, 163, 165, 166, 167, 171, 172

ACC Accuracy. 178, 179, 181, 196, 197, 199

ADC Apparent Diffusion Coefficient. 24, 37, 38, 55, 56, 57, 70, 108, 193, 194, 195, 197, 196, 197, 198, 199, 200, 210, 214

ADC$_{\mathbf{mean}}$ Mean Apparent Diffusion Coefficient. 38, 194, 196, 199

BF Blood Flow. 34, 36, 38, 45, 46, 48, 49, 57, 70, 84, 86, 90, 92, 141, 142, 143, 144, 150, 152, 153, 155, 156, 158, 159, 160, 161, 163, 165, 166, 169, 170, 171, 174, 176, 177, 178, 181, 209, 210, 214, 215

BS Bone Scintigraphy. 184

BV Blood Volume. 38, 49, 152

CE-CT Contrast Enhanced - Computed Tomography. 127, 128, 194

CEC Circulating Endothelial Cells. 44

CSC Cancer Stem Cells. 31

CT Computed Tomography. 23, 24, 26, 29, 36, 37, 38, 39, 41, 42, 43, 44, 50, 51, 57, 60, 61, 69, 70, 85, 96, 108, 109, 110, 120, 125, 126, 127, 128, 132, 142, 149, 150, 154, 169, 172, 176, 184, 186, 211

CT$_{\mathbf{N}}$ Computed Tomography Number. 42, 43

CTp CT perfusion. 17, 43, 44, 49, 139, 140, 139, 140, 141, 142, 143, 144, 146, 144, 148, 149, 150, 151, 152, 153, 154, 156, 158, 160, 162, 164, 166, 168, 170, 172, 181

CV Coefficient of Variation. 74, 85, 92, 140, 141, 143, 149

DCE Dynamic Contrast Enhanced. 24, 36, 37, 205

DCE-MRI Dynamic Contrast Enhanced - Magnetic Resonance Imaging. 36, 37, 38, 49

DCE-CT Dynamic Contrast Enhanced - Computed Tomography. 11, 15, 24, 26, 27, 28, 36, 37, 38, 41, 43, 45, 49, 50, 83, 86, 88, 89, 125, 127, 128, 132, 136, 139, 169, 203, 204

DWI Diffusion Weighted Imaging. 24, 37, 41, 54, 55, 56, 57, 108, 120, 194, 195, 210

EGFR Epidermal Growth Factor Receptor. 38

EUS Endoscopic UltraSound. 50, 194

FDA Food and Drug Administration. 34

FDG Fluorodeoxyglucose. 11, 24, 26, 28, 37, 38, 39, 59, 60, 61, 64, 66, 95, 108, 193, 194, 195, 199, 200, 204, 205, 214

FDG-PET Fluorodeoxyglucose-Positron Emission Tomography. 37, 59, 111, 120

FID Free-Induction Decay. 51

FLT Fluorothymidine F-18. 37, 38

FN False Negative. 131, 178

FP False Positive. 131, 178

GLCM Grey Level Co-occurrence Matrix. 74, 75, 76, 78, 79, 197, 196, 199, 214

GLRLM Grey Level Run Length Matrix. 78, 79, 210

GOJ Gastro-Oesophageal Junction. 11, 24, 26, 28, 50, 95, 108, 193, 194, 199, 200, 204, 205, 211

HU Hounsfield Unit. 38, 42, 43, 46, 70, 88, 90, 128, 135

ICC Intraclass Correlation Coefficient. 196, 199

IRB Institutional Review Board. 141, 154, 171, 194

LCC Large Cell Carcinoma. 171, 172

lCV local Coefficient of Variation. 85, 92, 141, 142, 143, 147, 204, 205

LDA Linear Discriminant Analysis. 195, 198

MANOVA Multivariate Analysis Of Variance. 178, 179, 196, 199

MD Motion Degrees. 141, 144

MRI Magnetic Resonance Imaging. 11, 23, 24, 26, 36, 37, 38, 41, 50, 51, 52, 54, 56, 57, 60, 61, 69, 70, 109, 184, 195, 199, 200

MTT Mean Transit Time. 49

MVD Micro-Vessel Density. 24, 44, 45, 152, 170

NET Neuroendocrine Tumors. 64, 65

NMR Nuclear Magnetic Resonance. 51

NPV Negative Predictive Value. 178, 179, 181, 196, 197, 199

NSCLC Non-Small-Cell Lung Cancer. 38, 49, 128, 132, 152, 153, 154, 156, 165, 166, 170, 171, 176, 181

OS Overall Survival. 38, 170, 171, 172, 178, 181, 193, 194, 205

PC Prostate cancer. 184, 185

PET Positron Emission Tomography. 11, 24, 26, 28, 36, 37, 38, 41, 58, 60, 61, 64, 65, 66, 69, 70, 95, 97, 108, 110, 111, 112, 115, 118, 119, 120, 126, 184, 186, 189, 194, 195, 199, 200, 203, 204, 211, 212, 214

PET/CT Positron Emission Tomography/Computed Tomography. 11, 24, 26, 37, 41, 60, 61, 95, 97, 108, 109, 110, 111, 115, 118, 119, 120, 185, 186, 187, 191, 194, 195, 199, 204, 210, 211, 212

PET/MRI Positron Emission Tomography/Magnetic Resonance Imaging. 11, 24, 26, 28, 37, 41, 61, 65, 95, 108, 109, 110, 111, 115, 118, 119, 120, 193, 194, 195, 200, 204, 205, 210, 211, 212

PPV Positive Predictive Value. 178, 179, 181, 196, 197, 199

PSA Prostate-Specific Antigen. 184, 185

PSMA Prostate-Specific Membrane Antigen. 24, 28, 29, 65, 95, 97, 183, 184, 185, 186, 187, 189, 191, 205

QIBA Quantitative Imaging Biomarkers Alliance. 49

RECIST Response Evaluation Criteria in Solid Tumors. 37, 65

RF Radiofrequency. 51, 52

ROI Region Of Interest. 46, 57, 59, 60, 66, 73, 74, 81, 84, 85, 86, 87, 88, 89, 90, 95, 96, 97, 99, 108, 110, 115, 118, 128, 131, 142, 143, 147, 155, 172, 176, 181, 184, 211

SCC Squamous Cell Carcinoma. 152, 153, 154, 155, 156, 158, 159, 161, 165, 166, 167, 171, 172

SE Sensitivity. 128, 132, 178, 179, 181, 196, 197, 199

SP Specificity. 128, 132, 178, 179, 181, 196, 197, 199

SPECT Single-Photon Emission Computed Tomography. 36

SUV Standardised Uptake Value. 38, 59, 60, 61, 65, 66, 70, 183, 184, 185, 186, 193, 194, 195, 197, 196, 197, 198, 199, 200, 203, 204, 210, 214

SUV$_{\mathbf{max}}$ Maximum Standard Uptake Value. 38, 60, 64, 66, 183, 184, 185, 186, 187, 189, 191, 194, 196, 199, 204, 205

SUV$_{\mathbf{mean}}$ Mean Standard Uptake Value. 60, 66, 184

TCC Time Concentration Curve. 44, 45, 46, 47, 49, 86, 88, 90, 92, 128, 136, 142, 147, 149, 152, 155, 156, 170, 174, 209

TN True Negative. 131, 178

TP True Positive. 131, 178

US Ultrasonography. 36

VEGF Vascular Endothelial Growth Factor. 24, 34, 44

VOI Volume Of Interest. 59, 60, 73

W/L Window/Level. 43, 99, 211

WHO World Health Organization. 37

Bibliography

[1] L. A. Torre, F. Bray, R. L. Siegel, J. Ferlay, J. Lortet-Tieulent, A. Jemal, Global cancer statistics, 2012, CA: a cancer journal for clinicians 65 (2) (2015) 87–108. (cit. on pp. 23)

[2] R. L. Siegel, K. D. Miller, A. Jemal, Cancer statistics, 2017, CA: a cancer journal for clinicians 67 (1) (2017) 7–30. (cit. on pp. 23)

[3] S. Ziyad, M. L. Iruela-Arispe, Molecular mechanisms of tumor angiogenesis, Genes & cancer 2 (12) (2011) 1085–1096. (cit. on pp. 23, 32)

[4] D. Hanahan, R. A. Weinberg, Hallmarks of cancer: the next generation, cell 144 (5) (2011) 646–674. (cit. on pp. 23, 32)

[5] K. Yasaka, H. Akai, M. Nojima, A. Shinozaki-Ushiku, M. Fukayama, J. Nakajima, K. Ohtomo, S. Kiryu, Quantitative computed tomography texture analysis for estimating histological subtypes of thymic epithelial tumors, European journal of radiology 92 (2017) 84–92. (cit. on pp. 23, 39)

[6] H. J. Aerts, E. R. Velazquez, R. T. Leijenaar, C. Parmar, P. Grossmann, S. Carvalho, J. Bussink, R. Monshouwer, B. Haibe-Kains, D. Rietveld, et al., Decoding tumour phenotype by noninvasive imaging using a quantitative radiomics approach, Nat. Commun. 5 (4006) (2014) 1–8. (cit. on pp. 23, 33, 36, 39, 70)

[7] M. Nakajo, M. Jinguji, Y. Nakabeppu, M. Nakajo, R. Higashi, Y. Fukukura, K. Sasaki, Y. Uchikado, S. Natsugoe, T. Yoshiura, Texture analysis of 18 F-FDG PET/CT to predict tumour response and prognosis of patients with esophageal cancer treated by chemoradiotherapy, European journal of nuclear medicine and molecular imaging 44 (2) (2017) 206–214. (cit. on pp. 23, 39, 200)

[8] S. H. Kim, A. Kamaya, J. K. Willmann, CT perfusion of the liver: principles and applications in oncology, Radiology 272 (2) (2014) 322–344. (cit. on pp. 23, 24, 36, 38, 49)

[9] L. Alic, W. J. Niessen, J. F. Veenland, Quantification of heterogeneity as a biomarker in tumor imaging: a systematic review, PloS one 9 (10) (2014) e110300. (cit. on pp. 23, 36, 70)

[10] E. Scalco, G. Rizzo, Texture analysis of medical images for radiotherapy applications, The British journal of radiology 90 (1070) (2017) 20160642. (cit. on pp. 23, 72)

[11] R. García-Figueiras, A. R. Padhani, A. J. Beer, S. Baleato-González, J. C. Vilanova, A. Luna, L. Oleaga, A. Gómez-Caamaño, D.-M. Koh, Imaging of Tumor Angiogenesis for Radiologists – Part 1: Biological and Technical Basis, Curr. Probl. Diagn. Radiol. 44 (5) (2015) 407–424. (cit. on pp. 24, 49, 57)

[12] K. Miles, T.-Y. Lee, V. Goh, E. Klotz, C. Cuenod, S. Bisdas, A. Groves, M. Hayball, R. Alonzi, T. Brunner, et al., Current status and guidelines for the assessment of tumour vascular support with dynamic contrast-enhanced computed tomography, European radiology 22 (7) (2012) 1430–1441. (cit. on pp. 24, 45, 49)

[13] Y. Li, Z.-g. Yang, T.-w. Chen, H.-j. Chen, J.-y. Sun, Y.-r. Lu, Peripheral lung carcinoma: correlation of angiogenesis and first-pass perfusion parameters of 64-detector row CT, Lung Cancer 61 (1) (2008) 44–53. (cit. on pp. 24, 45, 153)

[14] W. Thaiss, S. Kaufmann, C. Kloth, K. Nikolaou, H. Bösmüller, M. Horger, VEGFR-2 expression in HCC, dysplastic and regenerative liver nodules, and correlation with pre-biopsy Dynamic Contrast enhanced CT, European journal of radiology 85 (11) (2016) 2036–2041. (cit. on pp. 24, 45)

[15] T. Berghmans, M. Dusart, M. Paesmans, C. Hossein-Foucher, I. Buvat, C. Castaigne, A. Scherpereel, C. Mascaux, M. Moreau, M. Roelandts, et al., Primary tumor standardized uptake value (SUVmax) measured on fluorodeoxyglucose positron emission tomography (FDG-PET) is of prognostic value for survival in non-small cell lung cancer (NSCLC): a systematic review and meta-analysis (MA) by the european lung cancer working party

for the iaslc lung cancer staging project, Journal of Thoracic Oncology 3 (1) (2008) 6–12. (cit. on pp. 24, 38, 199)

[16] D. Groheux, S. Giacchetti, J.-L. Moretti, R. Porcher, M. Espié, J. Lehmann-Che, A. de Roquancourt, A.-S. Hamy, C. Cuvier, L. Vercellino, et al., Correlation of high 18 F-FDG uptake to clinical, pathological and biological prognostic factors in breast cancer, European journal of nuclear medicine and molecular imaging 38 (3) (2011) 426–435. (cit. on pp. 24, 38, 199)

[17] J. P. O'Connor, A. Jackson, M.-C. Asselin, D. L. Buckley, G. J. Parker, G. C. Jayson, Quantitative imaging biomarkers in the clinical development of targeted therapeutics: current and future perspectives, The lancet oncology 9 (8) (2008) 766–776. (cit. on pp. 24, 37, 39)

[18] R. García-Figueiras, A. R. Padhani, A. J. Beer, S. Baleato-González, J. C. Vilanova, A. Luna, L. Oleaga, A. Gómez-Caamaño, D.-M. Koh, Imaging of Tumor Angiogenesis for Radiologists-Part 2: Clinical Utility, Current problems in diagnostic radiology. (cit. on pp. 24, 127)

[19] C. Kenis, F. Deckers, B. De Foer, F. Van Mieghem, S. Van Laere, M. Pouillon, Diagnosis of liver metastases: can diffusion-weighted imaging (DWI) be used as a stand alone sequence?, European journal of radiology 81 (5) (2012) 1016–1023. (cit. on pp. 24, 57, 69)

[20] J. Czernin, M. Allen-Auerbach, H. R. Schelbert, et al., Improvements in cancer staging with PET/CT: literature-based evidence as of september 2006, Journal of Nuclear Medicine 48 (1) (2007) 78S. (cit. on pp. 24, 60, 69)

[21] J. Wang, N. Wu, M. D. Cham, Y. Song, Tumor response in patients with advanced non–small cell lung cancer: perfusion CT evaluation of chemotherapy and radiation therapy, American Journal of Roentgenology 193 (4) (2009) 1090–1096. (cit. on pp. 24, 49, 69, 140)

[22] B. Kamsu-Foguem, G. Tchuenté-Foguem, L. Allart, Y. Zennir, C. Vilhelm, H. Mehdaoui, D. Zitouni, H. Hubert, M. Lemdani, P. Ravaux, User-centered visual analysis using a hybrid reasoning architecture for intensive care units, Decision Support Systems 54 (1) (2012) 496–509. (cit. on pp. 24, 126)

[23] O. M. Topcuoğlu, M. Karçaaltıncaba, D. Akata, M. N. Özmen, Reproducibility and variability of very low dose hepatic perfusion CT in metastatic liver disease, Diagnostic and Interventional Radiology 22 (6) (2016) 495. (cit. on pp. 24, 49)

[24] D. Hanahan, R. A. Weinberg, The hallmarks of cancer, cell 100 (1) (2000) 57–70. (cit. on pp. 32)

[25] C. E. Meacham, S. J. Morrison, Tumour heterogeneity and cancer cell plasticity, Nature 501 (7467) (2013) 328. (cit. on pp. 32)

[26] L. Gay, A.-M. Baker, T. A. Graham, Tumour cell heterogeneity, F1000Research 5. (cit. on pp. 33)

[27] F. Michor, K. Polyak, The origins and implications of intratumor heterogeneity, Cancer prevention research (2010) 1940–6207. (cit. on pp. 33)

[28] J. E. Visvader, Cells of origin in cancer, Nature 469 (7330) (2011) 314. (cit. on pp. 33)

[29] M. Tellez-Gabriel, B. Ory, F. Lamoureux, M.-F. Heymann, D. Heymann, Tumour heterogeneity: the key advantages of single-cell analysis, International journal of molecular sciences 17 (12) (2016) 2142. (cit. on pp. 33, 194)

[30] A. Marusyk, V. Almendro, K. Polyak, Intra-tumour heterogeneity: a looking glass for cancer?, Nature Reviews Cancer 12 (5) (2012) 323. (cit. on pp. 33, 36, 129, 170)

[31] K. A. Miles, C. Charnsangavej, F. T. Lee, E. K. Fishman, K. Horton, T.-Y. Lee, Application of CT in the investigation of angiogenesis in oncology, Academic radiology 7 (10) (2000) 840–850. (cit. on pp. 33)

[32] C. Cuenod, L. Fournier, D. Balvay, J.-M. Guinebretiere, Tumor angiogenesis: pathophysiology and implications for contrast-enhanced MRI and CT assessment, Abdominal imaging 31 (2) (2006) 188–193. (cit. on pp. 33)

[33] R. Ronca, M. Benkheil, S. Mitola, S. Struyf, S. Liekens, Tumor angiogenesis revisited: Regulators and clinical implications, Medicinal research reviews 37 (6) (2017) 1231–1274. (cit. on pp. 33)

[34] W. D. Figg, J. Folkman, Angiogenesis: an integrative approach from science to medicine, Springer Science & Business Media, 2008. (cit. on pp. 33, 34)

[35] G. C. Jayson, R. Kerbel, L. M. Ellis, A. L. Harris, Antiangiogenic therapy in oncology: current status and future directions, The Lancet 388 (10043) (2016) 518–529. (cit. on pp. 33)

[36] H. Hashizume, P. Baluk, S. Morikawa, J. W. McLean, G. Thurston, S. Roberge, R. K. Jain, D. M. McDonald, Openings between defective endothelial cells explain tumor vessel leakiness, The American journal of pathology 156 (4) (2000) 1363–1380. (cit. on pp. 34)

[37] W. G. Roberts, G. E. Palade, Increased microvascular permeability and endothelial fenestration induced by vascular endothelial growth factor, Journal of cell science 108 (6) (1995) 2369–2379. (cit. on pp. 34)

[38] N. Ferrara, K. J. Hillan, H.-P. Gerber, W. Novotny, Discovery and development of bevacizumab, an anti-VEGF antibody for treating cancer, Nature reviews Drug discovery 3 (5) (2004) 391. (cit. on pp. 35)

[39] J. Ma, D. J. Waxman, Combination of antiangiogenesis with chemotherapy for more effective cancer treatment, Molecular cancer therapeutics 7 (12) (2008) 3670–3684. (cit. on pp. 35)

[40] G. I. Evan, K. H. Vousden, Proliferation, cell cycle and apoptosis in cancer, Nature 411 (6835) (2001) 342. (cit. on pp. 35)

[41] C. C.-W. Yu, A. L. Woods, D. A. Levison, The assessment of cellular proliferation by immunohistochemistry: a review of currently available methods and their applications, The Histochemical journal 24 (3) (1992) 121–131. (cit. on pp. 35)

[42] M. G. Vander Heiden, L. C. Cantley, C. B. Thompson, Understanding the warburg effect: the metabolic requirements of cell proliferation, science 324 (5930) (2009) 1029–1033. (cit. on pp. 35, 59)

[43] L. K. Boroughs, R. J. DeBerardinis, Metabolic pathways promoting cancer cell survival and growth, Nature cell biology 17 (4) (2015) 351. (cit. on pp. 35)

[44] J. Yun, C. Rago, I. Cheong, R. Pagliarini, P. Angenendt, H. Rajagopalan, K. Schmidt, J. K. Willson, S. Markowitz, S. Zhou, et al., Glucose deprivation contributes to the development of kras pathway mutations in tumor cells, Science 325 (5947) (2009) 1555–1559. (cit. on pp. 35)

[45] R. A. Cairns, I. S. Harris, T. W. Mak, Regulation of cancer cell metabolism, Nature Reviews Cancer 11 (2) (2011) 85. (cit. on pp. 35, 36, 59)

[46] R. J. DeBerardinis, J. J. Lum, G. Hatzivassiliou, C. B. Thompson, The biology of cancer: metabolic reprogramming fuels cell growth and proliferation, Cell metabolism 7 (1) (2008) 11–20. (cit. on pp. 36, 59)

[47] M. G. Vander Heiden, Targeting cancer metabolism: a therapeutic window opens, Nature reviews Drug discovery 10 (9) (2011) 671. (cit. on pp. 36, 59)

[48] D. A. Tennant, R. V. Durán, E. Gottlieb, Targeting metabolic transformation for cancer therapy, Nature reviews cancer 10 (4) (2010) 267. (cit. on pp. 36)

[49] C. Cuenod, D. Balvay, Perfusion and vascular permeability: basic concepts and measurement in DCE-CT and DCE-MRI, Diagnostic and interventional imaging 94 (12) (2013) 1187–1204. (cit. on pp. 37)

[50] D. Le Bihan, Apparent diffusion coefficient and beyond: what diffusion MR imaging can tell us about tissue structure (2013). (cit. on pp. 37, 56, 200)

[51] M.-C. Asselin, J. P. OConnor, R. Boellaard, N. A. Thacker, A. Jackson, Quantifying heterogeneity in human tumours using MRI and PET, European journal of cancer 48 (4) (2012) 447–455. (cit. on pp. 37, 39)

[52] D. Soloviev, D. Lewis, D. Honess, E. Aboagye, [18f] flt: An imaging biomarker of tumour proliferation for assessment of tumour response to treatment, European Journal of Cancer 48 (4) (2012) 416–424. (cit. on pp. 37)

[53] A. Schulze, A. L. Harris, How cancer metabolism is tuned for proliferation and vulnerable to disruption, Nature 491 (7424) (2012) 364. (cit. on pp. 37, 59)

[54] R. A. Gatenby, O. Grove, R. J. Gillies, Quantitative imaging in cancer evolution and ecology, Radiology 269 (1) (2013) 8–14. (cit. on pp. 38, 69)

[55] Y. Tsuchida, P. Therasse, Response evaluation criteria in solid tumors (RECIST): new guidelines, Medical and Pediatric Oncology: The Official Journal of SIOPInternational Society of Pediatric Oncology (Societé Internationale d'Oncologie Pédiatrique 37 (1) (2001) 1–3. (cit. on pp. 38)

[56] P. Therasse, S. G. Arbuck, E. A. Eisenhauer, J. Wanders, R. S. Kaplan, L. Rubinstein, J. Verweij, M. Van Glabbeke, A. T. van Oosterom, M. C. Christian, et al., New guidelines to evaluate the response to treatment in solid tumors, Journal of the National Cancer Institute 92 (3) (2000) 205–216. (cit. on pp. 38)

[57] E. Eisenhauer, P. Therasse, J. Bogaerts, L. Schwartz, D. Sargent, R. Ford, J. Dancey, S. Arbuck, S. Gwyther, M. Mooney, et al., New response evaluation criteria in solid tumours: revised RECIST guideline (version 1.1), Eur. J. Cancer 45 (2) (2009) 228–247. (cit. on pp. 38)

[58] J. O. Park, S. I. Lee, S. Y. Song, K. Kim, W. S. Kim, C. W. Jung, Y. S. Park, Y.-H. Im, W. K. Kang, M. H. Lee, et al., Measuring response in solid tumors: comparison of RECIST and WHO response criteria, Japanese journal of clinical oncology 33 (10) (2003) 533–537. (cit. on pp. 38)

[59] C. C. Jaffe, Measures of response: RECIST, WHO, and new alternatives, Journal of Clinical Oncology 24 (20) (2006) 3245–3251. (cit. on pp. 38)

[60] E. Coche, Assessment of lung tumor response by perfusion CT, JBR-BTR 96 (3) (2013) 172–174. (cit. on pp. 38)

[61] X. S. Li, H. X. Fan, H. Fang, H. Huang, Y. L. Song, C. W. Zhou, Value of whole-tumor dual-input perfusion CT in predicting the effect of multiarterial infusion chemotherapy on advanced non–small cell lung cancer, American journal of roentgenology 203 (5) (2014) W497–W505. (cit. on pp. 38)

[62] Y. Ohno, Y. Fujisawa, H. Koyama, Y. Kishida, S. Seki, N. Sugihara, T. Yoshikawa, Dynamic contrast-enhanced perfusion area-detector CT assessed with various mathematical models: Its capability for therapeutic outcome prediction for non-small cell lung cancer patients with chemoradiotherapy as compared with that of FDG-PET/CT, Eur. J. Radiol. 86 (2017) 83–91. (cit. on pp. 38, 156, 174)

[63] C. G. Willett, Y. Boucher, E. Di Tomaso, D. G. Duda, L. L. Munn, R. T. Tong, D. C. Chung, D. V. Sahani, S. P. Kalva, S. V. Kozin, et al., Direct evidence that the VEGF-specific antibody bevacizumab has antivascular effects in human rectal cancer, Nature medicine 10 (2) (2004) 145. (cit. on pp. 38)

[64] M. Braunagel, A. Graser, M. Reiser, M. Notohamiprodjo, The role of functional imaging in the era of targeted therapy of renal cell carcinoma, World journal of urology 32 (1) (2014) 47–58. (cit. on pp. 38)

[65] S. C. Ha, J. S. Oh, J.-L. Roh, H. Moon, J. S. Kim, K.-J. Cho, S.-H. Choi, S. Y. Nam, S. Y. Kim, Pretreatment tumor suv max predicts disease-specific and overall survival in patients with head and neck soft tissue sarcoma, European journal of nuclear medicine and molecular imaging 44 (1) (2017) 33–40. (cit. on pp. 38)

[66] B. H. Byun, K. M. Kim, G. J. Cheon, D. H. Choe, J. S. Koh, D. Y. Lee, B.-Y. Ryoo, H. Baek, S. M. Lim, S. H. Yang, et al., 18F-FDG uptake and EGFR mutations in patients with non-small cell lung cancer: a single-institution retrospective analysis, Lung Cancer 67 (1) (2010) 76–80. (cit. on pp. 38)

[67] W. Chen, S. Delaloye, D. H. Silverman, C. Geist, J. Czernin, J. Sayre, N. Satyamurthy, W. Pope, A. Lai, M. E. Phelps, et al., Predicting treatment response of malignant gliomas to bevacizumab and irinotecan by imaging proliferation with [18F] fluorothymidine positron emission tomography: a pilot study, Journal of Clinical Oncology 25 (30) (2007) 4714–4721. (cit. on pp. 38)

[68] G. Petralia, L. Preda, G. Dandrea, S. Viotti, L. Bonello, R. De Filippi, M. Bellomi, CT perfusion in solid-body tumours. Part I: technical issues, La radiologia medica 115 (6) (2010) 843–857. (cit. on pp. 42, 45, 170)

[69] J. Bryant, N. Drage, S. Richmond, CT number definition, Radiation Physics and Chemistry 81 (4) (2012) 358–361. (cit. on pp. 42)

[70] J. F. Barrett, N. Keat, Artifacts in CT: recognition and avoidance, Radiographics 24 (6) (2004) 1679–1691. (cit. on pp. 43, 50, 153, 159, 171)

[71] K. Klingenbeck-Regn, S. Schaller, T. Flohr, B. Ohnesorge, A. F. Kopp, U. Baum, Subsecond multi-slice computed tomography: basics and appli-

cations, European journal of radiology 31 (2) (1999) 110–124. (cit. on pp. 43)

[72] M. Prokop, A. van der Molen, Spiral and Multislice Computed Tomography of the Body, Georg Thieme Verlag, 2013. (cit. on pp. 43)

[73] K. Miles, M. Griffiths, Perfusion CT: a worthwhile enhancement?, Br J Radiol 76 (904) (2003) 220–231. (cit. on pp. 43, 46, 156)

[74] N. Murukesh, C. Dive, G. C. Jayson, Biomarkers of angiogenesis and their role in the development of VEGF inhibitors, British journal of cancer 102 (1) (2010) 8. (cit. on pp. 44)

[75] K. Miles, Functional computed tomography in oncology, European Journal of Cancer 38 (16) (2002) 2079–2084. (cit. on pp. 44, 140)

[76] S. Zhou, Y. Gu, G. Yuan, Z. Wang, L. Huang, Correlations between computed tomography perfusion enhancement parameters and lymph node metastasis in non-small cell lung cancer, Int J Clin Exp Med 9 (7) (2016) 12896–12903. (cit. on pp. 44, 45)

[77] G. Brix, S. Zwick, F. Kiessling, J. Griebel, Pharmacokinetic analysis of tissue microcirculation using nested models: multimodel inference and parameter identifiability, Medical physics 36 (7) (2009) 2923–2933. (cit. on pp. 44)

[78] M. Osimani, D. Bellini, C. Di Cristofano, G. Palleschi, V. Petrozza, A. Carbone, A. Laghi, Perfusion MDCT of prostate cancer: correlation of perfusion CT parameters and immunohistochemical markers of angiogenesis, American journal of roentgenology 199 (5) (2012) 1042–1048. (cit. on pp. 45)

[79] J. Yao, Z.-g. Yang, H.-j. Chen, T.-w. Chen, J. Huang, Gastric adenocarcinoma: can perfusion CT help to noninvasively evaluate tumor angiogenesis?, Abdominal imaging 36 (1) (2011) 15–21. (cit. on pp. 45)

[80] C. S. Reiner, M. Roessle, T. Thiesler, D. Eberli, E. Klotz, T. Frauenfelder, T. Sulser, H. Moch, H. Alkadhi, Computed tomography perfusion imaging of renal cell carcinoma: systematic comparison with histopathological angiogenic and prognostic markers, Investigative radiology 48 (4) (2013) 183–191. (cit. on pp. 45)

[81] A. Kambadakone, S. S. Yoon, T.-M. Kim, D. L. Karl, D. G. Duda, T. F. DeLaney, D. V. Sahani, CT perfusion as an imaging biomarker in monitoring response to neoadjuvant bevacizumab and radiation in soft-tissue sarcomas: comparison with tumor morphology, circulating and tumor biomarkers, and gene expression, American Journal of Roentgenology 204 (1) (2015) W11–W18. (cit. on pp. 45, 152, 165, 171)

[82] G. d'Assignies, A. Couvelard, S. Bahrami, M.-P. Vullierme, P. Hammel, O. Hentic, A. Sauvanet, P. Bedossa, P. Ruszniewski, V. Vilgrain, Pancreatic endocrine tumors: tumor blood flow assessed with perfusion CT reflects angiogenesis and correlates with prognostic factors, Radiology 250 (2) (2009) 407–416. (cit. on pp. 45, 142, 152, 171)

[83] Y. Li, Z. Yang, T. Chen, J. Yu, J. Sun, H. Chen, First-pass perfusion imaging of solitary pulmonary nodules with 64-detector row CT: comparison of perfusion parameters of malignant and benign lesions, The British journal of radiology 83 (993) (2010) 785–790. (cit. on pp. 45)

[84] N. Tacelli, T. Santangelo, A. Scherpereel, A. Duhamel, V. Deken, E. Klotz, A. Cortot, J.-J. Lafitte, F. Wallyn, J. Remy, et al., Perfusion CT allows prediction of therapy response in non-small cell lung cancer treated with conventional and anti-angiogenic chemotherapy, European radiology 23 (8) (2013) 2127–2136. (cit. on pp. 45, 50, 142, 170)

[85] K. Miles, Perfusion CT for the assessment of tumour vascularity: which protocol?, Br. J. Radiol. 76 (1) (2003) S36–42. (cit. on pp. 46)

[86] G. Brix, S. Zwick, J. Griebel, C. Fink, F. Kiessling, Estimation of tissue perfusion by dynamic contrast-enhanced imaging: simulation-based evaluation of the steepest slope method, European radiology 20 (9) (2010) 2166–2175. (cit. on pp. 46)

[87] K. A. Miles, M. P. Hayball, A. K. Dixon, Functional images of hepatic perfusion obtained with dynamic CT., Radiology 188 (2) (1993) 405–411. (cit. on pp. 46)

[88] M. Sansone, R. Fusco, A. Petrillo, A geometrical perspective on the 3TP method in DCE-MRI, Biomedical Signal Processing and Control 16 (2015) 32–39. (cit. on pp. 47)

[89] J. W. Mouton, M. N. Dudley, O. Cars, H. Derendorf, G. L. Drusano, Standardization of pharmacokinetic/pharmacodynamic (PK/PD) terminology for anti-infective drugs: an update, Journal of antimicrobial Chemotherapy 55 (5) (2005) 601–607. (cit. on pp. 47)

[90] S. Baiocco, A. Bevilacqua, D. Barone, A. Delmonte, G. Gavelli, L'eterogeneità perfusionale: un biomarker prognostico per il cancro del polmone non a piccole cellule (NSCLC), Il Giornale Italiano di Radiologia Medica 4 (4) (2017) 665–669. (cit. on pp. 48, 90, 209)

[91] S. Goutelle, M. Maurin, F. Rougier, X. Barbaut, L. Bourguignon, M. Ducher, P. Maire, The Hill equation: a review of its capabilities in pharmacological modelling, Fundamental & clinical pharmacology 22 (6) (2008) 633–648. (cit. on pp. 47, 156, 174)

[92] S. Turco, H. Wijkstra, M. Mischi, Mathematical models of contrast transport kinetics for cancer diagnostic imaging: a review, IEEE reviews in biomedical engineering 9 (2016) 121–147. (cit. on pp. 49)

[93] Y. Sun, M. Yang, D. Mao, F. Lv, Y. Yin, M. Li, Y. Hua, Low-dose volume perfusion computed tomography (VPCT) for diagnosis of solitary pulmonary nodules, European journal of radiology 85 (6) (2016) 1208–1218. (cit. on pp. 49)

[94] V. Goh, S. Halligan, J.-A. Hugill, C. I. Bartram, Quantitative assessment of tissue perfusion using MDCT: comparison of colorectal cancer and skeletal muscle measurement reproducibility, American Journal of Roentgenology 187 (1) (2006) 164–169. (cit. on pp. 49, 50, 140, 141)

[95] D. V. Sahani, N.-S. Holalkere, P. R. Mueller, A. X. Zhu, Advanced hepatocellular carcinoma: CT perfusion of liver and tumor tissueinitial experience, Radiology 243 (3) (2007) 736–743. (cit. on pp. 49)

[96] Q.-S. Ng, V. Goh, H. Fichte, E. Klotz, P. Fernie, M. I. Saunders, P. J. Hoskin, A. R. Padhani, Lung cancer perfusion at Multi–Detector Row CT: reproducibility of whole tumor quantitative measurements, Radiology 239 (2) (2006) 547–553. (cit. on pp. 49, 50, 140, 149)

[97] A. R. Larici, L. Calandriello, M. Amato, R. Silvestri, A. Del Ciello, F. Molinari, C. De Waure, M. L. Vita, G. Carnassale, L. Bonomo, First-pass per-

fusion of non-small-cell lung cancer (NSCLC) with 64-detector-row ct: a study of technique repeatability and intra-and interobserver variability, La radiologia medica 119 (1) (2014) 4–12. (cit. on pp. 49)

[98] C. S. Ng, A. G. Chandler, W. Wei, D. H. Herron, E. F. Anderson, R. Kurzrock, C. Charnsangavej, Reproducibility of CT perfusion parameters in liver tumors and normal liver, Radiology 260 (3) (2011) 762–770. (cit. on pp. 50, 140, 146)

[99] C. Coolens, B. Driscoll, J. Moseley, K. K. Brock, L. A. Dawson, Feasibility of 4D perfusion CT imaging for the assessment of liver treatment response following SBRT and sorafenib, Advances in radiation oncology 1 (3) (2016) 194–203. (cit. on pp. 50)

[100] Q. Qi, T. P. C. Yeung, T.-Y. Lee, G. Bauman, C. Crukley, L. Morrison, L. Hoffman, S. Yartsev, Evaluation of CT perfusion biomarkers of tumor hypoxia, PloS one 11 (4) (2016) e0153569. (cit. on pp. 50)

[101] A. Bevilacqua, S. Baiocco, Automatic classification of lung tumour heterogeneity according to a visual-based score system in dynamic contrast enhanced CT sequences, Int. J. Mod. Phys. C 27 (10) (2016) 1650106–1–1650106–14. (cit. on pp. 50, 136, 152, 170)

[102] N. K. Jensen, M. Lock, B. Fisher, R. Kozak, X. Chen, J. Chen, E. Wong, T.-Y. Lee, Prediction and reduction of motion artifacts in free-breathing dynamic contrast enhanced CT perfusion imaging of primary and metastatic intrahepatic tumors, Academic radiology 20 (4) (2013) 414–422. (cit. on pp. 50, 140, 141)

[103] A. Gibaldi, D. Barone, G. Gavelli, S. Malavasi, A. Bevilacqua, Effects of guided random sampling of TCCs on blood flow values in CT perfusion studies of lung tumors, Academic radiology 22 (1) (2015) 58–69. (cit. on pp. 50, 127, 140)

[104] B. M. Zussman, G. Boghosian, R. J. Gorniak, M. E. Olszewski, K. M. Read, K. M. Siddiqui, A. E. Flanders, The relative effect of vendor variability in CT perfusion results: a method comparison study, American Journal of Roentgenology 197 (2) (2011) 468–473. (cit. on pp. 50, 140)

[105] A. Sakurada, T. Takahara, T. C. Kwee, T. Yamashita, S. Nasu, T. Horie, M. Van Cauteren, Y. Imai, Diagnostic performance of diffusion-weighted magnetic resonance imaging in esophageal cancer, European radiology 19 (6) (2009) 1461–1469. (cit. on pp. 50)

[106] P. S. van Rossum, R. van Hillegersberg, F. M. Lever, I. M. Lips, A. L. van Lier, G. J. Meijer, M. S. van Leeuwen, M. van Vulpen, J. P. Ruurda, Imaging strategies in the management of oesophageal cancer: what's the role of MRI?, European radiology 23 (7) (2013) 1753–1765. (cit. on pp. 50)

[107] A. Riddell, W. Allum, J. Thompson, A. Wotherspoon, C. Richardson, G. Brown, The appearances of oesophageal carcinoma demonstrated on high-resolution, T2-weighted MRI, with histopathological correlation, European radiology 17 (2) (2007) 391–399. (cit. on pp. 51)

[108] R. T. Ripley, I. S. Sarkaria, R. Grosser, C. S. Sima, M. S. Bains, D. R. Jones, P. S. Adusumilli, J. Huang, D. J. Finley, V. W. Rusch, et al., Pretreatment dysphagia in esophageal cancer patients may eliminate the need for staging by endoscopic ultrasonography, The Annals of thoracic surgery 101 (1) (2016) 226–230. (cit. on pp. 51)

[109] V. P. Grover, J. M. Tognarelli, M. M. Crossey, I. J. Cox, S. D. Taylor-Robinson, M. J. McPhail, Magnetic resonance imaging: principles and techniques: lessons for clinicians, Journal of clinical and experimental hepatology 5 (3) (2015) 246–255. (cit. on pp. 51, 53, 57)

[110] A. Berger, How does it work?: Magnetic resonance imaging, British Medical Journal 324 (7328) (2002) 35. (cit. on pp. 51, 52)

[111] P. Hoskin, V. Goh, Radiotherapy in Practice-Imaging, Vol. 4, Oxford University Press, 2010. (cit. on pp. 52, 53)

[112] R. Bitar, G. Leung, R. Perng, S. Tadros, A. R. Moody, J. Sarrazin, C. McGregor, M. Christakis, S. Symons, A. Nelson, et al., MR pulse sequences: what every radiologist wants to know but is afraid to ask, Radiographics 26 (2) (2006) 513–537. (cit. on pp. 52)

[113] R. Bammer, Basic principles of diffusion-weighted imaging, European journal of radiology 45 (3) (2003) 169–184. (cit. on pp. 54)

[114] T. A. C. Society (Ed.), The American Cancer Society's Principles of Oncology: Prevention to Survivorship, Wiley, 2017. (cit. on pp. 54)

[115] D. M. Patterson, A. R. Padhani, D. J. Collins, Technology insight: water diffusion MRI-a potential new biomarker of response to cancer therapy, Nature Reviews Clinical Oncology 5 (4) (2008) 220. (cit. on pp. 54)

[116] A. Qayyum, Diffusion-weighted imaging in the abdomen and pelvis: concepts and applications, Radiographics 29 (6) (2009) 1797–1810. (cit. on pp. 54)

[117] D.-M. Koh, D. J. Collins, Diffusion-weighted MRI in the body: applications and challenges in oncology, American Journal of Roentgenology 188 (6) (2007) 1622–1635. (cit. on pp. 54, 56, 57, 58)

[118] C. K. Kim, B. K. Park, B. Kim, Diffusion-weighted MRI at 3 T for the evaluation of prostate cancer, American Journal of Roentgenology 194 (6) (2010) 1461–1469. (cit. on pp. 54)

[119] A. A. Malayeri, R. H. El Khouli, A. Zaheer, M. A. Jacobs, C. P. Corona-Villalobos, I. R. Kamel, K. J. Macura, Principles and applications of diffusion-weighted imaging in cancer detection, staging, and treatment follow-up, Radiographics 31 (6) (2011) 1773–1791. (cit. on pp. 54)

[120] M. A. Fischer, D. Nanz, T. Hany, C. S. Reiner, P. Stolzmann, O. F. Donati, S. Breitenstein, P. Schneider, D. Weishaupt, G. K. von Schulthess, et al., Diagnostic accuracy of whole-body MRI/DWI image fusion for detection of malignant tumours: a comparison with PET/CT, European radiology 21 (2) (2011) 246–255. (cit. on pp. 55)

[121] Y. Liu, R. Bai, H. Sun, H. Liu, X. Zhao, Y. Li, Diffusion-weighted imaging in predicting and monitoring the response of uterine cervical cancer to combined chemoradiation, Clinical radiology 64 (11) (2009) 1067–1074. (cit. on pp. 55)

[122] M. Y. K. Bilgili, Reproductibility of apparent diffusion coefficients measurements in diffusion-weighted MRI of the abdomen with different b values, European journal of radiology 81 (9) (2012) 2066–2068. (cit. on pp. 55)

[123] J. M. Ludwig, J. C. Camacho, N. Kokabi, M. Xing, H. S. Kim, The role of diffusion-weighted imaging (DWI) in locoregional therapy outcome prediction and response assessment for hepatocellular carcinoma (HCC): the new era of functional imaging biomarkers, Diagnostics 5 (4) (2015) 546–563. (cit. on pp. 55)

[124] A. R. Padhani, Diffusion magnetic resonance imaging in cancer patient management, in: Seminars in radiation oncology, Vol. 21, Elsevier, 2011, pp. 119–140. (cit. on pp. 56, 200)

[125] X.-r. Li, L.-q. Cheng, M. Liu, Y.-j. Zhang, J.-d. Wang, A.-l. Zhang, X. Song, J. Li, Y.-q. Zheng, L. Liu, DW-MRI ADC values can predict treatment response in patients with locally advanced breast cancer undergoing neoadjuvant chemotherapy, Medical oncology 29 (2) (2012) 425–431. (cit. on pp. 56)

[126] K. Rozovsky, E. C. Ventureyra, E. Miller, Fast-brain MRI in children is quick, without sedation, and radiation-free, but beware of limitations, Journal of Clinical Neuroscience 20 (3) (2013) 400–405. (cit. on pp. 57)

[127] M. Zaitsev, J. Maclaren, M. Herbst, Motion artifacts in mri: a complex problem with many partial solutions, Journal of Magnetic Resonance Imaging 42 (4) (2015) 887–901. (cit. on pp. 57)

[128] M. H. Bagheri, M. M. Hosseini, M. J. Emami, A. A. Foroughi, Metallic artifact in MRI after removal of orthopedic implants, European journal of radiology 81 (3) (2012) 584–590. (cit. on pp. 57)

[129] P. Van Rossum, A. van Lier, I. Lips, G. Meijer, O. Reerink, M. van Vulpen, M. Lam, R. van Hillegersberg, J. Ruurda, Imaging of oesophageal cancer with FDG-PET/CT and MRI, Clinical radiology 70 (1) (2015) 81–95. (cit. on pp. 57)

[130] F. De Cobelli, F. Giganti, E. Orsenigo, M. Cellina, A. Esposito, G. Agostini, L. Albarello, E. Mazza, A. Ambrosi, C. Socci, et al., Apparent diffusion coefficient modifications in assessing gastro-oesophageal cancer response to neoadjuvant treatment: comparison with tumour regression grade at histology, European radiology 23 (8) (2013) 2165–2174. (cit. on pp. 57)

[131] S. H. Kim, J. Y. Lee, J. M. Lee, J. K. Han, B. I. Choi, Apparent diffusion coefficient for evaluating tumour response to neoadjuvant chemoradiation therapy for locally advanced rectal cancer, European radiology 21 (5) (2011) 987–995. (cit. on pp. 57)

[132] R. Fattahi, N. C. Balci, W. H. Perman, E. C. Hsueh, S. Alkaade, N. Havlioglu, F. R. Burton, Pancreatic diffusion-weighted imaging (DWI): comparison between mass-forming focal pancreatitis (FP), pancreatic cancer (PC), and normal pancreas, Journal of Magnetic Resonance Imaging: An Official Journal of the International Society for Magnetic Resonance in Medicine 29 (2) (2009) 350–356. (cit. on pp. 57)

[133] M. A. Haider, T. H. Van Der Kwast, J. Tanguay, A. J. Evans, A.-T. Hashmi, G. Lockwood, J. Trachtenberg, Combined T2-weighted and diffusion-weighted MRI for localization of prostate cancer, American journal of roentgenology 189 (2) (2007) 323–328. (cit. on pp. 57)

[134] Y. Peng, Y. Jiang, T. Antic, I. Sethi, C. Schmid-Tannwald, S. Eggener, A. Oto, Apparent diffusion coefficient for prostate cancer imaging: impact of B values, American Journal of Roentgenology 202 (3) (2014) W247–W253. (cit. on pp. 57)

[135] A. Lecler, J. Savatovsky, D. Balvay, M. Zmuda, J.-C. Sadik, O. Galatoire, F. Charbonneau, O. Bergès, H. Picard, L. Fournier, Repeatability of apparent diffusion coefficient and intravoxel incoherent motion parameters at 3.0 tesla in orbital lesions, European radiology 27 (12) (2017) 5094–5103. (cit. on pp. 58)

[136] K. M. Waterstram-Rich, D. Gilmore, Nuclear Medicine and PET/CT-E-Book: Technology and Techniques, Elsevier Health Sciences, 2016. (cit. on pp. 58, 61)

[137] P. Zanzonico, Principles of nuclear medicine imaging: planar, SPECT, PET, multi-modality, and autoradiography systems, Radiation research 177 (4) (2012) 349–364. (cit. on pp. 58)

[138] J. F. Oliver, M. Rafecas, Modelling random coincidences in positron emission tomography by using singles and prompts: a comparison study, PloS one 11 (9) (2016) e0162096. (cit. on pp. 58)

[139] W. Wadsak, M. Mitterhauser, Basics and principles of radiopharmaceuticals for PET/CT, European journal of radiology 73 (3) (2010) 461–469. (cit. on pp. 59)

[140] T. Ido, C.-N. Wan, V. Casella, J. Fowler, A. Wolf, M. Reivich, D. Kuhl, Labeled 2-deoxy-d-glucose analogs. 18f-labeled 2-deoxy-2-fluoro-d-glucose, 2-deoxy-2-fluoro-d-mannose and 14c-2-deoxy-2-fluoro-d-glucose, Journal of Labelled Compounds and Radiopharmaceuticals 14 (2) (1978) 175–183. (cit. on pp. 59)

[141] S. Hess, B. A. Blomberg, H. J. Zhu, P. F. Høilund-Carlsen, A. Alavi, The pivotal role of FDG-PET/CT in modern medicine, Academic radiology 21 (2) (2014) 232–249. (cit. on pp. 59, 64, 65, 66)

[142] M. C. Adams, T. G. Turkington, J. M. Wilson, T. Z. Wong, A systematic review of the factors affecting accuracy of suv measurements, American Journal of Roentgenology 195 (2) (2010) 310–320. (cit. on pp. 60, 65, 67, 185)

[143] G. Lucignani, Suv and segmentation: pressing challenges in tumour assessment and treatment, European journal of nuclear medicine and molecular imaging 36 (4) (2009) 715–720. (cit. on pp. 60)

[144] P. Kinahan, J. Fletcher, PET/CT standardized uptake values (SUVs) in clinical practice and assessing response to therapy, Semin Ultrasound CT MR 31 (6) (2010) 496–505. (cit. on pp. 60)

[145] M. Hofmann, B. Pichler, B. Schölkopf, T. Beyer, Towards quantitative PET/MRI: a review of MR-based attenuation correction techniques, European journal of nuclear medicine and molecular imaging 36 (1) (2009) 93–104. (cit. on pp. 60)

[146] S. N. Histed, M. L. Lindenberg, E. Mena, B. Turkbey, P. L. Choyke, K. A. Kurdziel, Review of functional/anatomic imaging in oncology, Nuclear medicine communications 33 (4) (2012) 349. (cit. on pp. 60)

[147] B. J. Pichler, A. Kolb, T. Nägele, H.-P. Schlemmer, PET/MRI: paving the way for the next generation of clinical multimodality imaging applications, Journal of Nuclear Medicine 51 (3) (2010) 333. (cit. on pp. 61)

[148] S. Vandenberghe, P. K. Marsden, PET-MRI: a review of challenges and solutions in the development of integrated multimodality imaging, Physics in Medicine & Biology 60 (4) (2015) R115. (cit. on pp. 61)

[149] A. Martinez-Möller, S. G. Nekolla, Attenuation correction for PET/MR: problems, novel approaches and practical solutions, Zeitschrift für Medizinische Physik 22 (4) (2012) 299–310. (cit. on pp. 61)

[150] D. A. Torigian, H. Zaidi, T. C. Kwee, B. Saboury, J. K. Udupa, Z.-H. Cho, A. Alavi, PET/MR imaging: technical aspects and potential clinical applications, Radiology 267 (1) (2013) 26–44. (cit. on pp. 61, 65)

[151] R. Haubner, PET radiopharmaceuticals in radiation treatment planning–synthesis and biological characteristics, Radiotherapy and Oncology 96 (3) (2010) 280–287. (cit. on pp. 64, 65)

[152] D. Campana, V. Ambrosini, R. Pezzilli, S. Fanti, A. M. M. Labate, D. Santini, C. Ceccarelli, F. Nori, R. Franchi, R. Corinaldesi, et al., Standardized uptake values of 68Ga-DOTANOC PET: a promising prognostic tool in neuroendocrine tumors, Journal of Nuclear Medicine 51 (3) (2010) 353. (cit. on pp. 64)

[153] V. Ambrosini, D. Campana, G. Polverari, C. Peterle, S. Diodato, C. Ricci, V. Allegri, R. Casadei, P. Tomassetti, S. Fanti, Prognostic value of 68Ga-DOTANOC PET/CT SUVmax in patients with neuroendocrine tumors of the pancreas, J Nucl Med 56 (12) (2015) 1843–8. (cit. on pp. 64)

[154] B. Nilica, D. Waitz, V. Stevanovic, C. Uprimny, D. Kendler, S. Buxbaum, B. Warwitz, L. Gerardo, B. Henninger, I. Virgolini, et al., Direct comparison of 68Ga-DOTA-TOC and 18F-FDG PET/CT in the follow-up of patients with neuroendocrine tumour treated with the first full peptide receptor radionuclide therapy cycle, European journal of nuclear medicine and molecular imaging 43 (9) (2016) 1585–1592. (cit. on pp. 64)

[155] F. Matteucci, E. Mezzenga, P. Caroli, V. Di Iorio, A. Sarnelli, M. Celli, L. Fantini, A. Moretti, R. Galassi, U. De Giorgi, et al., Reduction of 68Ga-PSMA renal uptake with mannitol infusion: preliminary results, European journal of nuclear medicine and molecular imaging 44 (13) (2017) 2189–2194. (cit. on pp. 65, 183, 184, 186, 187)

[156] C. Brendle, J. Kupferschläger, K. Nikolaou, C. la Fougère, S. Gatidis, C. Pfannenberg, Is the standard uptake value (SUV) appropriate for quantification in clinical PET imaging?–variability induced by different SUV measurements and varying reconstruction methods, European journal of radiology 84 (1) (2015) 158–162. (cit. on pp. 65)

[157] R. L. Wahl, H. Jacene, Y. Kasamon, M. A. Lodge, From RECIST to PERCIST: evolving considerations for PET response criteria in solid tumors, Journal of nuclear medicine: official publication, Society of Nuclear Medicine 50 (Suppl 1) (2009) 122S. (cit. on pp. 66)

[158] M. Soret, S. L. Bacharach, I. Buvat, Partial-volume effect in PET tumor imaging, Journal of Nuclear Medicine 48 (6) (2007) 932. (cit. on pp. 66, 184)

[159] N. C. Krak, R. Boellaard, O. S. Hoekstra, J. W. Twisk, C. J. Hoekstra, A. A. Lammertsma, Effects of ROI definition and reconstruction method on quantitative outcome and applicability in a response monitoring trial, European journal of nuclear medicine and molecular imaging 32 (3) (2005) 294–301. (cit. on pp. 66)

[160] S. Y. Kang, G. J. Cheon, M. Lee, H. S. Kim, J.-W. Kim, N.-H. Park, Y. S. Song, H. H. Chung, Prediction of recurrence by preoperative intratumoral FDG uptake heterogeneity in endometrioid endometrial cancer, Translational oncology 10 (2) (2017) 178–183. (cit. on pp. 66, 184)

[161] R. S. Lim, S. Ramdave, P. Beech, B. Billah, M. N. Karim, J. A. Smith, A. Safdar, E. Sigston, Utility of SUV max on 18 F-FDG PET in detecting cervical nodal metastases, Cancer Imaging 16 (1) (2016) 39. (cit. on pp. 67, 185)

[162] R. Beckers, S. Trebeschi, M. Maas, R. Schnerr, J. Sijmons, G. Beets, J. Houwers, R. Beets-Tan, D. Lambregts, CT texture analysis in colorectal liver metastases and the surrounding liver parenchyma and its potential as an imaging biomarker of disease aggressiveness, response and survival, European journal of radiology 102 (2018) 15–21. (cit. on pp. 70, 126)

[163] R. Lopes, N. Betrouni, Fractal and multifractal analysis: a review, Medical image analysis 13 (4) (2009) 634–649. (cit. on pp. 70, 72)

[164] S. Chicklore, V. Goh, M. Siddique, A. Roy, P. K. Marsden, G. J. Cook, Quantifying tumour heterogeneity in 18 F-FDG PET/CT imaging by texture analysis, European journal of nuclear medicine and molecular imaging 40 (1) (2013) 133–140. (cit. on pp. 70, 71)

[165] Z. Yang, L. H. Tang, D. S. Klimstra, Effect of tumor heterogeneity on the assessment of ki67 labeling index in well-differentiated neuroendocrine tumors metastatic to the liver: implications for prognostic stratification, The American journal of surgical pathology 35 (6) (2011) 853–860. (cit. on pp. 70)

[166] B. Ganeshan, K. Skogen, I. Pressney, D. Coutroubis, K. Miles, Tumour heterogeneity in oesophageal cancer assessed by CT texture analysis: preliminary evidence of an association with tumour metabolism, stage, and survival, Clinical radiology 67 (2) (2012) 157–164. (cit. on pp. 70)

[167] E. R. Davies, Machine vision: theory, algorithms, practicalities, Elsevier, 2004. (cit. on pp. 70, 75)

[168] C. A. Harlow, S. A. Eisenbeis, The analysis of radiographic images, IEEE Transactions on Computers 100 (7) (1973) 678–689. (cit. on pp. 70)

[169] S. Herlidou-Meme, J. Constans, B. Carsin, D. Olivie, P. Eliat, L. Nadal-Desbarats, C. Gondry, E. Le Rumeur, I. Idy-Peretti, J. De Certaines, MRI texture analysis on texture test objects, normal brain and intracranial tumors, Magnetic resonance imaging 21 (9) (2003) 989–993. (cit. on pp. 71)

[170] N. Sharma, A. K. Ray, S. Sharma, K. Shukla, S. Pradhan, L. M. Aggarwal, Segmentation and classification of medical images using texture-primitive features: Application of BAM-type artificial neural network, Journal of medical physics/Association of Medical Physicists of India 33 (3) (2008) 119. (cit. on pp. 71)

[171] T. Tweed, S. Miguet, Automatic detection of regions of interest in mammographies based on a combined analysis of texture and histogram, in: Pattern Recognition, 2002. Proceedings. 16th International Conference on, Vol. 2, IEEE, 2002, pp. 448–452. (cit. on pp. 71)

[172] K. Holli, A.-L. Lääperi, L. Harrison, T. Luukkaala, T. Toivonen, P. Ryymin, P. Dastidar, S. Soimakallio, H. Eskola, Characterization of breast cancer

types by texture analysis of magnetic resonance images, Academic radiology 17 (2) (2010) 135–141. (cit. on pp. 71)

[173] H. Bayanati, R. E. Thornhill, C. A. Souza, V. Sethi-Virmani, A. Gupta, D. Maziak, K. Amjadi, C. Dennie, Quantitative CT texture and shape analysis: Can it differentiate benign and malignant mediastinal lymph nodes in patients with primary lung cancer?, European radiology 25 (2) (2015) 480–487. (cit. on pp. 71)

[174] G. Castellano, L. Bonilha, L. Li, F. Cendes, Texture analysis of medical images, Clinical radiology 59 (12) (2004) 1061–1069. (cit. on pp. 71, 72)

[175] S. W. Zucker, Toward a model of texture, Computer Graphics and Image Processing 5 (2) (1976) 190–202. (cit. on pp. 71)

[176] A. Materka, M. Strzelecki, et al., Texture analysis methods–a review, Technical university of lodz, institute of electronics, COST B11 report, Brussels (1998) 9–11. (cit. on pp. 71, 72)

[177] M. H. Bharati, J. J. Liu, J. F. MacGregor, Image texture analysis: methods and comparisons, Chemometrics and intelligent laboratory systems 72 (1) (2004) 57–71. (cit. on pp. 71)

[178] M. Tuceryan, A. K. Jain, TEXTURE ANALYSIS, World Scientific, 1993. (cit. on pp. 72)

[179] F. Davnall, C. S. Yip, G. Ljungqvist, M. Selmi, F. Ng, B. Sanghera, B. Ganeshan, K. A. Miles, G. J. Cook, V. Goh, Assessment of tumor heterogeneity: an emerging imaging tool for clinical practice?, Insights into imaging 3 (6) (2012) 573–589. (cit. on pp. 72, 79, 127, 170)

[180] F. Tixier, C. C. Le Rest, M. Hatt, N. M. Albarghach, O. Pradier, J.-P. Metges, L. Corcos, D. Visvikis, Intratumor heterogeneity characterized by textural features on baseline 18F-FDG PET images predicts response to concomitant radiochemotherapy in esophageal cancer, Journal of Nuclear Medicine 52 (3) (2011) 369. (cit. on pp. 72, 200)

[181] F. Ng, B. Ganeshan, R. Kozarski, K. A. Miles, V. Goh, Assessment of primary colorectal cancer heterogeneity by using whole-tumor texture analysis: contrast-enhanced CT texture as a biomarker of 5-year survival, Radiology 266 (1) (2013) 177–184. (cit. on pp. 72, 127, 170)

[182] B. Julesz, E. Gilbert, L. Shepp, H. Frisch, Inability of humans to discriminate between visual textures that agree in second-order statisticsrevisited, Perception 2 (4) (1973) 391–405. (cit. on pp. 72)

[183] B. Julesz, Experiments in the visual perception of texture, Scientific American 232 (4) (1975) 34–43. (cit. on pp. 72)

[184] N. Sebe, M. S. Lew, Robust computer vision: Theory and applications, Vol. 26, Springer Science & Business Media, 2013. (cit. on pp. 72)

[185] U. Bashir, M. M. Siddique, E. Mclean, V. Goh, G. J. Cook, Imaging heterogeneity in lung cancer: techniques, applications, and challenges, American Journal of Roentgenology 207 (3) (2016) 534–543. (cit. on pp. 73)

[186] R. M. Haralick, K. Shanmugam, et al., Textural features for image classification, IEEE Transactions on systems, man, and cybernetics (6) (1973) 610–621. (cit. on pp. 75, 77)

[187] S. Theodoridis, K. Koutroumbas, Pattern Recognition, Second Edition, Academic Press, Inc., Orlando, FL, USA, 2003. (cit. on pp. 76)

[188] G. J. Cook, M. Siddique, B. P. Taylor, C. Yip, S. Chicklore, V. Goh, Radiomics in PET: principles and applications, Clinical and Translational Imaging 2 (3) (2014) 269–276. (cit. on pp. 78)

[189] M. M. Galloway, Texture analysis using gray level run lengths, Computer Graphics and Image Processing 4 (2) (1975) 172–179. (cit. on pp. 78, 79, 82)

[190] J. M. Sanches, J. C. Nascimento, J. S. Marques, Medical image noise reduction using the sylvester–lyapunov equation, IEEE transactions on image processing 17 (9) (2008) 1522–1539. (cit. on pp. 83)

[191] J. Chen, W. Cranton, M. Fihn, Handbook of visual display technology, Vol. 131, Springer Berlin, 2012. (cit. on pp. 84)

[192] R. C. Gonzalez, R. E. Woods, Digital image processing second edition, 2001. (cit. on pp. 84)

[193] P.-E. Ng, K.-K. Ma, A switching median filter with boundary discriminative noise detection for extremely corrupted images, IEEE Transactions on image processing 15 (6) (2006) 1506–1516. (cit. on pp. 84)

[194] Z. Wang, D. Zhang, Progressive switching median filter for the removal of impulse noise from highly corrupted images, IEEE Transactions on Circuits and Systems II: Analog and Digital Signal Processing 46 (1) (1999) 78–80. (cit. on pp. 84)

[195] M. W. Huellner, T. D. Collen, P. Gut, R. Winterhalder, C. Pauli, J. Diebold, B. Seifert, K. Strobel, P. Veit-Haibach, Multiparametric PET/CT-perfusion does not add significant additional information for initial staging in lung cancer compared with standard PET/CT, EJNMMI research 4 (1) (2014) 6. (cit. on pp. 90)

[196] T. San Koh, C. H. Thng, S. Hartono, P. S. Lee, S. P. Choo, D. Y. Poon, H. C. Toh, S. Bisdas, Dynamic contrast-enhanced CT imaging of hepatocellular carcinoma in cirrhosis: feasibility of a prolonged dual-phase imaging protocol with tracer kinetics modeling, European radiology 19 (5) (2009) 1184. (cit. on pp. 90, 153)

[197] C. S. Ng, A. G. Chandler, W. Wei, E. F. Anderson, D. H. Herron, C. Charnsangavej, R. Kurzrock, Reproducibility of perfusion parameters obtained from perfusion CT in lung tumors, American Journal of Roentgenology 197 (1) (2011) 113–121. (cit. on pp. 90)

[198] C. S. Ng, A. G. Chandler, W. Wei, D. H. Herron, E. F. Anderson, R. Kurzrock, C. Charnsangavej, Reproducibility of CT perfusion parameters in liver tumors and normal liver, Radiology 260 (3) (2011) 762–770. (cit. on pp. 90)

[199] A. Bevilacqua, D. Barone, S. Malavasi, G. Gavelli, Quantitative assessment of effects of motion compensation for liver and lung tumors in CT perfusion, Academic radiology 21 (11) (2014) 1416–1426. (cit. on pp. 90, 127, 140, 141, 143)

[200] A. Bevilacqua, D. Barone, S. Baiocco, G. Gavelli, A novel approach for semi-quantitative assessment of reliability of blood flow values in DCE-CT perfusion, Biomed. Signal Process. Control 31 (2017) 257–264. (cit. on pp. 90, 93, 141, 153, 171)

[201] A. Bevilacqua, D. Barone, S. Malavasi, G. Gavelli, Automatic detection of misleading blood flow values in CT perfusion studies of lung cancer,

Biomedical signal processing and control 26 (2016) 109–116. (cit. on pp. 92, 130, 176)

[202] H. Zaidi, I. El Naqa, PET-guided delineation of radiation therapy treatment volumes: a survey of image segmentation techniques, European journal of nuclear medicine and molecular imaging 37 (11) (2010) 2165–2187. (cit. on pp. 96, 97)

[203] Q. Huang, F. Yang, L. Liu, X. Li, Automatic segmentation of breast lesions for interaction in ultrasonic computer-aided diagnosis, Information Sciences 314 (2015) 293–310. (cit. on pp. 96)

[204] P. Seow, M. Win, J. Wong, N. Abdullah, N. Ramli, Segmentation of solid subregion of high grade gliomas in MRI images based on active contour model (ACM), in: Journal of Physics: Conference Series, Vol. 694, IOP Publishing, 2016, p. 012043. (cit. on pp. 96)

[205] S. Ghose, L. Holloway, K. Lim, P. Chan, J. Veera, S. K. Vinod, G. Liney, P. B. Greer, J. Dowling, A review of segmentation and deformable registration methods applied to adaptive cervical cancer radiation therapy treatment planning, Artificial intelligence in medicine 64 (2) (2015) 75–87. (cit. on pp. 96)

[206] W. Grootjans, E. A. Usmanij, W. J. Oyen, E. H. van der Heijden, E. P. Visser, D. Visvikis, M. Hatt, J. Bussink, L.-F. de Geus-Oei, Performance of automatic image segmentation algorithms for calculating total lesion glycolysis for early response monitoring in non-small cell lung cancer patients during concomitant chemoradiotherapy, Radiotherapy and Oncology 119 (3) (2016) 473–479. (cit. on pp. 96)

[207] T. Zuva, O. O. Olugbara, S. O. Ojo, S. M. Ngwira, Image segmentation, available techniques, developments and open issues, Canadian Journal on Image Processing and Computer Vision 2 (3) (2011) 20–29. (cit. on pp. 96)

[208] D. L. Pham, C. Xu, J. L. Prince, Current methods in medical image segmentation, Annual review of biomedical engineering 2 (1) (2000) 315–337. (cit. on pp. 96)

[209] M. H. J. Vala, A. Baxi, A review on otsu image segmentation algorithm, International Journal of Advanced Research in Computer Engineering & Technology (IJARCET) 2 (2) (2013) pp–387. (cit. on pp. 96)

[210] R. Adams, L. Bischof, Seeded region growing, IEEE Transactions on pattern analysis and machine intelligence 16 (6) (1994) 641–647. (cit. on pp. 96)

[211] K.-S. Chuang, H.-L. Tzeng, S. Chen, J. Wu, T.-J. Chen, Fuzzy c-means clustering with spatial information for image segmentation, Computerized Medical Imaging and Graphics 30 (1) (2006) 9–15. (cit. on pp. 96)

[212] M. Ozkan, B. M. Dawant, R. J. Maciunas, Neural-network-based segmentation of multi-modal medical images: a comparative and prospective study, IEEE transactions on Medical Imaging 12 (3) (1993) 534–544. (cit. on pp. 96)

[213] C. A. Schneider, W. S. Rasband, K. W. Eliceiri, Nih image to imagej: 25 years of image analysis, Nature methods 9 (7) (2012) 671. (cit. on pp. 97, 108, 195)

[214] S. Bolte, F. Cordelieres, A guided tour into subcellular colocalization analysis in light microscopy, Journal of microscopy 224 (3) (2006) 213–232. (cit. on pp. 99)

[215] J. Ollion, J. Cochennec, F. Loll, C. Escude, T. Boudier, TANGO: a generic tool for high-throughput 3D image analysis for studying nuclear organization, Bioinformatics 29 (14) (2013) 1840–1841. (cit. on pp. 99)

[216] J. Tsao, Interpolation artifacts in multimodality image registration based on maximization of mutual information, IEEE Trans. Med. Imaging 22 (7) (2003) 854–864. (cit. on pp. 101)

[217] B. Zitova, J. Flusser, Image registration methods: a survey, Image and vision computing 21 (11) (2003) 977–1000. (cit. on pp. 101, 108)

[218] K. Rohr, H. S. Stiehl, R. Sprengel, T. M. Buzug, J. Weese, M. Kuhn, Landmark-based elastic registration using approximating thin-plate splines, IEEE Transactions on medical imaging 20 (6) (2001) 526–534. (cit. on pp. 102)

[219] S. Wörz, K. Rohr, Physics-based elastic registration using non-radial basis functions and including landmark localization uncertainties, Computer Vision and Image Understanding 111 (3) (2008) 263–274. (cit. on pp. 102)

[220] A. Klein, S. S. Ghosh, B. Avants, B. T. Yeo, B. Fischl, B. Ardekani, J. C. Gee, J. J. Mann, R. V. Parsey, Evaluation of volume-based and surface-based brain image registration methods, Neuroimage 51 (1) (2010) 214–220. (cit. on pp. 104)

[221] M. A. Viergever, J. A. Maintz, S. Klein, K. Murphy, M. Staring, J. P. Pluim, A survey of medical image registration–under review (2016). (cit. on pp. 104)

[222] V. Roshni, K. Revathy, Using mutual information and cross correlation as metrics for registration of images., Journal of Theoretical & Applied Information Technology 4 (6) (2008) 474–481. (cit. on pp. 105)

[223] J. Kim, J. A. Fessler, Intensity-based image registration using robust correlation coefficients, IEEE transactions on medical imaging 23 (11) (2004) 1430–1444. (cit. on pp. 106)

[224] F. Klevebro, G. Johnsen, E. Johnson, A. Viste, T. Myrnäs, E. Szabo, A.-B. Jacobsen, S. Friesland, J. Tsai, S. Persson, et al., Morbidity and mortality after surgery for cancer of the oesophagus and gastro-oesophageal junction: A randomized clinical trial of neoadjuvant chemotherapy vs. neoadjuvant chemoradiation, European Journal of Surgical Oncology (EJSO) 41 (7) (2015) 920–926. (cit. on pp. 108)

[225] S. Lagarde, A. Phillips, M. Navidi, B. Disep, A. Immanuel, S. Griffin, The presence of lymphovascular and perineural infiltration after neoadjuvant therapy and oesophagectomy identifies patients at high risk for recurrence, British journal of cancer 113 (10) (2015) 1427. (cit. on pp. 108)

[226] T. Andersson, M. Borga, O. D. Leinhard, Geodesic registration for interactive atlas-based segmentation using learned multi-scale anatomical manifolds, Pattern Recognition Letters. (cit. on pp. 111)

[227] S. Klein, M. Staring, K. Murphy, M. A. Viergever, J. P. Pluim, Elastix: a toolbox for intensity-based medical image registration, IEEE transactions on medical imaging 29 (1) (2010) 196–205. (cit. on pp. 120)

[228] D. Bird, A. F. Scarsbrook, J. Sykes, S. Ramasamy, M. Subesinghe, B. Carey, D. J. Wilson, N. Roberts, G. McDermott, E. Karakaya, et al., Multimodality imaging with CT, MR and FDG-PET for radiotherapy target volume delineation in oropharyngeal squamous cell carcinoma, BMC cancer 15 (1) (2015) 844. (cit. on pp. 120)

[229] A. C. Paulino, M. Koshy, R. Howell, D. Schuster, L. W. Davis, Comparison of CT-and FDG-PET-defined gross tumor volume in intensity-modulated radiotherapy for head-and-neck cancer, International Journal of Radiation Oncology* Biology* Physics 61 (5) (2005) 1385–1392. (cit. on pp. 120)

[230] D. Daunoravicius, J. Besusparis, E. Zurauskas, A. Laurinaviciene, D. Bironaite, S. Pankuweit, B. Plancoulaine, P. Herlin, J. Bogomolovas, V. Grabauskiene, et al., Quantification of myocardial fibrosis by digital image analysis and interactive stereology, Diagnostic pathology 9 (1) (2014) 114. (cit. on pp. 126)

[231] A. E. Rizzardi, A. T. Johnson, R. I. Vogel, S. E. Pambuccian, J. Henriksen, A. Skubitz, G. J. Metzger, S. C. Schmechel, Quantitative comparison of immunohistochemical staining measured by digital image analysis versus pathologist visual scoring, Diagn Pathol 7 (42) (2012) 1596–7. (cit. on pp. 126)

[232] B. F. Meyers, R. J. Downey, P. A. Decker, R. J. Keenan, B. A. Siegel, R. J. Cerfolio, R. J. Landreneau, C. E. Reed, D. M. Balfe, F. Dehdashti, et al., The utility of positron emission tomography in staging of potentially operable carcinoma of the thoracic esophagus: results of the american college of surgeons oncology group z0060 trial, The Journal of thoracic and cardiovascular surgery 133 (3) (2007) 738–745. (cit. on pp. 126)

[233] S. Obenauer, K. Hermann, E. Grabbe, Applications and literature review of the BI-RADS classification, European radiology 15 (5) (2005) 1027–1036. (cit. on pp. 127)

[234] S. K. Kinoshita, P. M. de Azevedo-Marques, R. R. Pereira Jr, J. A. H. Rodrigues, R. M. Rangayyan, Content-based retrieval of mammograms using visual features related to breast density patterns, Journal of Digital Imaging 20 (2) (2007) 172–190. (cit. on pp. 127)

[235] F. Ng, R. Kozarski, B. Ganeshan, V. Goh, Assessment of tumor heterogeneity by CT texture analysis: can the largest cross-sectional area be used as an alternative to whole tumor analysis?, European journal of radiology 82 (2) (2013) 342–348. (cit. on pp. 127)

[236] P. Lambin, E. Rios-Velazquez, R. Leijenaar, S. Carvalho, R. G. van Stiphout, P. Granton, C. M. Zegers, R. Gillies, R. Boellard, A. Dekker, A. Hugo J, Radiomics: extracting more information from medical images using advanced feature analysis, European Journal of Cancer 48 (4) (2012) 441–446. (cit. on pp. 127, 170)

[237] V. Goh, B. Ganeshan, P. Nathan, J. K. Juttla, A. Vinayan, K. A. Miles, Assessment of response to tyrosine kinase inhibitors in metastatic renal cell cancer: CT texture as a predictive biomarker, Radiology 261 (1) (2011) 165–171. (cit. on pp. 127)

[238] Y. Xu, H. Sun, A. Song, Q. Yang, X. Lu, W. Wang, Predictive Significance of Tumor Grade Using 256-Slice CT Whole-Tumor Perfusion Imaging in Colorectal Adenocarcinoma, Academic radiology 22 (12) (2015) 1529–1535. (cit. on pp. 127)

[239] V. Goh, B. Sanghera, D. M. Wellsted, J. Sundin, S. Halligan, Assessment of the spatial pattern of colorectal tumour perfusion estimated at perfusion CT using two-dimensional fractal analysis, European radiology 19 (6) (2009) 1358–1365. (cit. on pp. 127)

[240] M. Cao, Y. Liang, C. Shen, K. D. Miller, K. M. Stantz, Developing DCE-CT to quantify intra-tumor heterogeneity in breast tumors with differing angiogenic phenotype, Medical Imaging, IEEE Transactions on 28 (6) (2009) 861–871. (cit. on pp. 127)

[241] J. Zar, Biostatistical Analysis, 5th Edition, Prentice Hall, Upper Saddle River, New Jersey, 2010. (cit. on pp. 131)

[242] X. Yuan, J. Zhang, C. Quan, J. Cao, G. Ao, Y. Tian, H. Li, Differentiation of malignant and benign pulmonary nodules with first-pass dual-input perfusion CT, European radiology 23 (9) (2013) 2469–2474. (cit. on pp. 140)

[243] M. Bellomi, S. Viotti, L. Preda, G. D'Andrea, L. Bonello, G. Petralia, Perfusion CT in solid body-tumours part II. Clinical applications and future development, La radiologia medica 115 (6) (2010) 858–874. (cit. on pp. 140)

[244] D. L. Raunig, L. M. McShane, G. Pennello, C. Gatsonis, P. L. Carson, J. T. Voyvodic, R. L. Wahl, B. F. Kurland, A. J. Schwarz, M. Gönen, et al., Quantitative imaging biomarkers: A review of statistical methods for technical performance assessment, Stat. Methods Med. Res. 24 (1) (2015) 27–67. (cit. on pp. 140)

[245] V. Goh, S. Halligan, A. Gharpuray, D. Wellsted, J. Sundin, C. I. Bartram, Quantitative assessment of colorectal cancer tumor vascular parameters by using perfusion CT: Influence of tumor region of interest, Radiology 247 (3) (2008) 726–732. (cit. on pp. 140)

[246] M. König, E. Bültmann, L. Bode-Schnurbus, D. Koenen, E. Mielke, L. Heuser, Image quality in CT perfusion imaging of the brain, Eur. Radiol. 17 (1) (2007) 39–47. (cit. on pp. 141, 143, 149)

[247] B. Ganeshan, E. Panayiotou, K. Burnand, S. Dizdarevic, K. Miles, Tumour heterogeneity in non-small cell lung carcinoma assessed by CT texture analysis: a potential marker of survival, Eur. Radiol. 22 (4) (2012) 796–802. (cit. on pp. 143, 170, 177)

[248] J. Zar, Biostatistical Analysis, Prentice Hall, 1999. (cit. on pp. 144)

[249] C. J. Feltz, G. E. Miller, An asymptotic test for the equality of coefficients of variation from k populations, Statistics in Medicine 15 (6) (1996) 647–658. (cit. on pp. 144)

[250] C. S. Ng, A. G. Chandler, W. Wei, E. F. Anderson, D. H. Herron, R. Kurzrock, C. Charnsangavej, Effect of sampling frequency on perfusion values in CT perfusion of lung tumors, AJR. American journal of roentgenology 200 (2). (cit. on pp. 149)

[251] R. N. Eskander, K. S. Tewari, Incorporation of anti-angiogenesis therapy in the management of advanced ovarian carcinomamechanistics, review of phase III randomized clinical trials, and regulatory implications, Gynecol. Oncol. 132 (2) (2014) 496–505. (cit. on pp. 152)

[252] B. Romain, L. Rouet, D. Ohayon, O. Lucidarme, F. dAlch Buc, V. Letort, Parameter estimation of perfusion models in dynamic contrast-enhanced imaging: a unified framework for model comparison, Med. Image Anal. 35 (1) (2017) 360–374. (cit. on pp. 152)

[253] A. B. Gill, N. J. Hilliard, S. T. Hilliard, M. J. Graves, D. J. Lomas, A. Shaw, A semi-automatic method for the extraction of the portal venous input function in quantitative dynamic contrast-enhanced CT of the liver, Br. J. Radiol. 90 (1075) (2017) 20160875. (cit. on pp. 152)

[254] S. Malavasi, D. Barone, G. Gavelli, A. Bevilacqua, Multislice Analysis of Blood Flow Values in CT Perfusion Studies of Lung Cancer, BioMed Res. Int. 2017 (Article ID 3236893) (2017) 11 pages. (cit. on pp. 152)

[255] A. So, E. Stewart, C. d'Esterre, T. Pok Chi Yeung, G. Bauman, N. Jensen, E. Wong, T.-Y. Lee, CT Perfusion: Principles, Implementation, and Clinical Applications, in: J. Fagerberg, D. C. Mowery, R. R. Nelson (Eds.), Multidetector CT Imaging: Principles, Head, Neck, and Vascular Systems, CRC Press, 2013, Ch. 2, p. 29. (cit. on pp. 152)

[256] R. García-Figueiras, V. J. Goh, A. R. Padhani, S. Baleato-González, M. Garrido, L. León, A. Gómez-Caamaño, CT perfusion in oncologic imaging: a useful tool?, Am. J. Roentgenol. 200 (1) (2013) 8–19. (cit. on pp. 152)

[257] F. Shan, Z. Zhang, W. Xing, J. Qiu, S. Yang, J. Wang, Y. Jiang, G. Chen, Differentiation between malignant and benign solitary pulmonary nodules: Use of volume first-pass perfusion and combined with routine computed tomography, Eur. J. Radiol. 81 (11) (2012) 3598–3605. (cit. on pp. 152)

[258] F. Fraioli, M. Anzidei, F. Zaccagna, M. L. Mennini, G. Serra, B. Gori, F. Longo, C. Catalano, R. Passariello, Whole-tumor perfusion CT in patients with advanced lung adenocarcinoma treated with conventional and antiangiogenetic chemotherapy: initial experience, Radiology 259 (2) (2011) 574–582. (cit. on pp. 152)

[259] E. E. Graves, A. Maity, Q.-T. Le, The tumor microenvironment in non–small-cell lung cancer, Semin. Radiat. Oncol. 20 (3) (2010) 156–163. (cit. on pp. 152)

[260] H. C. Mandeville, Q. S. Ng, F. M. Daley, P. R. Barber, G. Pierce, J. Finch, M. Burke, A. Bell, E. R. Townsend, R. Kozarski, et al., Operable non–small cell lung cancer: correlation of volumetric helical dynamic contrast-enhanced CT parameters with immunohistochemical markers of tumor hypoxia, Radiology 264 (2) (2012) 581–589. (cit. on pp. 153, 166)

[261] J. Shi, G. Schmid-Bindert, C. Fink, S. Sudarski, P. Apfaltrer, L. R. Pilz, B. Liu, U. Haberland, E. Klotz, C. Zhou, et al., Dynamic volume perfusion CT in patients with lung cancer: baseline perfusion characteristics of different histological subtypes, Eur. J. Radiol. 82 (12) (2013) e894–e900. (cit. on pp. 153, 166)

[262] S.-H. Ma, K. Xu, Z.-W. Xiao, M. Wu, Z.-Y. Sun, Z.-X. Wang, Z.-G. Hu, X. Dai, M.-J. Han, Y.-G. Li, Peripheral lung cancer: relationship between multi-slice spiral CT perfusion imaging and tumor angiogenesis and cyclin D1 expression, Clin. Imaging 31 (3) (2007) 165–177. (cit. on pp. 153)

[263] A. W. Sauter, S. Winterstein, D. Spira, J. Hetzel, M. Schulze, M. Mueller, C. Pfannenberg, C. D. Claussen, E. Klotz, C. H. von Weyhern, et al., Multifunctional profiling of non–small cell lung cancer using 18F-FDG PET/CT and volume perfusion CT, J. Nucl. Med. 53 (4) (2012) 521–529. (cit. on pp. 153, 166)

[264] W. van Elmpt, C. M. Zegers, B. Reymen, A. J. Even, A.-M. C. Dingemans, M. Oellers, J. E. Wildberger, F. M. Mottaghy, M. Das, E. G. Troost, et al., Multiparametric imaging of patient and tumour heterogeneity in non-small-cell lung cancer: quantification of tumour hypoxia, metabolism and perfusion, Eur. J. Nucl. Med. Mol. Imaging 43 (2) (2016) 240–248. (cit. on pp. 153)

[265] S. Nakano, J. Gibo, Y. Fukushima, K. Kaira, N. Sunaga, A. Taketomi-Takahashi, Y. Tsushima, M. Mori, Perfusion evaluation of lung cancer: assessment using dual-input perfusion computed tomography, J. Thorac. Imaging 28 (4) (2013) 253–262. (cit. on pp. 153, 155, 158, 166)

[266] D. Spira, H. Neumeister, S. M. Spira, J. Hetzel, W. Spengler, C. H. von Weyhern, M. Horger, Assessment of tumor vascularity in lung cancer using volume perfusion CT (VPCT) with histopathologic comparison: a further

step toward an individualized tumor characterization, J. Comput. Assist. Tomogr. 37 (1) (2013) 15–21. (cit. on pp. 153)

[267] E.-J. Kang, K.-N. Lee, J.-Y. Han, M. S. Roh, C. Son, Evaluation of dual-input perfusion in lung cancer using a 320-detector CT: Its correlation with tumor size, location, and presence of metastasis, J. Korean Soc. Radiol. 75 (5) (2016) 354–362. (cit. on pp. 153)

[268] A. Bevilacqua, D. Barone, S. Malavasi, G. Gavelli, Automatic detection of misleading blood flow values in CT perfusion studies of lung cancer, Biomed. Signal Process. Control 26 (2016) 109–116. (cit. on pp. 153, 156, 165)

[269] F. Kiessling, J. Boese, C. Corvinus, J. Ederle, I. Zuna, S. Schoenberg, G. Brix, A. Schmähl, S. Tuengerthal, F. Herth, et al., Perfusion CT in patients with advanced bronchial carcinomas: a novel chance for characterization and treatment monitoring?, Eur. Radiol. 14 (7) (2004) 1226–1233. (cit. on pp. 153, 155, 166, 167)

[270] D. Ippolito, G. Querques, S. Okolicsanyi, C. T. Franzesi, M. Strazzabosco, S. Sironi, Diagnostic value of dynamic contrast-enhanced CT with perfusion imaging in the quantitative assessment of tumor response to sorafenib in patients with advanced hepatocellular carcinoma: A feasibility study, Eur. J. Radiol. 90 (2017) 34–41. (cit. on pp. 156)

[271] E. A. S. Bretas, U. S. Torres, L. R. Torres, D. Bekhor, C. F. Saito Filho, D. J. Racy, L. Faggioni, G. D'Ippolito, Is liver perfusion CT reproducible? A study on intra- and interobserver agreement of normal hepatic hemodynamic parameters obtained with two different software packages, Br. J. Radiol. 90 (1078) (2017) 20170214. (cit. on pp. 156)

[272] D. Lardinois, P. De Leyn, P. Van Schil, R. R. Porta, D. Waller, B. Passlick, M. Zielinski, K. Junker, E. A. Rendina, H.-B. Ris, et al., Ests guidelines for intraoperative lymph node staging in non-small cell lung cancer, Eur. J. Cardio-Thorac. Surg. 30 (5) (2006) 787–792. (cit. on pp. 158)

[273] L. Eldridge, A. Moldobaeva, Q. Zhong, J. Jenkins, M. Snyder, R. H. Brown, W. Mitzner, E. M. Wagner, Bronchial artery angiogenesis drives lung tumor growth, Cancer Res. 76 (20) (2016) 5962–5969. (cit. on pp. 160)

[274] A. Bevilacqua, G. Gavelli, S. Baiocco, D. Barone, CT Perfusion in Patients with Lung Cancer: Squamous Cell Carcinoma and Adenocarcinoma Show a Different Blood Flow, BioMed Research International 2018, 6942131. (cit. on pp. 165, 176)

[275] T. D. L. Nguyen-Kim, T. Frauenfelder, K. Strobel, P. Veit-Haibach, M. W. Huellner, Assessment of bronchial and pulmonary blood supply in non-small cell lung cancer subtypes using computed tomography perfusion, Invest. Radiol. 50 (3) (2015) 179–186. (cit. on pp. 165, 166)

[276] Z. Chen, C. M. Fillmore, P. S. Hammerman, C. F. Kim, K.-K. Wong, Non-small-cell lung cancers: a heterogeneous set of diseases, Nat. Rev. Cancer 14 (8) (2014) 535–546. (cit. on pp. 170)

[277] H. Wang, M. Naghavi, C. Allen, R. M. Barber, Z. A. Bhutta, A. Carter, D. C. Casey, F. J. Charlson, A. Z. Chen, M. M. Coates, et al., Global, regional, and national life expectancy, all-cause mortality, and cause-specific mortality for 249 causes of death, 1980–2015: a systematic analysis for the Global Burden of Disease Study 2015, The lancet 388 (10053) (2016) 1459–1544. (cit. on pp. 170)

[278] Y. Xu, H. Sun, Z. Zhang, A. Song, W. Wang, X. Lu, Assessment of relationship between CT features and serum tumor marker index in early-stage lung adenocarcinoma, Acad. Radiol. 23 (11) (2016) 1342–1348. (cit. on pp. 170)

[279] M. Reck, D. F. Heigener, T. Mok, J.-C. Soria, K. F. Rabe, Management of non-small-cell lung cancer: recent developments, Lancet 382 (9893) (2013) 709–719. (cit. on pp. 170)

[280] M. Alexander, R. Wolfe, D. Ball, M. Conron, R. G. Stirling, B. Solomon, M. MacManus, A. Officer, S. Karnam, K. Burbury, et al., Lung cancer prognostic index: a risk score to predict overall survival after the diagnosis of non-small-cell lung cancer, British journal of cancer 117 (5) (2017) 744. (cit. on pp. 170)

[281] S. G. Spiro, N. T. Tanner, G. A. Silvestri, S. M. Janes, E. Lim, J. F. Vansteenkiste, R. Pirker, Lung cancer: progress in diagnosis, staging and therapy, Respirology 15 (1) (2010) 44–50. (cit. on pp. 170)

[282] C. Yip, D. Landau, R. Kozarski, B. Ganeshan, R. Thomas, A. Michaelidou, V. Goh, Primary esophageal cancer: heterogeneity as potential prognostic biomarker in patients treated with definitive chemotherapy and radiation therapy, Radiology 270 (1) (2014) 141–148. (cit. on pp. 170)

[283] T. Lee, T. Purdie, E. Stewart, CT imaging of angiogenesis, The Quarterly Journal of Nuclear Medicine and Molecular Imaging 47 (3) (2003) 171. (cit. on pp. 170)

[284] B. Ganeshan, K. A. Miles, Quantifying tumour heterogeneity with CT, Cancer imaging 13 (1) (2013) 140. (cit. on pp. 170)

[285] D. Prezzi, A. Khan, V. Goh, Perfusion CT imaging of treatment response in oncology, European journal of radiology 84 (12) (2015) 2380–2385. (cit. on pp. 170)

[286] S. Baiocco, D. Barone, G. Gavelli, A. Bevilacqua, Analysis of CT Perfusion Blood Flow maps in Patients with Lung Cancer: Correlation with the Overall Survival, in: 23rd Conference of Open Innovations Association (FRUCT), IEEE, 2018, pp. 55–61. (cit. on pp. 171)

[287] M. G. Lubner, A. D. Smith, K. Sandrasegaran, D. V. Sahani, P. J. Pickhardt, CT Texture Analysis: Definitions, Applications, Biologic Correlates, and Challenges, Radiographics 37 (5) (2017) 1483–1503. (cit. on pp. 176)

[288] B. Ganeshan, K. A. Miles, R. C. Young, C. R. Chatwin, Hepatic enhancement in colorectal cancer: texture analysis correlates with hepatic hemodynamics and patient survival, Academic radiology 14 (12) (2007) 1520–1530. (cit. on pp. 176)

[289] K. Skogen, B. Ganeshan, T. Good, G. Critchley, K. Miles, Imaging heterogeneity in gliomas using texture analysis., Cancer Imaging 11 (2011) S113. (cit. on pp. 176)

[290] J.-H. Kim, E. S. Ko, Y. Lim, K. S. Lee, B.-K. Han, E. Y. Ko, S. Y. Hahn, S. J. Nam, Breast cancer heterogeneity: MR imaging texture analysis and survival outcomes, Radiology 282 (3) (2016) 665–675. (cit. on pp. 176)

[291] M. Craigie, J. Squires, K. Miles, Can CT measures of tumour heterogeneity stratify risk for nodal metastasis in patients with non-small cell lung cancer?, Clinical radiology 72 (10) (2017) 899–e1. (cit. on pp. 181)

[292] F. Wagner, Y. A. Hakami, G. Warnock, G. Fischer, M. W. Huellner, P. Veit-Haibach, Comparison of contrast-enhanced CT and [18F] FDG PET/CT analysis using kurtosis and skewness in patients with primary colorectal cancer, Molecular imaging and biology 19 (5) (2017) 795–803. (cit. on pp. 181)

[293] A. Afshar-Oromieh, E. Avtzi, F. L. Giesel, T. Holland-Letz, H. G. Linhart, M. Eder, M. Eisenhut, S. Boxler, B. A. Hadaschik, C. Kratochwil, et al., The diagnostic value of PET/CT imaging with the 68 Ga-labelled PSMA ligand HBED-CC in the diagnosis of recurrent prostate cancer, European journal of nuclear medicine and molecular imaging 42 (2) (2015) 197–209. (cit. on pp. 184)

[294] S. Han, S. Woo, Y. J. Kim, C. H. Suh, Impact of 68 Ga-PSMA PET on the Management of Patients with Prostate Cancer: A Systematic Review and Meta-analysis, European urology. (cit. on pp. 184)

[295] A. Afshar-Oromieh, C. M. Zechmann, A. Malcher, M. Eder, M. Eisenhut, H. G. Linhart, T. Holland-Letz, B. A. Hadaschik, F. L. Giesel, J. Debus, et al., Comparison of PET imaging with a 68 Ga-labelled PSMA ligand and 18 F-choline-based PET/CT for the diagnosis of recurrent prostate cancer, European journal of nuclear medicine and molecular imaging 41 (1) (2014) 11–20. (cit. on pp. 184)

[296] S. Mannweiler, P. Amersdorfer, S. Trajanoski, J. A. Terrett, D. King, G. Mehes, Heterogeneity of prostate-specific membrane antigen (psma) expression in prostate carcinoma with distant metastasis, Pathology & Oncology Research 15 (2) (2009) 167–172. (cit. on pp. 184)

[297] A. Baccala, L. Sercia, J. Li, W. Heston, M. Zhou, Expression of prostate-specific membrane antigen in tumor-associated neovasculature of renal neoplasms, Urology 70 (2) (2007) 385–390. (cit. on pp. 184)

[298] N. C. Schwertman, M. A. Owens, R. Adnan, A simple more general boxplot method for identifying outliers, Computational statistics & data analysis 47 (1) (2004) 165–174. (cit. on pp. 186)

[299] S. Okamoto, A. Thieme, J. Allmann, C. DAlessandria, T. Maurer, M. Retz, R. Tauber, M. M. Heck, H.-J. Wester, N. Tamaki, et al., Radiation Dosime-

try for 177Lu-PSMA I&T in Metastatic Castration-Resistant Prostate Cancer: Absorbed Dose in Normal Organs and Tumor Lesions, Journal of Nuclear Medicine 58 (3) (2017) 445–450. (cit. on pp. 187)

[300] M. A. Lodge, M. A. Chaudhry, R. L. Wahl, Noise considerations for PET quantification using maximum and peak standardized uptake value, Journal of nuclear medicine: official publication, Society of Nuclear Medicine 53 (7) (2012) 1041. (cit. on pp. 189)

[301] O. Ercelep, O. Alan, D. Sahin, T. Telli, H. Salva, T. Tuylu, N. Babacan, S. Kaya, F. Dane, T. Ones, et al., Effect of PET/CT standardized uptake values on complete response to treatment before definitive chemoradiotherapy in stage III non-small cell lung cancer, Clinical and Translational Oncology (2018) 1–6. (cit. on pp. 191)

[302] T. Yahata, S. Yagi, Y. Mabuchi, Y. Tanizaki, A. Kobayashi, M. Yamamoto, M. Mizoguchi, S. Nanjo, M. Shiro, N. Ota, et al., Prognostic impact of primary tumor suvmax on preoperative 18f-fluoro-2-deoxy-D-glucose positron emission tomography and computed tomography in endometrial cancer and uterine carcinosarcoma, Molecular and clinical oncology 5 (4) (2016) 467–474. (cit. on pp. 191)

[303] I. Pergolini, S. Crippa, M. Salgarello, G. Belfiori, S. Partelli, G. Ruffo, A. Pucci, G. Zamboni, M. Falconi, SUVmax after (18) fluoro-deoxyglucose positron emission tomography/computed tomography: A tool to define treatment strategies in pancreatic cancer, Digestive and Liver Disease 50 (1) (2018) 84–90. (cit. on pp. 191)

[304] B.-R. Sah, K. Owczarczyk, M. Siddique, G. J. Cook, V. Goh, Radiomics in esophageal and gastric cancer, Abdominal Radiology (2018) 1–11. (cit. on pp. 194)

[305] W. H. Allum, S. P. Stenning, J. Bancewicz, P. I. Clark, R. E. Langley, Long-term results of a randomized trial of surgery with or without preoperative chemotherapy in esophageal cancer, Journal of clinical oncology 27 (30) (2009) 5062–5067. (cit. on pp. 194)

[306] D. Cunningham, W. H. Allum, S. P. Stenning, J. N. Thompson, C. J. Van de Velde, M. Nicolson, J. H. Scarffe, F. J. Lofts, S. J. Falk, T. J. Iveson, et al., Perioperative chemotherapy versus surgery alone for resectable

gastroesophageal cancer, New England Journal of Medicine 355 (1) (2006) 11–20. (cit. on pp. 194)

[307] P. van Hagen, M. Hulshof, J. Van Lanschot, E. Steyerberg, M. v. B. Henegouwen, B. Wijnhoven, D. Richel, G. Nieuwenhuijzen, G. Hospers, J. Bonenkamp, et al., Preoperative chemoradiotherapy for esophageal or junctional cancer, New England Journal of Medicine 366 (22) (2012) 2074–2084. (cit. on pp. 194)

[308] P. Lagergren, K. N. Avery, R. Hughes, C. P. Barham, D. Alderson, S. J. Falk, J. M. Blazeby, Health-related quality of life among patients cured by surgery for esophageal cancer, Cancer: Interdisciplinary International Journal of the American Cancer Society 110 (3) (2007) 686–693. (cit. on pp. 194)

[309] G. Lee, I. Hoseok, S.-J. Kim, Y. J. Jeong, I. J. Kim, K. Pak, D. Y. Park, G. H. Kim, Clinical implication of PET/MR imaging in preoperative esophageal cancer staging: comparison with pet/ct, endoscopic ultrasonography, and ct, Journal of Nuclear Medicine 55 (8) (2014) 1242–1247. (cit. on pp. 194)

[310] R. J. Gillies, P. E. Kinahan, H. Hricak, Radiomics: images are more than pictures, they are data, Radiology 278 (2) (2015) 563–577. (cit. on pp. 194)

[311] M. Secrier, X. Li, N. De Silva, M. D. Eldridge, G. Contino, J. Bornschein, S. MacRae, N. Grehan, M. O'Donovan, A. Miremadi, et al., Mutational signatures in esophageal adenocarcinoma define etiologically distinct subgroups with therapeutic relevance, Nature genetics 48 (10) (2016) 1131. (cit. on pp. 194)

[312] J. W. Fletcher, B. Djulbegovic, H. P. Soares, B. A. Siegel, V. J. Lowe, G. H. Lyman, R. E. Coleman, R. Wahl, J. C. Paschold, N. Avril, et al., Recommendations on the use of 18F-FDG PET in oncology, Journal of Nuclear Medicine 49 (3) (2008) 480–508. (cit. on pp. 199)

[313] D. Tamandl, J. Ta, R. Schmid, M. Preusser, M. Paireder, S. F. Schoppmann, A. Haug, A. Ba-Ssalamah, Prognostic value of volumetric PET parameters in unresectable and metastatic esophageal cancer, European journal of radiology 85 (3) (2016) 540–545. (cit. on pp. 200)

[314] T. Kajiwara, Y. Hiasa, T. Nishina, T. Matsumoto, S. Hori, S. Nadano, H. Iguchi, S. Takeji, E. Tsubouchi, Y. Ikeda, et al., Maximum standardized uptake value in 18F-fluoro-2-deoxyglucose positron emission tomography is associated with advanced tumor factors in esophageal cancer, Molecular and Clinical Oncology 2 (2) (2014) 313–321. (cit. on pp. 200)

[315] J. Jeon, J. Lee, D. Moon, H. Yang, M. Kim, G.-K. Lee, J. Zo, Prognostic significance of venous invasion and maximum standardized uptake value of 18F-FDG PET/CT in surgically resected T1N0 esophageal squamous cell carcinoma, European Journal of Surgical Oncology (EJSO) 43 (2) (2017) 471–477. (cit. on pp. 200)

[316] O. Palie, P. Michel, J.-F. Ménard, C. Rousseau, E. Rio, B. Bridji, A. Benyoucef, M.-E. Meyer, K. Jalali, S. Bardet, et al., The predictive value of treatment response using FDG PET performed on day 21 of chemoradiotherapy in patients with oesophageal squamous cell carcinoma. a prospective, multicentre study (RTEP3), European journal of nuclear medicine and molecular imaging 40 (9) (2013) 1345–1355. (cit. on pp. 200)

[317] W. Zhu, L. Xing, J. Yue, X. Sun, X. Sun, H. Zhao, J. Yu, Prognostic significance of SUV on PET/CT in patients with localised oesophagogastric junction cancer receiving neoadjuvant chemotherapy/chemoradiation: a systematic review and meta-analysis, The British journal of radiology 85 (1017) (2012) e694–e701. (cit. on pp. 200)

[318] K. G. Foley, R. K. Hills, B. Berthon, C. Marshall, C. Parkinson, W. G. Lewis, T. D. Crosby, E. Spezi, S. A. Roberts, Development and validation of a prognostic model incorporating texture analysis derived from standardised segmentation of PET in patients with oesophageal cancer, European radiology 28 (1) (2018) 428–436. (cit. on pp. 200)

[319] R. J. Beukinga, J. B. Hulshoff, L. V. van Dijk, C. T. Muijs, J. G. Burgerhof, G. Kats-Ugurlu, R. H. Slart, C. H. Slump, V. E. Mul, J. T. M. Plukker, Predicting response to neoadjuvant chemoradiotherapy in esophageal cancer with textural features derived from pretreatment 18F-FDG PET/CT imaging, Journal of nuclear medicine 58 (5) (2017) 723–729. (cit. on pp. 200)

[320] P. van Rossum, D. V. Fried, L. Zhang, W. L. Hofstetter, M. van Vulpen, G. J. Meijer, S. H. Lin, et al., The incremental value of subjective and quantitative assessment of 18F-FDG PET for the prediction of pathologic complete response to preoperative chemoradiotherapy in esophageal cancer, J Nucl Med 57 (5) (2016) 691–700. (cit. on pp. 200)

[321] G. Belli, S. Busoni, A. Ciccarone, A. Coniglio, M. Esposito, M. Giannelli, L. N. Mazzoni, L. Nocetti, R. Sghedoni, R. Tarducci, et al., Quality assurance multicenter comparison of different MR scanners for quantitative diffusion-weighted imaging, Journal of Magnetic Resonance Imaging 43 (1) (2016) 213–219. (cit. on pp. 200)

[322] P. S. van Rossum, A. L. van Lier, M. van Vulpen, O. Reerink, J. J. Lagendijk, S. H. Lin, R. van Hillegersberg, J. P. Ruurda, G. J. Meijer, I. M. Lips, Diffusion-weighted magnetic resonance imaging for the prediction of pathologic response to neoadjuvant chemoradiotherapy in esophageal cancer, Radiotherapy and Oncology 115 (2) (2015) 163–170. (cit. on pp. 200)

[323] S. E. Heethuis, L. Goense, P. S. van Rossum, A. S. Borggreve, S. Mook, F. E. Voncken, A. Bartels-Rutten, B. M. Aleman, R. van Hillegersberg, J. P. Ruurda, et al., DW-MRI and DCE-MRI are of complementary value in predicting pathologic response to neoadjuvant chemoradiotherapy for esophageal cancer, Acta Oncologica (2018) 1–8. (cit. on pp. 200)

[324] H. Zhang, P. Tang, X. Miao, Y. Gao, X. Shang, L. Gong, Z. Ma, M. Yang, H. Jiang, Z. Zhan, et al., Does tumor size improve the accuracy of prognostic prediction in patients with esophageal squamous cell carcinoma after surgical resection?, Oncotarget 7 (41) (2016) 66623. (cit. on pp. 200)

[325] E. Meldolesi, N. Dinapoli, R. Gatta, A. Damiani, V. Valentini, A. Farchione, How Can Radiomics Improve Clinical Choices?, in: Multidisciplinary Management of Rectal Cancer, Springer, 2018, pp. 135–149. (cit. on pp. 206)

[326] L. P. Clarke, R. J. Nordstrom, H. Zhang, P. Tandon, Y. Zhang, G. Redmond, K. Farahani, G. Kelloff, L. Henderson, L. Shankar, et al., The quantitative imaging network: NCI's historical perspective and planned goals, Translational oncology 7 (1) (2014) 1–4. (cit. on pp. 206)

[327] A. J. Buckler, L. Bresolin, N. R. Dunnick, D. C. Sullivan, Group, A collaborative enterprise for multi-stakeholder participation in the advancement of quantitative imaging, Radiology 258 (3) (2011) 906–914. (cit. on pp. 206)

[328] B. Ganeshan, K. A. Miles, R. C. Young, C. R. Chatwin, Texture analysis in non-contrast enhanced CT: impact of malignancy on texture in apparently disease-free areas of the liver, European journal of radiology 70 (1) (2009) 101–110. (cit. on pp. 206)

Acknowledgements

Ringraziamenti

Undertaking a Research Doctorate inevitably leads to high personal expectations. The main one is to acquire the research methodology skills. Of course, I did not imagine that this path could change me so deeply and that all the people around me would have irreversibly influenced this change.

I would like to thank Prof. Alessandro Bevilacqua for welcoming me to the Computer Vision Group, transmitting the care, I would almost say obsession, for details. Thank you for believing in me and for giving me the chance to work independently, teaching me that progress begins where our comfort zone ends.

I would like to thank Prof. Giampaolo Gavelli because his passion has inspired me during all these years. Thanks for the endless readings and for your interest in my work. It was an honour to collaborate with you.

Intraprendere un Dottorato di Ricerca porta inevitabilmente a concentrare su se stessi delle alte aspettative. La principale è quella di acquisire le metodologie per poter far ricerca. Certo non immaginavo che questo percorso potesse cambiarmi tanto nel profondo e che tutte le persone che mi sono state accanto avrebbero influenzato irreversibilmente questo cambiamento.

Vorrei ringraziare il Prof. Alessandro Bevilacqua per avermi accolto nel Computer Vision Group trasmettendomi la cura, direi quasi ossessione, per i dettagli. Grazie per aver creduto in me e per avermi dato la possibilità di lavorare in autonomia, insegnandomi che il progresso inizia dove finisce la propria zona di conforto.

Vorrei ringraziare il Prof. Giampaolo Gavelli perchè la sua passione mi ha ispirata durante tutti questi anni. Grazie per gli infiniti spunti di lettura e per il suo interesse nel mio lavoro. È stato un onore potermi confrontare con lei.

I would like to thank Dr. Domenico Barone and the Radiology Unit team of IRCCS-IRST in Meldola for being available, for the time they spent with me even when there was none. In the last PhD period, I had the pleasure of collaborating with Dr. Matteucci, Dr. Sarnelli and Prof. Paganelli, whom I thank for being professional and available. I take this opportunity to also thank Filippo Piccinini, a brilliant young researcher always ready to share his experiences.

Probably the most intense and stimulating period was that abroad, in London. I have met exceptional people and I carry with me the feeling that with some of them the bond will never break. First of all, I would like to thank Prof. Vicky Goh, an extraordinary woman who has never lost an opportunity to teach me and encourage me, making me get more in a few months than I had hoped. I would like to thank Prof. Gary Cook for his professionalism and for all the time he has dedicated to my work. The Department of Cancer Imaging is so prestigious because of you and your work. It was an honour to be part of it.

My work at King's College London would not have been the same without

Vorrei ringraziare il Dott. Domenico Barone e tutto il team dell'U.O. di Diagnostica per Immagini dell'IRCCS-IRST di Meldola per la grande disponibilità, per avermi dedicato il proprio tempo anche quando non ce n'era. Nell'ultimo periodo di Dottorato ho avuto il piacere di collaborare con la Dott.ssa Matteucci, la Dott.ssa Sarnelli e il Prof. Paganelli, che ringrazio per la professionalità e la disponibilità. Colgo l'occasione per ringraziare anche Filippo Piccinini, un brillante giovane ricercatore sempre pronto a condividere le proprie esperienze.

Probabilmente il periodo più intenso e stimolante è stato quello vissuto all'estero, a Londra. Ho conosciuto persone eccezionali e porto con me la sensazione che con alcune di loro il legame non si scioglierà mai. Vorrei ringraziare innanzitutto la Prof.ssa Vicky Goh, una donna straordinaria che non ha mai perso occasione per insegnarmi e incoraggiarmi, facendomi ottenere in pochi mesi più di quanto non avessi sperato. Vorrei ringraziare il Prof. Gary Cook per la sua professionalità e per tutto il tempo che ha dedicato al mio lavoro. Il Dipartimento del Cancer Imaging è così prestigioso grazie a voi e al vostro lavoro. È stato un onore farne parte.

Il mio lavoro presso il King's College London non sarebbe stato lo stesso sen-

Musib Siddique, Laura Zappulla, Amrita Guha, Yanjun Zou, Davide Prezzi and Bert-Ram Sah. Thanks Musib, you have immediately believed in me, encouraging me to demand the most from life, sure of my abilities. Thanks Laura for your infinite kindness. Even before leaving, I felt I could count on someone in London. Thanks Amrita for being my friend since the first day, for having dragged me with you even to the theatre, because in a life that deserves to be lived it is essential to find time for themselves and friends. Yanjun thanks for everything. Kindness and empathy speak only one language. You will always remain one of my best friends. Davide was a pleasure and an honour to work close to you. Thank you Bert-Ram for your collaboration. Your ambition pushed me to give my best.

za Musib Siddique, Laura Zappulla, Amrita Guha, Yanjun Zou, Davide Prezzi e Bert-Ram Sah. Grazie Musib per aver creduto in me sin dal primo giorno, incoraggiandomi a pretendere il massimo dalla vita, sicuro delle mie capacità. Grazie Laura per la tua infinita disponibilità. Prima ancora di partire ho sentito di poter contare su qualcuno a Londra. Grazie Amrita per essermi stata subito amica, per avermi trascinata con te anche a teatro, perché in una vita che meriti di esser vissuta è fondamentale trovare anche il tempo per sé e per gli amici. Yanjun grazie per tutto. La gentilezza e l'empatia parlano una sola lingua. Resterai sempre una delle mie migliori amiche. Davide è stato un piacere e un onore lavorare accanto a te. Grazie Bert-Ram per la tua collaborazione. La tua ambizione mi ha spinto a dare il massimo.

During these years, among many difficulties, sometimes I felt I could not go on. Nevertheless, I have never stopped. For this I must thank you mum and dad. Constantly present, part of me, you have patiently listened to me, always offering me the best scenario. Thanks for staying with me and for always being able to get a smile out of me. I dedicate all my successes to you because I consider them yours too.

Nel corso di questi anni, tra mille difficoltà, a volte ho sentito venir meno la forza per continuare. Eppure, non mi sono mai fermata. Per questo devo ringraziare voi, mamma e papà. Costantemente presenti, parte di me, mi avete pazientemente ascoltato, offrendomi sempre la più rosea delle prospettive. Grazie per essermi stati accanto e per esser sempre riusciti a strapparmi un sorriso. È a voi che dedico tutti i miei successi perché li considero anche vostri.

Although in life and especially during an obstacle course like this you can feel alone, I know that I will never be alone because my brother, Francesco, will always be there ready to run to me. Thanks to you and Lara for always being there.

Per quanto nella vita e soprattutto nel corso di un percorso a ostacoli come questo ci si possa sentir soli, io so che non sarò mai sola perché ci sarà sempre mio fratello, Francesco, pronto a correre da me. Grazie a te e Lara per esserci sempre.

In these three years I have met many people and all have contributed to a certain extent to make me the person I am now. I would like to especially thank those people who have been closer to me in the last period and who supported me when I needed it most.

In questi tre anni ho avuto modo di conoscere molte persone e tutte hanno contributo in una certa misura a rendermi la persona che sono ora. Vorrei ringraziare in particolare coloro che mi sono stati più vicini in quest'ultimo periodo e che mi hanno sostenuto quando ne ho avuto più bisogno.

I thank Caterina Campailla because she is always able to cheer me up. Valeria Mondini for being close to me in the darkest moments and for sharing with me the joys and the fears of this path. I thank Daniele Bellavista for always being ready to help me and for never having stopped believing in me. I thank Cecilia Muzzati, Luisa Parenzi, Federica Ponzi, Alessia Bene and Erika Ioannucci for strolls, phone calls and fun. Even if we cannot see each other frequently, I love I can count on you.

Ringrazio Caterina Campailla perché riesce sempre a farmi tornare il buon umore. Valeria Mondini per essermi stata vicina nei momenti più bui e per aver condiviso con me le gioie e le paure di questo percorso. Ringrazio Daniele Bellavista per essere sempre pronto ad aiutarmi e per non aver mai smesso di credere in me. Ringrazio Cecilia Muzzati, Luisa Parenzi, Federica Ponzi, Alessia Bene ed Erika Ioannucci per le uscite, le telefonate e il divertimento. Anche se non riusciamo a vederci spesso è bello poter contare su di voi.

These years would not have been the same without Fabio Viola and Francesco Antoniazzi, my companions in "misfortune". You have animated my days, improving both the good and the bad ones, constantly giving me advices. In particular, an infinite thank you goes to Fabio for sharing with me this journey and every single deadline of this doctorate. Thank you for being at my side in these moments and for patiently listening to me. I reached this goal thanks to you too.

Unable to create a complete list of names, I take this opportunity to thank all the "UNIBO" friends, both those who accompanied me during the graduation pathway both the new ones, for making the university life more interesting and pleasant.

Last but not least, I would like to thank all the members of my family, grandparents, uncles, cousins and little Leonardo. You are a reference point and I am lucky to have you.

Questi anni non sarebbero stati gli stessi senza Fabio Viola e Francesco Antoniazzi, miei compagni di sventura. Avete animato le mie giornate, migliorando sia le buone che le cattive, consigliandomi costantemente. In particolare, un grazie infinito va a Fabio per aver condiviso con me l'intero percorso e ogni singola scadenza di questo dottorato. Grazie per essermi stato accanto in questi momenti e per avermi pazientemente ascoltata. Ho raggiunto questo traguardo anche grazie a te.

Impossibile creare una lista completa dei nomi, colgo l'occasione per ringraziare anche tutti gli amici "UNIBO", sia quelli che mi hanno accompagnato durante il percorso di Laurea che i nuovi, per aver reso più interessante e piacevole la vita universitaria.

Ultimi ma non ultimi, desidero ringraziare tutti i componenti della mia famiglia, i nonni, gli zii, i cugini ed il piccolo Leonardo. Siete un punto di riferimento e sono fortunata ad avervi.

THESIS END

Serena Baiocco

Biomedical Engineer
PhD in Biomedical, Electrical and Systems Engineering (IBES) (2015-2018)

E-mail: s.baiocco@unibo.it; baiocco.serena@gmail.com
Research group website: http://cvg.deis.unibo.it
Personal website: https://www.unibo.it/sitoweb/s.baiocco/cv-en
(Curriculum Vitae available on the personal website)

Office address
Via Toffano 2/2, IT-40125, Bologna (BO), Italy

Home address
Via Mazzini 2/2, IT-40138, Bologna (BO), Italy